

TSUNAMIS--THE PROPAGATION OF

LONG WAVES ONTO A SHELF

Thesis by

Derek Garard Goring

In Partial Fulfillment of the Requirements

for the Degree of

Doctor of Philosophy

California Institute of Technology

Pasadena, California

1979

(Submitted November 17, 1978)

TSUNAMIS--THE PROPAGATION OF
LONG WAVES ONTO A SHELF

by

Derek Garard Goring

Project Supervisor:

Fredric Raichlen
Professor of Civil Engineering

Supported by
National Science Foundation
Grant Numbers ENV72-03587 and ENV77-20499
The New Zealand Ministry of Works and Development

W. M. Keck Laboratory of Hydraulics and Water Resources
Division of Engineering and Applied Science
California Institute of Technology
Pasadena, California

ACKNOWLEDGMENTS

Several people assisted in the execution of this investigation and it is with sincere gratitude that the writer acknowledges their help here.

Professor Fredric Raichlen, my thesis advisor, generously provided guidance, encouragement and assistance in all aspects of the project.

Professor Thomas J. R. Hughes gave advice and encouragement in the development of the finite element program. Discussions with Dr. Robert C. Y. Koh were of great help in the development of many of the numerical techniques used in the analysis and data reduction. His program, MAGIC, was used extensively, especially for plotting many of the figures. Fellow student Thierry Lepelletier often acted as a sounding board and his advice was helpful.

Mr. Elton F. Daly, supervisor of the shop and laboratory, gave invaluable assistance in all aspects of the design, construction and maintenance of laboratory equipment which made the experimental phase of this project a pleasure. Mr. Joseph J. Fontana and Mr. Richard Eastvedt constructed the laboratory equipment; Mr. David Byrum assisted with the experiments and drafted the figures; Mr. Peter Chang and Miss Ella Wong assisted with the experiments and with data reduction; Mrs. Adelaide R. Massengale typed the manuscript.

My wife, Trish, and children, Sonia and Todd, supported and helped me with their patience and love.

The research was supported by NSF Grant Nos. ENV72-03587 and ENV77-20499. The New Zealand Ministry of Works and Development generously granted the writer leave on full pay with allowances for the entire period of study. Experiments were conducted at the W. M. Keck Laboratory of Hydraulics and Water Resources.

This report is essentially the thesis of the same title submitted by the writer on 17 November 1978 to the California Institute of Technology in partial fulfillment of the requirements for the degree of Doctor of Philosophy in Civil Engineering.

ABSTRACT

The various aspects of the propagation of long waves onto a shelf (i.e., reflection, transmission and propagation on the shelf) are examined experimentally and theoretically. The results are applied to tsunamis propagating onto the continental shelf.

A numerical method of solving the one-dimensional Boussinesq equations for constant depth using finite element techniques is presented. The method is extended to the case of an arbitrary variation in depth (i.e., gradually to abruptly varying depth) in the direction of wave propagation. The scheme is applied to the propagation of solitary waves over a slope onto a shelf and is confirmed by experiments.

A theory is developed for the generation in the laboratory of long waves of permanent form, i.e., solitary and cnoidal waves. The theory, which incorporates the nonlinear aspects of the problem, applies to wave generators which consist of a vertical plate which moves horizontally. Experiments have been conducted and the results agree well with the generation theory. In addition, these results are used to compare the shape, celerity and damping characteristics of the generated waves with the long wave theories.

The solution of the linear nondispersive theory for harmonic waves of a single frequency propagating over a slope onto a shelf is extended to the case of solitary waves. Comparisons of this analysis with the nonlinear dispersive theory and experiments are presented.

Comparisons of experiments with solitary and cnoidal waves with the predictions of the various theories indicate that, apart from propagation, the reflection of waves from a change in depth is a linear process except in extreme cases. However, the transmission and the propagation of both the transmitted and the reflected waves in general are nonlinear processes. Exceptions are waves with heights which are very small compared to the depth. For these waves, the entire process of propagation onto a shelf in the vicinity of the shelf is linear. Tsunamis propagating from the deep ocean onto the continental shelf probably fall in this class.

TABLE OF CONTENTS

<u>Chapter</u>		<u>Page</u>
1	INTRODUCTION	1
	1.1 Objectives and Scope	2
2	LITERATURE SURVEY	4
3	THEORETICAL ANALYSIS	9
	3.1 Outline Derivation of the Long Wave Equations and Exact Solutions	11
	3.1.1 The Solitary Wave	25
	3.1.2 Cnoidal Waves	28
	3.2 Wave Generation	32
	3.2.1 The Derivation of a Generation Equation for Long Waves	32
	3.2.1.1 The Generation of Solitary Waves	37
	3.2.1.2 The Generation of Cnoidal Waves	40
	3.3 The Propagation of Long Waves onto a Shelf by the Nonlinear Dispersive Theory	43
	3.3.1 The Numerical Solution of the Boussinesq Equations for Constant Depth by a Finite Element Method	
	3.3.1.1 Analytical Formulation of the Problem	44
	3.3.1.2 Finite Element Formulation	47
	3.3.1.3 The Time Integration Algorithm	
	3.3.1.4 The Iterative Scheme	52
	3.3.1.5 Convergence and Accuracy	53
	3.3.2 Extension to the Case of Variable Depth	65
	3.4 The Propagation of Long Waves Onto a Shelf by the Linear Nondispersive Theory	69
	3.5 The Propagation of Long Waves to Infinity by the Nonlinear Dispersive Theory	80
	3.5.1 Summary of the Inverse Scattering Theory	81

<u>Chapter</u>		<u>Page</u>
3.5.2	The Analytic Solution for a Wave with sech ² Shape	82
3.5.3	Numerical Solutions for Waves with Arbitrary Shape	85
3.5.3.1	Scheme 1: A Sum of Functions	87
3.5.3.2	Scheme 2: A Single Function	89
4	EXPERIMENTAL EQUIPMENT AND PROCEDURES	92
4.1	The Wave Tank	92
4.2	The Wave Generator	96
4.2.1	The Hydraulic System	96
4.2.2	The Servo-System	103
4.2.3	The Carriage and Wave Plate	112
4.4	The Measurement of Wave Amplitudes	114
5	RESULTS AND DISCUSSION OF RESULTS	121
5.1	Wave Generation and Propagation in a Constant Depth	125
5.1.1	The Generation of Solitary Waves	125
5.1.2	The Propagation of Solitary Waves in a Constant Depth	142
5.1.3	The Generation of Cnoidal Waves	150
5.1.4	The Propagation of Cnoidal Waves in a Constant Depth	168
5.2	The Reflection of Long Waves from a Change in Depth	176
5.2.1	The Reflection of Solitary Waves from a Step	176
5.2.2	The Reflection of Cnoidal Waves from a Step	192
5.2.3	The Reflection of Solitary Waves from a Slope	205
5.3	The Transmission of Long Waves over a Change in Depth	226
5.3.1	The Transmission of Solitary Waves over a Step	226

<u>Chapter</u>	<u>Page</u>
5.3.2 The Transmission of Cnoidal Waves over a Step	232
5.3.3 The Transmission of Solitary Waves over a Slope	234
5.4 The Propagation of Long Waves on the Shelf	258
5.4.1 The Propagation of Solitary Waves on the Shelf	258
5.4.2 The Propagation of Cnoidal Waves on the Shelf	285
5.5 Waves Propagating off the Shelf	292
5.6 Application of the Results to the Tsunami Problem	294
6 CONCLUSIONS	301
LIST OF REFERENCES	306
LIST OF SYMBOLS	311
APPENDIX A Cnoidal Wave Relationships and Numerical Methods of Evaluation	315
APPENDIX B The Equation from Boussinesq (1872), the Boussinesq Equations and Solitary Waves	320
APPENDIX C The Linear Nondispersive Theory for a Single Harmonic Wave	322
APPENDIX D Tests of the Inverse Scattering Numerical Schemes	327
APPENDIX E The Nonlinear Nondispersive Theory for the Propagation of sech^2 Waves	322
APPENDIX F	337

LIST OF FIGURES

<u>Figure</u>		<u>Page</u>
3.1	(a) Incident wave propagating towards the shelf, (b) Wave transforming on the slope and (c) Reflected and transmitted waves	10
3.2	Definition sketch of flow situation	11
3.3	(a) and (b) The propagation of a sech^2 wave by various theories	20
3.3	(c) and (d) The propagation of a sech^2 wave by various theories	21
3.4	Various cnoidal waves	28
3.5	Comparison of the first three harmonic components of cnoidal waves (—) and Stokes waves (---)	31
3.6	Wave generation phase plane	33
3.7	Phase plane showing typical wave plate trajectory for a solitary wave	39
3.8	Typical wave plate trajectory for cnoidal wave generation	42
3.9	Definition sketch for numerical scheme	45
3.10	Finite element mesh	48
3.11	Wave profiles calculated using the numerical scheme for (a) $H/h = 0.7$ and (b) $H/h = 0.1$	58
3.12	Shapes of the waves after they have travelled ten wave lengths for (a) $H/h = 0.7$ and (b) $H/h = 0.1$	59
3.13	Comparison of wave propagation using the scheme developed for this project (—) with the scheme of Hughes, Liu and Zimmermann (1978) (---)	63
3.14	Wave propagation using the scheme of Hughes, Liu and Zimmermann (1978) with two elements in the depth	64
3.15	Definition sketch for extension to variable depth	65
3.16	The varying bottom considered as a series of steps	68

<u>Figure</u>		<u>Page</u>
3.17	Definition sketch for <u>linear nondispersive</u> theory	71
4.1	Schematic drawing of a typical tank module (after French (1969))	93
4.2	(a) Cross-section of the shelf, (b) Elevation of the slopes ($L = 150$ cm, 300 cm and 450 cm) and (c) Elevation of the half-sine transition	95
4.3	(a) Schematic drawing of the wave generator with the "long" cylinder and (b) Schematic drawing of the wave generator with the "short" cylinder	97
4.4	Overall view of the wave generator	98
4.5	View of the hydraulic supply system	99
4.6	Block circuit diagram of the function generator	105
4.7	View of the front face of the electronics	106
4.8	Block circuit diagram of the servo-controller	111
4.9	Examples of the actual and programmed wave plate displacements for (a) solitary wave generation and (b) cnoidal wave generation	113
4.10	Drawing of the blade holder	115
4.11	Drawing of a typical wave gauge (after Raichlen (1965))	116
4.12	Circuit diagram for wave gauges (after Okoye (1970))	116
4.13	(a) View of the calibration device and (b) View of the master control	118
4.14	Calibration curves for (a) manual calibration and (b) calibration using the A/D converter	120
5.1	The layout and the various aspects of a typical experiment	122
5.2	Oscillograph record from a typical experiment of a solitary wave propagating over a step onto a shelf	123
5.3	Oscillograph record of the waves generated by a ramp trajectory ($S = 10.33$ cm, $\tau = 0.80$ sec and $h = 10$ cm)	126

<u>Figure</u>		<u>Page</u>
5.4	Solitary wave generation trajectories, $H/h = 0.1$ to 0.7	129
5.5	Oscillograph record of the waves generated by the solitary wave trajectory with $H/h = 0.2$ ($S = 10.33$ cm, $\tau = 2.044$ sec and $h = 10$ cm)	130
5.6	Comparison of the shape of solitary waves with relative heights (a) $H/h = 0.15$ and (b) $H/h = 0.61$ with the theories of Boussinesq and McCowan	132
5.7	Variation of H/S with the relative wave height, H/h , for solitary wave generation	135
5.8	Comparison of the "frequency" of experimental solitary waves with that of the Boussinesq theory	138
5.9	Variation of the inverse scattered to measured wave height ratio, H_{INV}/H , with relative wave height, H/h	140
5.10	Comparison of the volume under experimental solitary waves with that of the Boussinesq and McCowan theories	141
5.11	Variation of the damping exponent, f , with relative wave height H/h for solitary waves	144
5.12	Variation of the inverse scattered to measured height ratio, H_{INV}/H , with relative wave height H/h of solitary waves as they propagate	146
5.13	Variation of the "frequency," $\Omega\sqrt{h/g}$, with relative wave height, H/h , of solitary waves as they propagate	147
5.14	Variation of celerity, c/\sqrt{gh} , with relative wave height, H/h , from (a) this study and (b) Naheer (1977)	149
5.15	Trajectory shapes, waves and associated data for cnoidal wave trajectories CN1 to CN6	152
5.16	(a) Comparison of the shape of experimental cnoidal waves with theory (Trajectories CN1, CN2 and CN3)	154
5.16	(b) Comparison of the shape of experimental cnoidal waves with theory (Trajectories CN4, CN5 and CN6)	155
5.17	Oscillograph record showing the waves generated by trajectory CN4 with $h = 20$ cm, $S = 11.18$ cm and $T = 2.90$ sec	156

<u>Figure</u>		<u>Page</u>
5.18	Oscillograph record showing the waves generated by trajectory CN4 with $h = 20$ cm, $S = 11.18$ and $T = 4.28$ sec	157
5.19	Variation of the relative time, t_o/T , with non-dimensional period, $T\sqrt{g/h}$, for cnoidal wave generation trajectories	160
5.20	Theoretical variation of H/S with the inverse non-dimensional period, $1/T\sqrt{g/h}$, for cnoidal waves	162
5.21	Variation of H/S with the inverse nondimensional period $1/T\sqrt{g/h}$ for cnoidal wave generation	164
5.22	Oscillograph record of the waves generated by trajectory CN6 with $h = 5$, $S = 6.07$ cm and $T = 3.40$ sec	167
5.23	Variation of the damping exponent, f , with relative wave height, H_o/h , for cnoidal waves	170
5.24	Comparison of the amplitudes of the first three Fourier components of experimental cnoidal waves with the theory	172
5.25	Variation of the celerity parameter, α , with Ursell Number, HL^2/h^3 , for cnoidal waves	173
5.26	Variation of celerity of solitary and cnoidal waves with relative wave height, H/h	175
5.27	Variation of the wave height ratio, H_R/H_I , with the relative incident wave height, H_I/h_1	179
5.28	Variation of the inverse scattered wave height ratio, H_{R_INV}/H_I , with the relative incident wave height, H_I/h_1	180
5.29	Variation of the volume ratio, V_R/V_I , with the relative incident wave height, H_I/h_1	181
5.30	Variation of the wave height ratio, H_R/H_I , with depth ratio, h_1/h_2	188
5.31	Variation of the inverse scattered wave height ratio, H_{R_INV}/H_I , with depth ratio, h_1/h_2	189
5.32	Variation of the volume ratio, V_R/V_I , with depth ratio, h_1/h_2	190

<u>Figure</u>		<u>Page</u>
5.33	Incident cnoidal waves ($H_I/h_1 = 0.1$, $T\sqrt{g/h} = 27.2$) and the waves reflected from the step for various depths	194
5.34	Variation of the wave height ratio, H_R/H_I , with relative incident wave height, H_I/h_1 , for cnoidal waves	196
5.35	Variation of the wave height ratio, H_R/H_I , with depth ratio, h_1/h_2 , for cnoidal waves	198
5.36	Comparison of the experimental reflected cnoidal waves with those calculated from the <u>linear dispersive theory</u>	201
5.37	Comparison of the experimental reflected cnoidal waves with those calculated from the <u>nonlinear dispersive theory</u>	202
5.38	Theoretical variation of (a) the Fourier transform of a solitary wave and (b) the reflection coefficient with frequency	207
5.39	The waves reflected when a solitary wave propagates up various slopes as predicted by the <u>linear nondispersive theory</u>	210
5.40	Variation of the reflected wave height ratio, H_R/H_I , with length ratio, L/λ , as predicted by the <u>linear nondispersive theory</u>	212
5.41	Variation of the relative reflected wave height, $H_R(L/\lambda)/H_R(0)$, with length ratio, L/λ , as predicted by the <u>linear nondispersive theory</u>	213
5.42	(a) Variation of the reflected wave height ratio, H_R/H_I , with length ratio, L/λ , for a depth ratio of $h_1/h_2 = 3$	216
5.42	(b) Variation of the inverse scattered reflected wave height ratio, $H_{R_{INV}}/H_I$, with length ratio, L/λ , for a depth ratio of $h_1/h_2 = 3$	217
5.43	(a) Variation of the reflected wave height ratio, H_R/H_I , with length ratio, L/λ , for a depth ratio of $h_1/h_2 = 4$	218

<u>Figure</u>		<u>Page</u>
5.43	(b) Variation of the inverse scattered reflected wave height ratio, $H_{R_{INV}}/H_I$, with length ratio, L/ℓ , for a ratio of $h_1/h_2 = 4$	219
5.44	Comparison of the theoretical reflected waves with the experimental wave	224
5.45	Variation of the transmitted wave height ratio, H_T/H_I , with the relative incident wave height, H_I/h_1 , for solitary waves	227
5.46	Variation of the transmitted wave height ratio, H_T/H_I , with depth ratio, h_1/h_2 , for solitary waves	229
5.47	Variation of the transmitted wave frequency ratio, Ω_T/Ω_I , with relative incident wave height, H_I/h_1	231
5.48	Variation of the transmitted wave height ratio, H_T/H_I , with relative incident wave height, H_I/h_1 , for cnoidal waves	233
5.49	Theoretical variation of (a) the Fourier transform of a solitary wave and (b) the transmission coefficient with frequency	236
5.50	Theoretical variation of (a) the transmitted wave height ratio, H_T/H_I , and (b) the sum-of-the-squares with length ratio, L/ℓ , for solitary waves as predicted by the <u>linear nondispersive theory</u>	238
5.51	Comparison of physical and numerical experiments for a solitary wave with height $H_I = 3.1$ cm propagating from a depth $h_1 = 31.08$ cm over a slope with length $L = 15.54$ cm onto a shelf with depth $h_2 = 15.54$ cm	241
5.52	Comparison of physical and numerical experiments for a solitary wave with height $H_I = 3.1$ cm propagating from a depth $h_1 = 31.08$ cm over a slope with length $L = 150$ cm onto a shelf with depth $h_2 = 15.54$ cm	242
5.53	Comparison of physical and numerical experiments for a solitary wave with height $H_I = 3.1$ cm propagating from a depth $h_1 = 31.08$ cm over a slope with length $L = 300$ cm onto a shelf with depth $h_2 = 15.54$	243

<u>Figure</u>	<u>Page</u>
5.54 Comparison of physical and numerical experiments for a solitary wave with height $H_I = 3.1$ cm propagating from a depth $h_1 = 31.08$ cm over a slope with length $L = 450$ cm onto a shelf with depth $h_2 = 15.54$ cm	244
5.55 Comparison of transmitted waves for incident waves of various heights for a length ratio of $L/\ell = 2.00$	248
5.56 (a) Comparison of transmitted waves for incident waves of various heights and for various length ratios for a depth ratio of $h_1/h_2 = 3$	250
5.56 (b) Comparison of transmitted waves for incident waves of various heights and for various length ratios for a depth ratio of $h_1/h_2 = 3$	251
5.57 Variation with length ratio of (a) the relative difference for slopes, $(S - S_{lin})/S_{lin}$ and (b) the relative difference for wave heights, $(H_T - H_{Tlin})/H_{Tlin}$ and the Ursell Number, U (for $h_1/h_2 = 3$)	255
5.58 Comparison of the actual and the predicted quantities given by (a) Eq. (5.24) and (b) Eq. (5.25)	256
5.59 Experimental wave records showing sech^2 waves with approximate relative wave height of $H_T/h_2 = 0.1$ propagating on the shelf	261
5.60 Experimental wave records showing sech^2 waves with approximate relative wave height of $H_T/h_2 = 0.3$ propagating on the shelf	262
5.61 Experimental wave records showing sech^2 waves with approximate relative wave height of $H_T/h_2 = 0.5$ propagating on the shelf	263
5.62 Comparison of waves measured experimentally with those calculated by various theories at locations given by $x/h_2 = 0, 8.88$ and 13.31	266
5.63 Comparison of waves measured experimentally with those calculated by various theories at locations given by $x/h_2 = 17.75, 22.19$ and 26.63	267
5.64 Comparison of waves measured experimentally with those calculated by various theories at locations given by $x/h_2 = 31.07, 35.50$ and 39.94	268

FiguresPage

5.65	Views of the separation caused by a solitary wave propagating over (a) the step and (b) the half-sine transition ($h_1 = 20.5$ cm, $h_2 = 4.96$ cm, $H_T = 2.0$ cm)	270
5.66	Variation of the relative height, H/h_2 , of a wave as it propagates on the shelf. Comparison of experiments in which the step was used with those in which the half-sine transition was used	272
5.67	Theoretical variation of the distance a sech^2 wave propagates to breaking, $\Omega_T x_b / \sqrt{gh_2}$, with relative wave height, H_T/h_2	275
5.68	Theoretical variation of the Ursell Number, $U\Omega_T^2 h_2/g$, with propagation distance, x/x_b , for an initial relative wave height of $H_T/h_2 = 0.1$; nonlinear dispersive and nondispersive theories	277
5.69	Theoretical variation of the Ursell Number, $U\Omega_T^2 h_2/g$, with propagation distance, x/x_b , for an initial relative wave height of $H_T/h_2 = 0.3$; nonlinear dispersive and nondispersive theories	278
5.70	Theoretical variation of the Ursell Number, $U\Omega_T^2 h_2/g$, with propagation distance, x/x_b , for an initial relative wave height of $H_T/h_2 = 0.5$; nonlinear dispersive and nondispersive theories	279
5.71	Theoretical variation of the distance for dispersive effects to become important, x_d/h_2 , with relative wave height, H_T/h_2	282
5.72	Theoretical variation of the distance for nonlinear effects to become important, $\Omega_T x_n / \sqrt{gh_2}$, with relative wave height, H_T/h_2	284
5.73	Oscillograph records of experiments in which cnoidal waves of the same height, $H_T/h_2 = 0.28$, propagate on the shelf	287
5.74	Oscillograph records of experiments in which cnoidal waves of the same period, $T\sqrt{g/h_2} = 57.1$, propagate on the shelf	289
5.75	Comparison for the propagation of cnoidal waves on the shelf between experiment and the <u>nonlinear dispersive theory</u>	291

<u>Figure</u>		<u>Page</u>
5.76	Comparison for the propagation of solitary waves off the shelf into deep water between experiment and the linear <u>dispersive theory</u>	293
5.77	Schematic drawing of the continental slope off the coast of California	295
E.1	The $x - t$ plane for a sech^2 wave propagating into still water by the <u>nonlinear nondispersive theory</u>	333

<u>Table</u>		<u>Page</u>
3.1	Number of iterations for convergence for various nodal spacing numbers, N_x , and time step numbers, N_T	55
3.2	Comparison of initial and final conserved quantities for the numerical scheme	56
3.3	Maximum Ursell Numbers for a particular number of solitary waves to emerge from a sech^2 wave	85
5.1	Solutions of the solitary wave due to Boussinesq, McCowan and Laitone (Naheer (1977))	133
5.2	Comparison of generation trajectories for $t_o/T = 0.200$. ξ/ξ_{max} for a half period for various wave height and period combinations	161
5.3	Maximum relative incident wave heights for non-breaking waves on the shelf as predicted by the <u>linear nondispersive theory</u>	185
5.4	Wave height ratios for experiments, (H_R/H_I) , <u>linear nondispersive theory</u> , (H_R/H_I) _{L.N.} ^{Expt} , <u>linear dispersive theory</u> , (H_R/H_I) _{L.D.} , and <u>nonlinear dispersive theory</u> , (H_R/H_I) _{N.D.}	204
5.5	Reflected wave height ratios, (a) H_R/H_I and (b) $H_{R_{\text{INV}}}/H_I$, for various length ratios and relative incident wave heights for depth ratio $h_1/h_2 = 3$ (<u>nonlinear dispersive theory</u>)	221
5.6	Reflected wave height ratios, (a) H_R/H_I and (b) $H_{R_{\text{INV}}}/H_I$, for various length ratios and relative incident wave heights for depth ratio $h_1/h_2 = 1.5$ (<u>nonlinear dispersive theory</u>)	223
5.7	Transmitted waves calculated using the <u>nonlinear dispersive theory</u> for $h_1/h_2 = 3$	228
5.8	Details of the experiments for propagation of solitary waves on a shelf, shown in Figs. 5.58 to 5.60	264
5.9	Comparison of transmitted wave data for the experiments presented in Fig. 5.66	273
5.10	Relative differences between the theories in (a) the slope of the front face and (b) the transmitted wave height for tsunamis which are solitary waves	298

CHAPTER 1

INTRODUCTION

Long waves are waves with lengths which are large compared to the depth of water in which they are propagating. Among the waves which fall in this class are "tsunamis" or, as they are sometimes called, "tidal waves." The word "tsunami" is a Japanese word which means "harbor wave." It has been adopted by the scientific community in preference to "tidal wave" to mean an earthquake-generated sea wave.

The earthquakes which generate tsunamis usually involve vertical movements of the sea bed. Such an earthquake occurred in Alaska in 1964; it generated a tsunami which propagated throughout the Pacific causing damage at various locations along the West Coast of the United States, particularly in Crescent City, California. An important aspect in trying to either avoid or prepare for such a disaster is to understand how a tsunami propagates.

In the deep ocean where the depth may be 3500 m a tsunami might typically have a length of about 300 km and a height of 1 m and travel at a speed of 700 km/hr. The propagation of the tsunami would proceed essentially in constant depth through the deep ocean until it reached the region of shallower depth which surrounds most land masses--the continental shelf. Here the depth decreases considerably; of interest in this investigation was to determine

how such changes in depth affect tsunamis or tsunami-like waves.

Since field observations of tsunamis are difficult except at the coast, the investigation was carried out by means of physical and analytical models.

1.1 Objectives and Scope

The objective of this investigation was to examine, both experimentally and theoretically, the various aspects of the propagation of long waves onto a shelf, i.e., the reflection, transmission and propagation of the waves on the shelf, for both abrupt and gradual changes in depth. Of equal importance was to determine if the linear mathematical models which commonly are used in the analysis of tsunamis are sufficient or if it is necessary to use more complicated nonlinear models.

The waves used in this study were primarily solitary waves. These were chosen because it can be shown theoretically that waves which have net positive volume eventually, if the propagation distance is sufficient, will break up into a series of solitary waves. For analysis, solitary waves have the advantage that, although nonlinear, they can be described with just two parameters: the wave height and the depth. Additional benefits are: they propagate with constant form in constant depth and generally they can be separated from reflected waves. Periodic waves in the form of cnoidal waves also were considered for propagation over abrupt changes in depth.

To facilitate the experimental investigation, a theory was developed for the generation in the laboratory of long waves of

permanent form, i.e., solitary and cnoidal waves. The theoretical investigation included the development of a finite element technique of solving the one-dimensional Boussinesq equations. This was applied to the full problem of solitary waves propagating over a slope onto a shelf and was confirmed by physical experiments.

A review of previous studies of the propagation of long waves onto a shelf is presented in Chapter 2. The theoretical analysis which includes a review of the classical long wave theories and their application to this problem, wave generation theory and the development of the finite element numerical method are presented in Chapter 3. The experimental equipment and procedures are described in Chapter 4. The results of the investigation are presented and discussed in Chapter 5, and conclusions based upon these are described in Chapter 6.

CHAPTER 2

LITERATURE SURVEY

The nonlinear partial differential equations which govern the propagation of long waves have been known since the 19th century. However, until recently, only the equation arising from a linear approximation to these equations has been used for predicting the propagation of long waves onto a shelf.

The theory arising from this equation is termed the linear nondispersive theory. The solutions of the theory for long waves of arbitrary shape propagating over abrupt and gradual slopes are presented in Lamb (1932). (Note, this represents the sixth edition of the work. It was originally published in 1879.) Lamb (1932, §176) shows, for a step, the reflection and transmission coefficients are given by:

$$K_R = \frac{(1 - \sqrt{h_1/h_2})}{(1 + \sqrt{h_1/h_2})} \quad , \quad (2.1)$$

and

$$K_T = \frac{2}{1 + \sqrt{h_2/h_1}} \quad , \quad (2.2)$$

respectively, where h_1 is the upstream depth and h_2 is the depth on the shelf.

For a "gradual" slope, i.e., a slope on which the depth changes by only a small fraction of itself within the limits of a wavelength,

Lamb (1932, §185) shows the reflection and transmission coefficients are given by Green's Law:

$$K_R = 0 \quad , \quad (2.3)$$

and

$$K_T = (h_1/h_2)^{\frac{1}{4}} \quad , \quad (2.4)$$

respectively.

Solutions of the linear nondispersive theory for the slopes between an abrupt slope (i.e., a step) and a gradual slope have been presented by Kajiura (1961), Wong *et al.* (1963) and Dean (1964). For all of these studies the solution was obtained for an harmonic wave with a single frequency in the steady state.

Kajiura (1961) proposed a method of solution for slopes of general shape and presented the solutions for two cases:

- i) A slope on which the depth varies as the square of the distance along it. The solution for the wave on the slope is a function of $x^{\frac{1}{2}}$.
- ii) A continuous slope determined such that the basic equation is transformed into an equation which gives simple expressions for the reflection and transmission coefficients.

Wong *et al.* (1963) and Dean (1964) obtained the solution for a slope on which the depth varies linearly as a function of the distance along it. The solution of the wave on the slope is a function of Bessel functions.

Recall, the solutions for the two extremes of abrupt and gradual slopes were for long waves of arbitrary shape; therefore, if it is valid to do so, the solutions can be applied directly to solitary or cnoidal waves. However, for slopes between the two extremes, the solutions are for harmonic waves with a single frequency only; therefore the solutions, even if valid, cannot be applied directly to solitary or cnoidal waves.

The full nonlinear equations were first solved for the problem of long waves propagating onto a shelf by Madsen and Mei (1969). Using the equations developed by Mei and Le Méhauté (1966), which incorporate the effect of a slowly varying depth, Madsen and Mei (1969) developed a numerical method of solution based on the method-of-characteristics scheme of Long (1964). The slowly varying depth assumption used by Madsen and Mei (1969) is equivalent to the gradual slope mentioned earlier.

Madsen and Mei (1969) found theoretically and experimentally that as a solitary wave propagates up a gradual slope its shape changes, with the front face of the wave steepening and secondary waves emerging from the back face of the wave. Eventually, either on the slope or on the shelf, the waves separate into a series of solitary waves followed by a train of oscillatory waves. Earlier, Street *et al.* (1968) experimentally had observed similar behavior but over a propagation distance which was insufficient for the solitary waves to emerge fully from the main train.

Analytical solutions of the problem of solitary waves propagating over a gradual slope were found independently by Tappert and Zabusky (1971) and Johnson (1973). By assuming zero reflection and slowly varying depth, a variable depth form of the KdV equation can be derived and, using the same techniques as were used by Gardner *et al.* (1967) to solve the KdV in constant depth, asymptotic solutions for the solitary waves which emerge on the shelf can be obtained. The number of solitary waves which will emerge on the shelf is a function of only the depth ratio, h_1/h_2 , as given by:

$$P = \frac{1}{2} \left[1 + \left\{ 1 + 8 \left(\frac{h_1}{h_2} \right)^{9/4} \right\}^{-1/2} \right] \quad (2.5)$$

$$N < P$$

where the number of waves, N , is strictly less than P . The height of the solitary waves which emerge is given by:

$$\frac{H_n}{H_0} = \left(\frac{h_1}{h_2} \right)^{-2} (P - n)^2 \quad , \quad (2.6)$$

$$n = 1, 2, \dots, N$$

where H_0 is the height of the incident solitary wave.

To summarize, previous investigations in the field of long waves propagating onto a shelf have dealt with one of the following aspects of the problem:

- (i) Linear waves of arbitrary shape propagating over an extreme slope (i.e., either gradual or abrupt);

(ii) Linear harmonic waves with a single frequency propagating over a slope; or

(iii) Solitary waves propagating over a gradual slope.

The question of which of the theories to use for the propagation of long waves in various situations is addressed by Hammack and Segur (1978). They show, using asymptotic arguments and a rectangular wave shape, the choice of which theory to use depends on the volume of the initial wave and an Ursell Number based on the amplitude and length of the initial wave. Applying their criteria to tsunamis, they show the linear nondispersive theory is the relevant theory for the propagation of the leading wave of a tsunami in a constant depth from the generation region to the beach.

CHAPTER 3

THEORETICAL ANALYSIS

The theoretical aspects of the problem can be described referring to Fig. 3.1 which shows the series of events which takes place as a long wave propagates onto a shelf.

Fig. 3.1(a) shows the incident wave propagating towards the shelf in a region of constant depth. The various theories for long waves propagating in a constant depth are reviewed in Section 3.1 and exact solutions are described.

As with other investigators (e.g. Madsen and Mei (1969)), for the analysis the incident wave was assumed to be a solitary wave (although, as mentioned previously, recent work by Hammack and Segur (1978) has cast some doubt on the practical validity of this). A theory for the generation, in the laboratory, of solitary waves and also of cnoidal waves is presented in Section 3.2.

As the wave propagates through a region of variable depth its shape changes as shown in Fig. 3.1(b), and eventually the wave splits up into two waves: a reflected wave traveling to the left in the deep water and a transmitted wave traveling to the right on the shelf, see Fig. 3.1(c). Two theories are presented which solve the problem. In Section 3.3 a finite element method of solution of the Boussinesq equations for the case of waves propagating in a constant depth is presented, then the method is extended to the case of waves propagating

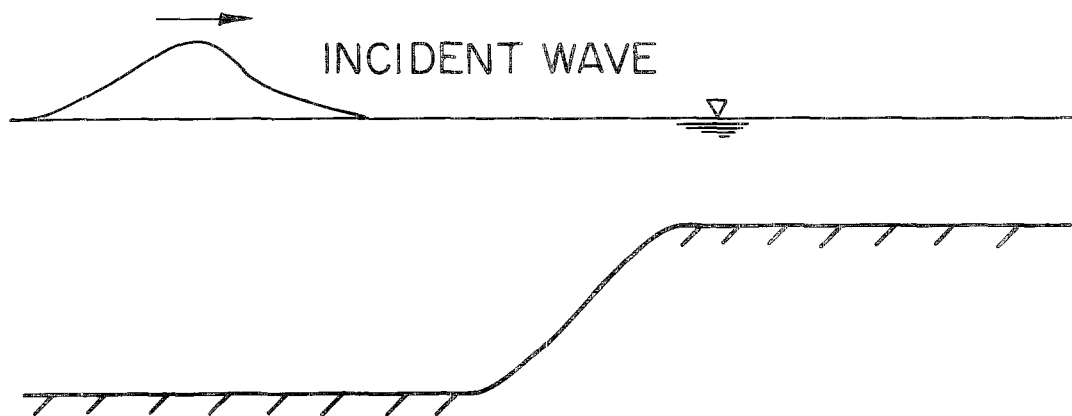


Fig. 3.1(a) Incident wave propagating towards the shelf.

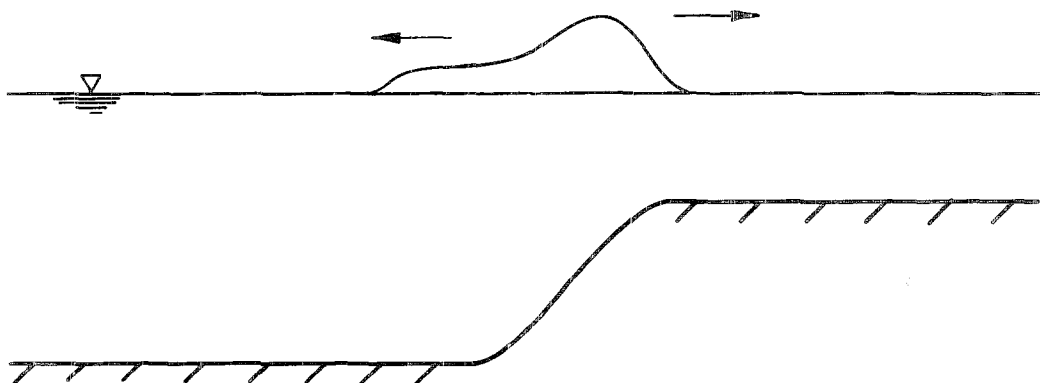


Fig. 3.1(b) Wave transforming on the slope.

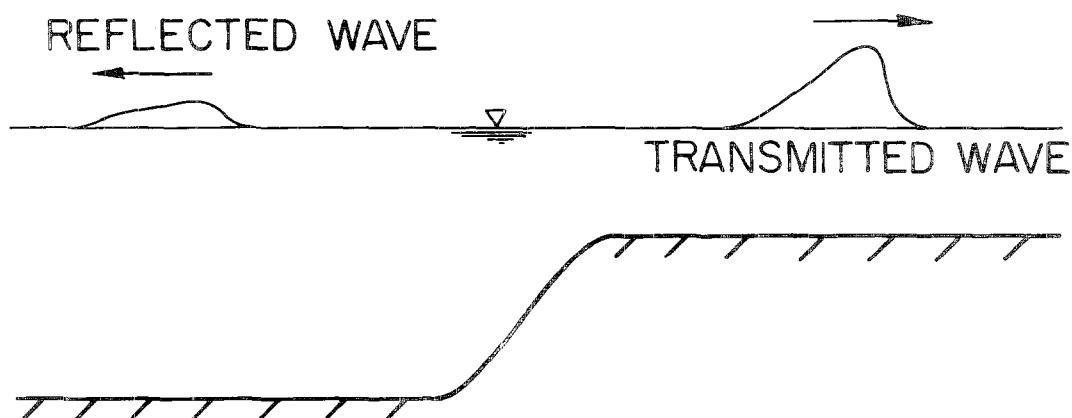


Fig. 3.1(c) Reflected and transmitted waves.

in a region with variable depth. This solution is the more accurate of those considered because it incorporates, up to second order, the effects of dispersion and nonlinearity. A first order solution in which these effects are neglected is presented in Section 3.4 where the theory developed by others for the solution for incident waves which are harmonic is reviewed and applied to the case of an incident wave which is a solitary wave.

Finally in this chapter the technique of inverse scattering is described and numerical schemes for its solution are presented. Inverse scattering allows one to determine the final state of a long wave if it propagates to infinity in constant depth in the absence of friction. It was used in this study to analyze the reflected wave. (This will be discussed in detail in Section 5.2.)

3.1 Outline Derivation of the Long Wave Equations and Exact Solutions

The long wave equations can be derived in numerous ways; the approach which is outlined here follows that of Whitham (1974).

Consider the flow situation shown in Fig. 3.2 which shows a

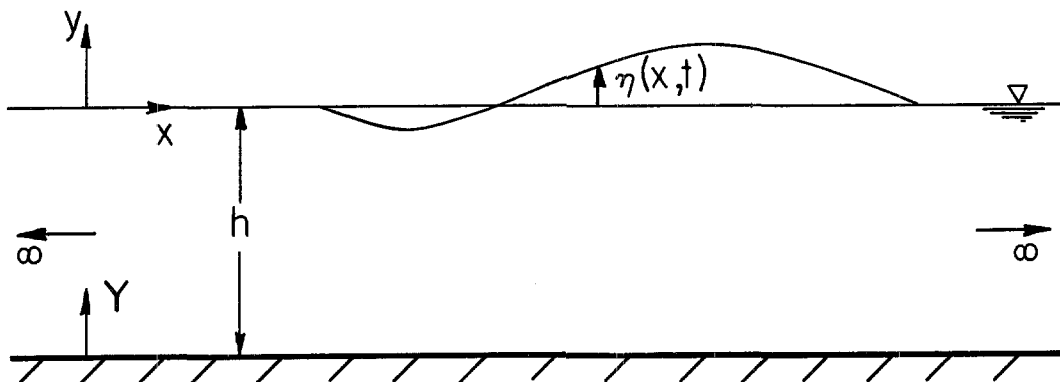


Fig. 3.2 Definition Sketch of the Flow Situation

wave propagating in water of depth h in a region of infinite horizontal extent. The vertical y axis has its origin at the still water level. The displacement of the free surface from the still water level is $\eta(x, t)$. Assuming inviscid, irrotational, incompressible flow, there exists a velocity potential $\Phi(x, y, t)$ which satisfies the Laplace equation:

$$\nabla^2 \Phi = 0 \quad -h \leq y \leq \eta \quad . \quad (3.1)$$

The boundary conditions are:

i) No flow through the bottom boundary:

$$\Phi_y = 0 \quad y = -h \quad , \quad (3.2)$$

ii) Kinematic boundary condition at the surface:

$$\eta_t + \Phi_x \eta_x = \Phi_y \quad y = \eta \quad , \quad (3.3)$$

iii) Dynamic boundary condition at the surface:

$$\Phi_t + \frac{1}{2} (\Phi_x^2 + \Phi_y^2) + g\eta = 0 \quad y = \eta \quad . \quad (3.4)$$

The waves under consideration are long waves which are defined as waves whose characteristic horizontal length ℓ is large compared to the depth h , i.e. $\ell > h$. For long waves the horizontal velocity Φ_x is approximately constant over the depth so the velocity potential can be expanded in terms of the parameter $Y = h + y$ which is small compared to the characteristic horizontal length ℓ .

$$\Phi(x, y, t) = \sum_{n=0}^{\infty} y^n f_n(x, t) . \quad (3.5)$$

By substituting Eq. (3.5) into Eq. (3.1), equating like powers of Y and applying the boundary condition $\frac{\Phi}{y} = 0$ at $Y = 0$, the expansion is simplified to:

$$\Phi(x, y, t) = \sum_{n=0}^{\infty} \frac{y^{2n}}{(2n)!} \frac{\partial^{2n} f_0}{\partial x^{2n}} . \quad (3.6)$$

Each variable is now normalized by scaling by a characteristic quantity:

$$x = \frac{x^*}{\ell} \quad y = \frac{y^*}{h} \quad \eta = \frac{\eta^*}{H}$$

$$t = \frac{t^* \sqrt{gh}}{\ell} \quad \Phi = \frac{\Phi^*}{\ell H} \sqrt{\frac{h}{g}}$$

where ℓ is the characteristic horizontal length and H is the characteristic height of the wave and starred symbols denote the original dimensional variables. (Henceforth all equations will be dimensionless unless specifically stated otherwise.) When these variables are substituted into the expansion, Eq. (3.6), and the remaining boundary conditions, Eqs. (3.3) and (3.4), two dimensionless numbers emerge: $\alpha = H/h$ and $\beta = h^2/\ell^2$. In writing the expansion, Eq. (3.5), it was assumed that $\beta < 1$ (i.e. the length of the wave is large compared to the depth). It is also necessary to assume that $\alpha < 1$ (i.e. the wave height is small compared to the depth).

The equations which arise by substituting the expansion, Eq. (3.6), into the boundary conditions, Eqs. (3.3) and (3.4), and retaining terms to order α^2 , β^2 and $\alpha\beta$ are termed the Boussinesq equations after Boussinesq (1872) and are as follows:

$$\eta_t + \{(1 + \alpha\eta)u\}_x - \frac{1}{6}\beta u_{xxx} = 0 \quad (3.7)$$

$$u_t + \alpha uu_x + \eta_x - \frac{1}{2}\beta u_{xxt} = 0 \quad . \quad (3.8)$$

Notice in Eqs. (3.7) and (3.8) the dimensionless numbers, α and β , have different roles. The number α appears before the nonlinear terms indicating their importance relative to the other terms depends on the wave height to depth ratio, H/h . The number β modifies the third derivative terms which are a correction for vertical acceleration. Hence as β decreases (i.e. as the wave gets longer) the importance of vertical accelerations decreases (or, equivalently, the pressure distribution with depth approaches hydrostatic).

For Eqs. (3.7) and (3.8) to apply, it is further required that α and β be of the same order. (To illustrate the reason for this, consider the case where β is so much greater than α that $\beta^2 > \alpha$; then terms of order β^2 should be included in preference to terms of order α , and Eqs. (3.7) and (3.8) are not appropriate.) This introduces another dimensionless number $U = \alpha/\beta$, noted by Stokes (1847) but named after Ursell who, in his 1953 paper, explicitly expounded the importance of the ratio α/β . Hence for the Boussinesq equations

to be applicable, the Ursell Number must be of order unity. Since α represents the magnitude of nonlinear effects and β represents the magnitude of dispersive effects, the Ursell Number of order unity implies a balance of nonlinear and dispersive effects.

The velocity u appearing in Eqs. (3.7) and (3.8) is the velocity at the bottom $y = -1$. It is often more convenient to use the depth averaged velocity:

$$\bar{u} = \int_{-1}^{\eta} \Phi_x dy \quad . \quad (3.9)$$

The Boussinesq equations then take the form:

$$\eta_t + \{(1 + \alpha\eta)\bar{u}\}_x = 0 \quad , \quad (3.10)$$

$$\bar{u}_t + \alpha\bar{u}\bar{u}_x + \eta_x - \frac{1}{3}\beta\bar{u}_{xxt} = 0 \quad . \quad (3.11)$$

The Boussinesq equations cannot, in general, be solved in closed form so it is necessary to resort to a numerical scheme such as that which will be described in Section 3.3.

The Boussinesq equations are the most general form of the long wave equations since the other well known equations can be deduced from them. These will now be listed along with their general solutions:

- i) For small amplitude, very long waves ($\alpha \ll 1$, $\beta \ll 1$) Eqs. (3.10) and (3.11) reduce to:

$$\eta_t + \bar{u}_x = 0 \quad ,$$

$$\text{and} \quad \bar{u}_t + \eta_x = 0 \quad , \quad (3.12)$$

$$\text{or} \quad \bar{u}_{tt} - \bar{u}_{xx} = 0 \quad .$$

These are the linear nondispersive equations which have solutions in dimensional terms of the form:

$$\bar{u} = f(kx - \omega t) + g(kx + \omega t) \quad ,$$

$$\text{where} \quad \omega^2 = c_o^2 k^2 \quad \text{and} \quad c_o = \sqrt{gh} \quad . \quad (3.13)$$

Waves propagate at constant speed and with permanent shape in $+x$ and $-x$ directions.

ii) For small amplitude waves whose length is not as great as those considered above ($\alpha \ll 1$, $\beta < 1$ and $U \ll 1$), Eqs. (3.10) and (3.11) reduce to:

$$\eta_t + \bar{u}_x = 0 \quad ,$$

$$\text{and} \quad \bar{u}_t + \eta_x - \frac{1}{3} \beta \bar{u}_{xxt} = 0 \quad , \quad (3.14)$$

$$\text{or} \quad \bar{u}_{tt} - \bar{u}_{xx} = \frac{1}{3} \beta \bar{u}_{xxtt} \quad .$$

These are the linear dispersive equations which have solutions in dimensional terms of the form:

$$\bar{u} = A e^{i(kx - \omega t)} + B e^{i(kx + \omega t)} \quad ,$$

where $\omega^2 = \frac{c_o^2 k^2}{1 + \frac{1}{3} k^2 h^2}$, (3.15)

This implies that waves propagate with speeds which are a function of the length of the wave and the waves do not have a permanent shape.

iii) For finite amplitude, very long waves ($\alpha < 1$, $\beta \ll 1$ and $U \gg 1$), Eqs. (3.10) and (3.11) reduce to:

$$\eta_t + \{(1 + \alpha\eta)\bar{u}\}_x = 0 ,$$

$$\bar{u}_t + \alpha\bar{u}\bar{u}_x + \eta_x = 0 , \quad (3.16)$$

which are the nonlinear nondispersing equations (sometimes called the Airy equations). By reverting back to dimensional quantities, Eqs. (3.16) can be expressed more simply in characteristic form:

$$\frac{d}{dt} (\bar{u} \pm 2c) = 0 \text{ on } \frac{dx}{dt} = \bar{u} \pm c , \quad (3.17)$$

where $c = \sqrt{g(h + \eta)}$.

For waves propagating to the right into still water, Eqs. (3.17) predict that the wave amplitude and the velocity are constant along the characteristic curves $dx/dt = \bar{u} + c$, which are straight lines. Thus, each portion of the wave travels at its own speed, $\bar{u} + c$. This process was termed amplitude dispersion by Lighthill and Whitham (1955). At the leading edge the velocity and amplitude are zero, hence

the leading edge travels at speed \sqrt{gh} ; under a crest the velocity and the amplitude are each greater than zero, hence the crest moves faster than the leading edge. Eventually therefore the crest will overtake the leading edge and the wave will break. Breaking may actually occur before this depending on the shape of the wave.

iv) For waves traveling to the right only, the velocity can be expressed in terms of the amplitude:

$$\bar{u} = \eta - \frac{\alpha}{4} \eta^2 + \frac{1}{6} \beta \eta_{xx} , \quad (3.18)$$

and the Boussinesq equations then reduce to the KdV equation (after Korteweg and de Vries (1896)):

$$\eta_t + \eta_x + \frac{3}{2} \alpha \eta \eta_x + \frac{1}{6} \beta \eta_{xxx} = 0 . \quad (3.19)$$

Since,

$$\eta_x = -\eta_t + O(\alpha, \beta) ,$$

Eq. (3.19) can be expressed to the same order as:

$$\eta_t + \eta_x + \frac{3}{2} \alpha \eta \eta_x - \frac{1}{6} \beta \eta_{xxt} = 0 , \quad (3.20)$$

which is more amenable to numerical solution (see, for example, Peregrine (1966)).

The KdV equation has exact analytical solutions in the form of waves of permanent shape--solitary waves and cnoidal waves.

Before discussing these waves in detail, an example is presented which illustrates how waves propagate by the theories discussed:

- (i) Linear Nondispersive
- (ii) Linear Dispersive
- (iii) Nonlinear Nondispersive
- (iv) Nonlinear Dispersive

Referring to Fig. 3.3(a), the problem is posed where at $t = 0$ there exists, in water of constant depth and infinite extent, a wave with profile given in dimensional terms by:

$$\eta(x, 0) = H \operatorname{sech}^2 \kappa x \quad , \quad (3.21)$$

For the example shown, the following conditions apply:

$$\frac{H}{h} = 0.05 \text{ and } \kappa = \sqrt{\frac{3}{4} \frac{H}{h^3}} \quad ,$$

and for $t > 0$ the wave is assumed to propagate to the right into still water. Figs. 3.3(a), (b), (c) and (d) show the wave profiles calculated using the various theories listed above at intervals of nondimensional time, $t\sqrt{g/h}$, of 25. The abscissas are $\left(\frac{x}{h} - t\sqrt{\frac{g}{h}}\right)$ which means that the figures are the series of events an observer would see if he were traveling at speed \sqrt{gh} .

In Fig. 3.3(a) the profiles from all four theories are plotted together. In Figs. 3.3(b), (c) and (d) the linear nondispersive theory is compared respectively with the linear dispersive theory, the nonlinear nondispersive theory and the nonlinear dispersive theory. Under the linear nondispersive theory, the wave would remain stationary and retain its original shape. Under the linear dispersive theory the wave would propagate as if it consisted of a linear

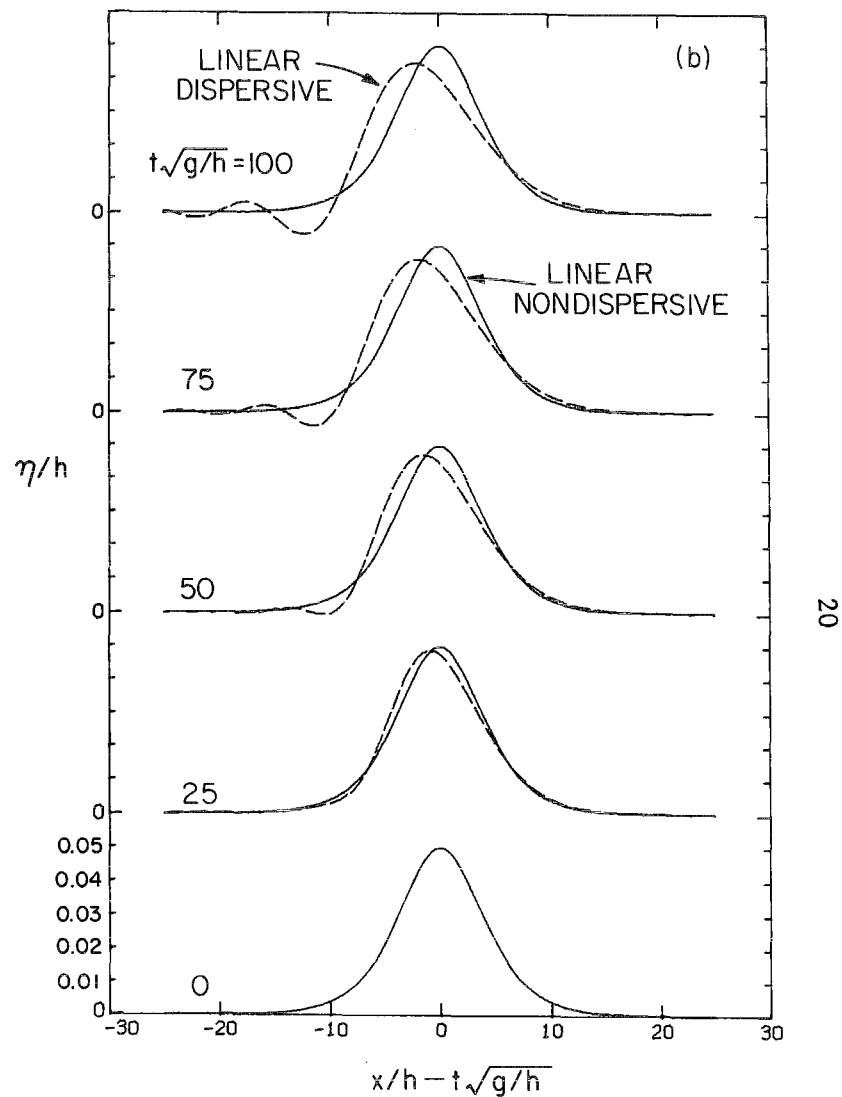
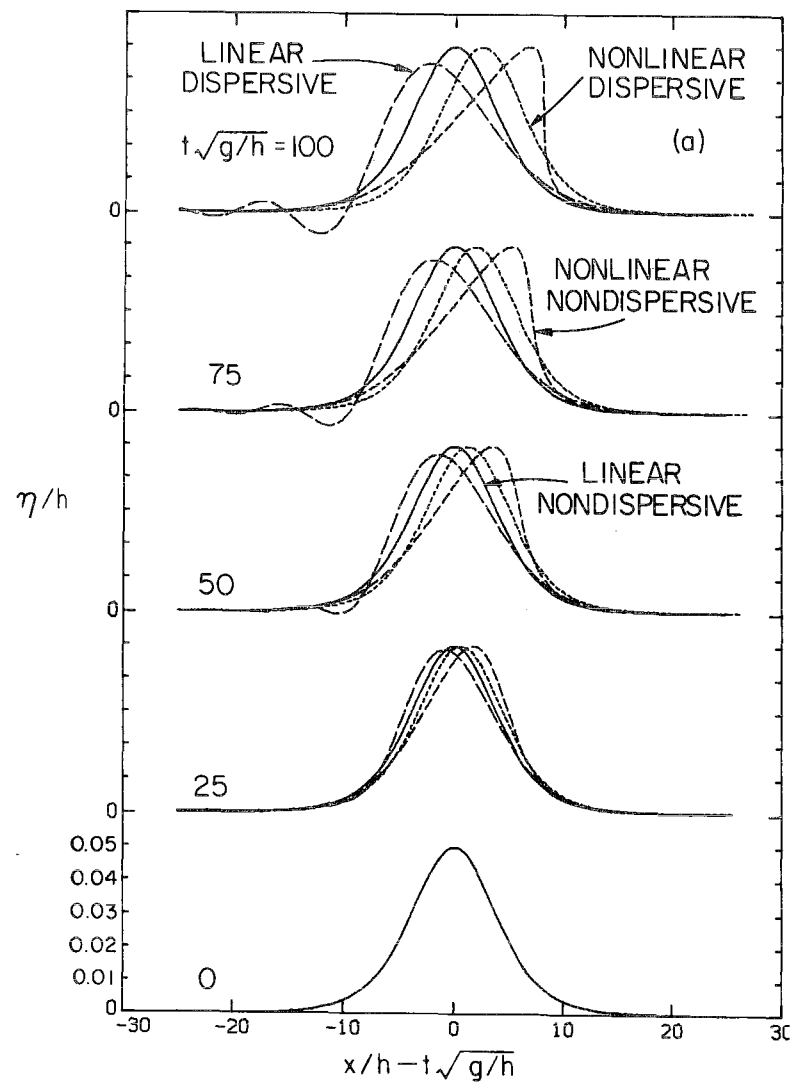


Fig. 3.3(a) and (b) The propagation of a sech^2 wave by various theories.

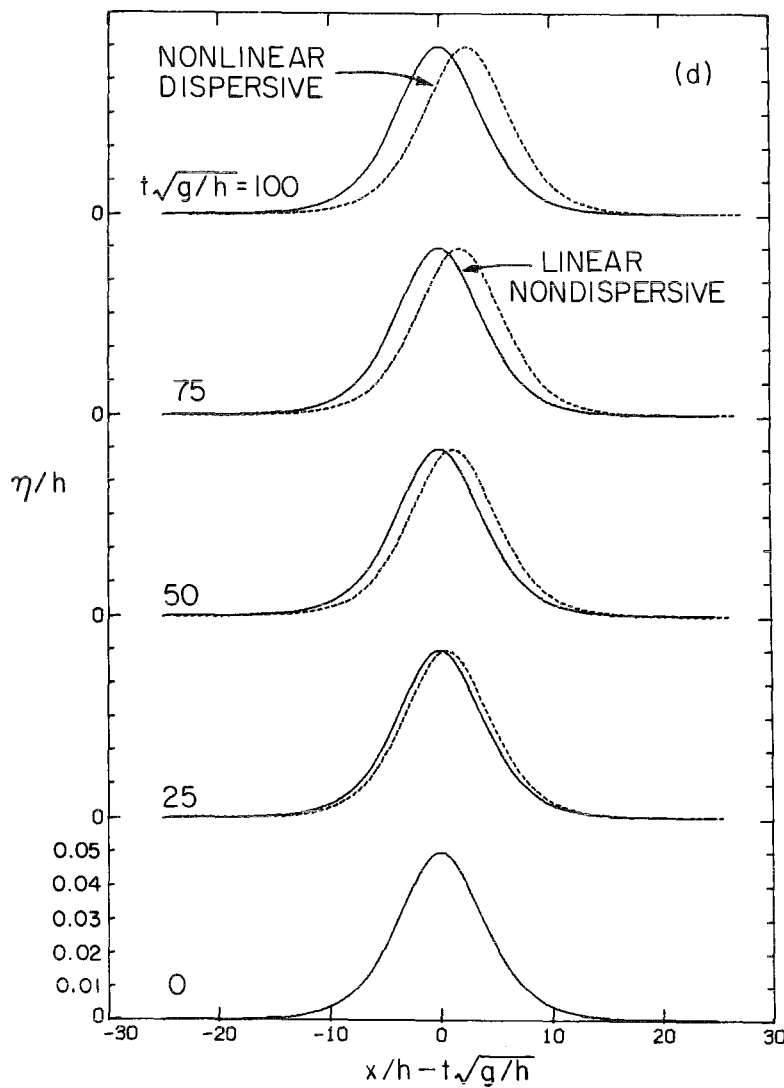
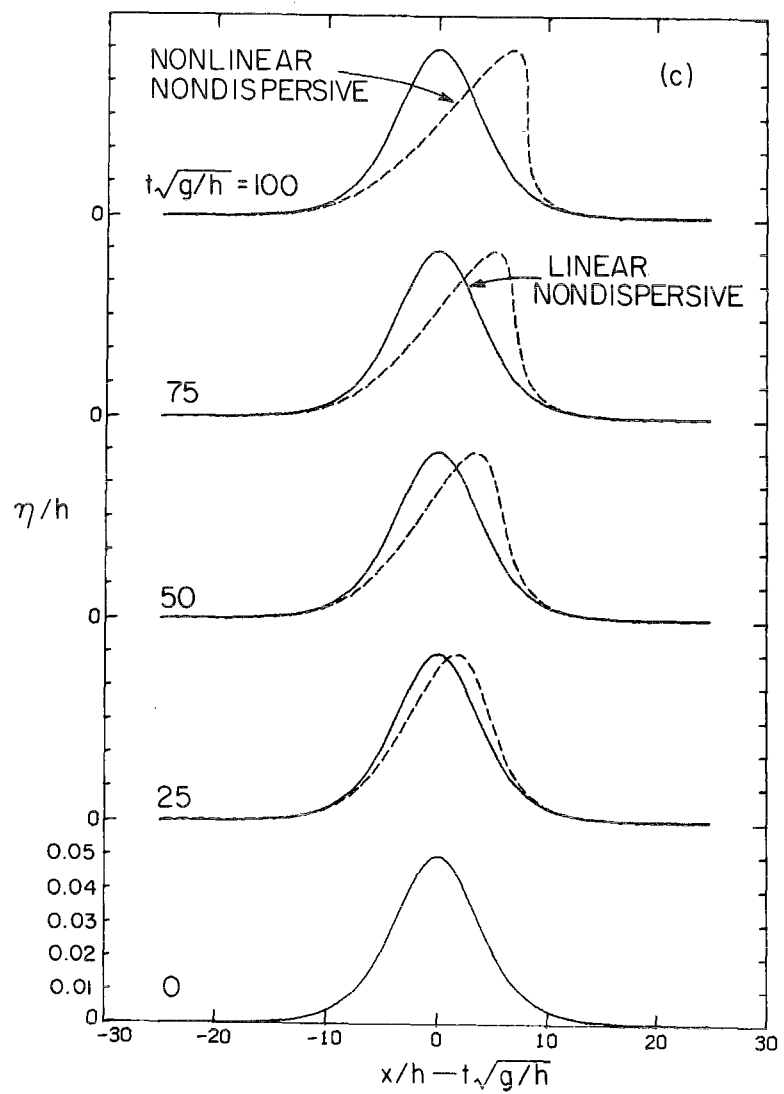


Fig. 3.3(c) and (d) The propagation of a sech^2 wave by various theories.

combination of periodic waves with different lengths each propagating with a speed given by the dispersion relation in Eq. (3.15). Since short waves travel slower than long waves, the waves disperse, hence the overall shape would change. The nonlinear nondispersive theory predicts that the wave would retain its integrity but that the coordinates behind the crest would stretch while those in front would contract causing the back face to flatten and the front face to steepen while the crest height remained constant. The wave would begin to break when the front face became vertical (at $t\sqrt{g/h} = 90.92$ in this case).

In fact for the wave chosen and described by Eq. (3.21) none of the above would occur because the wave number κ was selected such that the initial profile is a solitary wave, i.e. an exact solution of the KdV equation. Hence, the wave propagates unchanged in shape as shown in Fig. 3.3(d). The wave travels faster than it would under the linear nondispersive theory because the celerity is $c = \sqrt{g(h+H)}$.

The form the wave takes as it propagates in a particular case depends on the relative magnitudes of the dispersive term $\frac{1}{6} c_o h^2 \eta_{xxx}$ and the nonlinear term $\frac{3}{2} \frac{c_o}{h} \eta \eta_x$ in the dimensional form of the KdV equation:

$$\eta_t + c_o \left(1 + \frac{3}{2} \frac{\eta}{h} \right) \eta_x + \frac{1}{6} c_o h^2 \eta_{xxx} = 0 \quad , \quad (3.22)$$

where

$$c_o = \sqrt{gh} \quad .$$

For a wave with initial profile given by Eq. (3.21), $\kappa = \sqrt{\frac{3}{4} \frac{H}{h^3}}$ represents the case where the nonlinear term balances the dispersive term and the wave shape remains constant. If $\kappa \ll \sqrt{\frac{3}{4} \frac{H}{h^3}}$ the nonlinear term is larger than the dispersive term ($U \gg 1$) and amplitude dispersion as shown in Fig. 3.3(c) takes place. If $\kappa \gg \sqrt{\frac{3}{4} \frac{H}{h^3}}$ (i.e. the wave is more peaked than a solitary wave of the same height) the dispersive term is larger than the nonlinear term ($U \ll 1$) and frequency dispersion as shown in Fig. 3.3(b) takes place.

Since the KdV or Boussinesq equations can be solved in the near field only by approximate numerical techniques, it is desirable to use the other equations wherever possible since they can be solved exactly in many cases. The problem of which of the equations to use in various circumstances is addressed by Hammack and Segur (1978). They show that for initial conditions of a rectangular wave, the applicable equation depends on the initial volume and initial Ursell Number, but that eventually, after a propagation time which is a function of the initial conditions, only the KdV equation will apply. This introduces another important parameter in long wave propagation: the propagation time.

It is evident from Fig. 3.3 that if the time of interest is $0 \leq t\sqrt{g/h} < 25$ then any of the four theories can be used since they all provide essentially the same results. However for $t\sqrt{g/h} > 25$ the solutions become quite different. The interpretation of this is that both dispersive and nonlinear effects take some propagation time (or distance) to become important. For example, for the nonlinear

nondispersive theory a characteristic propagation time is the time to breaking, which for an initial condition given by Eq. (3.21) is approximately

$$t_b \sqrt{g/h} \approx \frac{0.9}{\kappa h} (H/h)^{-1} \quad (3.24)$$

Thus for this theory and for this type of wave, the propagation time for nonlinear effects to become important is some percentage of $t_b \sqrt{g/h}$. No similarly clear cut time is available for the linear dispersive theory.

For a particular problem of long wave propagation, such as the problem of long waves propagating onto a shelf which was considered in this study, it is difficult to say *a priori* under what conditions it is necessary to use the full Boussinesq equations and when it is possible to use one of the other theories.

One approach is to assume that the linear nondispersive theory applies unless the propagation time is sufficient for nonlinear or dispersive effects to become important; however the magnitude of this propagation time is, in general, ill-defined. The approach taken in this study was to use the nonlinear dispersive theory and experiments as a basis to find the conditions under which the other theories would give the same results. The sort of conclusion which can be drawn from this is that if, for example, the nonlinear dispersive theory and the nonlinear nondispersive theory give the same results in a particular case, then the propagation time was insufficient for dispersive effects to become important.

3.1.1 The Solitary Wave

The solitary wave was observed first by Scott Russell (1844). It consists of a single hump of water entirely above still water level and extends from $x = -\infty$ to $x = \infty$. Three theories are available which describe the wave profile; those obtained by: Boussinesq (1872), McCowan (1891) and Laitone (1963). The most important of these is that due to Boussinesq (1872) since it is this form which is an exact solution of the KdV equation. In dimensional quantities the Boussinesq solitary wave is:

$$\eta(x, t) = H \operatorname{sech}^2 \sqrt{\frac{3}{4} \frac{H}{h^3}} (x - ct) \quad ,$$

where (3.25)

$$c = \sqrt{g(h + H)} \quad .$$

The McCowan and Laitone solitary waves result from higher order theories but do not fit experimental data any better than does Eq. (3.25) (see for example Naheer (1977), French (1969)).

The solitary wave has the unique property that in a depth h it is completely defined by the wave height, H . This simplicity of shape along with its ease of generation in the laboratory and its propagation with constant shape make the solitary wave a particularly suitable model wave to study experimentally. For this study it had the added advantage that when considering reflections from a slope or a step the reflected wave was completely separate from the incident wave.

3.1.2 Cnoidal Waves

Cnoidal waves are periodic solutions of the KdV equation.

In dimensional form they are defined (e.g. Svendsen (1974)) as:

$$\eta(x, t) = y_t - h + H \operatorname{cn}^2 \left\{ 2K \left(\frac{x}{L} - \frac{t}{T} \right) \mid m \right\} , \quad (3.26)$$

where $m = \alpha/\beta$ is the elliptic parameter (sometimes called k^2), $K = K(m)$ is the first complete elliptic integral, cn is one of the Jacobian elliptic functions (hence the name cnoidal), y_t is the height of the trough above the bottom, L is the wave length and T is the period.

It is noted that for given depth h , cnoidal waves are defined by any two of the following:

- i) the wave length L (or the period T),
- ii) the wave height H ,
- iii) the elliptic parameter m (or the elliptic integral K).

The relationships between these and the other parameters were described by Wiegel (1960) and Svendsen (1974). They are presented in Appendix A along with the numerical techniques which were developed during this study for their evaluation.

The elliptic parameter m , by definition, is the Ursell Number, i.e., $U = \alpha/\beta$. Another type of Ursell Number which can be defined in terms of physical parameters is HL^2/h^3 . The difference in these two definitions is in the use of the characteristic length ℓ for $U = \alpha/\beta$ and the use of the wave length L for HL^2/h^3 . The two numbers are related by:

$$\frac{HL^2}{h^3} = \frac{16}{3} m K^2 , \quad (3.27)$$

hence the lengths are related by:

$$L = \frac{4}{\sqrt{3}} K \ell \quad . \quad (3.28)$$

Since the elliptic integral K is a function of only the parameter m , HL^2/h^3 is also a function only of m ; hence either of the Ursell Numbers can be used to define the shape of the cnoidal wave. The parameter m can take values between 0 and 1. At the two extremes:

i) As $m \rightarrow 0$ (and, consequently, $HL^2/h^3 \rightarrow 0$), the Jacobian elliptic function, cn , becomes the trigonometric function, \cos , and $K \rightarrow \frac{\pi}{2}$. Hence the equation for cnoidal waves, Eq. (3.26) becomes:

$$\eta = \frac{H}{2} \cos 2\pi \left(\frac{x}{L} - \frac{t}{T} \right) \quad , \quad (3.29)$$

i.e., a harmonic wave.

ii) As $m \rightarrow 1$ (and, consequently, $HL^2/h^3 \rightarrow \infty$), the Jacobian elliptic function, cn , becomes the hyperbolic function, sech , and K , L and $T \rightarrow \infty$. Hence the equation for cnoidal waves, Eq. (3.26), becomes:

$$\eta = H \operatorname{sech}^2 \sqrt{\frac{3}{4} \frac{H}{h^3}} (x - ct) \quad , \quad (3.30)$$

i.e., a solitary wave.

The range of cnoidal wave shapes from $m = 0$ and $HL^2/h^3 = 0$ to $m \rightarrow 1$ and $HL^2/h^3 \rightarrow \infty$ is shown in Fig. 3.4. For $HL^2/h^3 \leq 10$, the shape appears sinusoidal to the eye but in fact at $HL^2/h^3 = 10$ the crest amplitude is about 20% greater than the trough amplitude, i.e.,

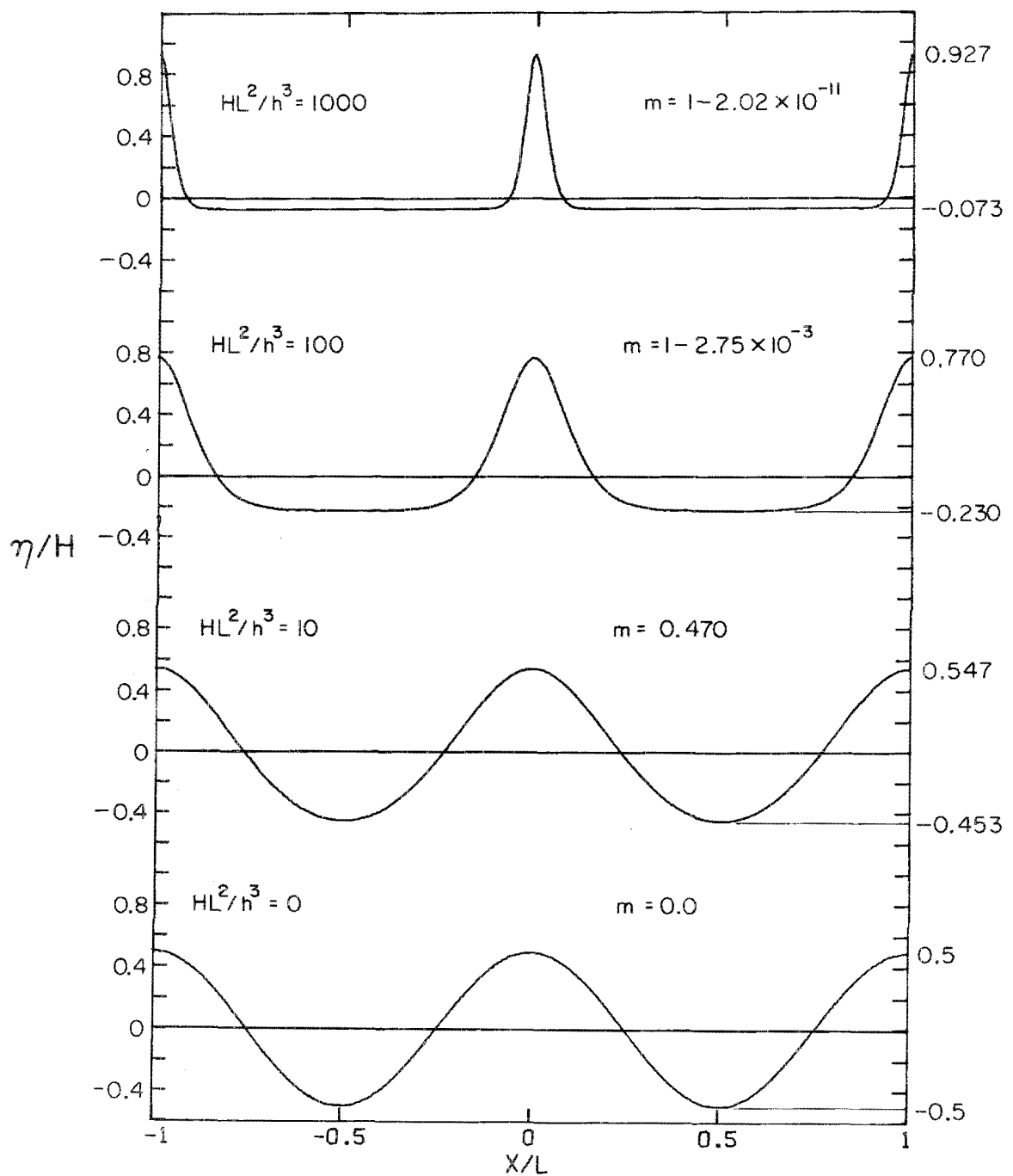


Fig. 3.4 Various cnoidal waves.

$\frac{\eta_{\text{crest}}}{H} = 0.547$, $\frac{\eta_{\text{trough}}}{H} = 0.453$. As HL^2/h^3 increases this difference increases, and as a consequence the crest becomes more peaked and the trough becomes flatter. At $HL^2/h^3 = 1000$, the cnoidal waves have the appearance of a train of solitary waves however the wave length L is still finite and there is still a trough below still water level; therefore, the waves are still cnoidal waves.

It is of interest to compare cnoidal waves with Stokes waves in shallow water. Stokes waves can be obtained as a perturbation solution of the KdV equation (see, for example, Whitham (p. 471)):

$$\eta_s(x, t) = \frac{H}{2} \cos \theta + \frac{3}{16} \frac{H^2}{k^2 h^3} \cos 2\theta + \frac{27}{512} \frac{H^3}{k^4 h^6} \cos 3\theta + \dots \quad (3.31)$$

where

$$\theta = kx - \omega t$$

The dispersion relation is:

$$\frac{\omega/k}{\sqrt{gh}} = 1 - \frac{1}{6} k^2 h^2 + \frac{9H^2}{64 k^2 h^2} + \dots \quad (3.32)$$

where

$$\omega = 2\pi/T \text{ and } k = 2\pi/L$$

Notice that the perturbation parameter $\frac{H}{k^2 h^3} = \frac{1}{(2\pi)^2} \frac{HL^2}{h^3}$

is another form of the Ursell Number. For the Stokes expansion to be valid, $\frac{H}{k^2 h^3} \ll 1$ or, equivalently $\frac{HL^2}{h^3} \ll (2\pi)^2$.

Stokes waves may be compared to cnoidal waves by expressing cnoidal waves in their Fourier Series form and comparing the harmonics of the Stokes waves with these cnoidal wave components:

$$\frac{\eta_c}{H} = \frac{y_t - h}{H} + \operatorname{cn}^2 \left(\frac{2K}{2\pi} \theta \mid m \right) = \sum_{n=1}^{\infty} a_n \cos n\theta \quad , \quad (3.33)$$

where

$$a_n = \frac{1}{2\pi} \int_0^{2\pi} \frac{\eta_c}{H} \cos n\theta \, d\theta \quad . \quad (3.34)$$

Now, since $\frac{(y_t - h)}{H} = \frac{(K - E)}{mK} - 1$, it is evident that η_c/H is a function only of m . The Ursell Number, HL^2/h^3 , is also a function only of m (as given by Eq. (3.27)); hence, it follows that η_c/H and thus the Fourier amplitudes a_n are functions only of HL^2/h^3 . Eq. (3.31) indicates the amplitudes of the series for η_s/H are also functions of only HL^2/h^3 ; therefore, Stokes waves and cnoidal waves can be compared by comparing the amplitudes of the components in Eqs. (3.31) and (3.33) as functions of HL^2/h^3 . This is done in Fig. 3.5 where the magnitude of the first three components in each case are plotted against HL^2/h^3 . The dashed lines represent the Stokes wave amplitudes given by Eq. (3.31). A continuous form for the a_n , defined by Eq. (3.34), could not be found so the integral was evaluated numerically using the Fast Fourier Transform algorithm. (It is noted that although only three Fourier amplitudes are plotted, the Fourier series representation of cnoidal waves is an infinite series.)

Fig. 3.5 shows the component amplitudes of Stokes waves and cnoidal waves are coincident for $HL^2/h^3 \leq 10$ but diverge as HL^2/h^3 increases. Since Stokes waves are only an approximate solution of the KdV equation while cnoidal waves are an exact solution, Fig. 3.5 indicates Eq. (3.31) is an accurate approximation only for $HL^2/h^3 \leq 10$.

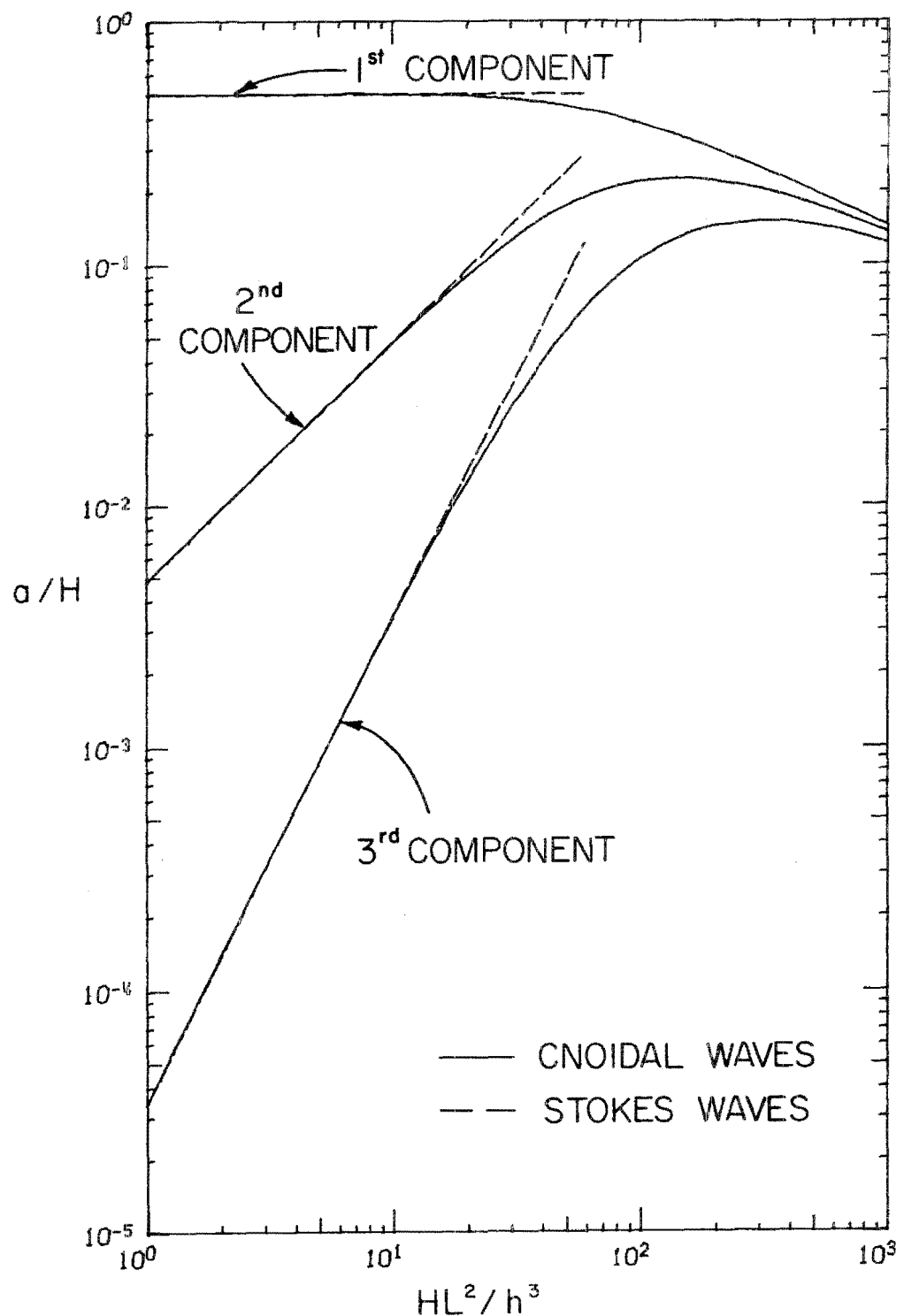


Fig. 3.5 Comparison of the first three harmonic components of cnoidal waves (—) and Stokes waves (---).

Notice that the range of validity of Stokes waves is not increased by inclusion of the third component. In fact, for $0 \leq HL^2/h^3 \leq 10$, the third component is at least two orders of magnitude less than the first component so for most applications it can be neglected. As HL^2/h^3 increases above 100, the second and third Fourier amplitudes for cnoidal waves reach a maximum and then tend asymptotically to the first amplitude. This corresponds to the wave becoming more peaked and the shape approaching that of a delta function for which the Fourier amplitudes are all equal.

3.2 Wave Generation

The wave generation theory presented here is applicable only to long waves which propagate with constant form (i.e. solitary and cnoidal waves). It was developed to prescribe the displacement-time history of the piston wave generator which was used in this study (see Section 4). The generator consists of a vertical plate which is moved in the horizontal direction by means of a hydraulic servo-system. The input voltage to the servo-system is supplied by a memory unit containing 1000 voltages equispaced in time. The memory is loaded from a paper tape on which the 1000 voltages which correspond to displacement points are punched. The object of the theory developed here is to determine the function from which the displacement points (and hence the voltages) for a given wave can be obtained.

3.2.1 The Derivation of a Generation Equation for Long Waves

Consider the generation phase plane, Fig. 3.6, which will be used to demonstrate the way in which the generation equation is

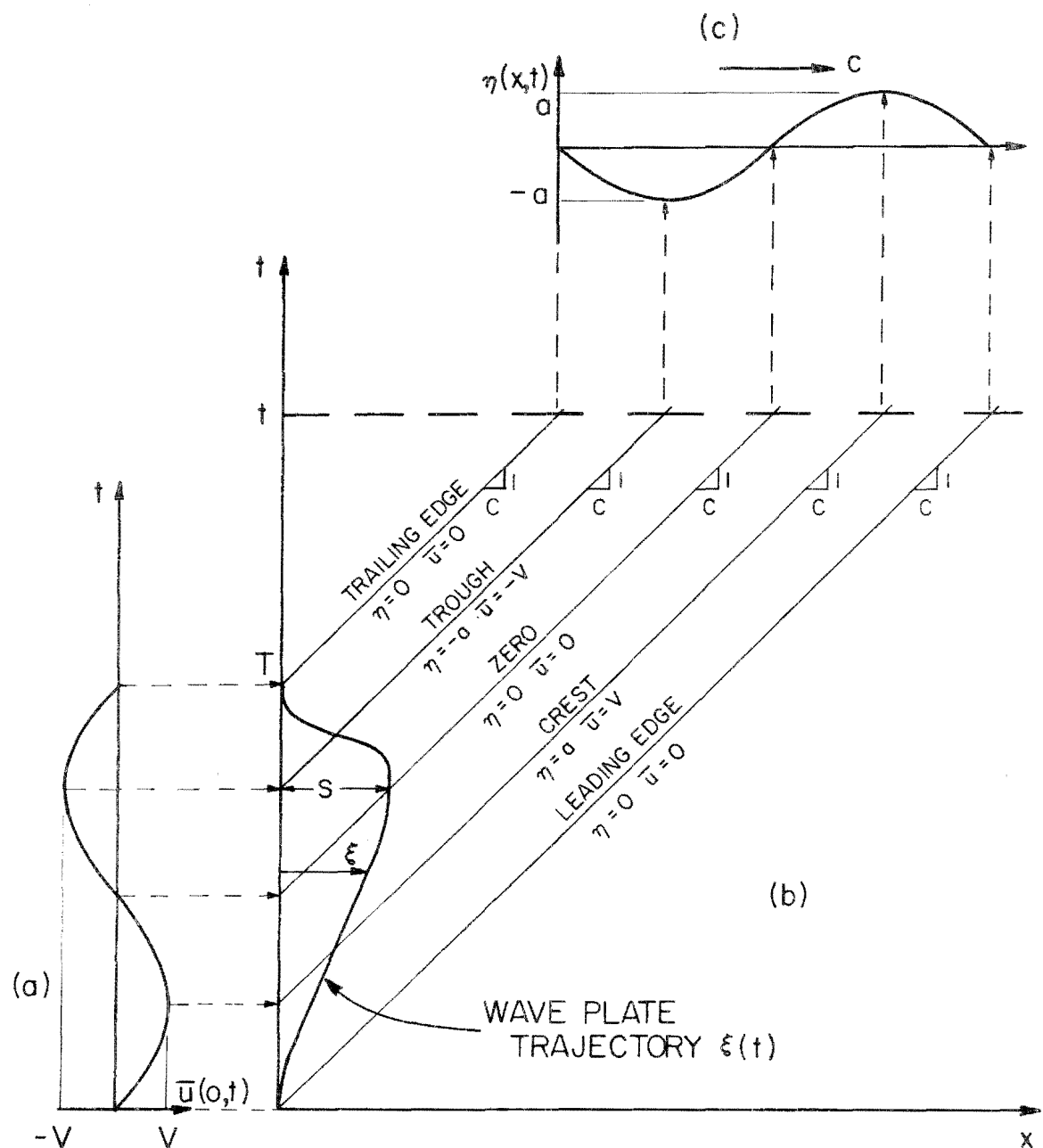


Fig. 3.6 Wave generation phase plane.

obtained. The figure shows a wave whose amplitude profile is sinusoidal (Fig. 3.6(c)) and whose velocity time record also is sinusoidal (Fig. 3.6(a)). The wave propagates to the right with constant form and with celerity c as shown in the x - t plane (Fig. 3.6(b)) where the wave properties such as amplitude and particle velocity propagate along lines (i.e. characteristics) which are straight and parallel and have slope $dx/dt = c$. The time history of the motion of the wave plate which generated the wave is represented in Fig. 3.6(b) by the curve $\xi(t)$ which will be termed the "trajectory" in this study. Initially, for time $t < 0$, the wave plate is at rest at $\xi = 0$. At time $t = 0$ the wave plate begins to move along the trajectory $\xi(t)$. The object of this development is to find the trajectory which will produce a particular long wave $\eta(x,t)$ of constant form propagating with celerity c . The basic concept is simply to match the velocity of the wave plate at all positions, $d\xi/dt$, with the corresponding velocity of the particles under the wave. For long waves the particle velocity is approximately constant over the depth, so the velocity averaged over the depth, $\bar{u}(x,t)$, is used:

$$\frac{d\xi}{dt} = \bar{u}(\xi, t) \quad . \quad (3.35)$$

Inclusion of the position of the plate, ξ , in the velocity, $\bar{u}(\xi, t)$, takes into account that during generation the wave is propagating away from the plate along the characteristics. The effect is to produce a trajectory which is distorted from what it would be if $\bar{u}(0, t)$ were used. This can be seen in Fig. 3.6, where for illustrative purposes

the particle velocity averaged over the depth (Fig. 3.6(a)) is a simple sine curve. For this case, if the velocity $\bar{u}(0,t)$ were used in Eq. (3.35), the trajectory would have sinusoidal shape and the crest of the trajectory, $\xi = S$, would occur at time $\frac{1}{2}T$. However, using the velocity $\bar{u}(\xi,t)$, Fig. 3.6(b) shows that the crest of the trajectory occurs at time $t = \frac{1}{2}T + S/c$. Thus the time taken for the plate to travel forward to its full extent is time S/c longer than it would be if the trajectory were sinusoidal and consequently the time taken for the plate to travel back to its original position is time S/c shorter than it would be if the trajectory were sinusoidal. The effect of including the position ξ in the velocity therefore is that when the plate and wave are moving in the same direction, the time coordinate stretches; when the plate and the wave are moving in opposite directions, the time coordinate contracts.

The simple sine water particle velocity shown in Fig. 3.6(a) was presented as an example; for waves of permanent form it can be shown (e.g. Svendsen (1974)) by continuity that the velocity averaged over the depth is:

$$\bar{u}(x,t) = \frac{c\eta(x,t)}{h+\eta(x,t)} . \quad (3.36)$$

Thus, in terms of the plate velocity, from Eq. (3.35):

$$\dot{\xi} = \frac{c\eta(x,t)}{h+\eta(x,t)} , \quad (3.37)$$

where $\dot{\xi} \equiv \frac{d\xi}{dt}$. Eq. (3.37) must be integrated to obtain the trajectory, $\xi(t)$. It is assumed that the wave has the form:

$$\eta(\xi, t) = Hf(\theta) \quad , \quad (3.38)$$

$$\text{where } \theta = k(ct - \xi) \quad . \quad (3.39)$$

The total derivative of Eq. (3.39) is:

$$\frac{d\theta}{dt} = k(c - \dot{\xi}) \quad , \quad (3.40)$$

$$\text{and } \frac{d\xi}{dt} = \frac{d\xi}{d\theta} \cdot \frac{d\theta}{dt} = \frac{d\xi}{d\theta} k(c - \dot{\xi}) \quad ,$$

or, by rearranging:

$$\frac{d\xi}{d\theta} = \frac{\dot{\xi}}{k(c - \dot{\xi})} \quad . \quad (3.41)$$

Substituting Eqs. (3.37) and (3.38) into Eq. (3.41), the latter reduces to the simple form:

$$\frac{d\xi}{d\theta} = \frac{Hf(\theta)}{kh} \quad , \quad (3.42)$$

$$\text{and } \xi(t) = \frac{H}{kh} \int_0^\theta f(w)dw \quad , \quad (3.43)$$

where w is the dummy variable of integration and θ is given by Eq. (3.39). Equation (3.43) is an implicit equation which can in general only be solved for a particular time t by numerical means. The most efficient method of solution was found to be Newton's Rule:

Using Eq. (3.39), θ is substituted for the displacement ξ in Eq. (3.43) to yield:

$$F = \theta - kct + \frac{H}{h} \int_0^\theta f(w)dw = 0 \quad . \quad (3.44)$$

The task is now to solve Eq. (3.44) for θ at a given time t . Differentiating Eq. (3.44):

$$\frac{\partial F}{\partial \theta} = 1 + \frac{H}{h} f(\theta) , \quad (3.45)$$

Newton's Rule is:

$$\theta^{(i+1)} = \theta^{(i)} - \frac{F(\theta^{(i)})}{F_\theta(\theta^{(i)})} , \quad (3.46)$$

where superscripts denote iteration number and $F_\theta = \partial F / \partial \theta$. Substituting for F and F_θ in Eq. (3.46) yields:

$$\theta^{(i+1)} = \theta^{(i)} - \frac{\theta^{(i)} - kct + \frac{H}{h} \int_0^{\theta^{(i)}} f(w) dw}{1 + \frac{H}{h} f(\theta^{(i)})} . \quad (3.47)$$

Having found θ for given time t , the displacement ξ is given by:

$$\xi = ct - \theta/k . \quad (3.48)$$

Eqs. (3.43), or (3.47) and (3.48) provide the wave plate displacement as a function of time $\xi(t)$ for a general wave form $f(\theta)$. These equations will now be applied for specific functions $f(\theta)$ which describe particular waves.

3.2.1.1. The Generation of Solitary Waves

For a solitary wave, the wave function $f(\theta)$ in Eq. (3.38) is:

$$f(\theta) = \operatorname{sech}^2 \theta , \quad (3.49)$$

where $\theta = \kappa(ct - \xi)$, $\kappa = \sqrt{\frac{3}{4} \frac{H}{h^3}}$ and $c = \sqrt{g(h+H)}$. Substituting Eq. (3.49) into the generation equation, Eq. (3.43), and performing the integration yields:

$$\xi(t) = \frac{H}{\kappa h} \tanh \kappa(ct - \xi) , \quad (3.50)$$

and the iterative equations, Eqs. (3.47) and (3.48), become:

$$\theta^{(i+1)} = \theta^{(i)} - \frac{\theta^{(i)} - \kappa ct + \frac{H}{h} \tanh \theta^{(i)}}{1 + \frac{H}{h} \operatorname{sech}^2 \theta^{(i)}} , \quad (3.51)$$

and

$$\xi = ct - \theta/\kappa . \quad (3.52)$$

The phase plane in Fig. 3.7 shows a typical trajectory $\xi(t)$ calculated from Eqs. (3.51) and (3.52). The origin of displacement ξ and of time t occurs under the wave crest because of the definition of the solitary wave, Eq. (3.49). In addition, since the function f in Eq. (3.49) tends to zero as θ goes to infinity, the intercepts of the characteristics associated with the leading and trailing edges of the wave with the time axis, $\pm t_0$, occur at $\pm\infty$. However, since precision of only three significant figures was available in the actual generating device, the intercepts, t_0 , were defined, for practical purposes, by:

$$t_0 = \frac{\tanh^{-1} (0.999)}{\kappa c} = \frac{3.80}{\kappa c} . \quad (3.53)$$

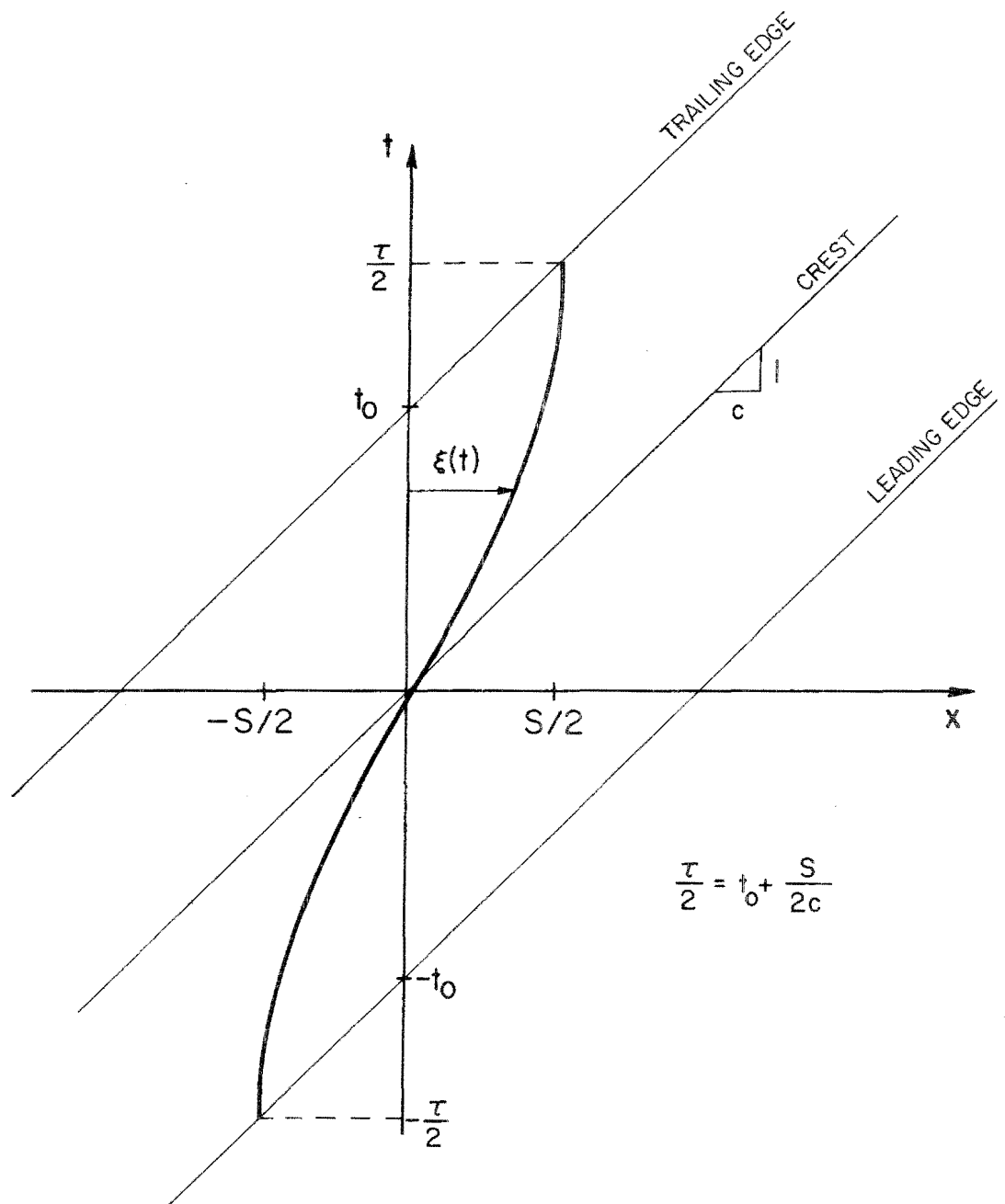


Fig. 3.7 Phase plane showing typical wave plate trajectory for a solitary wave.

The stroke S is obtained by evaluating Eq. (3.50) at times $t = +\infty$ and $t = -\infty$ and subtracting to yield:

$$S = \frac{2H}{\kappa h} = \sqrt{\frac{16}{3} \frac{H}{h}} h . \quad (3.54)$$

The duration of motion τ is obtained from Fig. 3.7 by computing the times at which the leading and trailing edge characteristics intersect the trajectory $\xi(t)$ and subtracting which gives:

$$\tau = 2t_o + S/c . \quad (3.55)$$

Substituting for the intercept t_o and stroke S yields for the duration:

$$\tau = \frac{2}{\kappa c} (3.80 + \frac{H}{h}) . \quad (3.56)$$

(The origin of the trajectory, $\xi(0)$, was moved to the point $(-\frac{1}{2}\tau, -\frac{1}{2}S)$ in the x - t plane so that motion started from rest and proceeded in a forward direction.)

3.2.1.2 The Generation of Cnoidal Waves

For cnoidal waves the function $f(\theta)$ in Eq. (3.38) is:

$$f(\theta) = \frac{y_t - h}{H} + cn^2(\theta | m) , \quad (3.57)$$

where $\theta = 2K(\frac{t}{T} - \frac{\xi}{L})$ (which, for convenience in this development, is of opposite sign to the θ defined earlier), and K is the first complete elliptic integral, cn is the Jacobian elliptic function, m is the elliptic parameter, T is the period and L is the wave length.

Substituting Eq. (3.57) into the generation equation, Eq. (3.43), and performing the integration yields:

$$\xi(t) = \frac{L}{2Kh} \left\{ (y_t - h)\theta + \frac{H}{m} (E(\theta|m) - m'\theta) \right\} , \quad (3.58)$$

where $E(\theta|m)$ is the second incomplete elliptic integral, and m' is the complementary parameter, $m' = 1 - m$.

Substituting this into Eq. (3.47) gives the iterative equation:

$$\theta^{(i+1)} = \theta^{(i)} - \frac{\frac{2Kht}{T} + (y_t - \frac{Hm'}{m}) \theta^{(i)} + \frac{H}{m} E(\theta^{(i)}|m)}{y_t + H \operatorname{cn}^2(\theta^{(i)}|m)} . \quad (3.59)$$

The elliptic functions $E(\theta^{(i)}|m)$ and $\operatorname{cn}^2(\theta^{(i)}|m)$ can most easily be evaluated by the numerical methods described in Appendix A.

Having found θ for given time t , the displacement ξ is given by:

$$\xi(t) = L \left(\frac{t}{T} - \frac{\theta}{2K} \right) . \quad (3.60)$$

Fig. 3.8 shows a typical trajectory $\xi(t)$, normalized with respect to the maximum, ξ_{\max} , calculated using Eqs. (3.59) and (3.60). Because of the form of the definition of the function $f(\theta)$ in Eq. (3.57), the origin occurs at a point of maximum velocity. However, it is desirable to start the motion of the wave plate at a position where the plate velocity and wave amplitude are zero, i.e. where:

$$\frac{d\xi}{dt} = \bar{u} = 0 , \quad (3.61)$$

and

$$\eta = y_t - h + H \operatorname{cn}^2(\theta_0|m) = 0 , \quad (3.62)$$

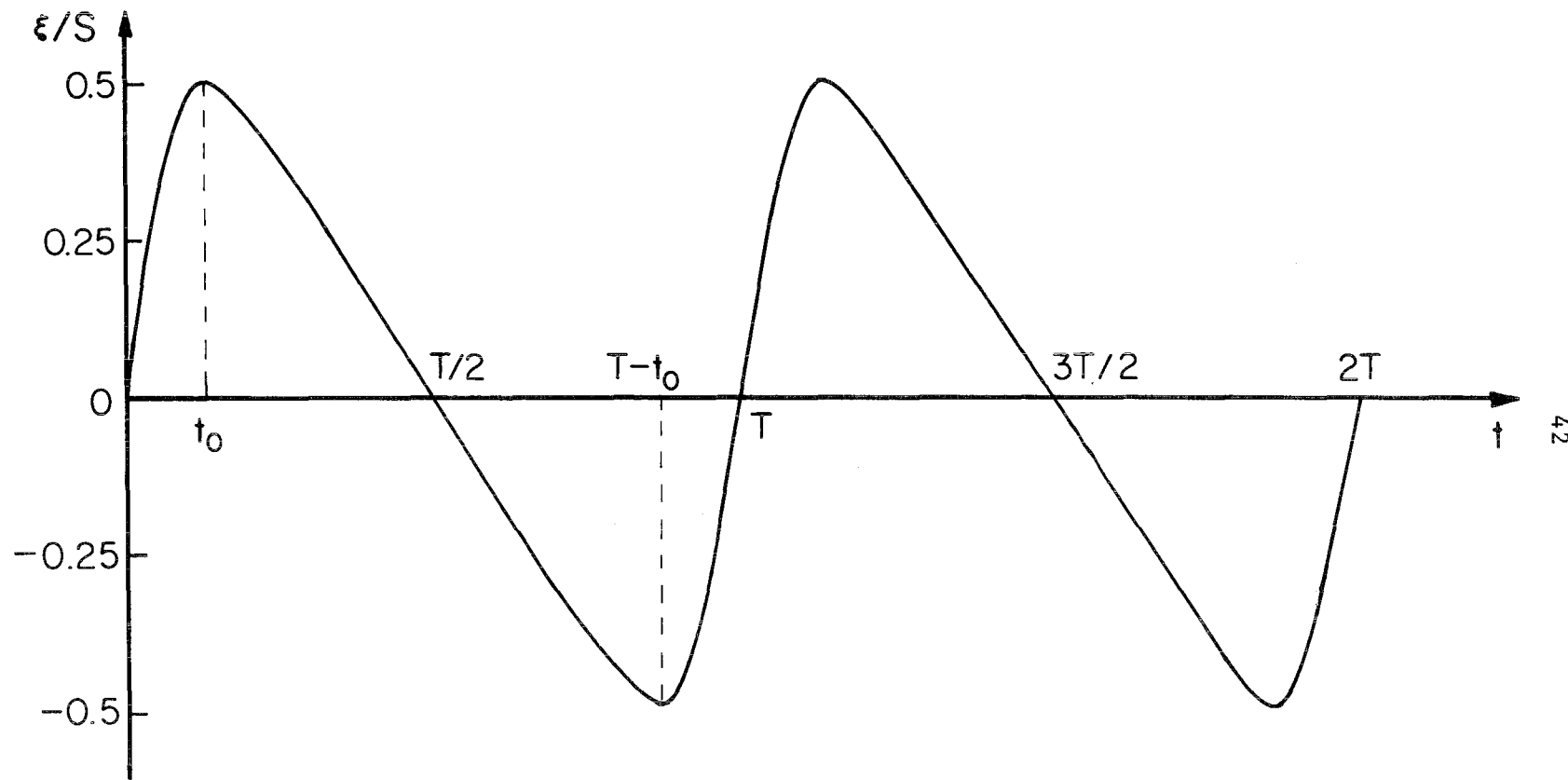


Fig. 3.8 Typical wave plate trajectory for cnoidal wave generation.

where θ_0 is the argument of the cnoidal function determined such that the wave amplitude is zero. Eq. (3.62) can be written as:

$$\theta_0 = \operatorname{cn}^{-1} \left(\frac{y_t - h}{H} \right)^{1/2}, \quad (3.63)$$

which can be evaluated for a given wave by the numerical method described in Appendix A.

Substituting for θ_0 in Eq. (3.51) gives:

$$\xi_{\max} = -\xi_{\min} = \frac{L}{2Kh} \left[(y_t - h)\theta_0 + \frac{H}{m} \{E(\theta_0|m) - m'\theta_0\} \right], \quad (3.64)$$

and

$$\frac{t_0}{T} = \frac{\xi_{\max}}{L} + \frac{\theta_0}{2K} \quad . \quad (3.65)$$

The maximum excursion of the wave plate or stroke S is:

$$S = 2 \xi_{\max} \quad . \quad (3.66)$$

Since the leading wave of a train of cnoidal waves is a transient wave, it was desirable to make it a positive wave rather than a negative wave so the train would not overtake it. Thus, the motion is started at a minimum point in Fig. 3.8, so the origin of the trajectory calculated from Eqs. (3.59) and (3.60) is moved forward by a time $T - t_0$.

The application of this theory and the waves which resulted from it are presented in Section 5.1.

3.3 The Propagation of Long Waves onto a Shelf by the Nonlinear Dispersive Theory

Two of the methods which presently exist for numerically solving

the Boussinesq equations in constant depth are the finite difference approach used by Peregrine (1966) and the method of characteristics which was employed by Long (1964). The finite element method described here has certain similarities to the scheme of Peregrine (1966) but in contrast to those of Peregrine (1966) and Long (1964) it is unconditionally stable and second order accurate. Madsen and Mei (1969) extended the approach of Long (1964) to solve the Boussinesq equations for the case of a gradually varying depth. In order to avoid the restriction of a gradual change in depth, the approach that was taken in this study was to first formulate a finite element solution of the Boussinesq equations for the case of a constant depth. The varying depth was then considered to consist of a series of steps between which the Boussinesq equations for a constant depth applied. The solutions in adjoining regions were matched at the steps by applying the boundary conditions of continuity of surface elevation and flow rate; the latter is equivalent to matching the surface slopes.

3.3.1 The Numerical Solution of the Boussinesq Equations for Constant Depth by a Finite Element Method

3.3.1.1 Analytical Formulation of the Problem

Consider the physical system shown in Fig. 3.9 which consists of a body of water, bounded at $x = 0$ and $x = X$ with a depth h , in which a wave propagates with characteristic horizontal length λ and characteristic height H .

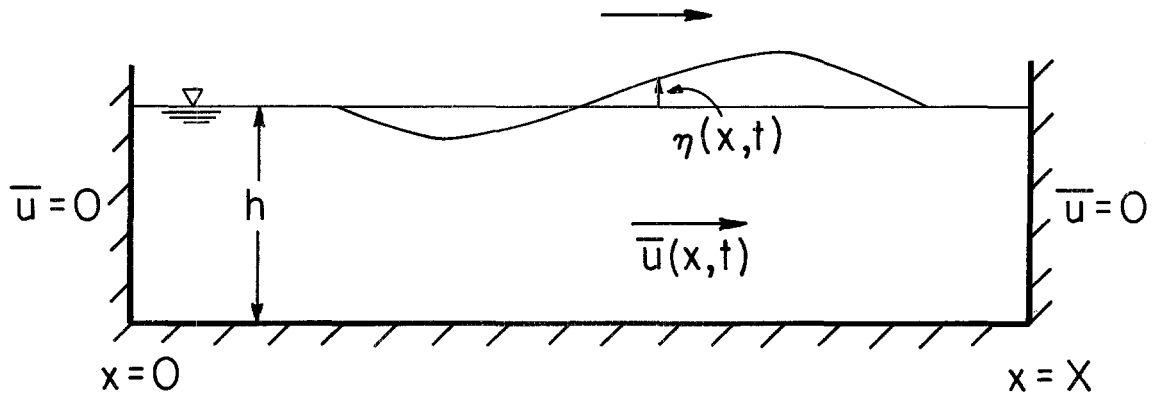


Fig. 3.9 Definition Sketch for Numerical Scheme

For long waves ($\ell \gg h$) of moderate amplitude ($H \ll h$) where the Ursell Number ($H\ell^2/h^3$) is of order unity, the governing equations are the Boussinesq equations, Eqs. (3.10) and (3.11), which in dimensional form are:

$$\eta_t + \{(h + \eta)\bar{u}\}_x = 0 \quad , \quad (3.67)$$

and $\bar{u}_t + \bar{u}\bar{u}_x + gn_x - \frac{1}{3}h^2\bar{u}_{xxt} = 0 \quad , \quad (3.68)$

where $\bar{u}(x,t)$ is the velocity averaged over the depth and defined by:

$$\bar{u}(x,t) = \int_0^{h+\eta} \bar{u}(x,y,t) dy \quad . \quad (3.69)$$

Following the usual finite element formulation, the problem is first stated in its three forms--Strong, Weak and Galerkin.

The Strong (or Classical) form of the problem denoted as (S) is:

$$(S) \left\{ \begin{array}{l} \text{Find the amplitude } \eta(x,t) \text{ and the velocity } \bar{u}(x,t), \text{ in the} \\ \text{intervals } 0 \leq x \leq X \text{ and } 0 \leq t \leq T, \text{ such that:} \\ \eta_t + \{(h + \eta)\bar{u}\}_x = 0 \\ \bar{u}_t + \bar{u}\bar{u}_x + g\eta_x - \frac{1}{3}h^2\bar{u}_{xxt} = 0 \quad , \\ \text{with the boundary conditions:} \\ \bar{u}(0,t) = \bar{u}_0(t) \quad \text{and} \quad \bar{u}(X,t) = \bar{u}_m(t) \quad , \\ \text{and the initial conditions:} \\ \eta(x,0) = H(x) \quad \text{and} \quad \bar{u}(x,0) = G(x) \quad . \end{array} \right.$$

A weak (or variational) form of (S) denoted as (W) is:

$$(W) \left\{ \begin{array}{l} \text{Find the amplitude } \eta(x,t) \text{ and the velocity } \bar{u}(x,t) \text{ which} \\ \text{satisfy the boundary conditions such that for all variations} \\ w(x) \text{ and } v(x): \\ (\dot{\eta}, w) + \int_0^X w \{\bar{u}(h + \eta)\}_x dx = 0 \\ (\dot{\bar{u}}, v) + \frac{1}{3}h^2 a(\dot{\bar{u}}, v) + \int_0^X v(\bar{u}\bar{u}_x + g\eta_x) dx = 0 \\ \text{and,} \quad (\{\eta(x,0) - G(x)\}, w) = 0 \\ (\{\bar{u}(x,0) - F(x)\}, v) = 0 \quad . \end{array} \right.$$

where w is the amplitude variation and v is the velocity variation
and $\dot{\eta} = \frac{\partial \eta}{\partial t}$, $\dot{\bar{u}} = \frac{\partial \bar{u}}{\partial t}$.

The inner product is defined as: $(u, v) = \int_0^X uv dx$,

and the bilinear form: $a(u, v) = \int_0^X u_x v_x dx$.

The Galerkin (or discrete) form of (W) which is denoted as (G) is:

$$\left. \begin{array}{l}
 \text{Find the discrete functions } \eta^h(x, t) \text{ and } \bar{u}^h(x, t) \text{ which satisfy} \\
 \text{the boundary conditions such that for all discrete functions} \\
 w^h \text{ and } v^h: \\
 (\dot{\eta}^h, w^h) + \int_0^X w^h \{ \bar{u}^h(h + \eta^h) \}_x dx = 0 \\
 (\dot{\bar{u}}^h, v^h) + \frac{1}{3} h^2 a(\dot{\bar{u}}^h, v^h) + \int_0^X v^h (\bar{u}^h \bar{u}_x^h + g \eta^h) dx = 0 \\
 \text{and, } \{(\bar{u}^h(x, 0) - G(x)), v^h\} = 0 \\
 \{(\eta^h(x, 0) - H(x)), w^h\} = 0
 \end{array} \right\} \quad (G)$$

In this manner, the problem has been transformed from one of finding the solutions, continuous in x and t , of a set of partial differential equations to one of finding the solutions, continuous in t but discrete in x , of a set of ordinary differential equations.

3.3.1.2 Finite Element Formulation

Consider the one-dimensional finite element mesh shown in Fig. 3.10 where the interval $0 \leq x \leq X$ has been divided into $N+1$ elements and $N+2$ nodes. Let the amplitude variation $w^h(x)$ and the velocity variation $v^h(x)$ be linear combinations of the finite element basis functions $\phi_i(x)$ and $\psi_i(x)$ respectively:

$$v^h(x) = \sum_{i=1}^N \psi_i(x) \quad (3.70)$$

$$w^h(x) = \sum_{i=0}^{N+1} \phi_i(x) \quad , \quad (3.71)$$

where subscripts denote the number of the node and $\phi_i(x)$ and $\psi_i(x)$ are functions which satisfy the following conditions:

$$\phi_i(x_j) = \begin{cases} 1 & j = i \\ 0 & j \neq i \end{cases} \quad \psi_i(x_j) = \begin{cases} 1 & j = i \\ 0 & j \neq i \end{cases} \quad (3.72)$$

The typical basis functions ϕ_i shown in Fig. 3.10 are the linear piecewise continuous functions defined by:

$$\phi_i(x_j) = \begin{cases} \frac{x - x_{i-1}}{\Delta x_i} & x_{i-1} \leq x \leq x_i \\ \frac{x_{i+1} - x}{\Delta x_{i+1}} & x_i \leq x \leq x_{i+1} \\ 0 & x_{i+1} < x < x_{i-1} \end{cases} \quad i = 1, 2, \dots, N \quad , \quad (3.73)$$

and

$$\phi_0(x) = \begin{cases} \frac{x}{\Delta x_1} & x \leq x_1 \\ 0 & x > x_1 \end{cases} \quad , \quad (3.74)$$

where $\Delta x_i = x_i - x_{i-1}$.

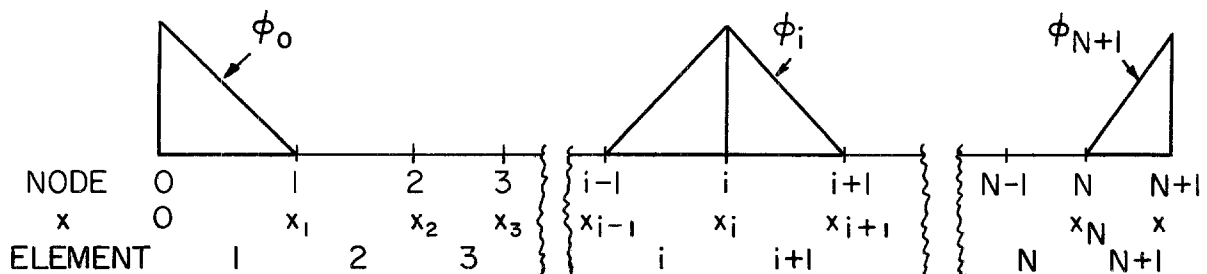


Fig. 3.10 Finite Element Mesh

Denoting the amplitudes at the nodes by $e_i(t)$ and the velocities at the nodes by $d_i(t)$, let:

$$\eta^h(x, t) = \sum_{i=0}^{N+1} \phi_i(x) e_i(t) \quad (3.75)$$

$$\bar{u}^h(x, t) = \sum_{i=1}^N \psi_i(x) d_i(t) + \psi_o(x) \bar{u}_o(t) + \psi_m(x) \bar{u}_m(t) \quad . \quad (3.76)$$

The object of the numerical scheme is to find the nodal amplitudes ($e_i(t)$ $i = 0, \dots, N+1$) and the nodal velocities ($d_i(t)$ $i = 1, 2, \dots, N$) for the interval $0 < t \leq T$. At a particular time, the amplitude and velocity between nodes is found by interpolation using the basis functions, $\phi(x)$ and $\psi(x)$. Linear basis functions imply linear variation of velocity and amplitude between nodes.

Substituting the discrete approximations of the amplitude and velocity given by Eqs. (3.75) and (3.76) into the Galerkin form of the problem (G) yields:

$$\sum_{i=1}^{N+1} (\phi_i, \phi_j) \dot{e}_j - f_j^C = 0 \quad j = 0, 1, 2, \dots, N+1 \quad (3.77)$$

$$\begin{aligned} \sum_{i=1}^N & \{(\psi_i, \psi_j) + \frac{1}{3} h^2 a(\psi_i, \psi_j)\} \dot{d}_j + \{(\psi_m, \psi_j) + \frac{1}{3} h^2 a(\psi_m, \psi_j)\} \dot{u}_m \\ & + \{(\psi_o, \psi_j) + \frac{1}{3} h^2 a(\psi_o, \psi_j)\} \dot{u}_o - f_j^M = 0 \end{aligned} \quad (3.78)$$

$$j = 1, 2, \dots, N$$

where

$$f_j^C = - \int_0^X \phi_j \left\{ \left(\sum_{i=1}^N \psi_i d_i + \psi_o \bar{u}_o + \psi_m \bar{u}_m \right) (h + \sum_{i=0}^{N+1} \phi_k e_k) \right\} x dx \quad (3.79)$$

and

$$f_j^M = - \int_0^X \left[\psi_j \left\{ \sum_{i=1}^N \psi_i d_i + \psi_o \bar{u}_o + \psi_m \bar{u}_m \right\} \left\{ \sum_{k=1}^{N+1} \psi_{k,x} d_i + \psi_{o,x} \bar{u}_o + \psi_{m,x} \bar{u}_m \right\} + g \sum_{i=0}^{N+1} \psi_j \phi_{i,x} e_i \right] dx \quad (3.80)$$

To write Eqs. (3.77) and (3.78) in matrix form, let:

$$M_{ij}^C = (\phi_i, \phi_j) \quad j = 0, 1, \dots, N+1$$

$$M_{ij}^M = (\psi_i, \psi_j) + \frac{1}{3} h^2 a(\psi_i, \psi_j)$$

$$m_{oj}^M = (\psi_o, \psi_j) + \frac{1}{3} h^2 a(\psi_o, \psi_j) \quad j = 1, 2, \dots, N \quad (3.81)$$

$$m_{mj}^M = (\psi_m, \psi_j) + \frac{1}{3} h^2 a(\psi_m, \psi_j) \quad .$$

The matrix form of the Galerkin Problem (G) which is denoted as (M) is:

$$(M) \left\{ \begin{array}{l} \text{Find the nodal amplitude } e_i(t) \quad i = 0, 1, \dots, N+1 \text{ and the nodal} \\ \text{velocity } d_i(t) \quad i = 1, 2, \dots, N, \text{ over the interval } 0 < t \leq T \text{ such that:} \\ M^C \dot{e} = f^C \\ M^M \dot{d} = f^M - m_o^M \dot{u}_o - m_m^M \dot{u}_m \\ e_i(0) = H(x_i) \quad d_i(0) = G(x_i) \end{array} \right. \quad (3.82)$$

$$M^M \dot{d} = f^M - m_o^M \dot{u}_o - m_m^M \dot{u}_m \quad (3.83)$$

The matrices \underline{M}^C and \underline{M}^M , arising from the continuity equation Eq. (3.67) and the momentum equation (3.68) are symmetric positive definite matrices of order $N+2$ and N respectively. (For linear shape functions they are tridiagonal.) The vectors \underline{f}^C and \underline{f}^M contain nonlinear terms in the nodal amplitudes \underline{e} and the nodal velocities \underline{d} . The vectors \underline{m}_o^M and \underline{m}_m^M contain only one nonzero term for linear shape functions.

3.3.1.3 The Time Integration Algorithm

The time integration algorithm used to solve the matrix form of the problem, (M), was the Midpoint Rule:

$$\underline{M}^C(\underline{e}_{n+1} - \underline{e}_n) = \Delta t \underline{f}_{n+\frac{1}{2}}^C , \quad (3.84)$$

$$\underline{M}^M(\underline{d}_{n+1} - \underline{d}_n) = \Delta t \left\{ \underline{f}_{n+\frac{1}{2}}^M - \underline{M}_o^M \dot{\underline{u}}_o_{n+\frac{1}{2}} - \underline{M}_m^M \dot{\underline{u}}_m_{n+\frac{1}{2}} \right\} , \quad (3.85)$$

where

$$\underline{f}_{n+\frac{1}{2}}^C = \underline{f}^C \left(\frac{1}{2} \{ \underline{e}_{n+1} + \underline{e}_n \} , \frac{1}{2} \{ \underline{d}_{n+1} + \underline{d}_n \} \right) , \quad (3.86)$$

$$\underline{f}_{n+\frac{1}{2}}^M = \underline{f}^M \left(\frac{1}{2} \{ \underline{e}_{n+1} + \underline{e}_n \} , \frac{1}{2} \{ \underline{d}_{n+1} + \underline{d}_n \} \right) , \quad (3.87)$$

$$\dot{\underline{u}}_o_{n+\frac{1}{2}} = \dot{\underline{u}}_o \left(\frac{1}{2} \{ t_n + t_{n+1} \} \right) ,$$

$$\dot{\underline{u}}_m_{n+\frac{1}{2}} = \dot{\underline{u}}_m \left(\frac{1}{2} \{ t_n + t_{n+1} \} \right) , \quad (3.88)$$

and the subscripts denote the number of the time step.

The Midpoint Rule differs from the well-known Trapezoidal Rule (or Crank-Nicholson Method) in a subtle way which is apparent only when considering nonlinear problems. For the Trapezoidal Rule, the

vector $\underline{f}_{n+\frac{1}{2}}^C$, for example, would be defined as:

$$\underline{f}_{n+\frac{1}{2}}^C = \frac{1}{2} \left[\underline{f}_n^C(e_n, d_n) + \underline{f}_{n+1}^C(e_{n+1}, d_{n+1}) \right] \quad . \quad (3.89)$$

Thus, in Midpoint Rule, the vector $\underline{f}_{n+\frac{1}{2}}^C$ is found by evaluating the function \underline{f}^C with arguments which are the average of those at the beginning and end of the time step, while for Trapezoidal Rule the vector $\underline{f}_{n+\frac{1}{2}}^C$ is found by evaluating the function \underline{f}^C at the beginning and end of the time step and averaging these functions. Clearly, if \underline{f}^C is a linear function, the Midpoint Rule and the Trapezoidal Rule are identical, however, if \underline{f}^C is a nonlinear function, Eqs. (3.86) and (3.89) are quite different. Although both the Midpoint Rule and the Trapezoidal Rule are unconditionally stable and second order accurate, the Midpoint Rule is preferred for nonlinear problems because the stability analysis more closely parallels the stability analysis for linear problems and thus results in a more definite statement of unconditional stability. The details of this and other aspects of the stability analysis of the Midpoint Rule and the Trapezoidal Rule for nonlinear problems are given by Hughes (1977).

3.3.1.4 The Iterative Scheme

The iterative scheme used to solve Eqs. (3.84) and (3.85) is similar to that used by Peregrine (1966) to solve a finite difference formulation of the Boussinesq equations:

1. First Iteration:

- i) Evaluate $\underline{f}_{n+\frac{1}{2}}^C = \underline{f}_n^C(e_n, d_n)$ and solve Eq. (3.84) for the nodal amplitudes $\underline{e}_{n+1}^{(1)}$.

ii) Evaluate $f_{\tilde{n}+1/2}^M = \tilde{f}^M \left(\frac{1}{2} \{ e_{\tilde{n}+1}^{(1)} + e_{\tilde{n}} \}, \tilde{d}_{\tilde{n}} \right)$ and solve Eq. (3.85) for nodal velocities $\tilde{d}_{\tilde{n}+1}^{(1)}$.

It is noted the bracketed superscripts denote iteration number.

2. Second and Subsequent Iterations $k = 2, 3, \dots$:

i) Evaluate $f_{\tilde{n}+1/2}^C = \tilde{f}^C \left(\frac{1}{2} \{ e_{\tilde{n}+1}^{(k-1)} + e_{\tilde{n}} \}, \frac{1}{2} \{ \tilde{d}_{\tilde{n}+1}^{(k-1)} + \tilde{d}_{\tilde{n}} \} \right)$ and solve Eq. (3.84) for the nodal amplitudes $e_{\tilde{n}+1}^{(k)}$.

ii) Evaluate $f_{\tilde{n}+1/2}^M = \tilde{f}^M \left(\frac{1}{2} \{ e_{\tilde{n}+1}^{(k)} + e_{\tilde{n}} \}, \frac{1}{2} \{ \tilde{d}_{\tilde{n}+1}^{(k-1)} + \tilde{d}_{\tilde{n}} \} \right)$ and solve Eq. (3.85) for the nodal velocities $\tilde{d}_{\tilde{n}+1}^{(k)}$.

The difference in this scheme from that of Peregrine is that, in the second and subsequent iterations, Peregrine's scheme evaluates the functions \tilde{f}^C and \tilde{f}^M for the nodal velocity at the previous time $\tilde{d}_{\tilde{n}}$ instead of the average of this and the best estimate of the nodal velocities at the forward time step, $\frac{1}{2} \{ \tilde{d}_{\tilde{n}} + \tilde{d}_{\tilde{n}+1}^{(k-1)} \}$. It was found that this change, which amounts to full instead of partial implementation of Midpoint Rule, eliminated numerical dissipation and thus errors in the quantities which should be conserved (volume and energy) were reduced from a few percent to zero.

3.3.1.5 Convergence and Accuracy

The convergence of the iterative scheme was tested by numerical experiments. The experiments involved first setting up the initial conditions for a solitary wave with height H and nodal spacing Δx . The nodal spacing was chosen by assuming that, for numerical purposes, the amplitude of a solitary wave is zero for $\eta/H < 0.001$.

Then from Eq. (3.25) the "length" of the wave can be defined as:

$$L = \frac{8.3}{\kappa} \quad (3.90)$$

where

$$\kappa = \sqrt{\frac{3}{4} \frac{H}{h^3}} \quad .$$

By selecting the number of nodes over which the wave is described, N_X , the nodal spacing is found from:

$$N_X \Delta x = L = \frac{8.3}{\kappa} \quad . \quad (3.91)$$

The number N_X will be termed the "nodal spacing number" and in similar manner the "time step number", N_T , is defined as:

$$N_T = \frac{L}{\Delta t \sqrt{gh}} \quad (3.92)$$

Having set up the initial conditions, iterations for one time step were performed to determine the minimum number of iterations k for which the error:

$$\epsilon = \max_{i=1,2,\dots,N_X} \left| \frac{n_i^{(k)} - n_i^{(k+1)}}{n_i^{(k)}} \right| < \frac{1}{1000} \quad . \quad (3.93)$$

The results for two waves with height $H/h = 0.1$ and 0.7 , are presented in Tables 3.1(a) and 3.1(b), where the number of iterations for convergence is given for various nodal spacing numbers N_X and time step numbers N_T . The data show the iterative scheme converges for the full range of N_X only if $N_T \geq 40$. It is noted that failure to converge for $N_T \leq 40$ does not contradict the unconditional stability

Table 3.1 Number of iterations for convergence for various nodal spacing numbers, N_X , and time step numbers, N_T . (NC implies not convergent.)

(a) $H/h = 0.1$

$N_T \backslash N_X$	5	10	20	40	80
5	NC	NC	NC	NC	NC
10	3	NC	NC	NC	NC
20	2	4	5	9	NC
40	2	2	2	3	3
80	1	2	2	2	2
160	1	1	1	2	2

(b) $H/h = 0.7$

$N_T \backslash N_X$	5	10	20	40	80
5	NC	NC	NC	NC	NC
10	5	NC	NC	NC	NC
20	3	4	7	NC	NC
40	2	3	3	3	4
80	2	2	2	2	2
160	2	2	2	2	2

of the algorithm; it is a feature of the iterative scheme chosen to solve the equations arising from the algorithm. Having selected a nodal spacing number which provides the desired degree of resolution in the wave profile, the optimum time step number is found by minimizing the product of N_T and the number of iterations for convergence. For the waves in this study, three iterations and $N_X = N_T = 40$ were used.

A measure of the accuracy of a numerical scheme is the accuracy with which quantities which are conserved analytically also are conserved numerically. For the Boussinesq equations these conserved quantities are the volume and the energy (potential + kinetic). The accuracy of the scheme described here was tested by propagating the two solitary waves described previously ($H/h = 0.1$ and 0.7) for ten wave lengths using three iterations and $N_X = N_T = 40$ and comparing the ratios of initial to final volumes, V_I/V_F , and initial to final energies, E_I/E_F . The results, which are presented in Table 3.2, show errors in the volume and energy ratios which are considered negligible. This implies, at least with regard to volume and energy, the numerical scheme has a high degree of accuracy.

Table 3.2 Comparison of initial and final conserved quantities for the numerical scheme.

	V_I/V_F	E_I/E_F	No. of Time Steps
$H/h = 0.1$	1.002	1.001	376
$H/h = 0.7$	0.998	1.005	312

Also of interest was the way in which these solitary waves propagate. The wave profiles at regular time intervals are presented in Fig. 3.11 where, it is noted, the abscissas are distance normalized with respect to wave length, L , as given by Eq. (3.90). The total distance of propagation in each case is ten wave lengths (10L); thus, the wave has propagated $1.25L$ between each profile.

In both cases the shape of the initial wave changes as it propagates. For the larger wave ($H/h = 0.7$) the wave height decreases to $H/h = 0.66$ over the first five wave lengths and then remains constant. The trough which forms initially behind the main wave is left behind by the main wave and, after propagating a distance of five wave lengths, they are completely separate. For the smaller wave ($H/h = 0.1$) the wave height decreases to $H/h = 0.090$ over the first five wave lengths and then remains constant. The trough which forms behind the main wave grows in amplitude, reaching a maximum of $a_t/h = 0.0066$ after the wave has travelled five wave lengths. Subsequently the amplitude of the trough slowly decreases accompanied by an increase in the length of the trough.

The shape of the main wave after it has travelled ten wave lengths is examined in Fig. 3.12. In Fig. 3.12(a) the larger wave ($H/h = 0.7$) is compared to the Boussinesq and McCowan solitary waves. The wave follows the theory of Boussinesq (1872) in the region of the crest and the theory of McCowan (1891) near the leading and trailing edges. (This also was found to be true for large waves ($H/h > 0.3$) generated in the laboratory, and will be discussed in Section 5.1.) In Fig. 3.12(b)

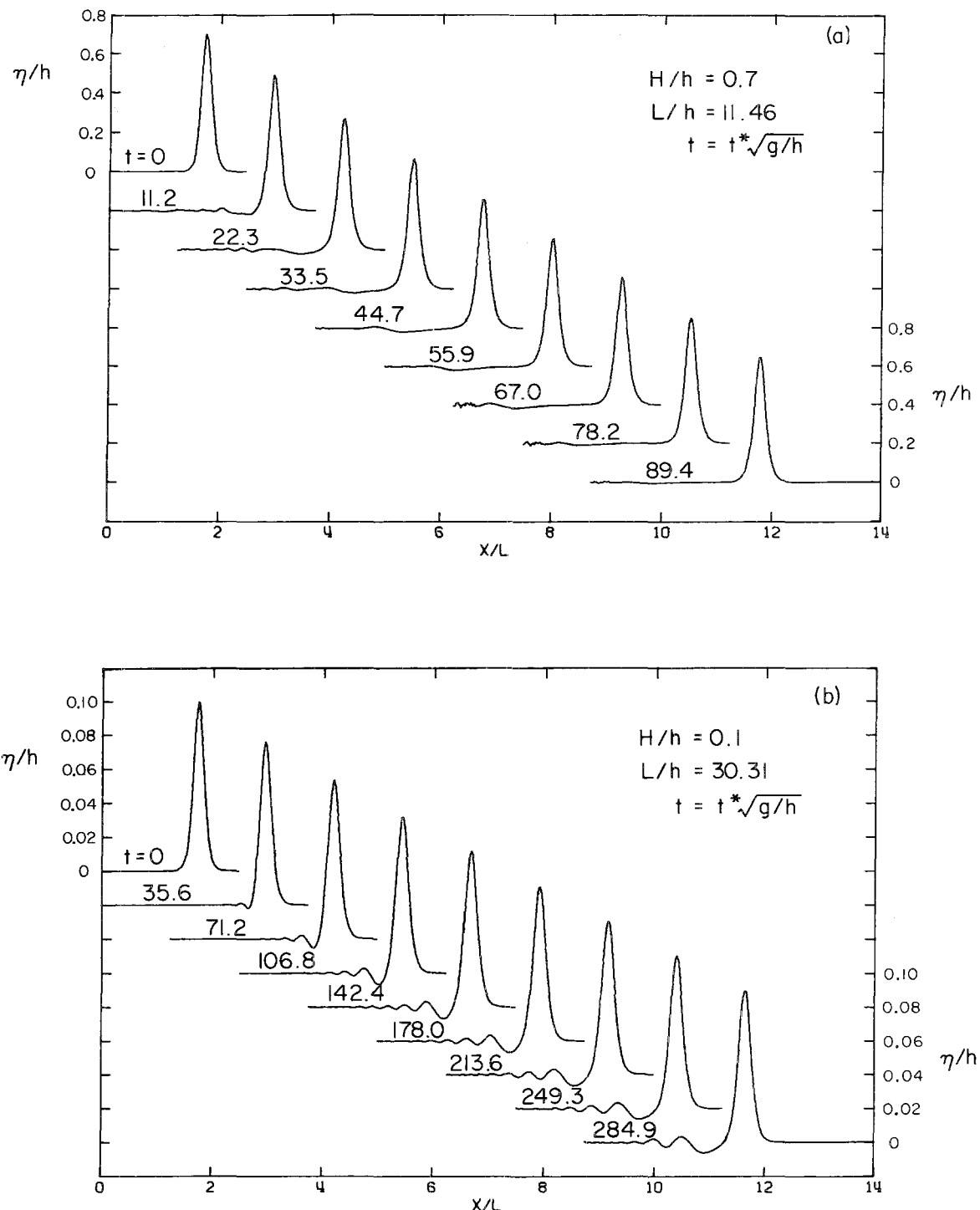


Fig. 3.11 Wave profiles calculated using the numerical scheme for
 (a) $H/h = 0.7$ and (b) $H/h = 0.1$.

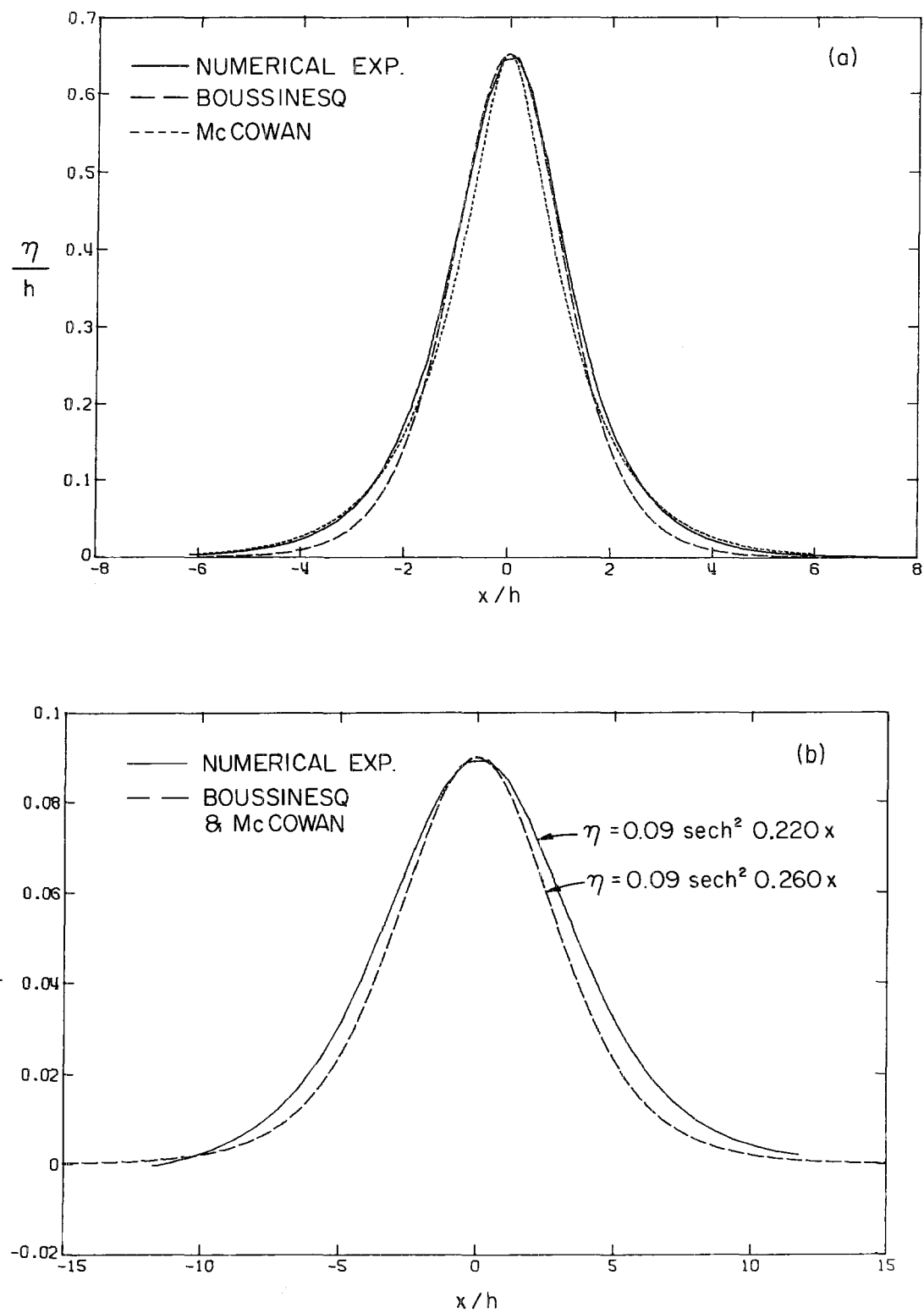


Fig. 3.12 Shapes of the waves after they have travelled ten wave lengths for (a) $H/h = 0.7$ and (b) $H/h = 0.1$.

the smaller wave ($H/h = 0.1$) is compared to the Boussinesq solitary wave. As indicated in the figure, the waves both have sech^2 shape but the "wave number" of the wave obtained numerically is 0.220 compared with 0.260 for the solitary wave of the same wave height.

Increasing the nodal spacing number, N_x , or the time step number, N_T , did not change the results presented in Figs. 3.11 and 3.12 significantly so it is assumed the behavior observed is not caused by that aspect of the numerical scheme. Also, it is pointed out that with the finite difference scheme of Peregrine (1966), numerical dissipation caused by the partial instead of the full implementation of the Midpoint Rule (as was discussed previously) eliminates some of the details of the profiles which are shown in Figs. 3.11 and 3.12.

In both cases considered, the initial wave is a solitary wave which is an exact solution of the KdV equation; however the shape of the wave changes as it propagates which is contrary to what the KdV equation predicts. A possible reason for this is that although the solitary wave is an exact solution of the KdV equation, the KdV equation is only an approximate form of the Boussinesq equations; therefore the solitary wave is not an exact solution of the Boussinesq equations. To demonstrate this, recall the expression for velocity, Eq. (3.18), which arises from the derivation of the KdV equation and which was used to compute the initial velocities for the waves being considered. If this expression is substituted into the first of the Boussinesq equations, Eq. (3.67), the following equation is obtained:

$$\begin{aligned}
 & \eta_t + c_o \eta_x + \frac{3}{2} \frac{c_o}{h} \eta \eta_x + \frac{c_o h^2}{6} \eta_{xxx} \\
 & = c_o \left\{ \frac{3}{4h^2} \eta^2 \eta_x - \frac{h}{6} (\eta \eta_{xxx} + \eta_x \eta_{xx}) \right\} , \quad (3.94)
 \end{aligned}$$

where

$$c_o = \sqrt{gh} .$$

The left hand side of Eq. (3.94) is the KdV equation which, if the right hand side were zero, would have the solitary wave as a solution. However, since the numerical scheme solves the Boussinesq equations with a high degree of accuracy, the presence of the higher order terms on the right hand side of Eq. (3.94) (which are $O(\alpha^2, \alpha\beta)$) prevents the solitary wave from being an exact solution. Further discussion of this with reference to Boussinesq (1872) and Keulegan and Patterson (1940) is presented in Appendix B.

The behavior of the larger wave ($H/h = 0.7$) is consistent with what is observed in the laboratory: the shape follows the theory of Boussinesq in the region of the crest and that of McCowan near the leading and trailing edges and the main wave quickly separates from the trailing oscillatory waves. However, some of the behavior of the smaller wave is contrary to what is observed in the laboratory; in particular, the growth of the trough and the slow rate at which the main wave separates from it. To investigate this further, use was made of the finite element program developed by Hughes, Liu and Zimmermann (1978) to solve the Navier Stokes equations. The program uses a penalty function approach to take account of the pressure (the

interested reader is referred to Hughes, Liu and Brooks (1978) for details of the method) and solves the problem of the free surface by allowing the finite element mesh to deform in the vertical direction. The scheme is two-dimensional so that, in contrast to the numerical method developed for this study, the velocities (horizontal and vertical) can vary with depth to a degree which is dependent on the number of elements which are taken in the depth. A comparison of wave propagation using this scheme with one element in the depth with wave propagation using the scheme developed for this study was conducted. Starting with the same initial wave profile (amplitude and velocity) for the two schemes, a wave with initial height $H/h = 0.086$ was propagated for a nondimensional time, $t\sqrt{g/h}$, of 78.4. In Fig. 3.13, the profiles at intervals of $t\sqrt{g/h} = 15.68$ are compared, with the scheme of Hughes, Liu and Zimmermann (1978) being the dashed curves. The figure shows the results agree remarkably well considering they arise from approaches which are quite different. Notice the rate of growth of the trough is even greater with the scheme of Hughes, Liu and Zimmerman (1978) ($a_t/h = 0.0101$ at $t = 78.4$) than it is for the scheme developed for this study ($a_t/h = 0.0063$ at $t = 78.4$). This growth almost can be eliminated by using the approach of Hughes, Liu and Zimmermann (1978) with two elements in the depth. The results are presented in Fig. 3.14 which shows the trough has been reduced to $a_t/h = 0.0033$ at $t = 78.4$ and the relative wave height is essentially constant with propagation. The difference in having two instead of one element in the depth is that the distributions of velocity (horizontal and vertical) are no longer constrained to be linear with depth.

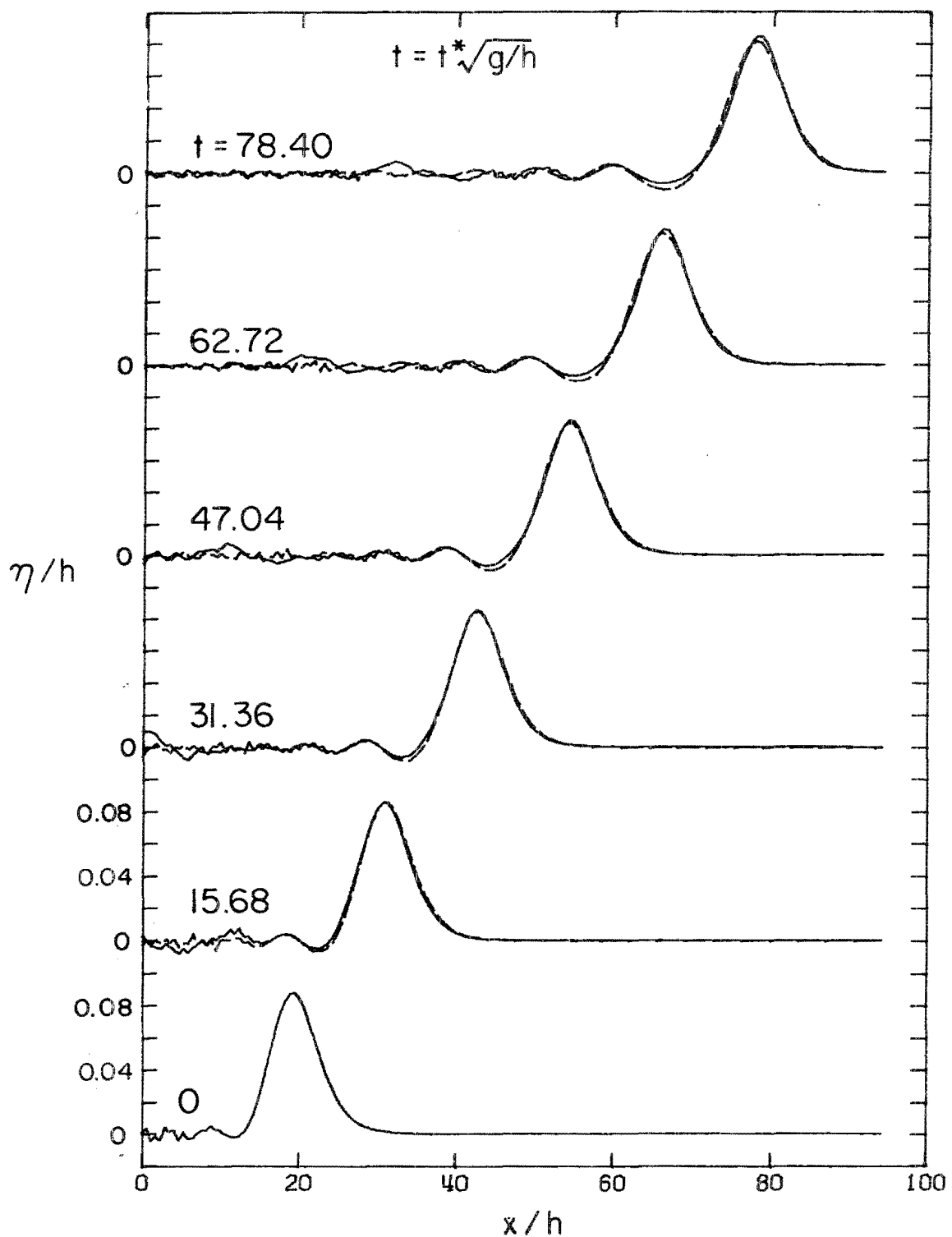


Fig. 3.13 Comparison of wave propagation using the scheme developed for this project (—) with the scheme of Hughes, Liu and Zimmermann (1978) (---).

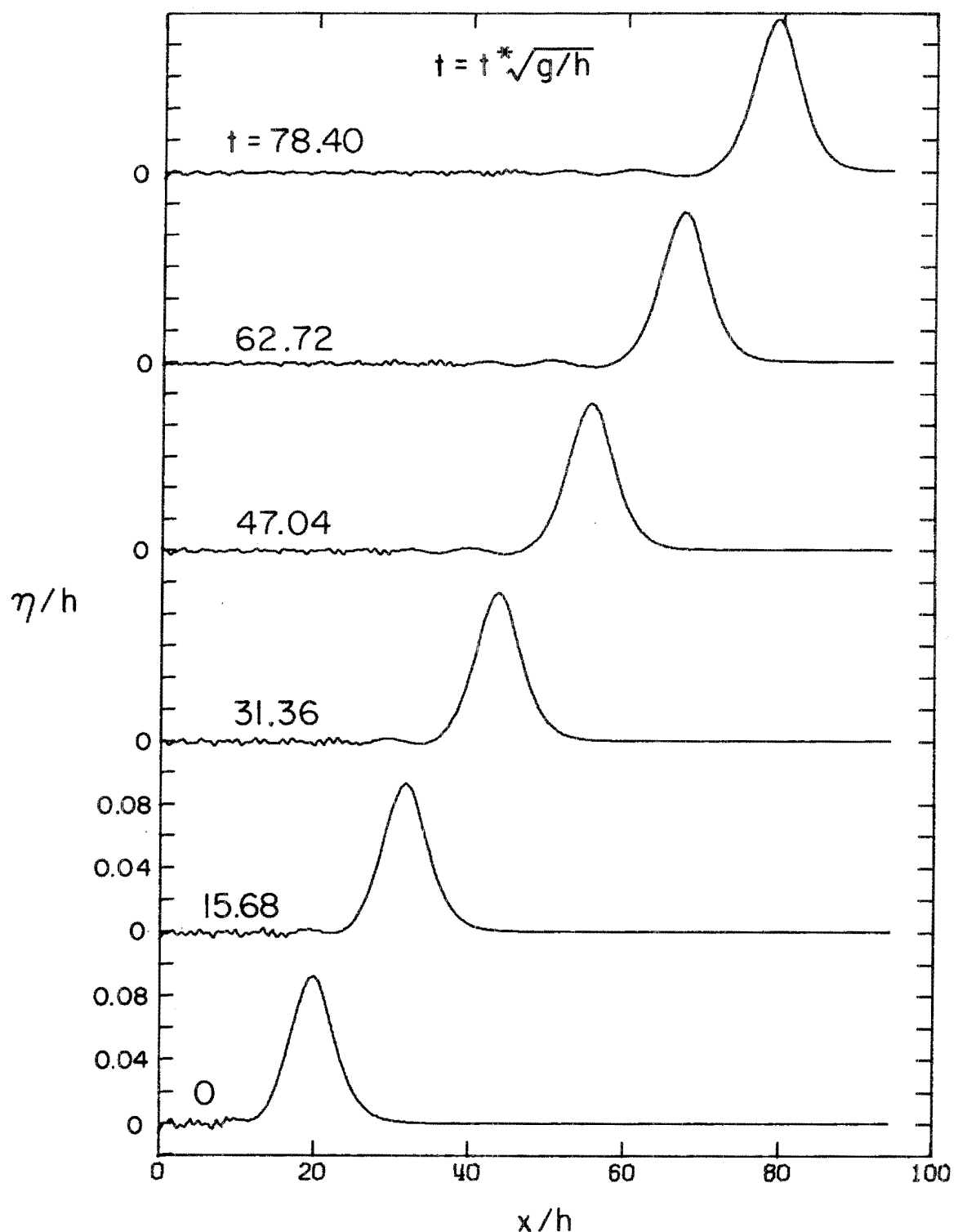


Fig. 3.14 Wave propagation using the scheme of Hughes, Liu and Zimmermann (1978) with two elements in the depth.

That this change reduces the rate of growth of the trough is taken to imply the growth of the trough is caused by the one-dimensional approximations. These approximations, for the scheme of Hughes, Liu and Zimmermann (1978), are made in the numerical scheme but for the scheme developed for this study they are inherent in the derivation of the Boussinesq equations.

Considering the dispersive nature of the trough, it is not surprising these effects are more pronounced for the smaller wave height because for the larger wave height the nonlinear effects would be expected to be stronger. In fact for the cases considered in this study where the numerical scheme was used to propagate solitary waves onto a shelf, problems with the formation of a trough did not arise. Part of the reason for this probably is that nonlinear effects caused by the reduced depth masked this behavior, but also the trough is small compared to the main wave ($\sim 6\%$) and its growth requires propagation over a greater distance than was considered for most cases.

3.3.2 Extension to the Case of Variable Depth

Consider the problem shown in Fig. 3.15 where a long wave is propagating from a region with a constant depth h_1 (Region I) over a step into Region II in which the depth also is constant but reduced to h_2 .

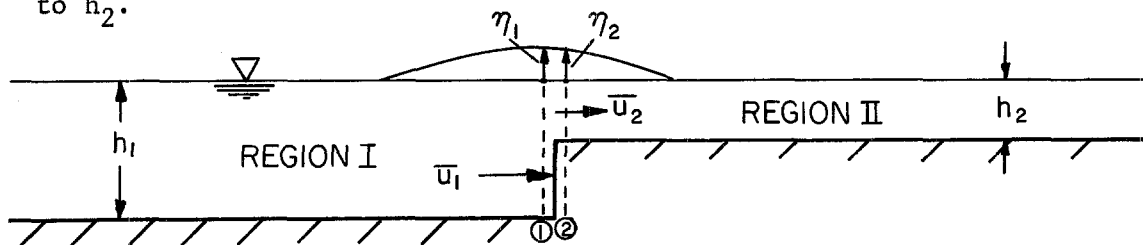


Fig. 3.15 Definition Sketch for Extension to Variable Depth

Section (1) in Region I and Section (2) in Region II are located close to the step on either side of it. At a particular instant of time, the amplitudes at Sections (1) and (2) are η_1 and η_2 , respectively, and the depth averaged velocities are given by:

$$\bar{u}_1 = \frac{1}{h_1 + \eta_1} \int_{-h_1}^{\eta_1} u_1(y) dy , \quad (3.95)$$

$$\bar{u}_2 = \frac{1}{h_2 + \eta_2} \int_{-h_2}^{\eta_2} u_2(y) dy . \quad (3.96)$$

If the distance between Sections (1) and (2) is decreased until the sections are an infinitesimal distance apart on either side of the step, then for continuity of the water surface profile:

$$\eta_1 = \eta_2 , \quad (3.97)$$

and for conservation of mass:

$$q_1 = q_2 , \quad (3.98)$$

where q_1 and q_2 are the flow rates per unit width through Sections (1) and (2), respectively, defined as:

$$q_1 = \int_{-h_1}^{\eta_1} u_1(y) dy , \quad (3.99)$$

$$q_2 = \int_{-h_2}^{\eta_2} u_2(y) dy . \quad (3.100)$$

Eq. 3.98 can be written in terms of the depth averaged velocities defined by Eqs. (3.95) and (3.96) as:

$$\bar{u}_1(h_1 + \eta_1) = \bar{u}_2(h_2 + \eta_2) \quad (3.101)$$

Since, for the problems under consideration, $\eta_1 < h_1$ and $\eta_2 < h_2$, as a first approximation Eq. (3.101) may be written as:

$$\bar{u}_1 h_1 = \bar{u}_2 h_2 \quad (3.102)$$

An estimate of the error ϵ in using Eq. (3.102) instead of Eq. (3.101) may be obtained by taking the difference between Eqs. (3.101) and (3.102) (which, using Eq. (3.97), gives: $\eta_1(\bar{u}_2 - \bar{u}_1)$) and dividing by the flow rate $\bar{u}_2 h_2$:

$$\epsilon = \left| \frac{\eta_1(\bar{u}_2 - \bar{u}_1)}{\bar{u}_2 h_2} \right| \quad . \quad (3.103)$$

Substituting for the velocity ratio from Eq. (3.102), Eq. (3.108) becomes:

$$\epsilon = \frac{H}{h_2} \frac{\Delta h}{h_1} \quad (3.104)$$

where η_1 has been replaced by a characteristic wave height H and $\Delta h = h_1 - h_2$. Thus, the error in using Eq. (3.102) is less than the maximum wave height ratio H/h_2 and may be made arbitrarily small by considering only small differences in depth.

The finite element method described in Section 3.3.1 is extended to the case of variable depth by considering the varying bottom as consisting of a series of steps, as shown in Fig. 3.16. In the

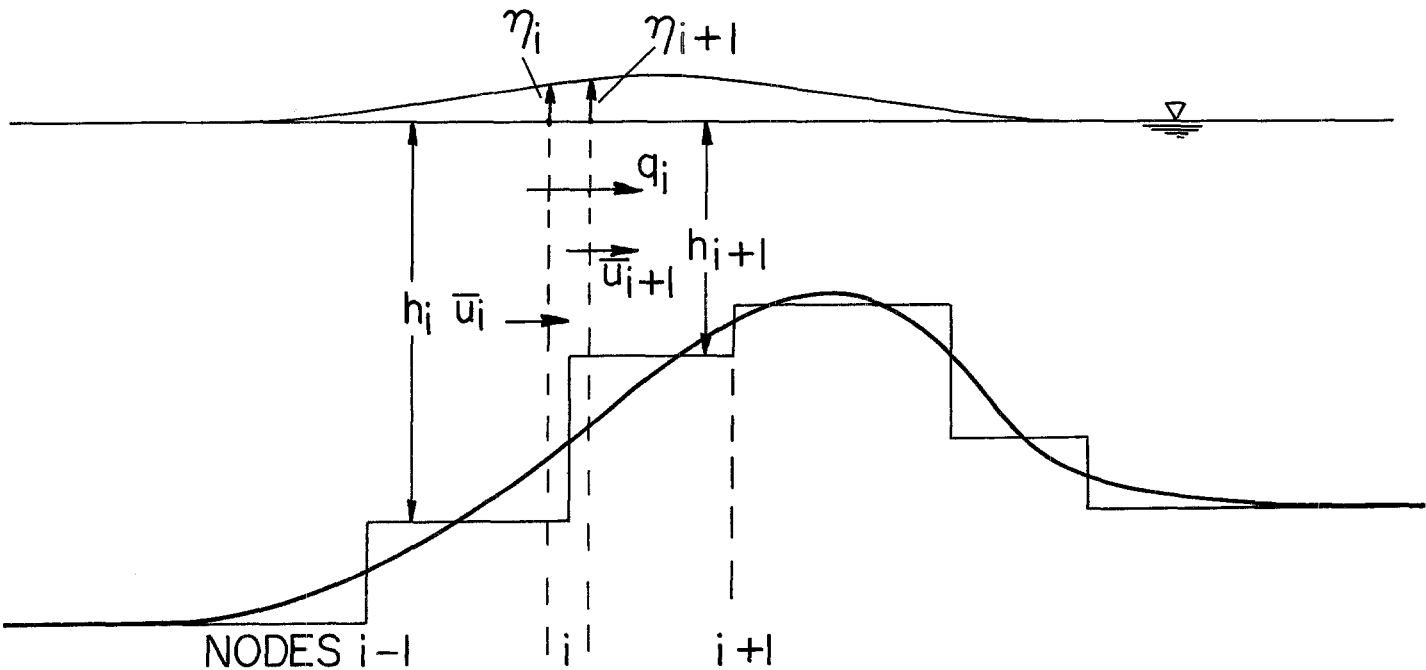


Fig. 3.16 The varying bottom considered as a series of steps

regions of constant depth between the steps, the Boussinesq equations, Eqs. (3.67) and (3.68), apply. However, these differential equations do not apply across the steps because at a node i which is at a step, although the surface profile is continuous, velocities jump from \bar{u}_i to \bar{u}_{i+1} and the depth jumps from h_i to h_{i+1} . To obtain a solution, the problem is simplified by restricting the change in depth between steps to be small enough so that the error given by Eq. (3.104) is negligible; hence the conservation of mass is as well represented by Eq. (3.102) as by Eq. (3.101). By introducing a volume flow rate defined as:

$$\bar{q} = \bar{u}h \quad , \quad (3.105)$$

the Boussinesq equations in constant depth may be rewritten in the form:

$$\eta_t + \left(1 + \frac{\eta}{h}\right) \bar{q}_x = 0 \quad (3.106)$$

$$\bar{q}_t + \frac{1}{h} \bar{q} \bar{q}_x + g h \eta_x - \frac{1}{3} h^2 \bar{q}_{xx} = 0 \quad (3.107)$$

These equations still are applicable only in a constant depth, since the depth h is discontinuous across a step; however both dependent variables, surface profile $\eta(x, t)$ and the flow rate $\bar{q}(x, t)$, now are continuous across a step. The finite element scheme is implemented by placing nodes at the steps as shown in Fig. 3.16. Upstream of Node i , Eqs. (3.106) and (3.107) apply with $h = h_i$; downstream of Node i , Eqs. (3.106) and (3.107) apply with $h = h_{i+1}$. Since the same η_i and \bar{q}_i are used for both regions, the continuity conditions across the step given by Eqs. (3.97) and (3.98) are automatically satisfied. The technique was tested by comparing with physical experiments and the results will be presented in Section 5.

3.4 The Propagation of Long Waves Onto a Shelf by the Linear Nondispersive Theory

In this section the method of solution of the linear nondispersive theory as reported by Wong *et al.* (1963) and Dean (1964) is applied to the case of solitary waves propagating onto a shelf over a transition in which the depth decreases linearly with distance. (These approaches differ from those of Kajiura (1961) who used transitions in which the depth varied in a more complicated manner with distance.)

Even though the solitary wave arises as a solution of a nonlinear dispersive theory, since nonlinear and dispersive effects take some distance (or time) to develop (Hammack and Segur (1978)), the linear nondispersive theory may predict the behavior for an initial distance (or time) which is limited. The limits of application of such an approach to propagating solitary waves was one of the objectives of this portion of the investigation. Certain aspects of this will be discussed more fully in Section 5.

The domain of solution in Fig. 3.17 consists of three regions. In Region I, which extends from $x = -\infty$ to $x = -L$, the depth is a constant h_1 . Initially, the incident wave will exist wholly in this region. Region III extends from $x = 0$ to $x = \infty$ and the depth is a constant h_2 . It is assumed that no waves propagate from $x = \infty$ in a negative x -direction. Region II is of length L and the depth changes linearly from h_1 to h_2 .

The linear nondispersive equation for variable depth as derived by Lamb (1932, §169) assuming small amplitude waves and hydrostatic pressure distribution, is:

$$\eta_{tt} = g(h\eta_x)_x \quad . \quad (3.108)$$

Wong *et al.* (1963), Dean (1964) and Kajiura (1961) solved Eq. (3.108) for a single harmonic incident wave:

$$\eta(x, t) = A_1 e^{i(kx - \omega t)} \quad , \quad (3.109)$$

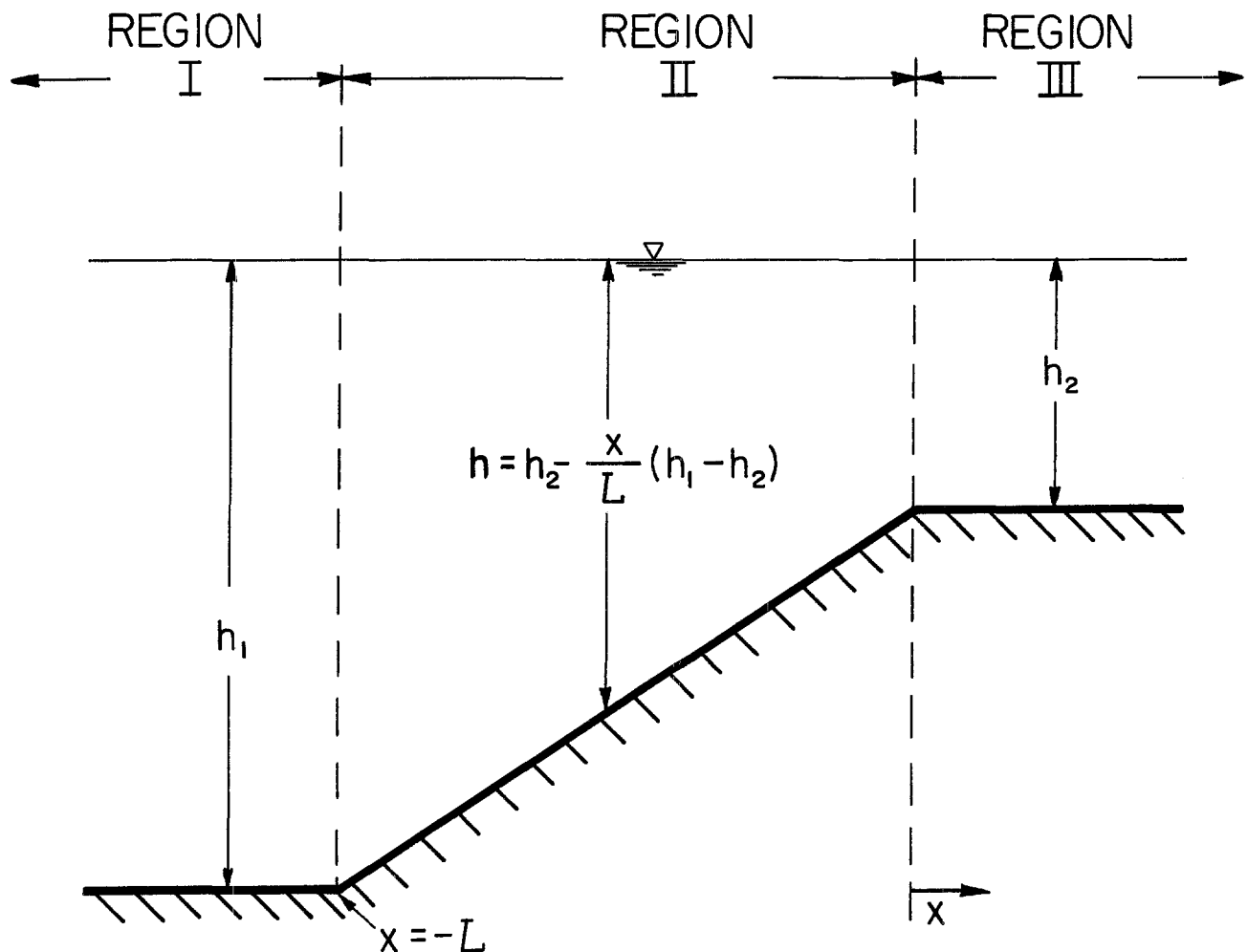


Fig. 3.17 Definition sketch for linear nondispersive theory.

where $i = \sqrt{-1}$, ω is the radial frequency, k is the wave number and, since it is assumed that there is no dispersion, $\omega = \sqrt{gh_1} k$. The method used was to solve Eq. (3.108) for each of the three regions in turn and then match the solutions at the boundaries by assuming continuity of surface elevation and surface slope. Details of the method are presented in Appendix C.

The solution is:

$$\text{Region I: } \eta_1(x, t) = A_1 e^{i(kx - \omega t)} + A_2 e^{-i(kx + \omega t)}, \quad (3.110)$$

$$\text{Region II: } \eta_2(x, t) = B_1 J_0(x) e^{-i\omega t} + B_2 Y_0(x) e^{-i\omega t}, \quad (3.111)$$

where
$$x = \frac{2\omega L}{\sqrt{gh_1} \left(1 - \frac{h_2}{h_1}\right)} \left[\frac{h_2}{h_1} - \left(1 - \frac{h_2}{h_1}\right) \frac{x}{L} \right]^{\frac{1}{2}}$$

$$\text{Region III: } \eta_3(x, t) = C_1 e^{i(k\sqrt{h_1/h_2} x - \omega t)}, \quad (3.112)$$

where $J_0(X)$ and $Y_0(X)$ are the zero order Bessel functions of the first and second kind respectively and the coefficients A_2 , B_1 , B_2 and C_1 are functions of the incident wave amplitude A_1 , the depth ratio h_2/h_1 and the dimensionless quantity $\omega L/\sqrt{gh_1}$. The relationships for the coefficients A_2 , B_1 , B_2 and C_1 as deduced by Wong *et al.* (1963) are listed in Appendix C. The reflection coefficient, defined as $K_R = A_2/A_1$, and the transmission coefficient, defined as $K_T = C_1/A_1$, can be determined in simple terms only for extreme values of $\omega L/\sqrt{gh_1}$.

For $\omega L/\sqrt{gh_1} \ll 1$ (i.e. $L = 0$, a step), the expressions for the Bessel functions of small argument can be used and the coefficients can be evaluated in terms of the depth ratio only:

$$K_R = \frac{1 - \sqrt{h_2/h_1}}{1 + \sqrt{h_2/h_1}}, \quad (3.113)$$

$$K_T = \frac{2}{1 + \sqrt{h_2/h_1}}. \quad (3.114)$$

(These also can be obtained by the more basic approach of Lamb (1932, §176).)

The magnitude of the reflection coefficient is bounded by $0 \leq K_R \leq 1$ and the transmission coefficient is bounded by $0 \leq K_T \leq 2$. When the depth ratio h_2/h_1 is unity (i.e. there is no shelf) there is zero reflection $K_R = 0$ and perfect transmission $K_T = 1$ as expected. For small depth ratios h_2/h_1 (i.e. $h_2 \ll h_1$) the reflection coefficient $K_R \rightarrow 1$ and the transmission coefficient $K_T \rightarrow 2$, however care must be exercised in using these expressions for small depth ratios to ensure that the small amplitude assumption is not violated on the shelf. For example, if $h_2/h_1 = 0.01$ and the incident wave amplitude to depth ratio $A_1/h_1 = 0.01$ (which is small enough to be considered small amplitude), then the transmitted wave amplitude to depth ratio $C_1/h_2 = 1.82$ which is certainly not small amplitude. In fact for the waves on the shelf to have amplitude to depth ratios $C_1/h_2 \leq 0.01$, the incident wave amplitude to depth would have to be $A_1/h_1 < 5.5 \times 10^{-5}$. Similar arguments apply when the depth ratio is large $h_2 \gg h_1$ except that in this case care must be taken to ensure that the long wave assumption is not violated.

For $\omega L/\sqrt{gh_1} \gg 1$ (i.e. a long slope), the reflection and transmission coefficients are:

$$K_R = 0 \quad , \quad (3.115)$$

$$K_T = \left(\frac{h_2}{h_1} \right)^{-\frac{1}{4}} \quad , \quad (3.116)$$

which represents the classical Green's Theorem (Lamb (1932, §185) for long waves propagating over gradual slopes.

Wong *et al.* (1963), Dean (1964) and Kajiura (1961) solved Eq. (3.108) for a single harmonic incident wave. Since Eq. (3.108) is a linear equation the solutions can be superimposed for an incident wave given by:

$$\eta(x, t) = \sum_{n=0}^N A_{1n} e^{i(k_n x - \omega_n t)} \quad . \quad (3.117)$$

Eqs. (3.110), (3.111) and (3.112), become:

$$\text{Region I: } \eta_1(x, t) = \sum_{n=0}^N A_{1n} e^{i(k_n x - \omega_n t)} + \sum_{n=0}^N A_{2n} e^{-i(k_n x + \omega_n t)} \quad (3.118)$$

$$\text{Region II: } \eta_2(x, t) = \sum_{n=0}^N \left\{ B_{1n} J_o(x_n) + B_{2n} Y_o(x_n) \right\} e^{-i\omega_n t} \quad (3.119)$$

$$x_n = \frac{2\omega_n L}{\sqrt{gh_1} \left(1 - \frac{h_2}{h_1} \right)} \left[\frac{h_2}{h_1} - \left(1 - \frac{h_2}{h_1} \right) \frac{x}{L} \right]^{\frac{1}{2}}$$

$$\text{Region III: } \eta_3(x, t) = \sum_{n=0}^N C_{1n} e^{i(k_n \sqrt{h_1/h_2} x - \omega_n t)} \quad (3.120)$$

For incident waves given by Eq. (3.117), the reflection and transmission coefficients for $\omega_n L / \sqrt{gh_1} = 0$ (Eqs. (3.113) and (3.114)) apply for two conditions:

a) $L/h_1 = 0$ (i.e. a step). Since Eqs. (3.113) and (3.114) are independent of frequency, each frequency component of the incident wave A_{1n} is reflected or transmitted by the same proportion. Thus,

the reflected and transmitted waves have the same shape as the incident wave. This is the classical result of Lamb (1932) who used a more fundamental approach and general functions $f(x, t)$ instead of harmonic functions.

b) $n = 0$ (i.e. $\omega_n = 0$). Since Eqs. (3.113) and (3.114) are independent of the slope length L , the proportion of the mean component (i.e. the volume) of the incident wave reflected or transmitted is the same for all slope lengths L . This rather surprising result will be discussed further in Section 5.

For the solutions, Eqs. (3.118), (3.119) and (3.120), to apply to a particular long wave given by Eq. (3.117), it is necessary first that the wave height be everywhere small compared to the depth and second that the wave satisfy either of the two conditions:

- a) The maximum frequency ω_N is small enough for the nondispersive assumption to be valid, or
- b) The entire wave form propagates without dispersing.

A solitary wave propagates in constant depth without dispersing but the wave height is not necessarily small compared to the depth. As the wave enters a region of changing depth such as Region II in Fig. 3.17, it is expected that amplitude and frequency dispersion will occur. However, Hammack and Segur (1978) point out that the linear nondispersive theory may apply for some time before it is necessary to use the full Boussinesq equations to model the propagation. It is to determine this range of applicability therefore that the linear nondispersive theory is applied to a solitary wave propagating

onto a shelf.

The solitary wave defined by Eq. (3.25) in Section 3.1 also can be written as:

$$\eta(x, t) = H \operatorname{sech}^2 \frac{3\sqrt{3}}{4} \left(\frac{x-ct}{\lambda} \right) , \quad (3.121)$$

where λ is the characteristic length defined by Hammack (1972):

$$\lambda = \frac{3}{2} \left(\frac{H}{h} \right)^{-\frac{1}{2}} h . \quad (3.122)$$

To implement the linear nondispersive theory it is necessary to use the celerity $c = \sqrt{gh}$. It is convenient to normalize the independent variables with respect to the slope length, L , as follows:

$$x = x^*/L \quad t = t^* \sqrt{gh_1} / L ,$$

(where * denotes the original dimensional variable) and to normalize the wave amplitude with respect to the wave height, $\eta = \eta^*/H$. Then Eq. (3.121) becomes:

$$\eta(x, t) = \operatorname{sech}^2 \frac{3\sqrt{3}}{4} \frac{L}{\lambda} (x-t) \quad (3.123)$$

To find the solution for an incident wave given by Eq. (3.123) it is necessary to resort to numerical techniques because the complicated form of the coefficients A_2 , B_1 , B_2 and C_1 makes the analytical Fourier Transform method difficult to implement. The development of the Fast Fourier Transform (FFT) algorithm however, has made numerical solution of the problem accurate and inexpensive.

The solution at a particular x is found in four steps:

1. The incident wave at $x = 0$ is approximated by the discrete function

$$n(0, t_m) = \operatorname{sech}^2 \frac{3\sqrt{3}}{4} \frac{L}{\lambda} t_m , \quad (3.124)$$

where the t_m are N equispaced points in the finite interval

$$-T/2 < t_m < T/2 ,$$

where the magnitudes of N and T are governed by the desired accuracy and resolution as will be discussed presently.

2. The discrete approximation of the incident wave Eq. (3.124) is put in the form:

$$n(0, t_m) = \sum_{n=-N/2}^{N/2} A_{1n} e^{-i\omega_n t_m} , \quad (3.125)$$

where $\omega_n = \frac{2\pi n}{T} ,$

by computing the discrete Fourier coefficients:

$$A_{1n} = \frac{1}{N} \sum_{m=0}^{N-1} n(0, t_m) e^{i\omega_n t_m} , \quad (3.126)$$

using the Fast Fourier Transform (FFT) algorithm.

3. The solutions, Eqs. (3.118), (3.119) and (3.120), normalized as described above and with $\omega_n = \omega_n^* L / \sqrt{gh_1}$ and $k_n = k_n^* L$ may be transformed from the time domain to the frequency domain to become:

Region I: $\bar{\eta}_{1_n}(x, \omega_n) = A_{1_n} e^{i k_n x} + A_{2_n} e^{-i k_n x}$ (3.127)

Region II: $\bar{\eta}_{2_n}(x, \omega_n) = B_{1_n} J_0(x_n) + B_{2_n} Y_0(x_n)$ (3.128)

where

$$x_n = \frac{2\omega_n}{\left(1 - \frac{h_2}{h_1}\right)} \left[\frac{h_2}{h_1} - \left(1 - \frac{h_2}{h_1}\right) x \right]^{\frac{1}{2}}$$

Region III: $\bar{\eta}_{3_n}(x, \omega_n) = C_{1_n} e^{i k_n \sqrt{h_1/h_2} x}$ (3.129)

$$n = -\frac{N}{2}, -\frac{N}{2} + 1, \dots, \frac{N}{2} - 1, \frac{N}{2}$$

The solution in the frequency domain for the wave at the particular location, x , (F_n) is calculated by evaluating one of Eqs. (3.127), (3.128) or (3.129) at that position, for the N components.

4. The solutions F_n are transformed back into the time domain:

$$\eta(x, t_m) = \frac{1}{N} \sum_{n=-N/2}^{N/2} F_n(\omega_n) e^{-i \omega_n t_m}, \quad (3.130)$$

using the inverse Fourier transformation.

The numerical scheme requires specifications of the two quantities T and N . The total length of the time record T must be made large enough to include the entire wave at the location x . The number of

points N in the time interval T determine the resolution with which the solution at x is determined. The accuracy is determined by the maximum frequency $\omega_{\max} = \frac{\pi N}{T}$ which must be large enough for $|F(\omega_{\max})|$ to be negligible. An estimate of the magnitude of ω_{\max} can be obtained by considering the analytical Fourier Transform of $\eta(t) = \operatorname{sech}^2 \frac{3\sqrt{3}}{4} \frac{L}{\lambda} t$, which gives:

$$A_1(\omega) = \frac{\pi \omega}{\Omega^2} \operatorname{cosech} \frac{\pi \omega}{2\Omega} \quad \omega \neq 0 ,$$

$$A_1(0) = 2/\Omega , \quad (3.131)$$

where $\Omega = \frac{3\sqrt{3}}{4} \frac{L}{\lambda} .$

For $A_1(\omega_{\max})/A_1(0) < 1 \times 10^{-5}$, Eq. (3.131) implies $\omega_{\max} > 30\Omega/\pi$ which, by substituting for ω_{\max} and Ω , becomes $\frac{N}{T} > \frac{4L}{\lambda}$, i.e., to accurately define the incident wave in the frequency domain, the ratio of the number of points in the interval to the length of the interval (N/T) must be greater than four times the length ratio.

Results of this analysis and comparison with the nonlinear dispersive theory and experiment will be presented in Section 5.

3.5 The Propagation of Long Waves to Infinity by the Nonlinear Dispersive Theory

Distant propagation by inverse scattering is a method of determining asymptotic solutions of the KdV equation. It provides a way of analyzing a wave of arbitrary shape which is being propagated by the nonlinear dispersive theory in an analogous manner to the way harmonic analysis could be used if the wave were being propagated by a linear dispersive theory.

Linear dispersive equations such as the long wave equation (Eq. 3.14) discussed in Section 3.1 have exact solutions in the form of sinusoidal waves. In a corresponding way the KdV equation has exact solutions in the form of solitary waves. A wave of arbitrary shape being propagated by a linear dispersive theory will eventually split up into an infinite number of sinusoidal waves of different wave numbers each travelling at a speed which is a function of the wave number; a wave of arbitrary shape being propagated by the nonlinear dispersive theory will eventually split up into a finite number of solitary waves of different height followed by a train of oscillatory waves and, since solitary waves propagate at a speed which is a function of the wave height, the solitary waves separate into a train with the largest wave leading and the smallest wave trailing. For the linear dispersive theory, harmonic analysis provides the amplitudes of the infinite number of sinusoidal waves which emerge; for the nonlinear dispersive theory, inverse scattering provides the number and the height of the solitary waves which emerge.

In this section the inverse scattering theory, which was derived by Gardner *et al.* (1967), is outlined, then one of the few analytical solutions is presented and, finally, numerical methods of solution are described.

3.5.1 Summary of the Inverse Scattering Theory

Consider the KdV equation, Eq. (3.22). By changing variables as follows:

$$r = \frac{x}{h} - t \sqrt{\frac{g}{h}}, \quad \tau = \frac{1}{6} t \sqrt{\frac{g}{h}}, \quad f(r, \tau) = \frac{3}{2h} \eta(x, t) \quad , \quad (3.132)$$

Eq. (3.22) becomes:

$$f_\tau + 6ff_r + f_{rrr} = 0 \quad . \quad (3.133)$$

Whitham (1974, P585) shows that the asymptotic solution of Eq. (3.133) can be transformed to the Sturm-Louiville problem:

$$\psi'' + [\lambda + f(r, 0)]\psi = 0 \quad , \quad (3.134)$$

where primes denote differentiation with respect to r , $f(r, 0)$ is the normalized initial wave profile and $\psi(r) \rightarrow 0$ as $|r| \rightarrow \infty$. Whitham shows the number of negative eigenvalues λ gives the number of solitary waves which will emerge as $\tau \rightarrow \infty$ and the height of these solitary waves is:

$$\frac{H_i}{h} = -\frac{4}{3} \lambda_i \quad . \quad (3.135)$$

The number of negative eigenvalues is found by solving the initial value problem (see Hammack and Segur (1974)):

$$\begin{aligned} \psi'' + f(r, 0)\psi &= 0 \\ \psi(0) = 1 & \quad \psi'(0) = 0 \end{aligned} \quad , \quad (3.136)$$

and counting the number of zero crossings of ψ .

The inverse scattering theory has been applied to practical problems by Hammack and Segur (1974, 1978) among others. Hammack and Segur (1974) show that if the initial wave profile has net positive volume, at least one solitary wave will emerge followed by a train of oscillatory waves. If the net volume is less than or equal to zero, solitary waves may or may not emerge depending on the form of the initial wave. If the wave amplitude is entirely negative, no solitary waves will emerge.

3.5.2 The Analytic Solution for a Wave with sech^2 Shape

Analytic solutions of the inverse scattering problem are available for only a few initial wave profiles, i.e., $\eta(x, 0)$. One of these, given by Whitham (1974, p597), is:

$$\eta(x, 0) = A \text{ sech}^2 B(x - x_0) \quad , \quad (3.137)$$

where A is the wave height and B is a type of wave number.

The number of solitary waves emerging as x and $t \rightarrow \infty$ is:

$$N < \frac{1}{2} P \quad , \quad (3.138)$$

where

$$P = \left(1 + \frac{6A}{h^3 B^2}\right)^{\frac{1}{2}} + 1 \quad . \quad (3.139)$$

Note that N is an integer which is strictly less than $\frac{1}{2} P$ (e.g. if $P = 4.0$, $N = 1$). The height of the emerging solitary waves is given by Whitham (1974) as:

$$\frac{H_n}{h} = \frac{1}{3} h^2 B^2 (P - 2n)^2 \quad . \quad (3.140)$$

$$n = 1, 2, \dots, N$$

Since A is a wave height and $1/B$ is a horizontal length, the nondimensional quantity $A/h^3 B^2$ is a type of Ursell Number. Eq. (3.139) can be rewritten in terms of the Ursell Number defined by Hammack (1972) as:

$$U = \frac{\eta_{\max}^3}{h^3 |\eta_x|_{\max}^2} \quad . \quad (3.141)$$

Evaluating the Ursell Number for a wave given by Eq. (3.137) using Eq. (3.141) gives:

$$U = \frac{27}{16} \frac{A}{B^2 h^3} \quad , \quad (3.142)$$

and substituting this in Eq. (3.139) yields:

$$P = \left(1 + \frac{32}{9} U\right)^{\frac{1}{2}} + 1 \quad . \quad (3.143)$$

A special case occurs when $B^2 = \frac{3}{4} \frac{A}{h^3}$ (i.e. a solitary wave); then $U = 9/4$ and, from Eq. (3.143), $P = 4$, hence, using the inequality of

Eq. (3.138), only one solitary wave will emerge.

If, for a particular initial wave with the form of Eq. (3.137), the Ursell Number lies in the interval $0 < U \leq 9/4$, then $2 < P \leq 4$ and therefore only one solitary wave will emerge. An important case in this class relevant to this study is when the initial wave has the form:

$$n(x, 0) = \alpha H \operatorname{sech}^2 \sqrt{\frac{3}{4} \frac{H}{h^3}} (x - x_0) \quad , \quad (3.144)$$

where $\alpha < 1$, i.e. a solitary wave whose amplitude has been reduced by a constant ratio over the entire wave. The height of the one solitary wave which emerges at infinity from Eq. (3.140) is:

$$H_1 = \frac{H}{4} \{ (1 + 8\alpha)^{\frac{1}{2}} - 1 \}^2 \quad . \quad (3.145)$$

Eq. (3.145) is surprising in that, although it is the solution of the nonlinear dispersive theory, the height of the emerging wave is linearly proportional to the wave height which defined its original shape. (This has important implications in data reduction and is discussed in detail in Section 5.2).

If the Ursell Number $U > 9/4$, then $P > 4$ and therefore more than one solitary wave will emerge. Table 3.3 gives the maximum Ursell Number for which a particular number of solitary waves will emerge. It shows that if for example the Ursell Number of a particular wave of sech^2 shape lies in the interval $2.25 < U < 6.75$, then two solitary waves will emerge.

Table 3.3 Maximum Ursell Numbers for a particular number of solitary waves to emerge from a sech^2 wave.

N	1	2	3	4	5	6	7
U_{\max}	2.25	6.75	13.5	22.5	33.75	46.75	63.

3.5.3 Numerical Solutions for Waves with Arbitrary Shape

The Sturm-Louiville problem Eq. (3.134) was solved using the Rayleigh-Ritz technique:

Define the linear operator:

$$L\psi = -\psi'' - f\psi \quad , \quad (3.146)$$

then Eq. (3.134) can be written as:

$$L\psi = \lambda\psi \quad , \quad (3.147)$$

where λ is the eigenvalue.

The Rayleigh Quotient is:

$$Q = \frac{(L\psi, \psi)}{(\psi, \psi)} \quad , \quad (3.148)$$

where the inner product is defined in general terms as:

$$(u, v) \equiv \int_{-\infty}^{\infty} uv \, dr \quad .$$

The eigenvalues λ are found by minimizing the Rayleigh Quotient Q over all functions $\psi(r)$:

$$\lambda = \min_{\psi(r)} Q \quad . \quad (3.149)$$

The calculated eigenvalue:

$$\mu = Q \quad , \quad (3.150)$$

resulting from evaluation of Eq. (3.148) for a particular function $\psi(r)$, is an upper bound on the actual eigenvalue λ :

$$\mu \geq \lambda \quad . \quad (3.151)$$

The proximity of the calculated eigenvalue μ to the actual eigenvalue λ depends on the choice of the function $\psi(r)$. Two schemes were developed using different functions $\psi(r)$ and although the basic Rayleigh-Ritz techniques were the same, the implementation and applications were quite different.

$$\text{Scheme 1: } \psi(r) = \sum_{i=1}^N c_i \phi_i(r); \quad \phi_i(-\infty) = \phi_i(\infty) = 0$$

$$\text{Scheme 2: } \psi(r) = \phi(kr); \quad \phi(-\infty) = \phi(\infty) = 0$$

Scheme 1 produces N eigenvalue estimates and involves $N^2/2$ numerical integrations and a matrix eigenvalue problem. Scheme 2 produces only the lowest eigenvalue but with as few as nine numerical integrations and no matrices. Thus, if the height of only the leading solitary wave is required, Scheme 2 is preferable, but if more than one height is required Scheme 1 must be used.

3.5.3.1 Scheme 1: A Sum of Functions

Let: $\psi(r) = \sum_{i=1}^N c_i \phi_i(r); \quad \phi_i(-\infty) = \phi_i(\infty) = 0 \quad , \quad (3.152)$

where the ϕ_i are arbitrary functions. Then substituting in Eq. (3.148) and minimizing Q with respect to c_i gives:

$$\sum_{i=1}^N c_i \left[\int_{-\infty}^{\infty} \phi_i' \phi_j' dr - \int_{-\infty}^{\infty} f(r, 0) \phi_i \phi_j dr - \mu \int_{-\infty}^{\infty} \phi_i \phi_j dr \right] = 0$$

$$j = 1, 2, \dots, N \quad , \quad (3.153)$$

where primes denote differentiation with respect to r , and $\mu = Q$.

Eq. (3.153) may be written in matrix form:

$$[\tilde{A} - \tilde{B} - \mu \tilde{D}] \tilde{c} = 0 \quad , \quad (3.154)$$

where $A_{ij} = \int_{-\infty}^{\infty} \phi_i' \phi_j' dr \quad ,$

$$B_{ij} = \int_{-\infty}^{\infty} f(r, 0) \phi_i \phi_j dr \quad ,$$

$$D_{ij} = \int_{-\infty}^{\infty} \phi_i \phi_j dr \quad .$$

Eq. (3.154) provides a standard matrix eigenvalue problem, the resulting eigenvalues μ_i being upper bounds on the actual eigenvalues λ_i :

$$\lambda_i \leq \mu_i \quad .$$

In order to simplify the matrix eigenvalue problems it was decided to use orthogonal base functions ϕ_i . The functions chosen were the trigonometric functions:

$$\phi_i = \sin \frac{i\pi r'}{L} \quad i = 1, 2, \dots, N \quad , \quad (3.155)$$

where L is a length large enough to be considered infinite for the particular initial wave $f(r, 0)$, and:

$$r' = r + \frac{L}{2} \quad .$$

The trigonometric functions are not ideal because the definition of the length L is arbitrary, but none of the other readily evaluated orthogonal functions such as the orthogonal polynomials have a suitable form for this problem. Substituting for the base functions given by Eq. (3.155) in Eq. (3.154) yields:

$$A_{ij} = \frac{ij\pi^2}{L^2} \int_0^L \cos \frac{i\pi r'}{L} \cos \frac{j\pi r'}{L} dr' \\ = \begin{cases} 0 & i \neq j \\ \frac{i^2\pi^2}{2L} & i = j \end{cases} \quad , \quad (3.156)$$

$$B_{ij} = \int_0^L f(r', 0) \sin \frac{i\pi r'}{L} \sin \frac{j\pi r'}{L} dr' \quad ,$$

$$D_{ij} = \begin{cases} 0 & i \neq j \\ \frac{L}{2} & i = j \end{cases} \quad ,$$

and using these relationships the matrix equation in Eq. (3.154) can be simplified to:

$$[\tilde{A}' - \tilde{B}' - \mu \tilde{I}] \tilde{\zeta} = 0 \quad , \quad (3.157)$$

where $A'_{ii} = \frac{i^2 \pi^2}{L^2} \quad , \quad A_{ij} = 0 \quad i \neq j \quad ,$

$$B'_{ij} = \frac{2}{L} \int_0^L f(r', 0) \sin \frac{i\pi r'}{L} \sin \frac{i\pi r'}{L} dr' \quad ,$$

and \tilde{I} is the identity matrix.

To test the numerical scheme, the eigenvalues of waves with initial shape given by Eq. (3.137) were calculated for various wave heights A and wave numbers B and compared with the theoretical eigenvalues. (The results are presented in Appendix D.) The tests indicated that this scheme is sensitive to the choice of the length L (which is discussed in Appendix D) and that it is most accurate for waves from which more than one solitary wave will emerge.

3.5.3.2 Scheme 2: A Single Function

Since the solution sought is the height of the leading solitary wave, an obvious choice for the trial function ψ is:

$$\psi = \operatorname{sech}^2 kr \quad , \quad (3.158)$$

which satisfies the boundary conditions $\psi(\pm \infty) = 0$. Using Eq. (3.158), the denominator of the Rayleigh Quotient (Eq. 3.149)) is:

$$(\psi, \psi) = \int_{-\infty}^{\infty} \operatorname{sech}^4 kr dr = \frac{4}{3k} \quad , \quad (3.159)$$

and the numerator is:

$$(L\psi, \psi) = \int_{-\infty}^{\infty} \{(\psi')^2 - f(r, 0)\} dr = \frac{16}{15} - I \quad , \quad (3.160)$$

where

$$I = \int_{-\infty}^{\infty} f(r, 0) \operatorname{sech}^4 kr dr \quad , \quad (3.161)$$

Thus, the Rayleigh Quotient becomes:

$$Q = \frac{(L\psi, \psi)}{(\psi, \psi)} = \frac{4}{5} k^2 - \frac{3k}{4} I \quad . \quad (3.162)$$

The best estimate of the lowest eigenvalue is found by minimizing the Rayleigh Quotient Q with respect to the parameter k :

$$\frac{\partial Q}{\partial k} = \frac{8}{5} k - \frac{3}{4} I - \frac{3}{4} k \frac{\partial I}{\partial k} \quad , \quad (3.163)$$

where

$$\frac{\partial I}{\partial k} = -4 \int_{-\infty}^{\infty} r f(r, 0) \operatorname{sech}^4 kr \tanh kr dr \quad . \quad (3.164)$$

Setting $\partial Q / \partial k = 0$, Eq. (3.163) was solved for the parameter k using Newton's Rule:

$$\text{Put } F = \frac{dQ}{dk} = \frac{8}{5} k - \frac{3}{4} I - \frac{3}{4} k \frac{\partial I}{\partial k} \quad , \quad (3.165)$$

then, differentiating with respect to the parameter k :

$$\frac{\partial F}{\partial k} = \frac{8}{5} - \frac{3}{2} \frac{\partial I}{\partial k} - \frac{3}{4} k \frac{\partial^2 I}{\partial k^2} \quad , \quad (3.166)$$

where

$$\frac{\partial^2 I}{\partial k^2} = -4 \int_{-\infty}^{\infty} r^2 f(r, 0) [\operatorname{sech}^6 kr - 4 \operatorname{sech}^4 kr \tanh^2 kr] dr \quad . \quad (3.167)$$

Newton's Rule is:

$$k^{(i+1)} = k^{(i)} - \frac{F(k^{(i)})}{F_k(k^{(i)})} \quad , \quad (3.168)$$

where superscripts denote iteration number. Having found k within given accuracy from Eq. (3.168) it can be substituted into Eq. (3.162) to evaluate the Rayleigh Quotient Q , then

$$\lambda \leq Q \quad .$$

The same tests which were performed for Scheme 1 also were carried out here, using Scheme 2 to calculate the lowest negative eigenvalue of waves with shape given by Eq. (3.137). The results, presented in Appendix D, show that this scheme also is most accurate for waves from which more than one solitary wave will emerge.

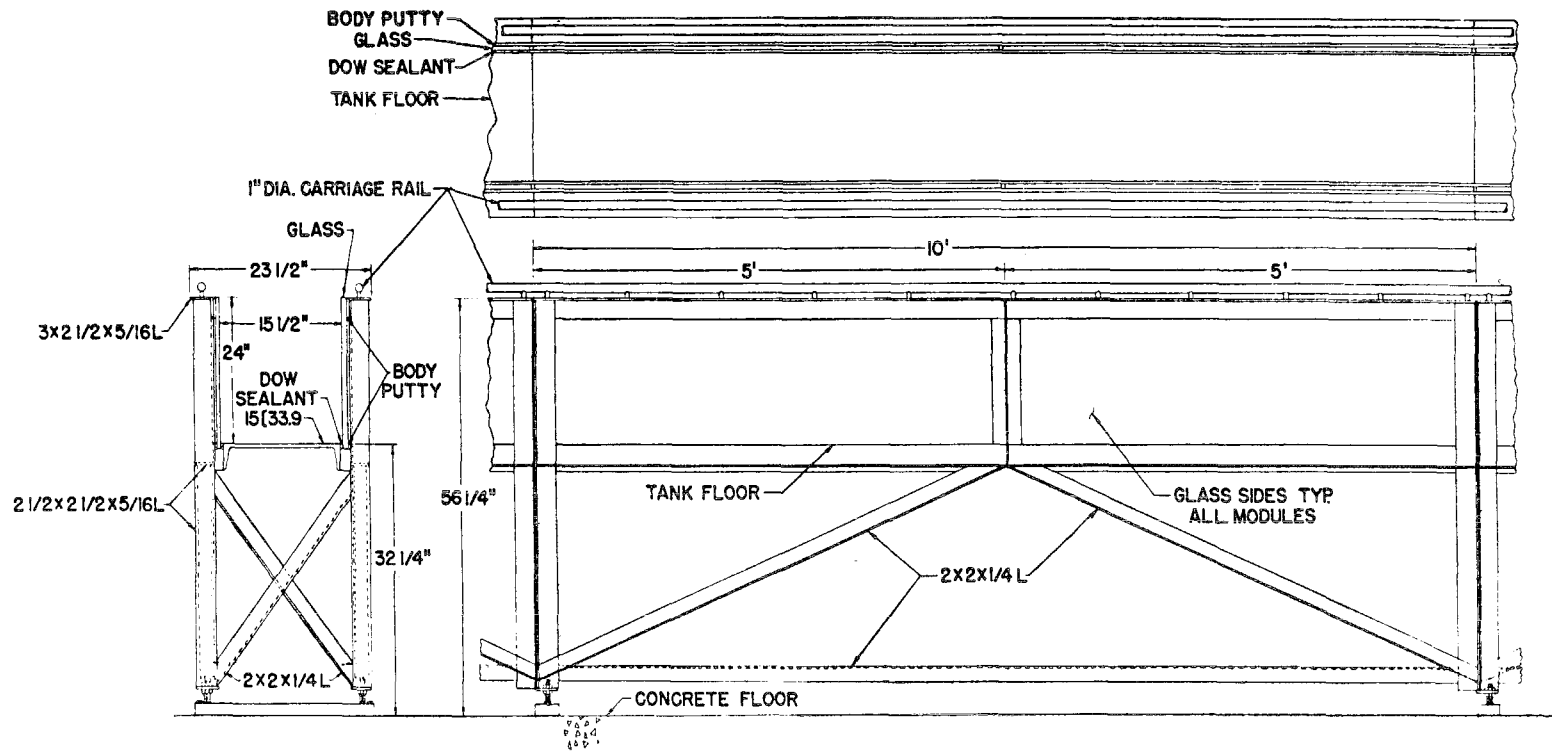
CHAPTER 4

EXPERIMENTAL EQUIPMENT AND PROCEDURES

Most of the equipment used in this investigation was constructed using "U.S. Customary" units; however, all experimental data were taken in SI (System Internationale) units. In this chapter, in describing the equipment, measurements in the system of units used in the construction of the equipment will be stated first and the equivalent measurement in the other system of units will be stated in parentheses.

4.1 The Wave Tank

The wave tank which was used for the experimental program measures 123.8 ft (37.73 m) long, 2 ft (61 cm) deep and $15\frac{1}{2}$ in. (39.4 cm) wide. The tank is constructed of thirteen separate modules, twelve of which are identical; the additional module is located at one end of the wave tank and contains a movable block section of the bed which was used by Hammack (1972). This module was sealed off and not used in this study. A schematic drawing of one of the ten similar modules of the wave tank is shown in Fig. 4.1. Details of the construction of these modules have been given previously by French (1969) and will be discussed only briefly here. The side walls of each module are constructed of glass panels measuring 5 ft (1.52 m) long, 25 in. (63.5 cm) high and $\frac{1}{2}$ in. (1.27 cm) thick. The instrument carriage rails are made of 1 in. (2.54 cm)



93

Fig. 4.1 Schematic drawing of a typical tank module (after French (1969)).

diameter stainless steel rod and are mounted on the top flanges of the tank sidewalls with studs spaced at 2 ft (61 cm) intervals. The rails were carefully leveled to within 0.001 ft (.3 mm) of a still water surface in the wave tank.

To simulate a shelf, a false bottom and four slopes were constructed; the details are shown in Fig. 4.2. The shelf was constructed of plywood in 8 ft units and each was weighted with lead bricks to prevent it floating. The ribs shown in Fig. 4.2(a) which were placed at 4 ft centers were shaped so as to allow the air to escape along the underside of the shelf as the water level rose during filling. The shelf was sealed by packing the gap between the shelf and the glass walls of the tank with 3/8 in. diameter polyethylene rod.

Three slopes with lengths of 150 cm, 300 cm and 450 cm were constructed of 3/4 in. plywood as shown in Fig. 4.2(b). Each slope was approximately 6 in. high (actually 15.54 cm) at the one end where it butted into the shelf and tapered to a feather-edge. The feather-edge was constructed of 16 gauge sheet metal. The half-sine transition shown in Fig. 4.2(c) was cut from a glued laminated pine block. The equation representing the shape of the face of the transition is:

$$y = 3 \left\{ 1 + \sin \frac{\pi}{6} (x - 3) \right\} , \quad (4.1)$$

where x and y are in units of inches.

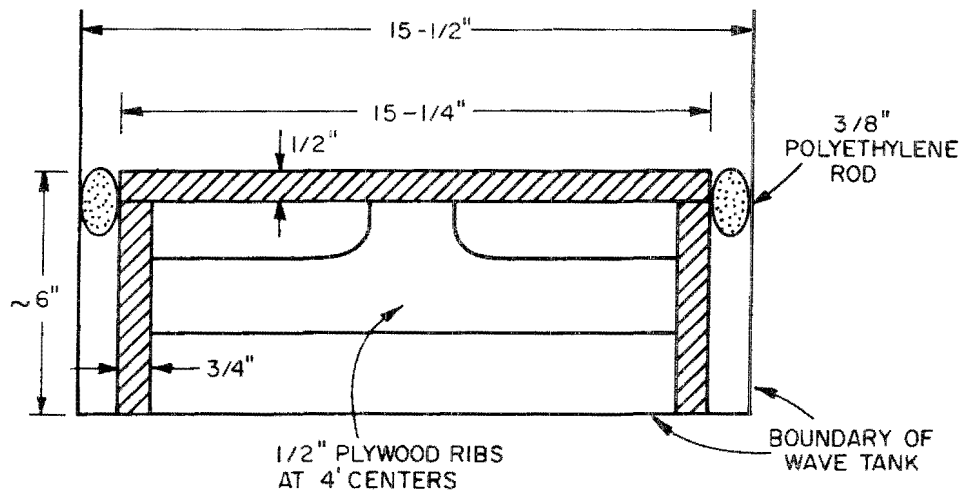


Fig. 4.2(a) Cross-section of the shelf.

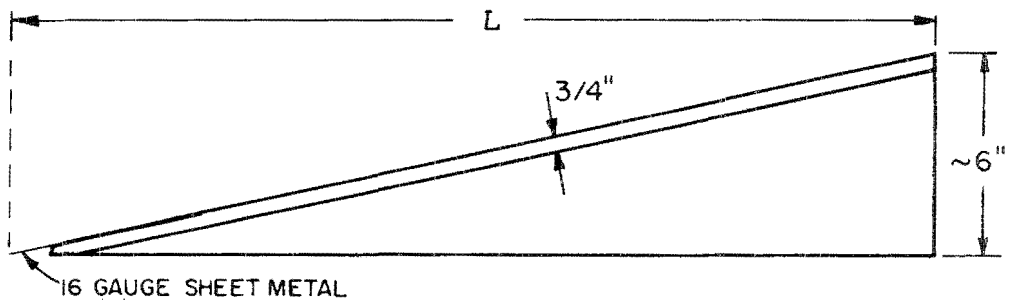


Fig. 4.2(b) Elevation of the slopes ($L = 150$ cm, 300 cm and 450 cm).

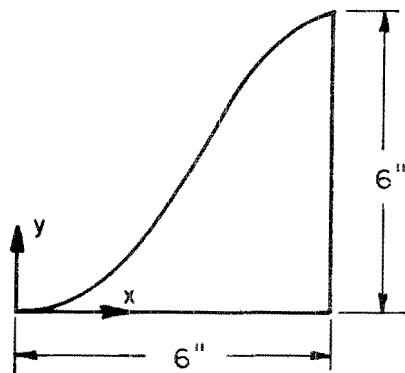


Fig. 4.2(c) Elevation of the half-sine transition.

4.2 The Wave Generator

The wave generator which was designed and constructed for this study consists of a vertical plate which is moved horizontally in a prescribed manner by means of a hydraulic servo-system. The system accepts a programmed input voltage and converts the input electrical signal into a displacement (which is directly proportional to the magnitude of the voltage); hence, the displacement-time history, or "trajectory", of the movement is proportional to the voltage-time history of the input signal. For purposes of discussion the overall wave generating system can be divided into three parts: the hydraulic system, the electrical servo-system and the carriage and wave plate. Schematic drawings of the entire system are shown in Fig. 4.3(a) and (b) and an overall view of the wave generator is shown in the photograph of Fig. 4.4; the various components shown in these figures now will be discussed.

4.2.1 The Hydraulic System

The hydraulic system consists of an oil reservoir, a pump, a filter, an unloading valve, a check valve, two accumulators, a second filter, a servo-valve and two hydraulic cylinders (only one of which can be used at a time). Figure 4.5 is a photograph of the hydraulic supply system which also can be seen in the lower left of Fig. 4.4. In the background of Fig. 4.5 is the reservoir which has a capacity of 40 gal. (0.152 m^3) of hydraulic oil. In front of the reservoir is the pump which is a Denison, constant volume, axial-piston-type pump, rated at 2.9 gpm ($0.012 \text{ m}^3/\text{min}$) at 3000 psi

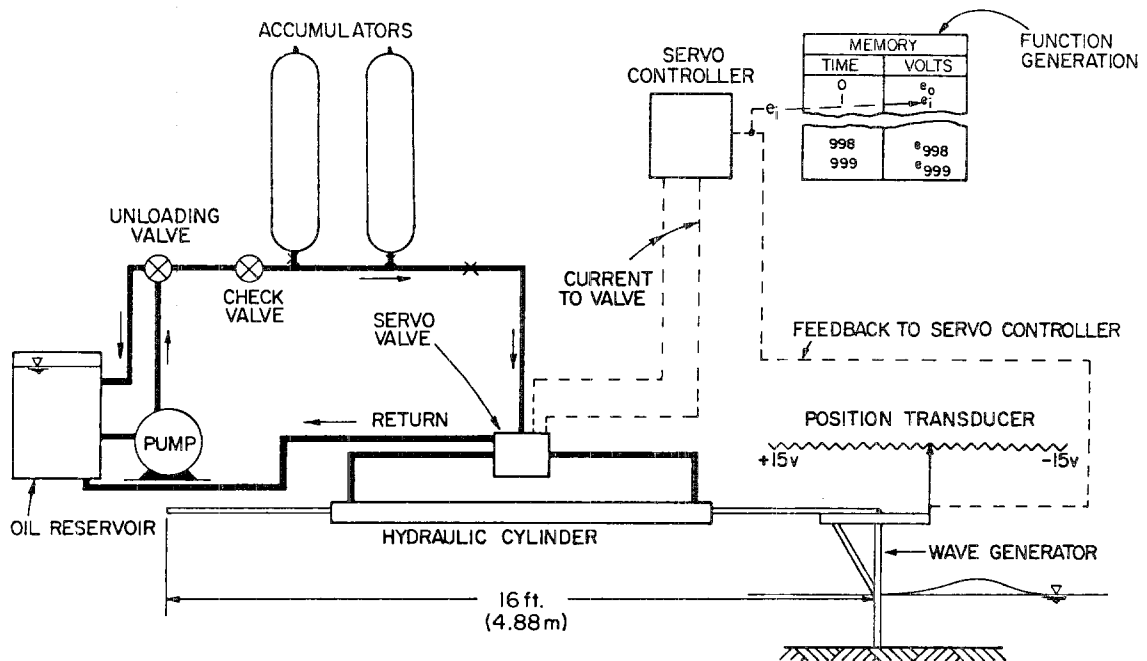


Fig. 4.3(a) Schematic drawing of the wave generator with the "long" cylinder.

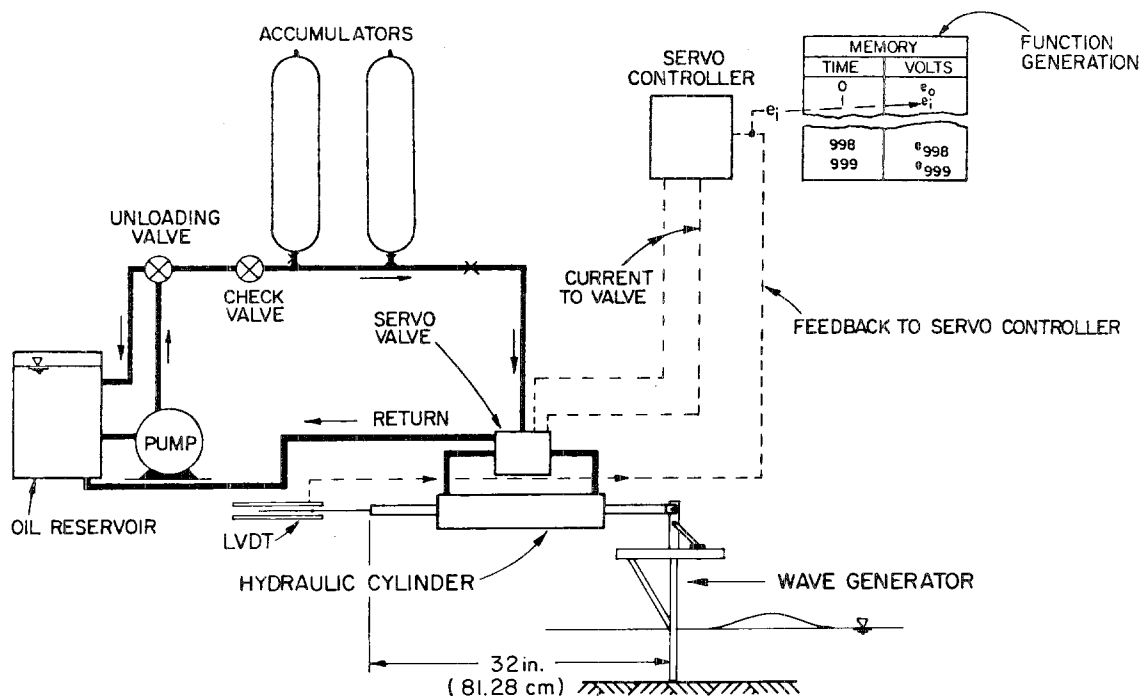


Fig. 4.3(b) Schematic drawing of the wave generator with the "short" cylinder.

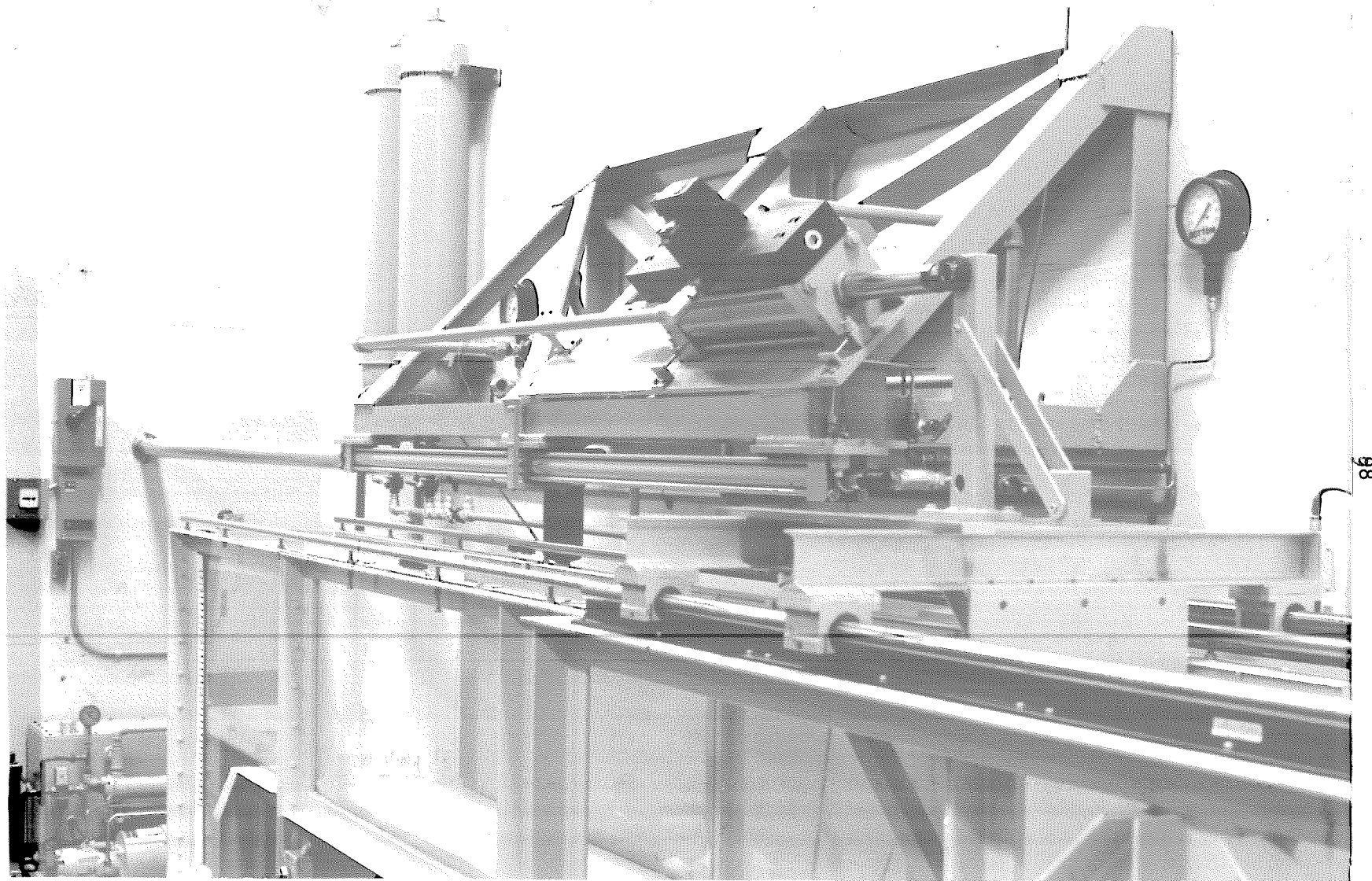


Fig. 4.4 Overall view of the wave generator.

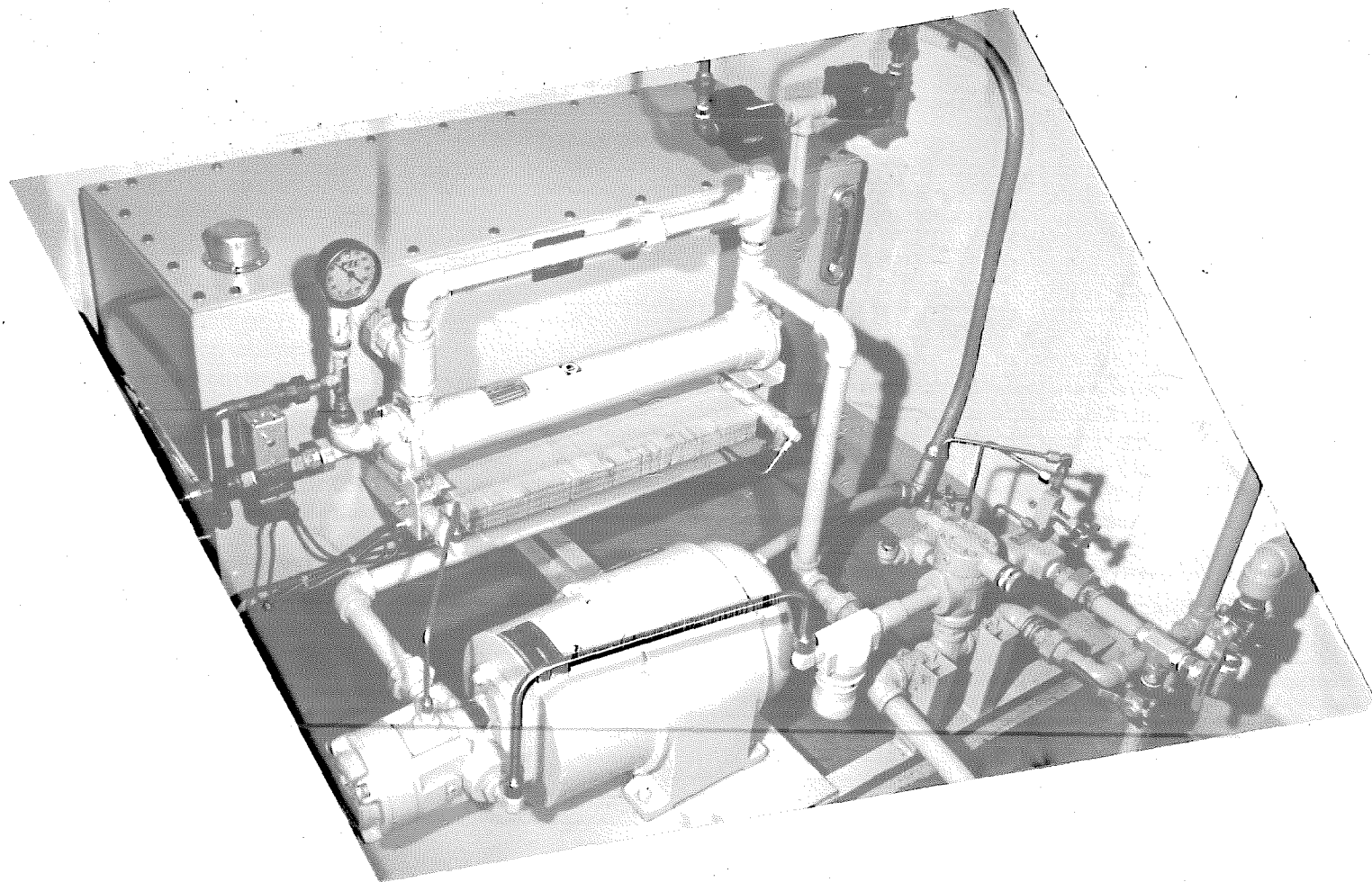


Fig. 4.5 View of the hydraulic supply system.

(20,000 kN/m²) and 2.8 gpm (0.011 m³/min) at 3500 psi (24,000 kN/m²); it is powered by a 7.5 hp (5.6 kW), 1800 rpm electric motor. Provision has been made for water cooling the oil but under present operating conditions the oil temperature has never exceeded 100°F (38°C) and thus the thermostat has never been activated. Immediately downstream of the pump is a filter constructed of stainless steel wire cloth with a nominal and absolute particle diameter rating of 5 microns and 15 microns respectively. Downstream of the filter is an unloading valve which is followed by a check valve. The unloading valve senses the system pressure at a point downstream of the check valve; when the system pressure is below a preset value (3000 psi during normal operation) the unloading valve directs the flow of hydraulic fluid into the system. Once the desired system pressure is reached, the system side of the valve closes and the flow is diverted through an air-cooled heat exchanger (the radiator structure shown in Fig. 4.5) and back to the reservoir. The check valve prevents a reverse flow through the pump from the pressurized system when power to the pump is turned off.

From the valves, the oil is pumped into two 10 gal. accumulators which are mounted on the wall above the hydraulic supply unit and can be seen in the background in Fig. 4.4. Each accumulator consists of a rubber bladder fixed inside a pressure vessel. The bladder is pre-charged with nitrogen gas at 600 psi (4000 kN/m²) and when there is no oil in the accumulator, the bladder fills the entire vessel. When oil is introduced at pressure, the increased pressure causes the nitrogen

gas and the bladder which contains it to compress. As more oil is pumped in, the pressure continues to rise until the rated pressure of 3000 psi (20,000 kN/m²) is reached when the unloading valve activates and directs flow back into the oil reservoir. At this pressure each accumulator holds approximately 7 gal. (0.027 m³) of oil which provides a reservoir to supply flows which exceed the capacity of the pump (i.e., 2.9 gpm). The accumulators also serve to damp out pressure fluctuations due to the opening and closing of the servo-valve and the unloading valve although this was not the primary purpose.

A second filter (Moog Buta N with nominal filtration of 10 microns) is installed downstream of the accumulators to protect the servo-valve which is the most sophisticated and sensitive item of the hydraulic system. The servo-valve adjusts the quantity and the direction of the flow of oil in direct proportion to the electrical current it receives. The servo-valve is a Moog Model 72-103 which has a rated flow of 60 gpm (0.24 m³/min) at 40 ma current.

The servo-valve directs the flow of oil to either end of a double-acting hydraulic cylinder. Two cylinders were used in this study, both of which can be seen in Fig. 4.4; a "long" cylinder which is mounted beneath the truss and a "short" cylinder which is mounted on the sloping face of the truss. In the photograph the servo-valve is mounted on the shorter cylinder indicating this cylinder was in use. For operation of the "long" cylinder the servo-valve must be moved to a position inside the truss not visible in the photograph. The truss

was made massive to avoid vibration problems and in fact there is no apparent vibration of the structure during operation. The long cylinder is a Miller Model DH77B cylinder with 2½ in. (6.35 cm) bore and 1 3/8 in. (3.49 cm) rod with a stroke of 96 in. (2.44 m). The cylinder is fitted with external drainbacks to eliminate oil leakage. This was important because it was found even a small amount of oil in the water caused the wave gauges to behave in an erratic manner.

The length of the cylinder was designed so as to be able to generate a single or a series of solitary waves; each use requires movement in the forward direction only. However, problems occurred in the generation of periodic waves with the actual motion being distorted from the desired motion at the ends of the stroke. The cause of this after some investigation was found to be the static friction between the seals and the piston rod and the piston and the cylinder walls which has to be overcome before the piston can move. At the end of a stroke when the piston is momentarily at rest, before it can begin to move a force termed the "break-loose force" must be applied to overcome the static friction. However, the force is provided by the differential pressure across the piston and this pressure takes a finite time to become sufficient to produce the break-loose force. In the meantime the input from the function generator is continuing so that when the break-loose force is reached the piston has to move faster than desired to catch up with the input function.

Two ways of reducing this problem are:

- i) To increase the bearing area of the piston so that the differential pressure required to produce the break-loose force is reduced, and
- ii) To improve the frictional characteristics of the seals, i.e., to reduce the break-loose force.

Both of these were employed in the design of the smaller cylinder which is a Miller Model DER-77 cylinder with 5 in. (12.7 cm) bore and 1 3/4 in. (4.45 cm) rod with a stroke of 16 in. (40.6 cm). The bearing area of this cylinder is 17.3 in.² (112 cm²) compared with 3.4 in.² (22 cm²) for the longer cylinder. To ensure friction would not cause problems for this cylinder, the manufactured seals were removed and replaced by low friction Shamban Varidry R. G. Seals Model S32573-132. For these seals the friction is reduced by reducing the bearing area of the seals to a knife edge. These two measures effectively eliminated the problem of friction for the short cylinder.

4.2.2 The Servo-System

The servo-system consists of a function generator, a feedback device and a servo-controller. The principle of operation is that the voltage from the function generator and the voltage from the feedback device which are of opposite sign are summed in the servo-controller which then amplifies the resulting current which is transmitted to the servo-valve. The servo-valve directs flow in one direction or the other depending on the sign of the current; the quantity of flow through the valve and hence the velocity of the piston is proportional to the magnitude of the current.

The purpose of the function generator is to provide the voltage-time history which is proportional to the desired displacement-time history, i.e., the trajectory of the wave plate. The function generator used in this study was designed and constructed by Shapiro Scientific Instruments, Corona del Mar, California; a block circuit diagram is presented in Fig. 4.6 and the front face of the electronics is shown in the photograph of Fig. 4.7. The various components of the function generator shown in Fig. 4.7 will be described briefly first and the details of operation will be given later.

The lower part of the photograph shows the paper tape reader which can be used either to load a memory unit which can be played back at a later time or to drive the motion directly. Located above the tape reader are the three digital thumbwheel potentiometers which allow scaling of the amplitude of the motion. The dial on the left in the uppermost panel is the time adjustment. When the switch beside it is in the UP position, the time base is calibrated internally and the rate at which the data are generated is determined by the larger knob and the dial. The data rate can range from 1 word/sec to 1×10^6 words/sec; thus, since the memory contains 1000 words, the duration can range from 1000 sec to 0.001 sec. When the switch is in the down position, the data rate may be set between the internally calibrated rates using the smaller fine tuning knob located on the outer part of the larger knob. The right side of the upper panel contains the controls for the mode of operation--Manual, Run or Load from Tape--and the switches which execute the various phases of operation--Load Data,

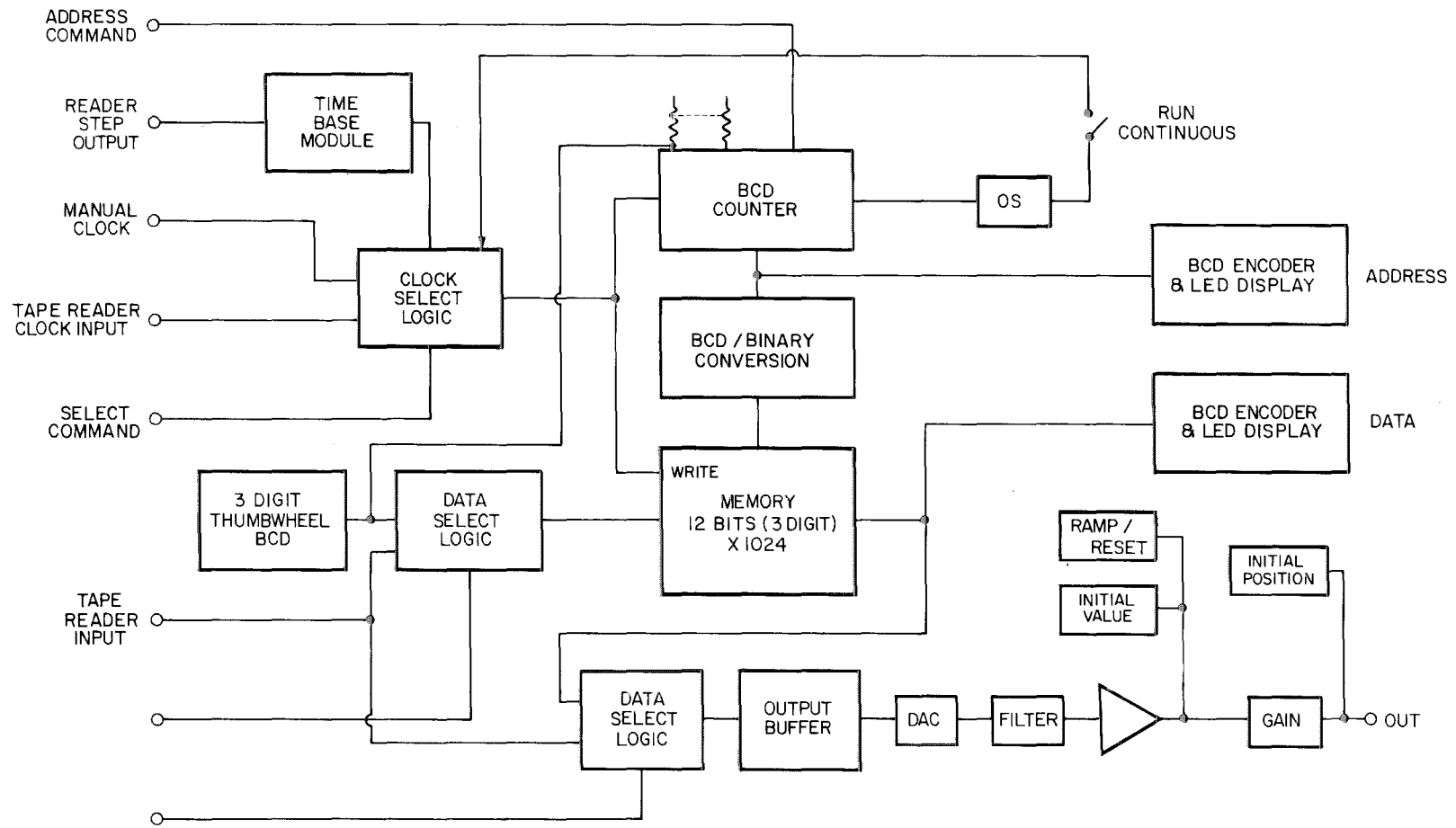
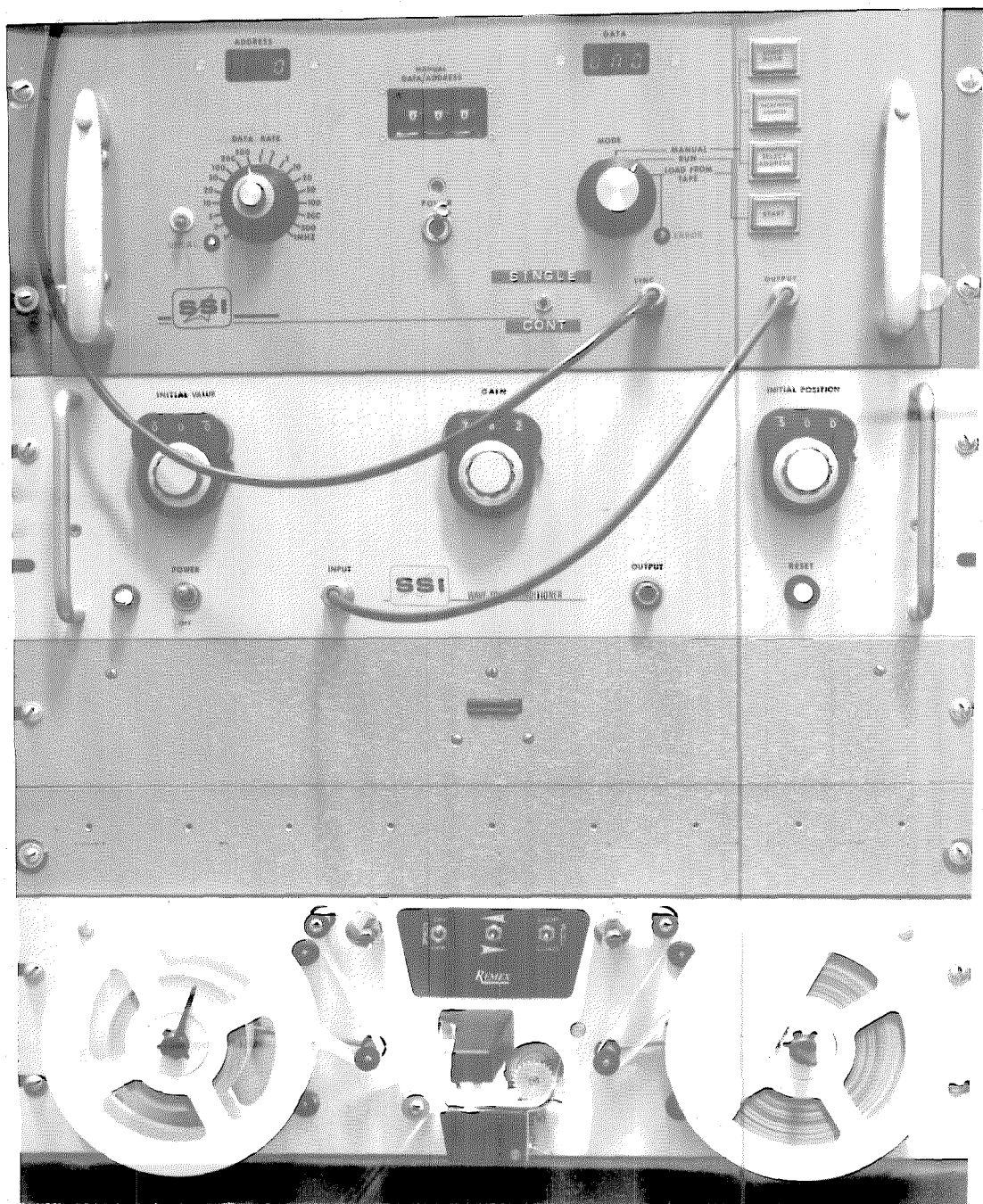


Fig. 4.6 Block circuit diagram of the function generator.



Increment Address, Select Address and Start. The number of cycles which the function generator will execute is governed by the single/continuous switch on the lower right of the upper panel. The LED's on the upper part of the upper panel display the address and the data continuously. Below these in the center are the digital thumb-wheel switches used for manual operation.

The function generator allows almost unlimited flexibility in programming the motion of the wave plate; however, due to the mechanical limitations of the system, the wave generator is less flexible in its operation. The only restrictions on the function are that it be adequately described by:

- i) Equispaced time steps, and
- ii) Normalizing the stroke between the limits of 0 and 999 with each word (i.e., point) represented by three digits.

The trajectory may be entered in any of the following three ways:

- i) With 1000 points punched on paper tape and stored in the memory. The paper tape, which may be punched either manually or by computer, is read into the memory by the tape reader. Once in the memory, the trajectory remains there until it is over-ridden or the unit is switched off.
- ii) With 1000 points entered manually by means of the digital thumbwheel switches and stored in the memory. This facility is useful if the paper tape described above contains a bad point (or points) because corrections can be made to the memory without repunching the tape.

- iii) With continuous tape reading, bypassing the memory. If the trajectory cannot be described by 1000 points, more points can be used and the trajectory read directly from paper tape into the servo-controller at the constant rate of 37.5 words per second.

The trajectory which either is stored in the memory or is to be read in by the tape reader is scaled from 0 to 999 in amplitude.

The actual total amplitude of the wave generator (i.e., the stroke) and the position of the wave plate are controlled by the three thumbwheel digital potentiometers shown in Fig. 4.7 labeled Initial Value, Gain, and Initial Position. Each contains 1000 divisions from 0 to 999 and they have the following purposes:

- i) Initial Value is the first integer of the trajectory.
- ii) Gain is an integer directly proportional to the stroke.

For a stroke of S cm the gain is:

$$\text{Gain} = \text{Integer portion of } \begin{cases} 9S \text{ for the long cylinder} \\ 51S \text{ for the short cylinder} \end{cases}$$

- iii) Initial Position allows adjustment of the at-rest position of the wave plate and gives the location of the plate prior to starting the motion. When the Initial Position reads 500 the piston is in the center of the cylinder and the input and feedback voltages are both zero. When the Initial Position reads 0, the piston rod is completely

retracted into the cylinder; when it reads 999 the piston rod is fully extended from the cylinder.

At the completion of the motion, the wave plate will be in a position given by the product of the Gain and the difference between the last and first integers of the program. Pressing the Reset button located beneath the Initial Position thumbwheel will return the plate to its original position at a constant rate of 5.5 cm/sec.

The duration time of the motion is set using the coarse and fine adjustment knobs shown in Fig. 4.7 (and discussed earlier) and a digital clock. Shutting the valve just downstream of the accumulators removes the pressure from the servo-valve. In this depressurized state, the function generator is put in the Continuous mode and the Run switch depressed. The trajectory will cycle continuously with the duration of alternate cycles displayed on the digital clock. Having set the desired time, the function generator is switched to the Single mode and the Reset button depressed. After pressurizing, the wave generator is ready for operation.

Two different devices are used for feedback for the two cylinders. For the long cylinder the feedback voltage is supplied by the voltage drop across a rotary potentiometer fixed to the carriage which is moved by a rack and pinion arrangement. The voltage drop across the potentiometer is directly proportional to the carriage position. The potentiometer is a Helipot Model 7603 with a ten turn, 10 K ohm resistance and 0.15% independent linearity. The anti-backlash gear which has a circular pitch of 48 and the precision rack are Bearing

Specialities Models AP48W-150 and RI-6-C2 respectively.

For the short cylinder the position of the carriage is converted into an electrical signal by means of an LVDT (linearly variable differential transformer), Collins Model LMT 711 P38. The LVDT consists of primary and secondary coils wound in the form of a tube inside which a ferro-magnetic core moves. The primary coil is supplied with 6 VAC from the servo-controller and the output of the secondary coil is returned to the servo-controller where it is demodulated into direct current. As the core moves within the coils, the field is changed and the demodulated voltage from the secondary coil varies linearly with the position of the core. The core is attached directly to one end of the piston rod; hence, as the piston moves, the core moves within the coils and the demodulated voltage from the secondary coil varies linearly with the position of the carriage.

The servo-controller referred to above is a Moog AC/DC servo-controller (Model 82-151) and power pack (Model 82-152). The servo-controller was modified slightly for this application and the modified circuit diagram is presented in Fig. 4.8. The modifications are:

- i) The addition of the bank of resistors which allows finer tuning of the electrical damping than would be available otherwise.
- ii) The addition of the integrator circuit after the summing point of the function generator and the feedback from the potentiometer. This improved the response for the longer cylinder.

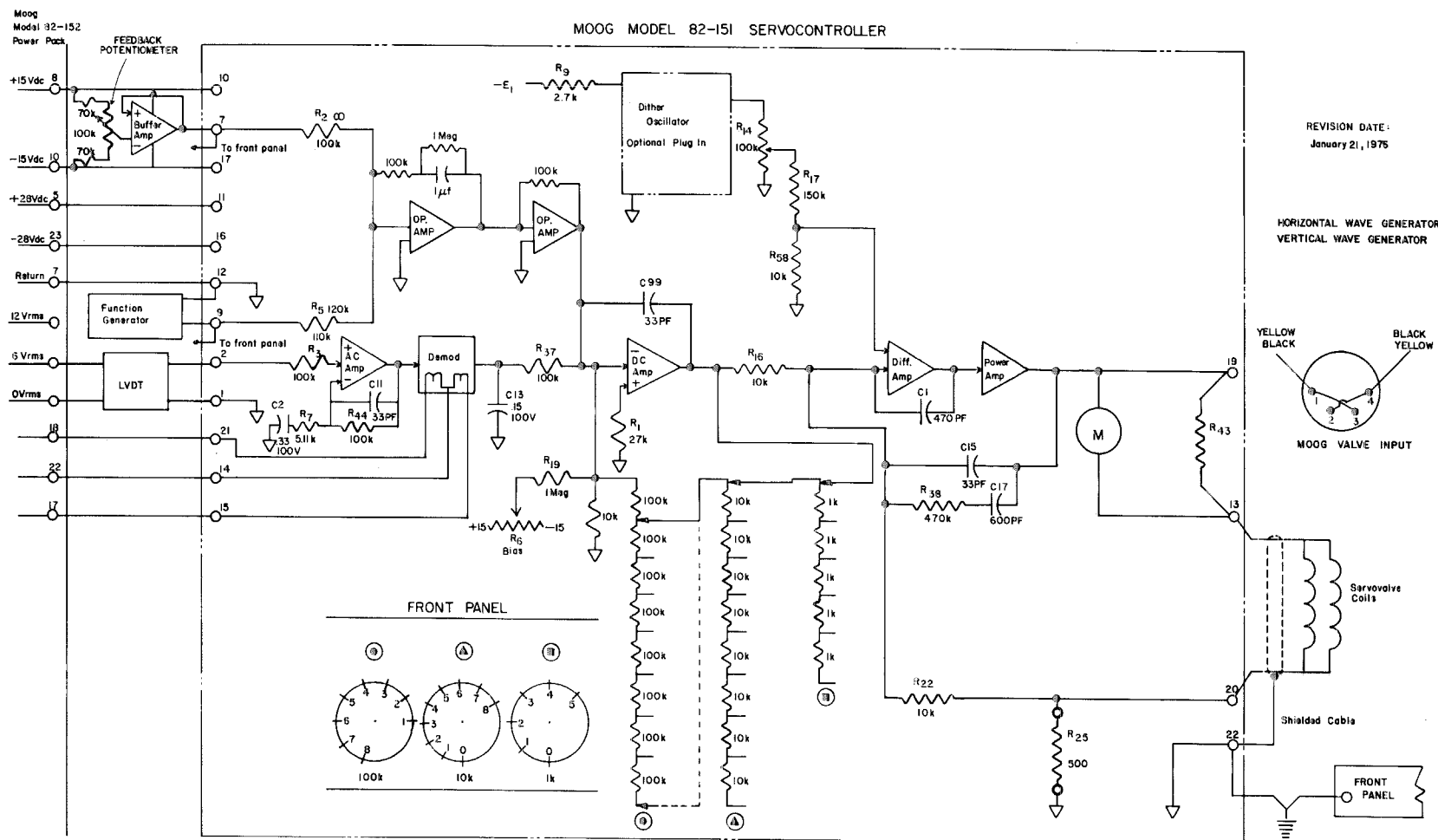


Fig. 4.8 Block circuit diagram of the servo-controller.

iii) The optional feature of the Dither Oscillator which provides a 600 Hz excitation to the servo-valve and hence improves the response was included also.

Examples of the response of the wave generator are presented in Fig. 4.9 where the solid curves are the programmed motion from the function generator and the dashed curves are the actual motion from the feedback device. Figure 4.9(a) shows the response to a hyperbolic tangent function which would be used to generate a solitary wave and Fig. 4.9(b) shows the response to the function which would be used to generate a series of cnoidal waves. The time lag of approximately 0.05 sec between programmed and actual motion which is evident in both figures is a feature of the servo-controller. In Fig. 4.9(a), near the start and finish of the motion, the curves for both the function and the motion exhibit some roughness. This is attributed to the function being described with voltages equispaced in time and with precision of only one part in one thousand. Apart from this, the actual motion shows good agreement with the programmed motion.

4.2.3 The Carriage and Wave Plate

The carriage and wave plate which are in the foreground in Fig. 4.4 are constructed of aluminum I-beams and plate. The carriage is supported on 1 $\frac{1}{4}$ in. (3.18 cm) hardened steel shaft rails (Pacific Bearings Model SA-20-120) by means of four linear ball bushings (Pacific Bearings Model SPB-20-OPN) mounted beneath the support plate as shown in Fig. 4.4. The vertical post extending upward from the carriage allows for the connection of either the

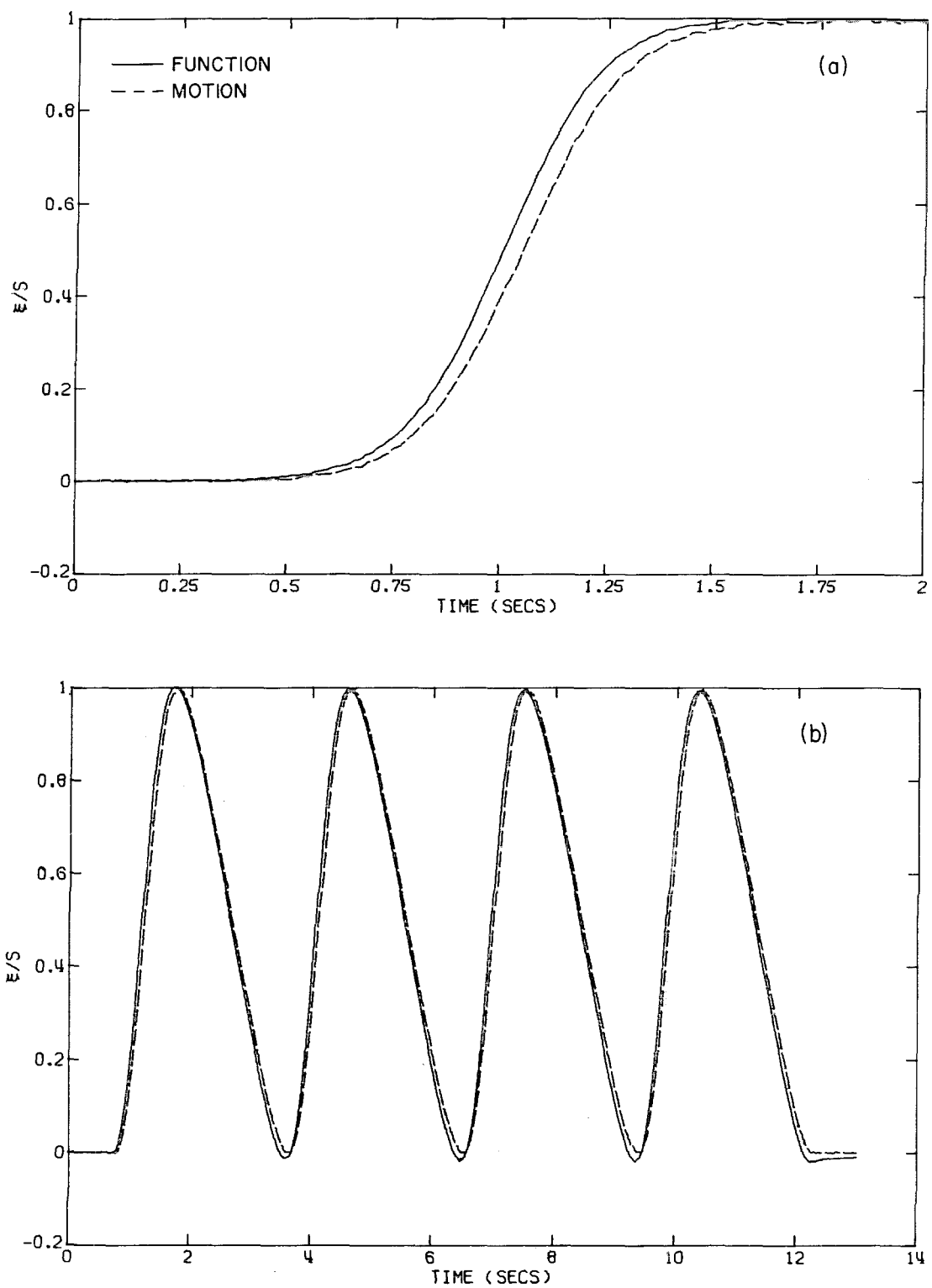


Fig. 4.9 Examples of the actual and programmed wave plate displacements for (a) solitary wave generation and (b) cnoidal wave generation.

upper short cylinder or the lower long cylinder depending on the motion desired.

To avoid problems of leakage around the wave plate, the wave plate is sealed against the glass side walls and steel bottom of the wave tank by means of rubber windshield wiper blades. The device which holds the wiper blades is shown in Fig. 4.10. It consists of two identical aluminum bars with grooves cut out to accept the body of the wiper blade. The blade is held in place by tightly bolting the two bars together. The wiper blade and holder are attached to the wave plate by #8 screws at 4 in. (10.2 cm) intervals. The holes in the holder through which the screws pass are slotted so as to allow adjustment of the distance the wiper blade protrudes beyond the edge of the plate. This distance was set such that the wiper blade bears against the glass sidewalls and steel bottom of the tank in the manner shown in Fig. 4.10 over the full length of the traverse of the wave plate.

4.4 The Measurement of Wave Amplitudes

Resistance wave gauges are used in conjunction with the Hewlett Packard (7700 Series) recorder in order to measure wave amplitudes as a function of time at a specific location in the wave tank. A drawing of a typical wave gauge is shown in Fig. 4.11. The wave gauge consists of two stainless steel wires 3.25 in. long with a diameter of 0.01 in., and spaced 0.16 in. apart. The wires are stretched taut and parallel in a frame constructed of 1/8 in. diameter

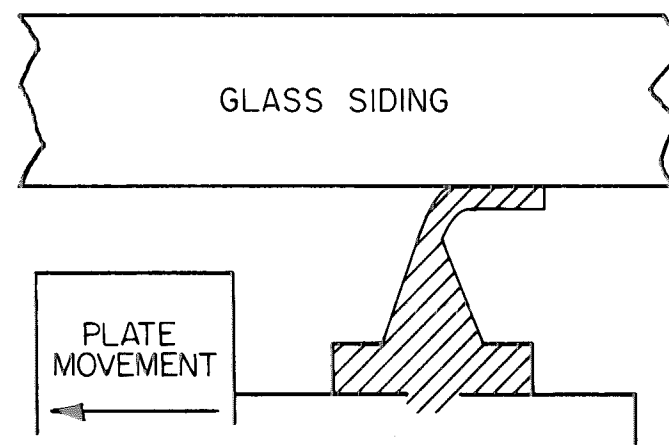
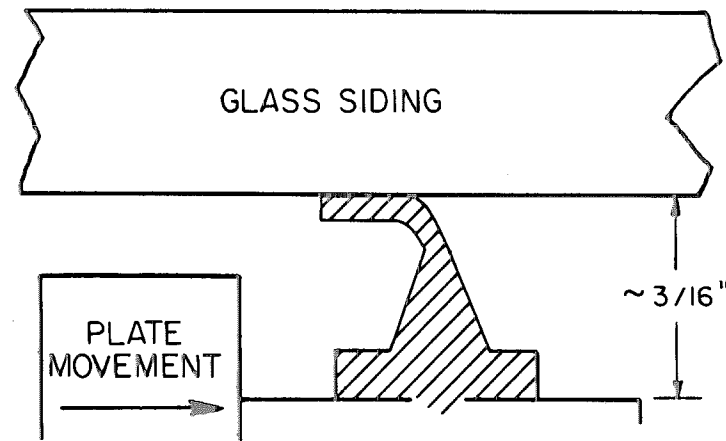
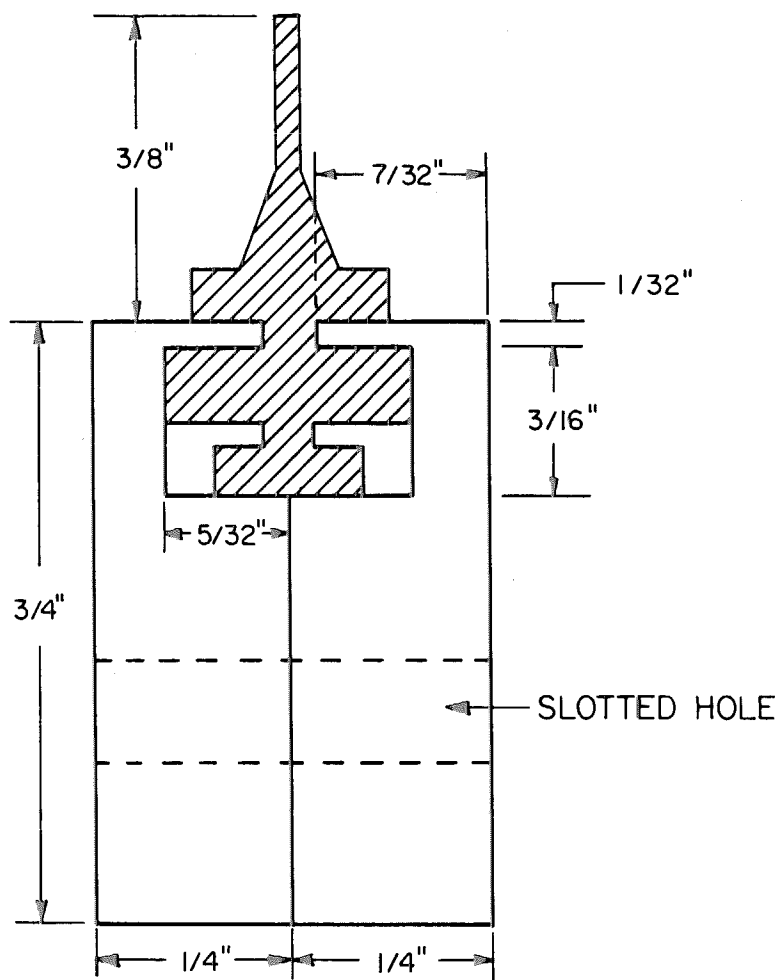


Fig. 4.10 Drawing of the blade holder.

a)

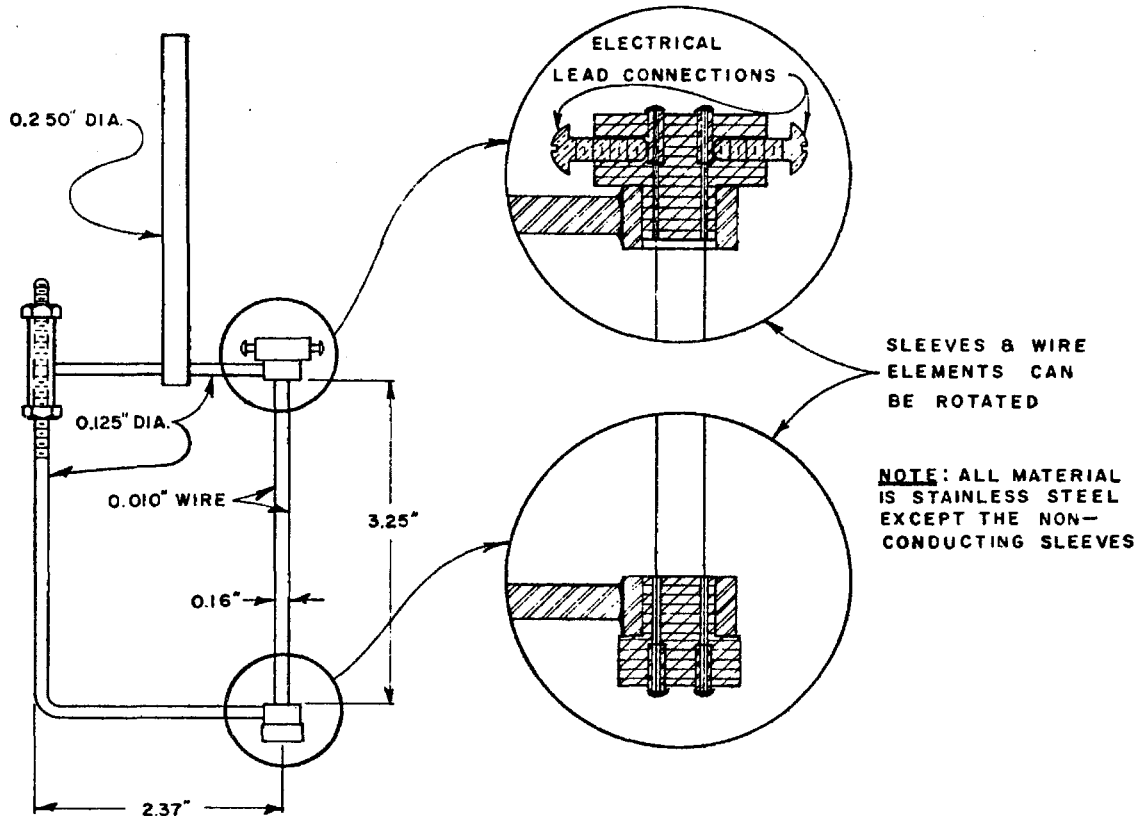


Fig. 4.11 Drawing of a typical wave gauge (after Raichlen (1965)).

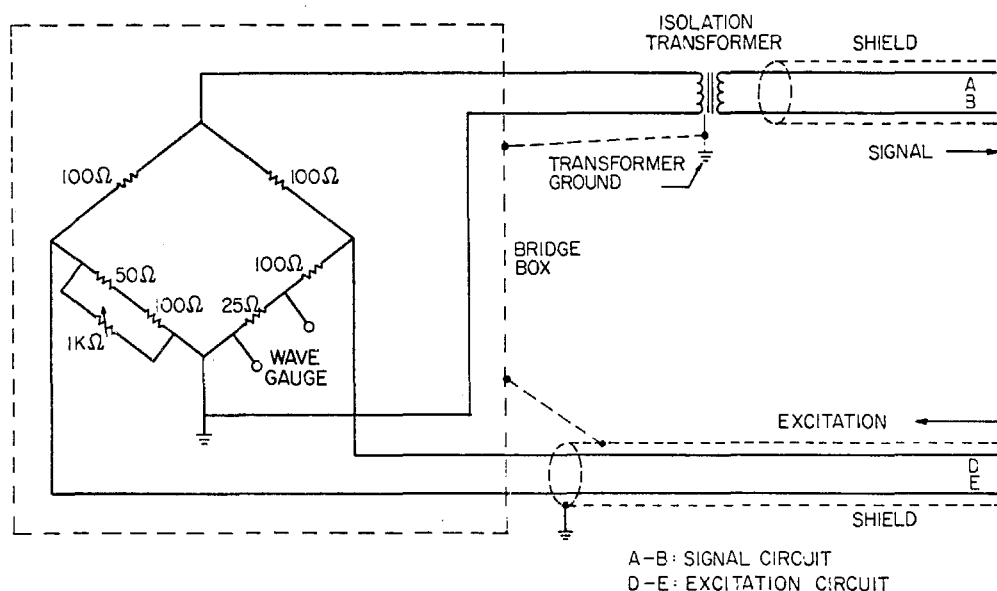


Fig. 4.12 Circuit diagram for wave gauges (after Okoye (1970)).

stainless steel rod. The wires are insulated electrically from each other in the frame, however, a current can pass between the wires when they are immersed in a conducting fluid. A Hewlett Packard Carrier Preamplifier (Model 8805 A) is used to supply the 2400 cps/4.5 volt excitation for the gauges as indicated by the circuit diagram in Fig. 4.12. The output signal from the wave gauge is also received by the Carrier Preamplifier which after demodulation and amplification is displayed on the recording unit. As the immersion of a wave gauge is varied in a conducting solution, the resistance in the circuit changes proportionally, causing an imbalance in the full bridge circuit shown in Fig. 4.12; this imbalance is recorded as a change from the balanced position.

The wave gauge is attached to a remotely controlled calibration device which allows five wave gauges to be calibrated simultaneously. The calibration device is mounted on an instrument carriage resting on the stainless steel rails which are mounted to the walls of the wave tank. The calibration device, which is shown in Fig. 4.13(a), consists of a rack and pinion driven by a synchronous motor. The wave gauge is attached to the rack and its weight is counterbalanced by a lead weight. The synchronous motor (GE Model SG 101) is connected to the master control shown in Fig. 4.13(b) which consists of a synchronous generator (GE Model SF 142) which is driven by a pinion and the rack of a point gauge. When the point gauge is moved, a current is generated and relayed to the motors which move the wave gauges vertically. There is a one-to-one relationship between movement

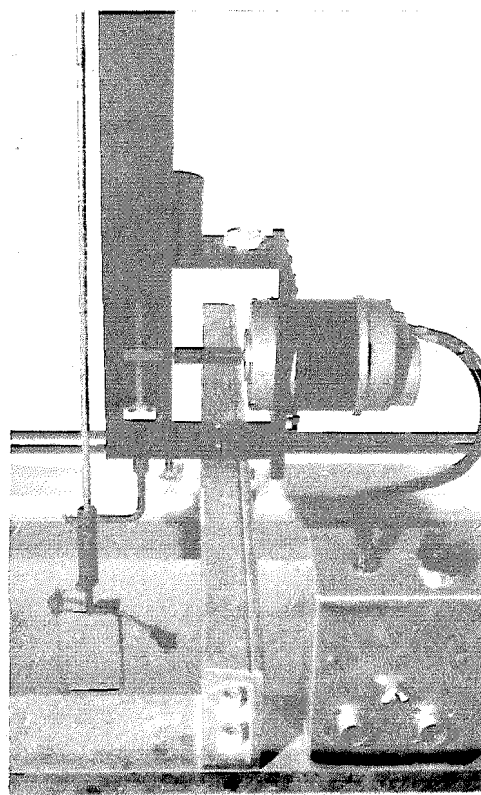


Fig. 4.13(a) View of the calibration device.

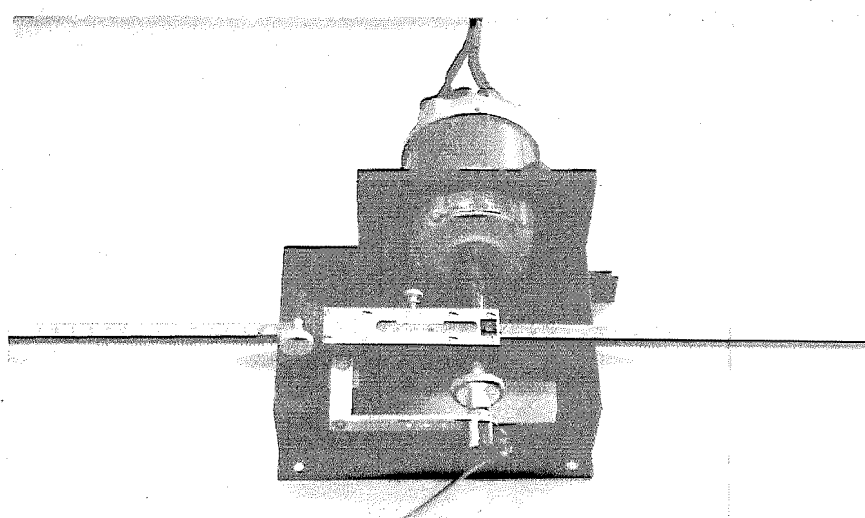


Fig. 4.13(b) View of the master control.

of the point gauge and vertical displacement of the wave gauge so that, for example, a 1 cm deflection of the point gauge will move the wave gauge 1 cm vertically. To calibrate, the full bridge circuit first is balanced at a fixed gauge immersion, then the gauge is immersed and withdrawn a known distance from the balanced position by means of the point gauge and the deflection of the stylus is noted. This procedure is repeated for various immersions and withdrawals and a typical calibration curve which results is shown in Fig. 4.14(a). If the wave gauge record is to be recorded using an analog-to-digital converter, the position of the point gauge may be represented electrically by means of the potentiometer shown in the foreground of Fig. 4.13(b). A typical calibration curve using this method is shown in Fig. 4.14(b). Notice the clusters of points at regular intervals along the curve. These occur because, when turning the wheel on the point gauge shown in Fig. 4.13(b), after turning to the limit one's wrist will rotate, the hand is lifted and the wrist rotated back in order to continue turning. During the time it takes to lift one's hand and rotate the wrist back, data still are being recorded by the A/D converter and these appear as clusters of points in the calibration curve. The scatter is caused by errors in the A/D converter.

Every wave gauge is calibrated before each experiment; however, no calibration curves were obtained at the end of the experiment, since each experiment was completed within minutes of the initial calibration.

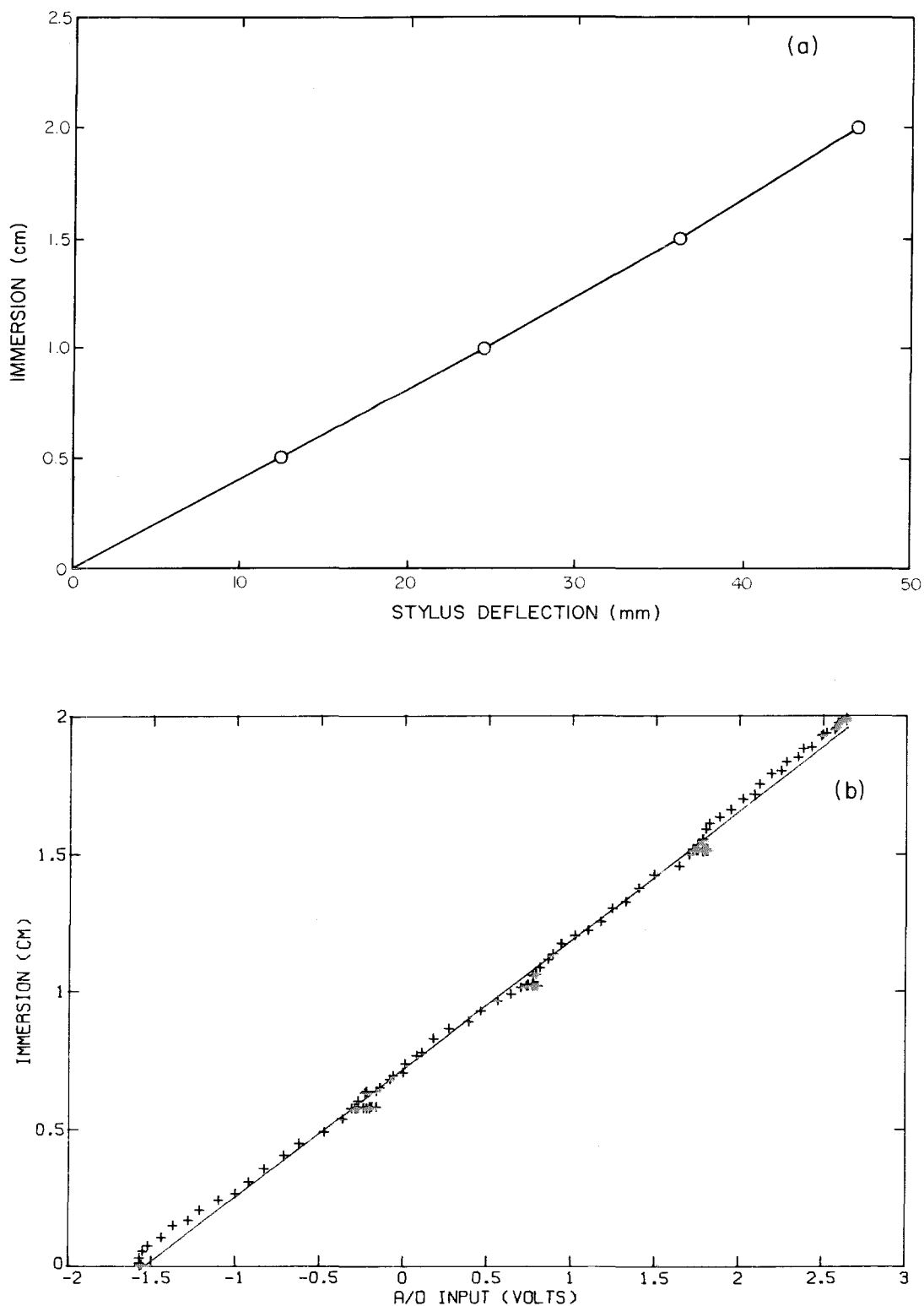


Fig. 4.14 Calibration curves for (a) manual calibration and (b) calibration using the A/D converter.

CHAPTER 5

RESULTS AND DISCUSSION OF RESULTS

The various aspects of the problem of long waves propagating onto a shelf to be discussed in this section can be illustrated best by considering a typical experiment, the layout of which is shown in Fig. 5.1. For this experiment, the upstream depth h_1 was 25 cm and the height of the shelf was 15.54 cm, thus the depth ratio (h_1/h_2) was 2.64. The front face of the shelf was vertical (i.e. a step). Five wave gauges were located as shown in the figure: Gauge 1 was placed 23 h_1 (5.75 m) upstream of the step; Gauge 2 was placed at the step; and Gauges 3, 4 and 5 were placed at intervals of 60 h_2 (5.68 m) downstream of the step. The distance from Gauge 5 to the end of the wave tank was 30 h_2 , so that waves had travelled 60 h_2 between being first recorded at Gauge 5, reflecting off the tank endwall and being recorded a second time at Gauge 5.

A solitary wave was generated by moving the wave generator with the trajectory given by Eq. (3.50) for a relative wave height of $H/h = 0.1$, a stroke of 18.25 cm and a period of 4.24 sec. The variation of the water surface elevation as a function of time as recorded by the wave gauge is shown in Fig. 5.2. The incident wave is the first wave recorded at Gauge 1; it has a height H_I of 2.5 cm. Notice that it is symmetric about the crest and there are no trailing oscillatory waves.

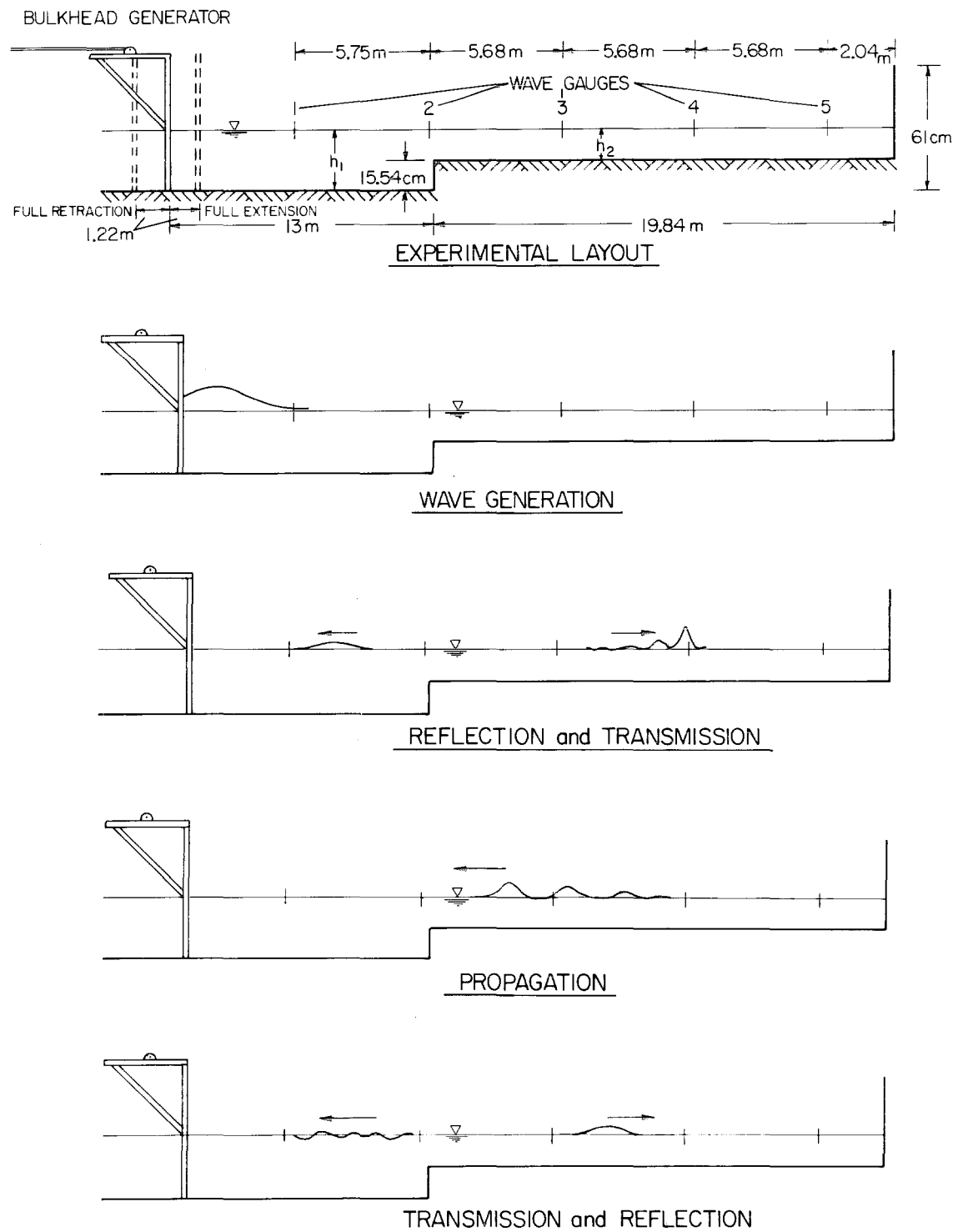


Fig. 5.1 The layout and the various aspects of a typical experiment.

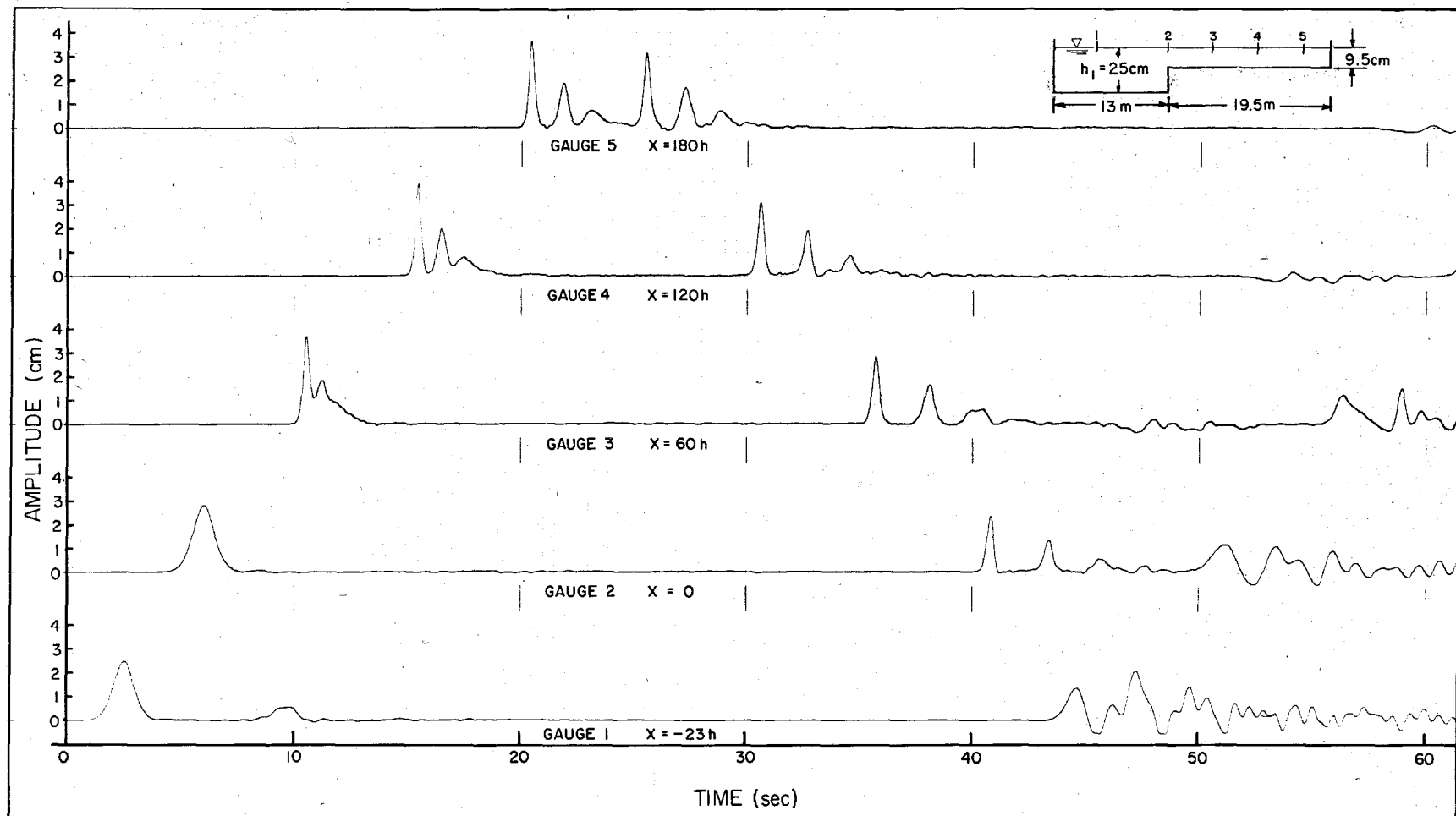


Fig. 5.2 Oscillograph record from a typical experiment of a solitary wave propagating over a step onto a shelf.

As the incident wave propagates over the step and onto the shelf, part of it is reflected and travels back towards the wave generator. The second wave recorded at Gauge 1 is this reflected wave. Its height is 0.5 cm and its shape is somewhat different than the incident wave.

At the location of Gauge 2 the wave is at the step. Its height is 2.8 cm compared to 2.5 cm for the incident wave but its shape appears to be about the same as that of the incident wave. In fact if the reflection-transmission process were entirely linear it would be possible to superpose the incident and reflected waves to obtain the wave at the step; clearly this is not possible in this case and the reasons will be discussed in some detail later.

As the wave propagates on the shelf a rather remarkable event takes place: the single wave recorded at the step splits up into a number of solitary waves of different heights followed by a train of small amplitude, oscillatory waves. This is a practical example of the inverse scattering theory discussed in Section 3.5. For this particular case the theory can be used to predict the number and height of the waves as follows: the time record of the wave at the step is transformed approximately into a spacial record by multiplying the time coordinate by a phase speed determined such that the volumes of the transmitted and reflected waves sum to the incident wave volume; then Eqs. (3.138) and (3.140) predict four solitary waves will emerge with wave heights 4.5, 2.5, 1.1 and 0.2 cm. The theory takes no account of friction, so applying an experimentally determined damping

equation (the details of which will be discussed later), the corrected wave heights which are predicted at $x = 360 h_2$ (the second pass of Gauge 3) are 2.6, 1.5, 0.7 and 0.1 cm. The first three are similar to the wave heights recorded experimentally at $x = 360 h_2$.

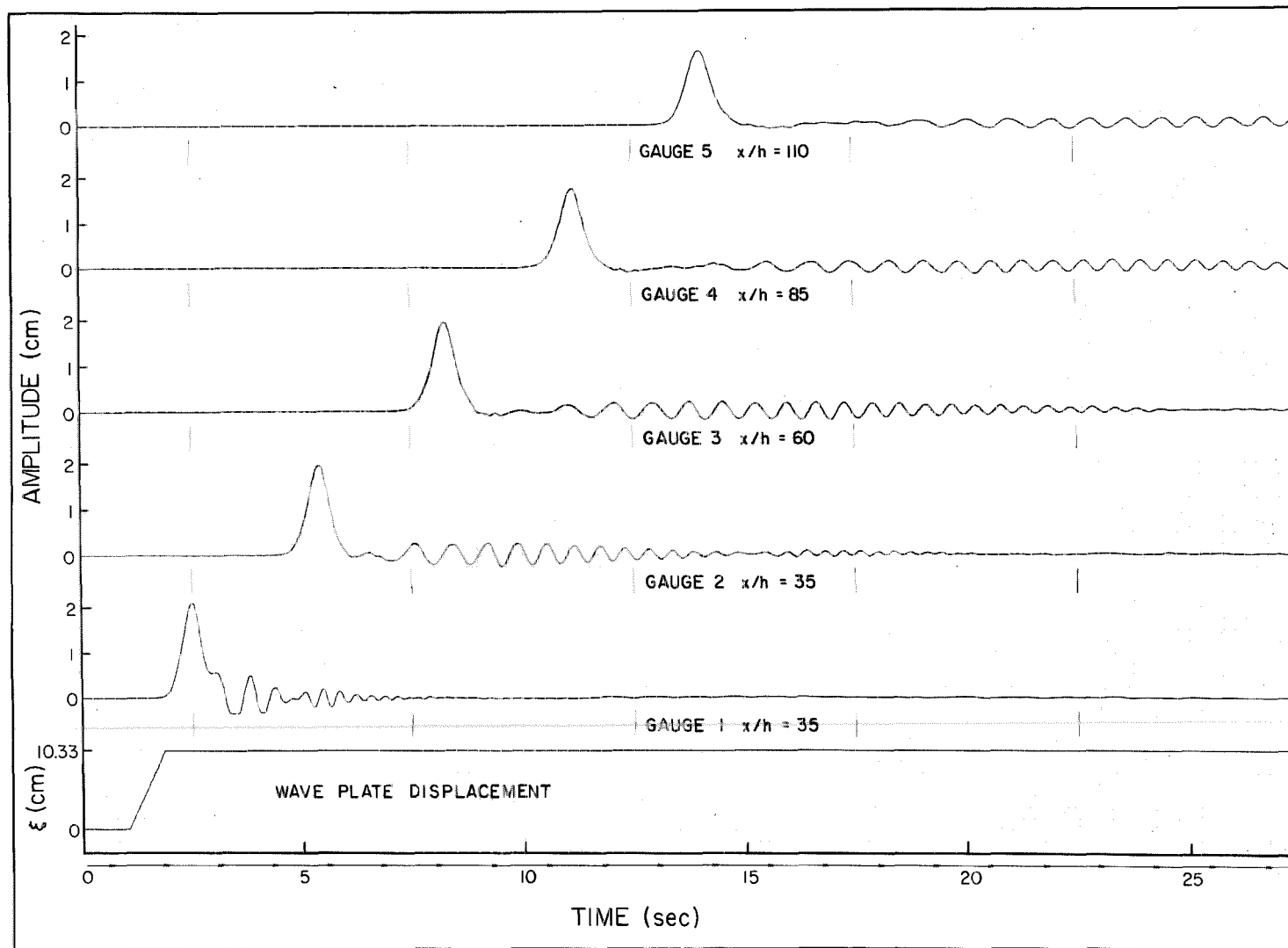
As the wave train propagates off the shelf into deep water, dispersion takes place immediately. The small waves which appear at Gauge 3 at about 48 sec are those which were reflected back from the step when the wave train propagated into deep water.

The various aspects of Figs. 5.1 and 5.2 (wave generation and propagation in constant depth, reflection, transmission, transformation on the shelf and propagation into deep water) will now be considered sequentially and in detail, including theoretical aspects of the problem.

5.1 Wave Generation and Propagation in a Constant Depth

5.1.1 The Generation of Solitary Waves

Hammack and Segur (1974) showed theoretically and experimentally that from any block of water with net positive volume at least one solitary wave followed by a train of oscillatory waves will eventually evolve. Consequently, solitary waves can be generated in the laboratory simply by producing a block of water above the still water level and allowing it to propagate a sufficient distance for solitary waves to emerge. Figure 5.3 is an oscillograph record showing the waves which evolve from such a block of water which was produced by a linear displacement-time history of the wave generator. For this case the depth was constant throughout the tank and equal to 10 cm, the



stroke was 10.33 cm and the duration of motion was 0.8 sec. The gauges were spaced 2.5 m apart (i.e., 25 depths) with Gauge 1 placed 1.0 m from the wave plate. Initially (Gauge 1) the wave has an arbitrary shape with a single main crest followed by a deep trough and several oscillatory waves. By the time the wave has propagated the 25 depths to Gauge 2, a solitary wave with a relative height of $H/h = 0.18$ has emerged followed by a train of oscillatory waves with heights which are about 25% of the height of the leading solitary wave. As the waves propagate, the solitary wave quickly outpaces the remainder of the train until at Gauge 5, 110 depths from generation, the solitary wave is completely separate from the trailing oscillatory waves. For many laboratory studies this method of wave generation would be satisfactory; however, in this study the solitary wave interacted with a step or a slope producing a reflected wave whose characteristics it was desired to measure. Trailing waves such as those following the main wave in Fig. 5.3 would have interacted with the reflected wave causing difficulties in interpreting the measured wave. Therefore, considerable effort was made to eliminate the trailing waves from the initially generated wave.

Referring to the wave generation theory developed in Section 3.2, if the position of the wave plate is neglected in the velocity of the water particles (i.e., if $\bar{u}(0,t)$ is used instead of $\bar{u}(\xi,t)$), the generation trajectory for solitary waves of all heights is:

$$\frac{\xi(t)}{S} = \tanh 7.6 \left(\frac{t}{\tau} - \frac{1}{2} \right) , \quad (5.1)$$

5.3 Oscillograph record of the waves generated by a ramp trajectory ($S = 10.33$ cm, $\tau = 0.80$ sec and $h = 10$ cm).

where, as before, S is the stroke given by Eq. (3.54) and τ is the duration of motion given by Eq. (3.56). Using this trajectory the oscillatory tail, which was about 25% of the height of the main wave when a linear trajectory was used (as shown in Fig. 5.3), could be reduced to as little as 10%. Reduction of the oscillatory tail any further, however, required implementation of the full theory of Section 3.2. In the theory, it will be recalled, the trajectory is a function of the relative wave height H/h . Thus seven trajectories were prepared for relative wave heights of from 0.1 to 0.7 in increments of 0.1. These trajectories, with displacement normalized with respect to the stroke, and time normalized with respect to the duration, are plotted in Fig. 5.4. The trajectories are evidently of similar shape, being distinguishable from one another only by the nondimensional slope at midstroke:

$$\frac{\bar{u}(\frac{1}{2}S, \frac{1}{2}\tau)}{S/\tau} = \frac{3.8 + H/h}{1 + H/h} , \quad (5.2)$$

which implies the slope of the trajectory for a relative wave height of $H/h = 0.7$ is 75% of that for a relative wave height of $H/h = 0.1$. The difference in trajectories from one relative wave height to another is small; however, since the degree of "tuning" being attempted was so fine, it was considered necessary, initially at least, to take details as fine as this into account.

The oscillograph record from a typical wave generation experiment is presented in Fig. 5.5. The setup was precisely the same as was described for Fig. 5.3, but in this case the trajectory used was the solitary wave trajectory for a wave height $H/h = 0.2$. As before the

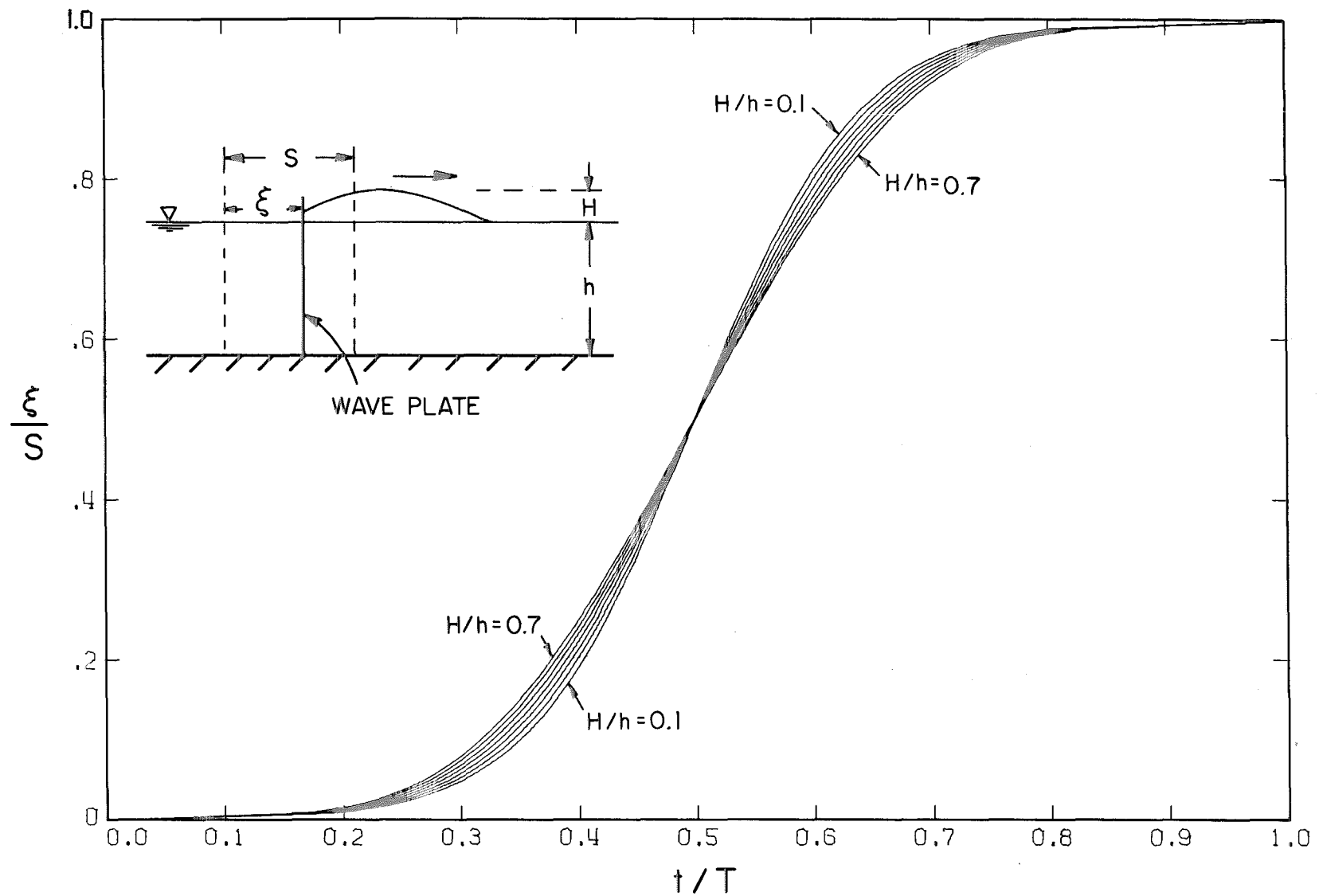
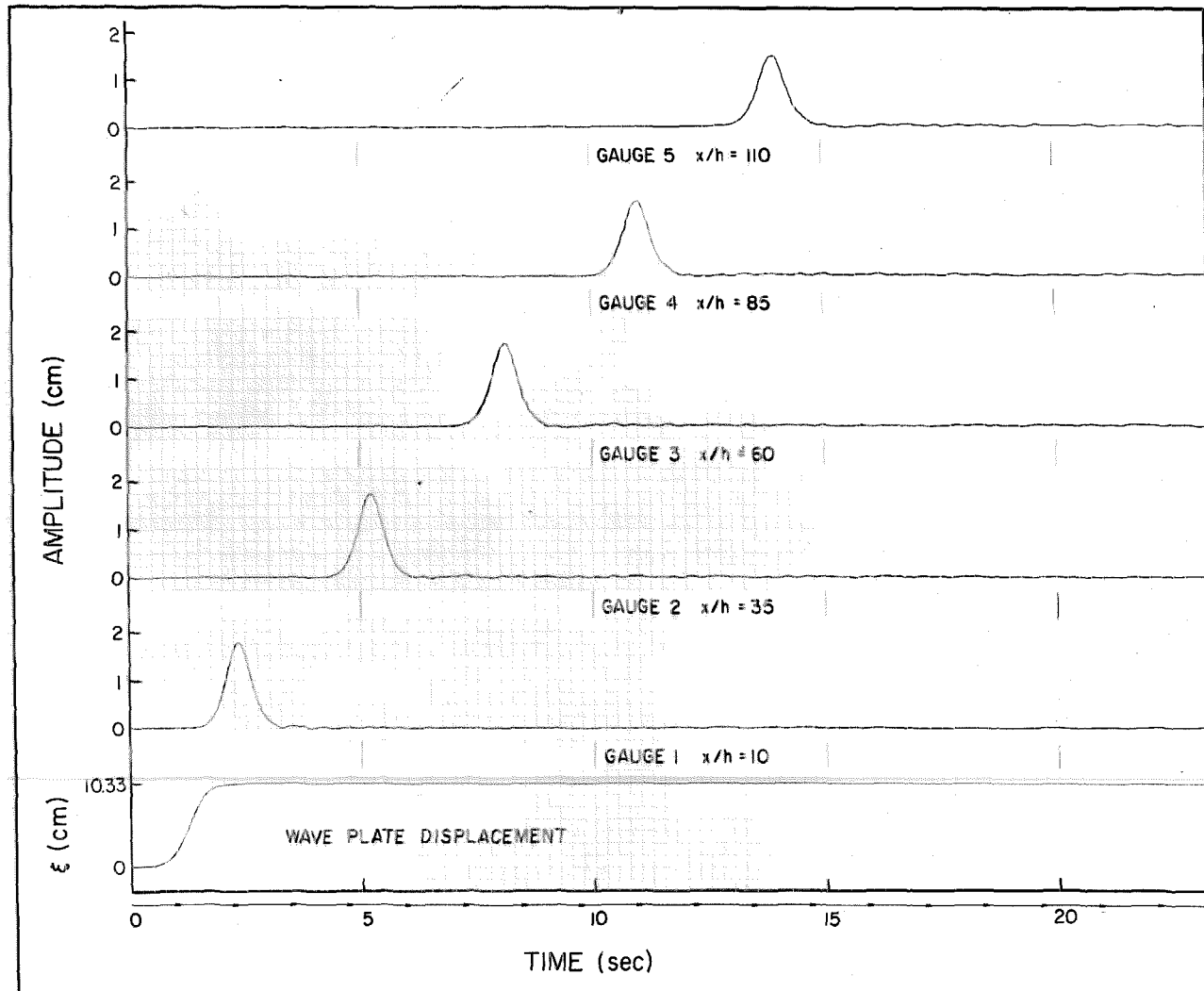


Fig. 5.4 Solitary wave generation trajectories, $H/h = 0.1$ to 0.7.



310

Fig. 5.5 Oscillograph record of the waves generated by the solitary wave trajectory with $H/h = 0.2$ ($S = 10.33$ cm, $\tau = 2.044$ sec and $h = 10$ cm).

depth was 10 cm and the stroke was 10.33 cm, but in this case the duration was 2.044 sec. The figure shows the trailing waves nearly have been eliminated, except for small amplitude, high frequency waves which are attributed to surface tension effects.

The duration, $\tau = 2.044$ sec, is 7.4% greater than the theoretical duration calculated using Eq. (3.56). It was found that increasing the duration of the trajectory by 10% the amplitude of the trailing waves was reduced by 1% to 2%. It is at this stage that using the refined trajectories is important because if one attempts to generate a wave with the wrong trajectory, the trailing waves cannot be reduced as much by adjusting the duration as they can be if the correct trajectory is used.

That the optimum duration is not the theoretical duration is attributed to the approximate nature of the assumptions that:

- i) the actual motion of the wave plate is the programmed motion (see Section 4.2.2);
- ii) the velocity distribution is constant with depth (see Eq. (3.5) in Section 3.1); and
- iii) a laboratory solitary wave is given by the Boussinesq profile (Eq. (3.25)).

The latter assumption is addressed in Fig. 5.6 in which the shape of solitary waves with relative heights of $H/h = 0.15$ and 0.61 are compared with the theories of Boussinesq (1872) and McCowan (1891). (A summary of these theories is presented in Table 5.1 which was extracted from Naheer (1977)). For small wave heights, the solitary waves derived

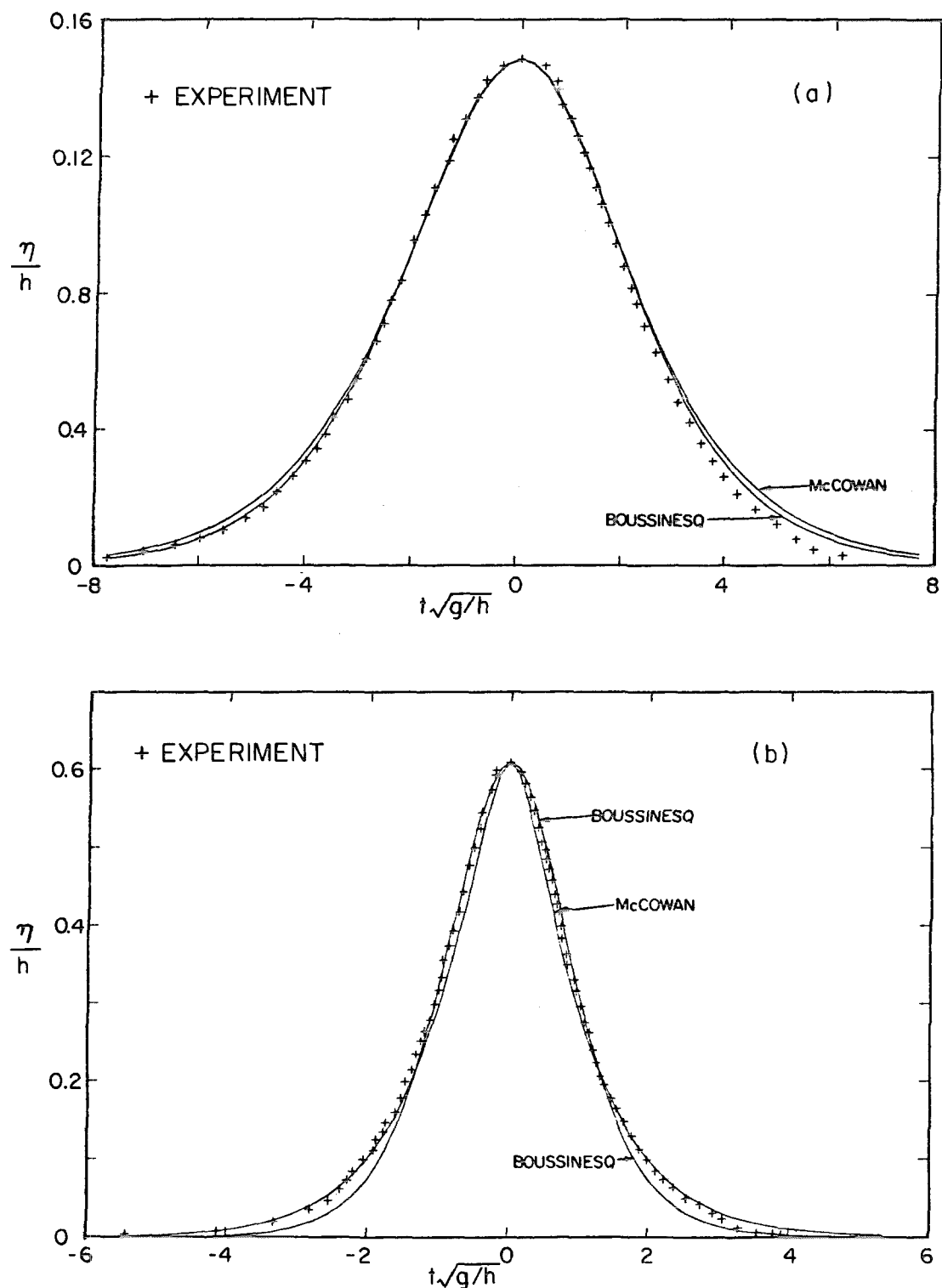


Fig. 5.6 Comparison of the shape of solitary waves with relative heights (a) $H/h = 0.15$ and (b) $H/h = 0.61$ with the theories of Boussinesq and McCowan.

Table 5.1 Solutions of the solitary wave due to Boussinesq, McCowan and Laitone. (Naheer (1977))

	Boussinesq	McCowan	Laitone
Wave profile $n =$	$H \operatorname{sech}^2 \sqrt{\frac{3H}{4h}} \frac{X}{h}$	$\frac{h N \sin M(1+n/h)}{M \left[\cos M(1+n/h) + \cosh M \frac{X}{h} \right]} \quad (3)$	$H \operatorname{sech}^2 \left(\alpha \frac{X}{h} \right) \left[1 - \frac{3}{4} \frac{H}{h} \left(1 - \operatorname{sech}^2 \frac{\alpha X}{h} \right) \right] \quad (4)$
Wave speed $C =$	$\sqrt{gh(1+H/h)}$	$\sqrt{\frac{gh}{M}} \tan M$	$\sqrt{gh} \left[1 + \frac{1}{2} \frac{H}{h} - \frac{3}{20} \left(\frac{H}{h} \right)^2 + O \left(\frac{H}{h} \right)^3 \right]$
Fluid particle velocities horizontal $u =$	$\frac{Cn}{h+n}$	$\frac{(1)}{\frac{CN \left(1 + \cos M \frac{z}{h} \cosh M \frac{X}{h} \right)}{\left(\cos M \frac{z}{h} + \cosh M \frac{X}{h} \right)^2}}$	$\sqrt{gh} \left\{ \frac{H}{h} \left[1 + \frac{H/1}{h/4} - \frac{3z^2}{2h^2} \right] \operatorname{sech}^2 \left(\alpha \frac{X}{h} \right) + \left(\frac{H}{h} \right)^2 \left(\frac{9z^2}{4h^2} - 1 \right) \operatorname{sech}^4 \left(\alpha \frac{X}{h} \right) \right\}$
vertical $v =$		$\frac{(2)}{\frac{CN \sin M \frac{z}{h} \sinh M \frac{X}{h}}{\left(\cos M \frac{z}{h} + \cosh M \frac{X}{h} \right)^2}}$	$- \sqrt{gh} \left[\frac{z}{h} \frac{dn}{dx} + O \left(\frac{H}{h} \right)^{5/2} \right]$
Notes	1) u is averaged over the depth applying continuity consideration 2) expression for the vertical velocity was not presented by Boussinesq for solitary waves	3) the relationships for N and M are $N = \frac{2}{3} \sin^2 \left[M \left(1 + \frac{2}{3} \frac{H}{h} \right) \right]$ $\frac{H}{h} = \frac{N}{M} \tan \left[\frac{1}{2} M \left(1 + \frac{H}{h} \right) \right]$	4) $\alpha = \sqrt{\frac{3H}{4h}} \left(1 - \frac{5}{8} \frac{H}{h} \right) + O \left(\frac{H}{h} \right)^{5/2}$

by Boussinesq (1872) and McCowan (1891) are coincident except at the leading and trailing edges and, as shown by Fig. 5.6(a), the shape of small experimental waves compares well with the theories. However, as the wave height increases, the Boussinesq and McCowan profiles become different, with the Boussinesq profile being wider at the crest and narrower at the leading and trailing edges. For relative wave heights which are greater than 0.3, the experimental waves were found to follow Boussinesq near the crest and McCowan at the edges, as shown in Fig. 5.6(b). (This same phenomenon was observed by French (1969) in experiments conducted in the same wave tank as was used for these experiments, but with a different method of wave generation.)

The generation and propagation data for solitary waves which will be presented were obtained from two different sets of experiments. In the first set, the data were obtained from the incident waves of experiments to be described in Section 5.2. The experiments were for relative wave heights of from $H/h = 0.05$ to 0.65 and for depths of from 17.27 cm to 31.08 cm. The data were obtained from a wave gauge placed 8.4 m from the initial position of the wave plate. The second set of experiments was performed to investigate the behavior of solitary waves as they propagate. Five wave gauges were used, with Gauge 1 placed 1.0 m from the wave plate and the other four gauges spaced at 4.0 m intervals downstream. Two depths were considered, $h = 5.0$ cm and 10.0 cm, and relative wave heights varied from $H/h = 0.1$ to 0.6 . In this discussion, the data from the first set of experiments and the data from Gauge 1 of the second set of experiments will be presented first. Later the data from the remaining four gauges of the second set of experiments will be compared to the data from Gauge 1.

The solitary wave generation data are presented in Fig. 5.7 where the ratio of wave height to stroke H/S is plotted as a function of the relative wave height H/h . The equation of the theoretical curve, which can be derived from Eq. (3.54), is:

$$\frac{H}{S} = \sqrt{\frac{3}{16} \frac{H}{h}} \quad . \quad (5.3)$$

For small wave heights ($H/h \leq 0.1$) the theory agrees quite well

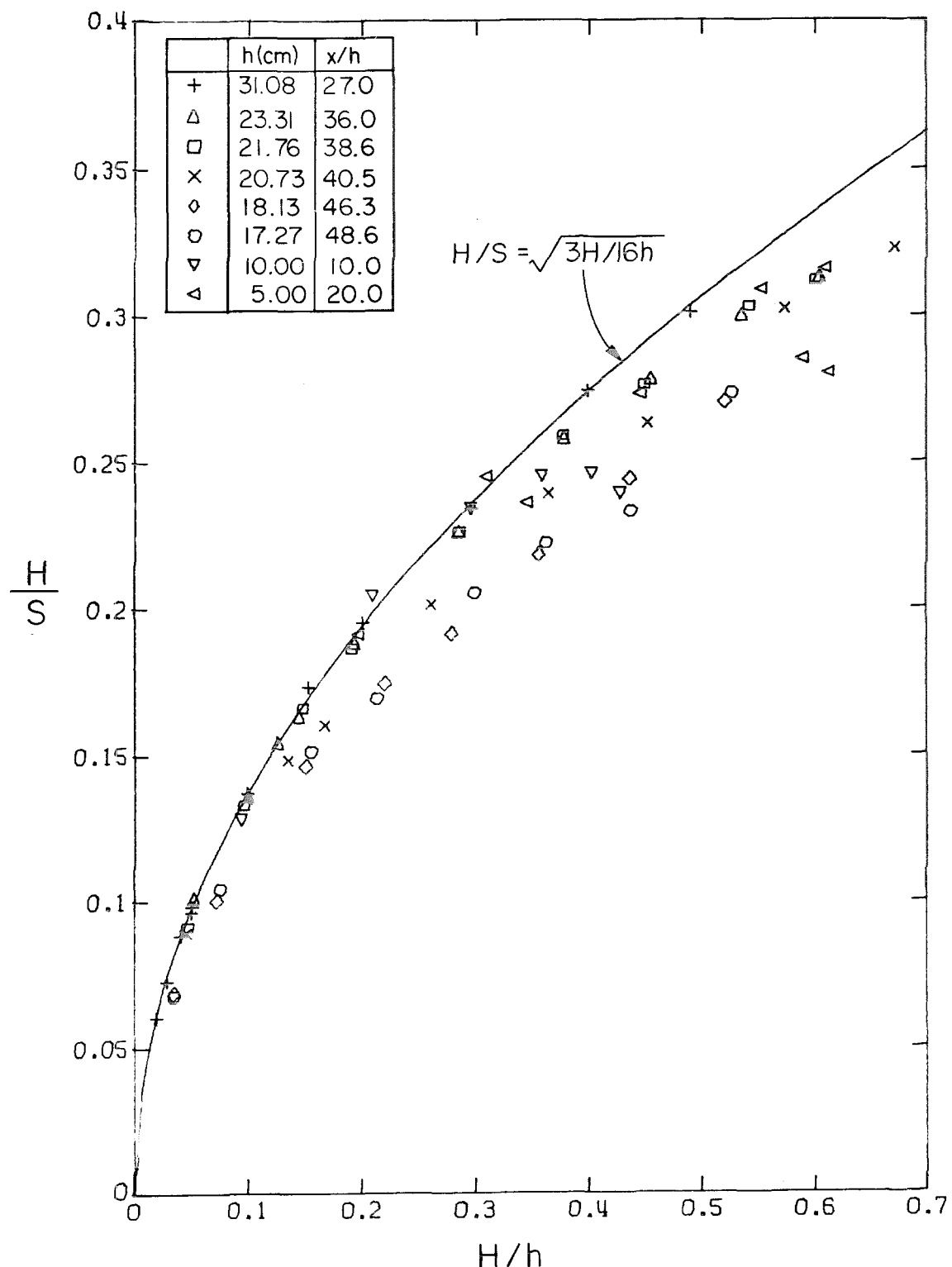


Fig. 5.7 Variation of H/S with the relative wave height, H/h , for solitary wave generation.

with the data; however, as the relative wave height increases, the measured wave height is generally less than is predicted and the agreement is worse the greater the distance in depths the wave gauge is from the wave generator. Friction cannot be the only cause of this because both ordinate and abscissa have wave height in the numerator.

The time-amplitude histories from which the data presented in Fig. 5.7 were obtained were digitized and a comparison of the following properties with those of theoretical solitary waves was made:

- i) The shape of the solitary waves was compared to the shape of the Boussinesq solitary wave by noting that, in Fig. 5.6, both waves follow the Boussinesq theory for the upper $\frac{2}{3}$ of the wave height. Therefore, a regression analysis could be performed on the part of the wave where the amplitude exceeded $\frac{1}{3}H$ to determine H_{Reg} , Ω and t_0 in the expression:

$$\eta = H_{Reg} \operatorname{sech}^2 \Omega(t - t_0) \quad . \quad (5.4)$$

For all but 11 of the 65 experimental waves considered, the coefficient of determination, r^2 , was greater than 0.999 and the minimum for all 65 experiments was 0.990 which indicates the surface profiles of the waves are well described by a sech^2 curve. (In this discussion, waves with this feature frequently will be referred to as having "sech² shape.") The calculated wave height, H_{Reg} , agreed with the measured wave height to within the wave gauge

error of ± 0.04 cm for waves less than 2 cm in height and $\pm 2\%$ for larger waves. The frequency, Ω , is compared with that of the Boussinesq theory described by:

$$\Omega = \sqrt{\frac{g}{h}} \sqrt{\frac{3}{4} \frac{H}{h} \left(1 + \frac{H}{h}\right)} . \quad (5.5)$$

in Fig. 5.8 where the nondimensional frequency $\Omega\sqrt{h/g}$ is plotted as a function of the relative wave height H/h . The data follow the theory for small wave heights ($H/h < 0.2$) but for larger wave heights the frequency is less than the theory predicts. This implies the experimental waves were less peaked than the theory predicts. The dashed curve in Fig. 5.8 represents the best fit of the data to an expression with the form:

$$\Omega = \sqrt{\frac{g}{h}} \sqrt{\frac{3}{4} \frac{H}{h} \left(1 + \alpha \frac{H}{h}\right)} . \quad (5.6)$$

(The regression analysis gave $\alpha = 0.28$ with coefficient of determination $r^2 = 0.69$.)

- ii) Since the gauge at which the solitary waves were measured was less than 50 depths from generation, it was possible that the propagation distance was insufficient for the leading solitary wave to completely separate from the remainder of the train. To check this, the waves were propagated analytically to infinity using the technique of inverse scattering. For a particular initial wave, the analysis yields the number and heights of solitary waves

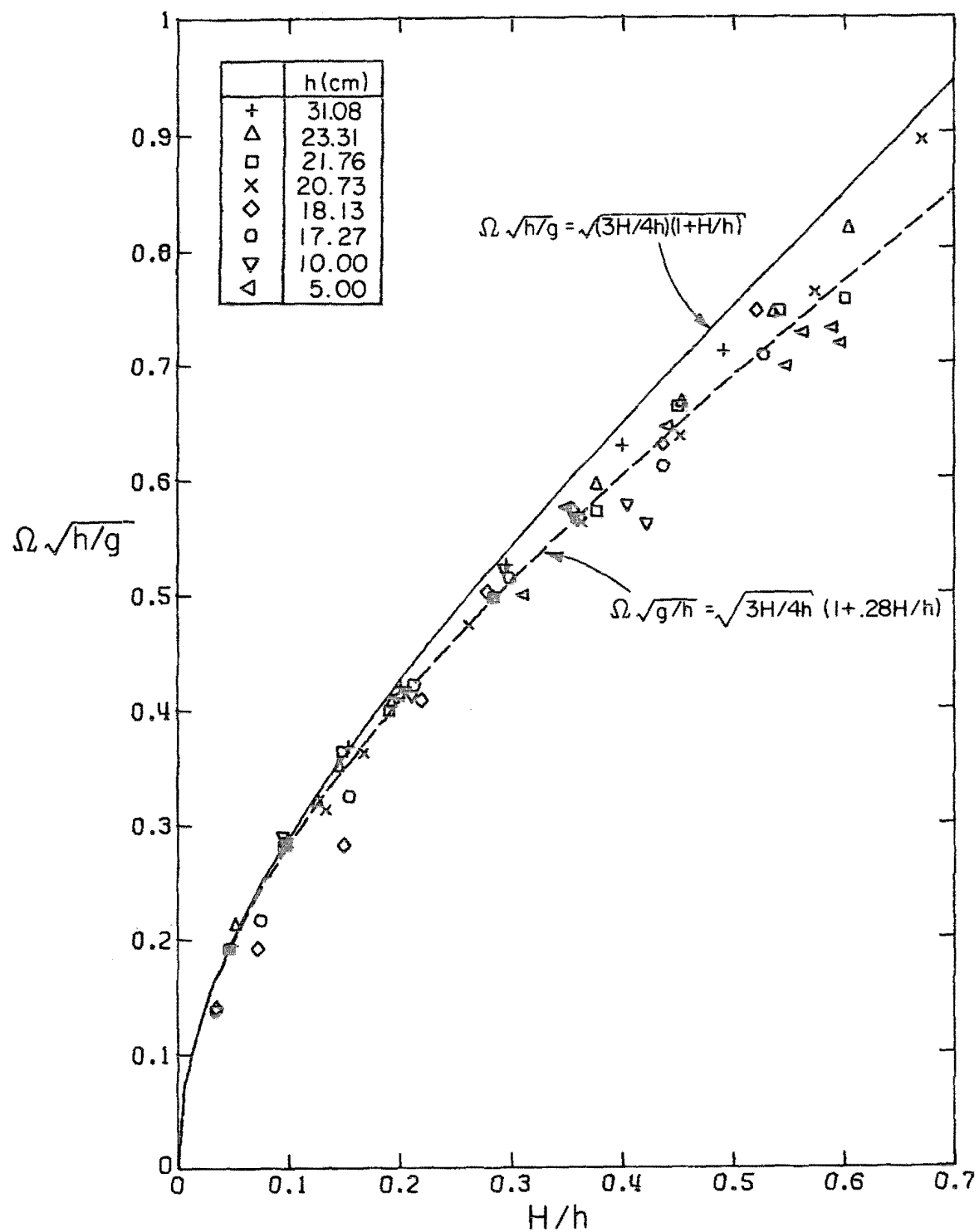


Fig. 5.8 Comparison of the "frequency" of experimental solitary waves with that of the Boussinesq theory.

which emerge at infinity. For a wave which is initially a solitary wave, only one solitary wave with the same height as the initial wave will emerge at infinity. The results of this analysis on the 65 waves considered here are presented in Fig. 5.9 where the ratio of the wave height calculated from inverse scattering to the wave height which was measured, H_{INV}/H , is plotted as a function of the measured relative wave height, H/h . The horizontal line represents the theoretical result that a wave which is initially a solitary wave will retain its height at infinity. The data from the second set of experiments all lie below the theoretical line and this will be discussed in detail presently. The majority of the data from the first set of experiments lie between $H_{INV}/H = 0.98$ and 1.08 indicating the waves would have retained their shape if they had propagated to infinity in the absence of friction. One exception is the wave with height $H/h = 0.61$ in depth $h = 21.76$ and for this wave the theory predicted two solitary waves would emerge at infinity.

- iii) The volume under the experimental solitary waves is compared to the theories of Boussinesq (1872) and McCowan (1891) in Fig. 5.10 where nondimensional volume per unit width, V/h^2 , is plotted as a function of the relative wave height, H/h . The solid curve is the theory of Boussinesq (1872) and the dashed curve is the theory of McCowan (1891).

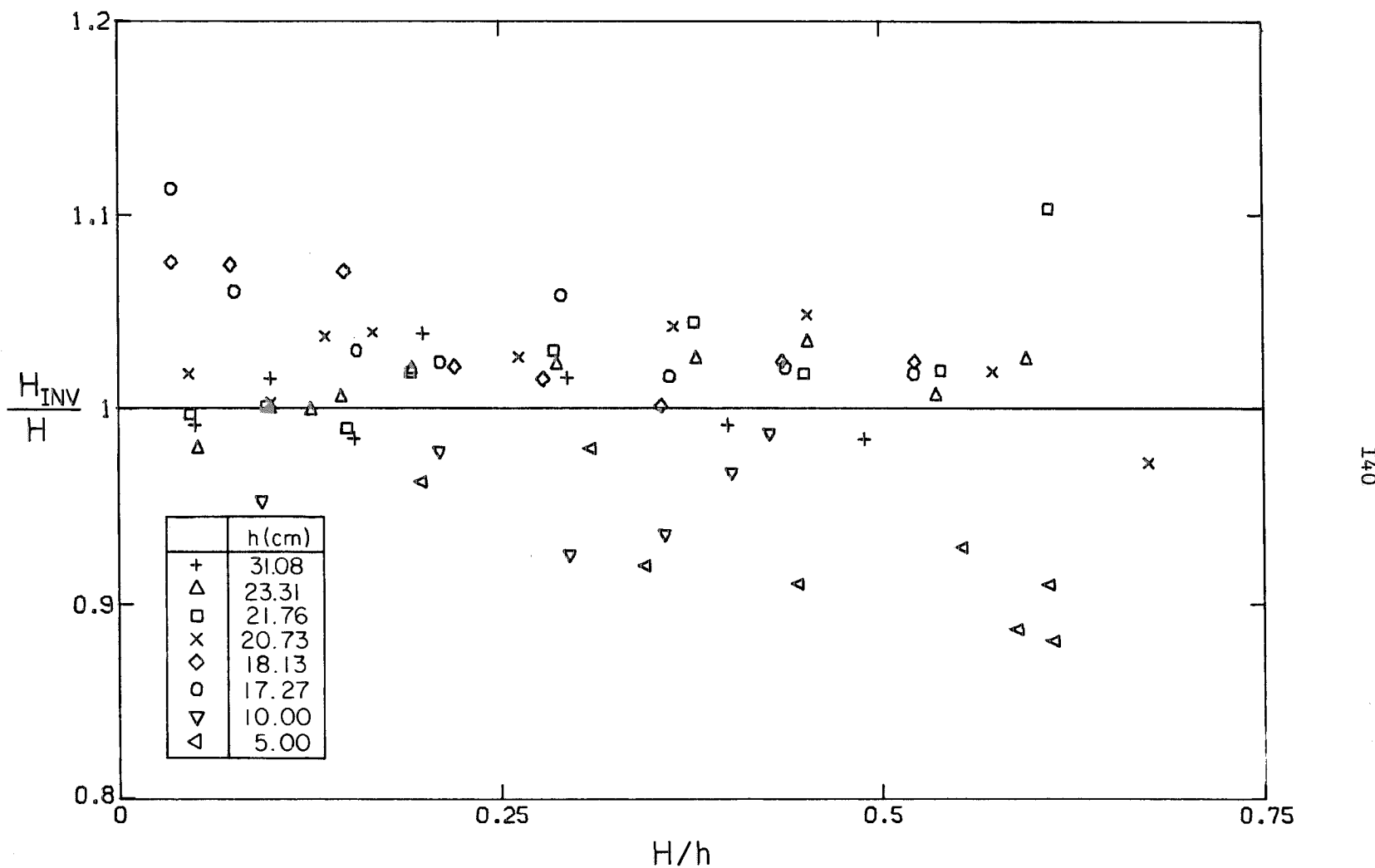


Fig. 5.9 Variation of the inverse scattered to measured wave height ratio, H_{INV}/H , with relative wave height, H/h .

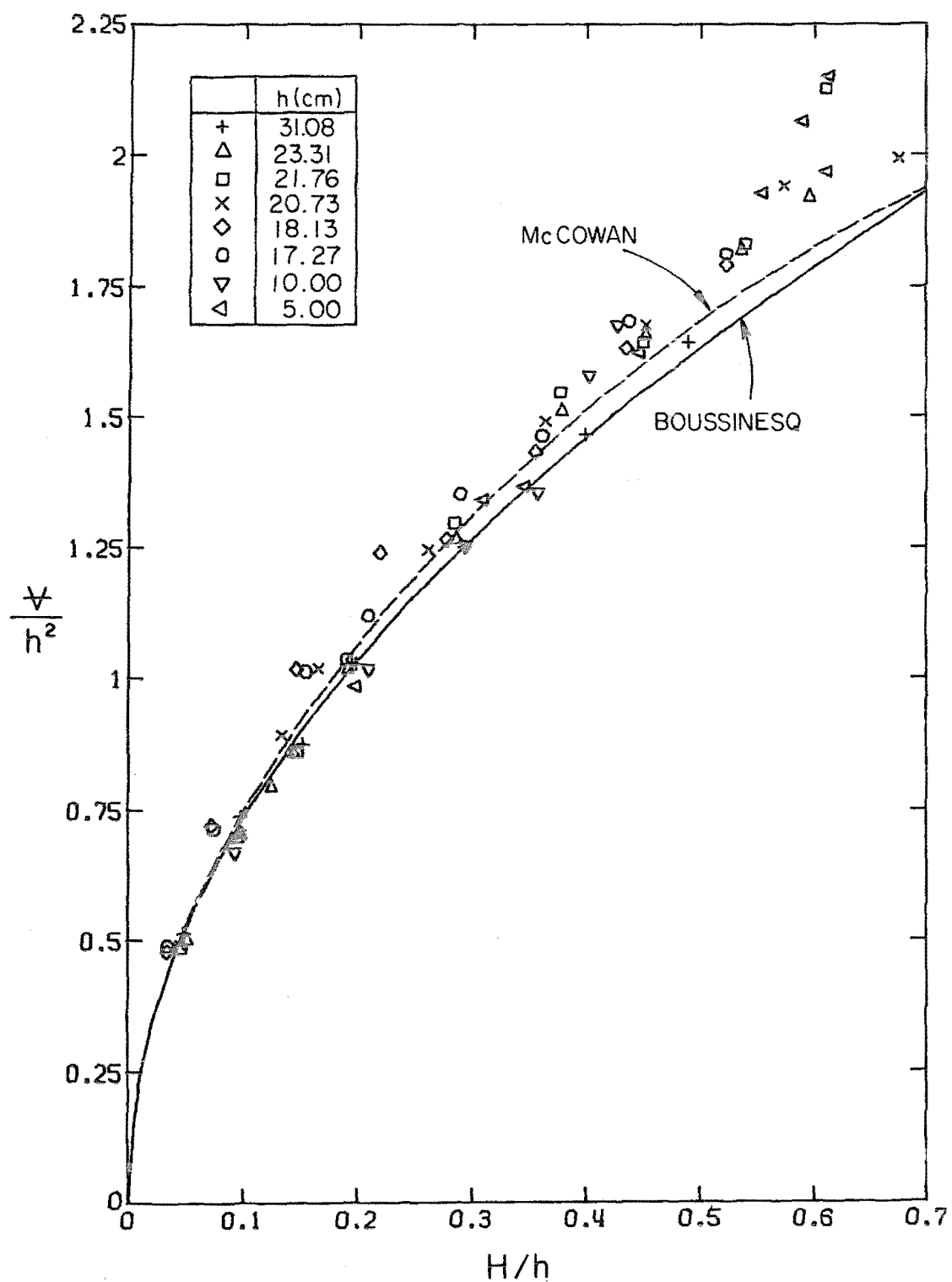


Fig. 5.10 Comparison of the volume under experimental solitary waves with that of the Boussinesq and McCowan theories.

For small wave heights, the theories are coincident but as wave height increases, McCowan's theory predicts a greater volume than Boussinesq's theory, then as the height approaches breaking ($H/h \approx 0.7$), the theories converge again. For small wave heights ($H/h < 0.2$) the data agree well with the theories but as the relative wave height increases the experimental waves have greater volume than either of the theories predict. The reason for this is evident from Fig. 5.6 which shows the experimental profile follows Boussinesq's theory in the crest and McCowan's at the edges which can only make the total volume greater than either theory.

These results show the solitary waves generated in the laboratory generally agree well with the theories for small relative wave heights ($H/h < 0.2$) but diverge slightly for larger wave heights.

5.1.2 The Propagation of Solitary Waves in a Constant Depth

As a solitary wave propagates in a laboratory flume the effect of friction on the side walls and the bottom of the flume causes the wave height to decrease. This problem has received considerable attention in the past by, e.g., Scott-Russell (1844), Keulegan (1948), Ippen and Kulin (1955), Van Dorn (1966), Naheer (1977), but in none of these studies is the agreement between theory and experiment sufficiently good to be confident in applying the theory without corroborative experiments. Therefore, a set of experiments (described previously as the second set) was conducted to determine

the damping characteristics of solitary waves in this flume and in particular to determine, for a range of wave height and depth, the damping exponent f in:

$$H = H_0 e^{-fx/h} \quad , \quad (5.7)$$

where H_0 is the initial wave height. The exponential form was used because the data seem to fit Eq. (5.7) quite well. As mentioned previously, five wave gauges were used, with Gauge 1 placed 1.0 m from the wave plate and the other four gauges spaced at 4.0 m intervals downstream. A solitary wave was generated and recorded on the oscillograph and, in addition, on magnetic tape using an analog-to-digital (A/D) converter.

The crest height H , the inverse scattered wave height H_{INV} , and the wave height H_{Reg} and frequency Ω from regression on the upper 2/3 of the wave records were obtained from each digitized record. The data are presented in Figs. 5.11 to 5.13. Fig. 5.11 is a plot of the damping exponent f as a function of the relative wave height H_0/h , where both f and H_0 were obtained by semi-log regression using Eq. (5.7). Data from Naheer (1977) which were for greater depths than were considered here and for a tank width of 110 cm are included in the figure. The curves are the theory of Keulegan (1948) which also can be expressed approximately in the form of Eq. (5.7) with the damping exponent given by:

$$f = \frac{1}{3} \left(\frac{H_0}{h} \right)^{\frac{1}{4}} \left(1 + \frac{2h}{b} \right) \left[\frac{v}{g^{1/2} h^{3/2}} \right]^{\frac{1}{2}} \quad , \quad (5.8)$$

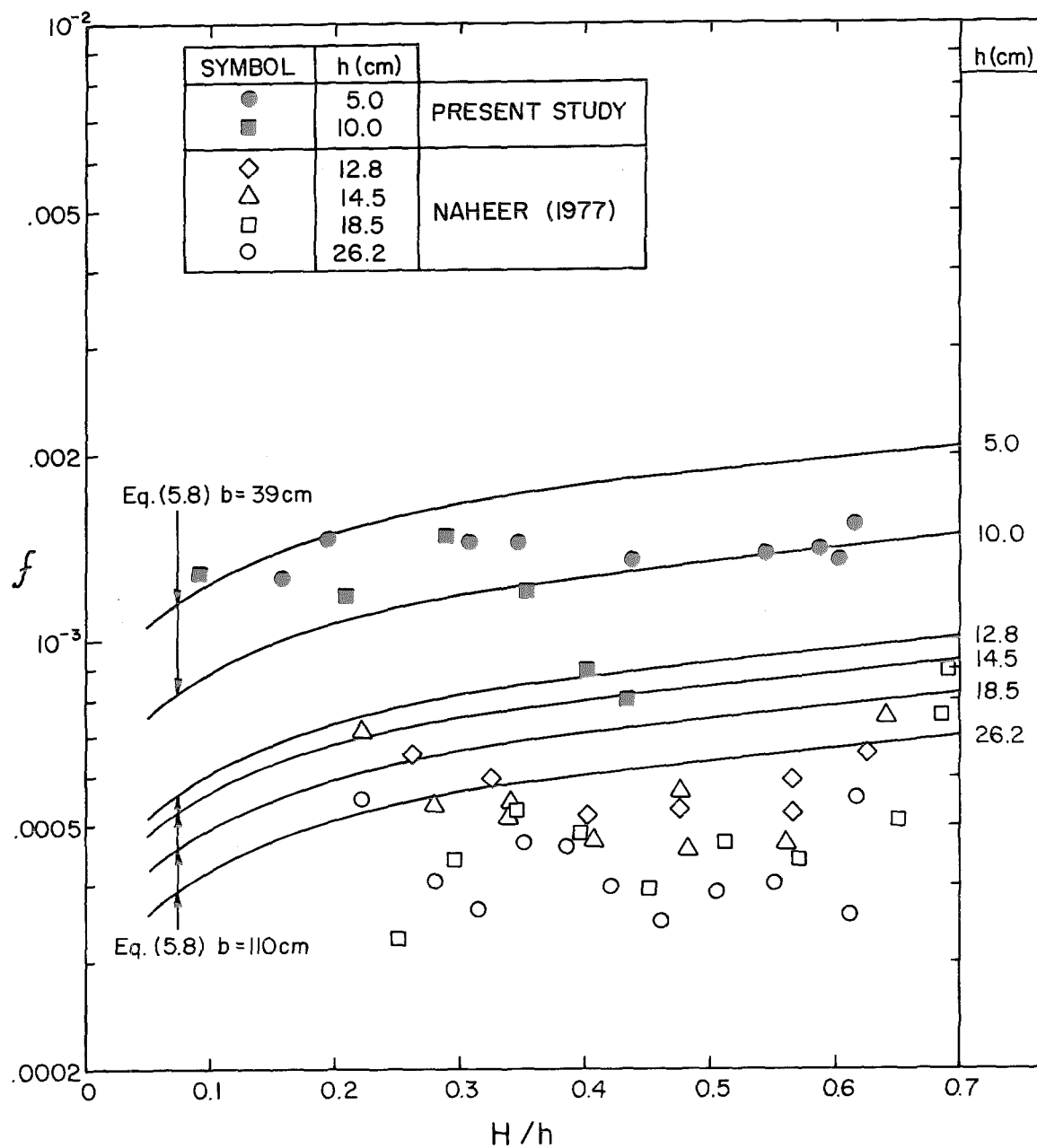


Fig. 5.11 Variation of the damping exponent, f , with relative wave height H/h for solitary waves.

where ν is the kinematic viscosity, b is the width of the tank and all other quantities are as have been defined previously. The theory predicts a small variation of the exponent, f , with wave height but the data do not appear to exhibit this. However, the increase in the exponent with decreasing depth which the theory predicts also is exhibited by the data.

The other quantities (H_{INV} , H_{Reg} and Ω) were calculated from the wave records in an effort to determine if and how the shape of the wave changed as it propagated. In Fig. 5.12 the ratio of the wave height calculated by inverse scattering to the measured wave height, H_{INV}/H , is plotted as a function of the measured relative wave height, H/h . Each symbol refers to a different experiment and the ticks on the symbol denote the gauge from which that particular point was taken, e.g., symbols with a vertical tick above denote Gauge 1. The figure shows, for all experiments, the wave height ratio H_{INV}/H of the waves at Gauge 1 is less than unity but for the other gauges the wave height ratio is scattered about unity. The interpretation of this is that since Gauge 1 was only 1.0 m from the wave plate, the wave had not yet reached its steady state but by the time it reached Gauge 2 it had, and as it propagated reduction in wave height due to friction was accompanied by the appropriate change in shape for that wave height.

This is further illustrated in Fig. 5.13 where the frequency, Ω , calculated from regression on the upper 2/3 of the wave is plotted as a function of relative height, H/h . The solid curve in Fig. 5.13 is

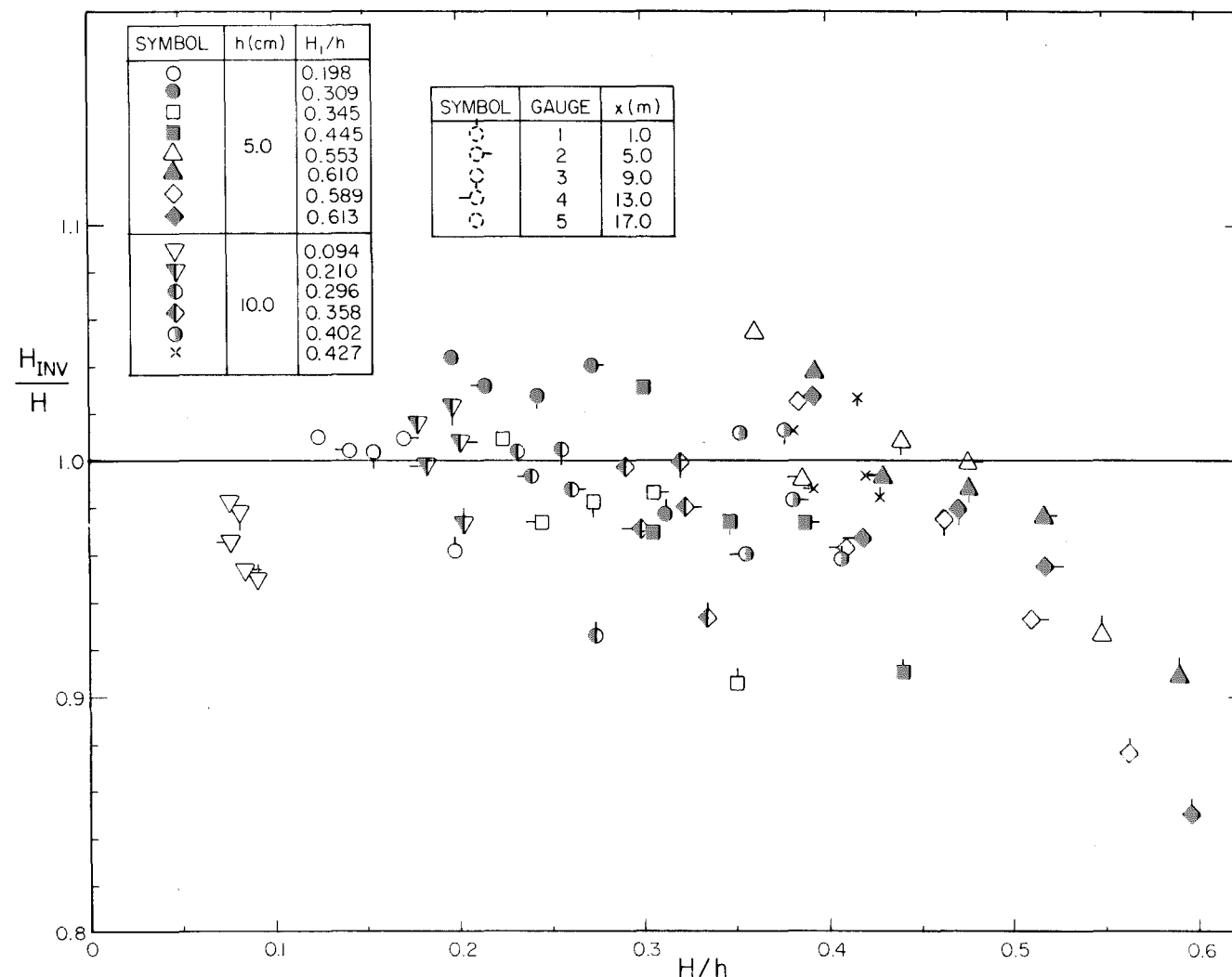


Fig. 5.12 Variation of the inverse scattered to measured height ratio, H_{INV}/H , with relative wave height H/h of solitary waves as they propagate.

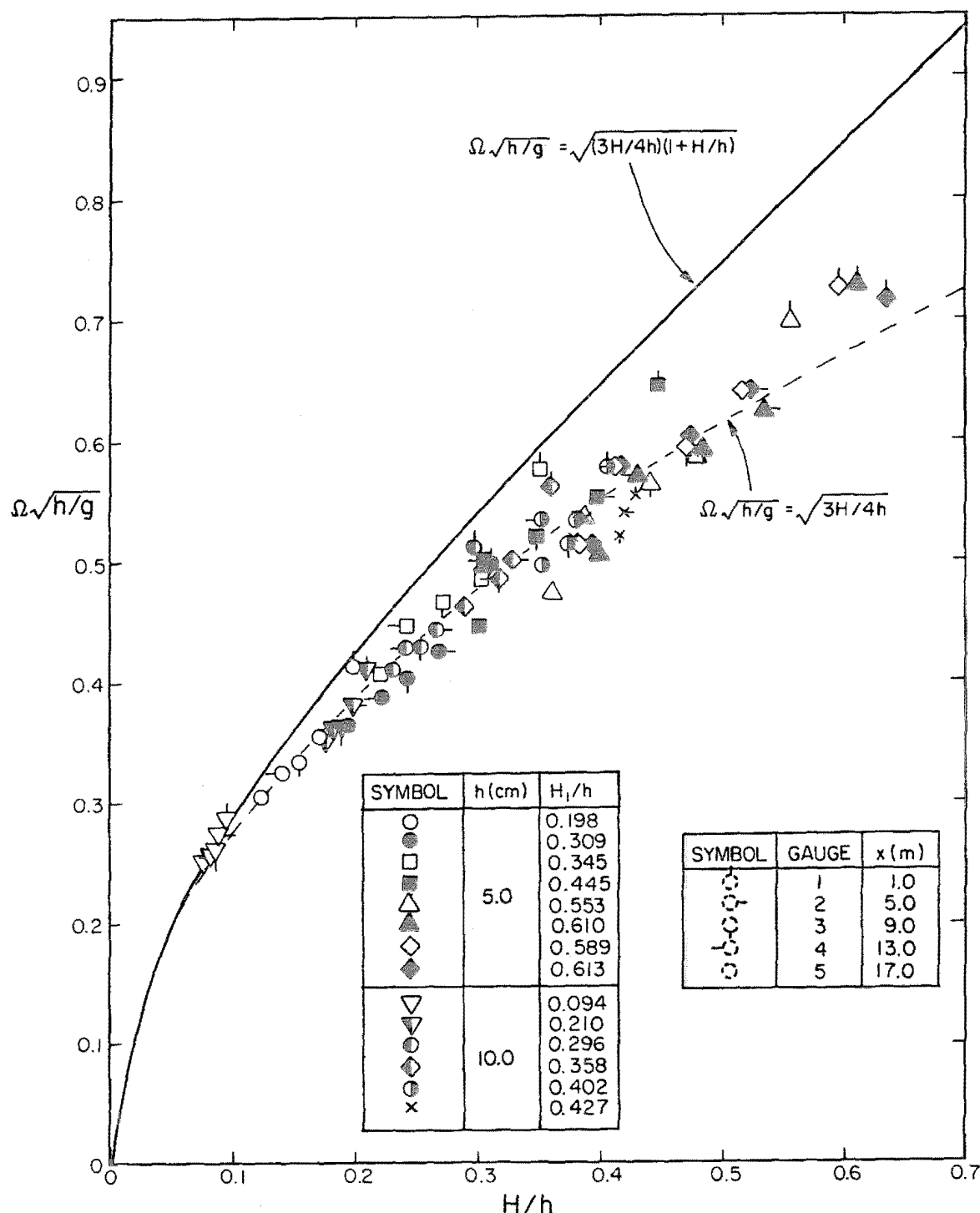


Fig. 5.13 Variation of the "frequency," $\Omega\sqrt{h/g}$, with relative wave height, H/h , of solitary waves as they propagate.

the theory of Boussinesq as given by Eq. (5.5); the dashed curve represents the best fit of the data, other than those from Gauge 1, to an expression with the form of Eq. (5.6) (in this case it was found $\alpha = -.004$). The frequency of the wave at Gauge 1 in all cases is greater than the frequency of the wave when it passes the other gauges. This implies the wave becomes less peaked as it propagates from Gauge 1 to Gauge 2. However, the data from the other gauges appear to be less scattered which indicates the shape is not changing as rapidly as it does between Gauges 1 and 2.

The speed of propagation, or celerity, of solitary waves was measured by placing five wave gauges 0.45 m apart, generating a wave and recording the times at which the crest passed each gauge. The celerity was calculated by linear regression from the five pairs of x and t and is plotted as a function of the relative wave height in Fig. 5.14(a). With the gauges only 0.45 m apart, the change in height of the wave between the first and fifth gauges was negligible so the average of the five wave heights was used. The three curves in Fig. 5.14(a) represent the theories of Boussinesq (1872), McCowan (1891) and Laitone (1963). The theories of Boussinesq and Laitone agree up to a wave height $H/h = 0.2$, then diverge slightly with the Boussinesq theory predicting a larger celerity (2% larger for $H/h = 0.7$). The theory of McCowan agrees with the other two up to a wave height $H/h = 0.12$, then diverges to predict celerities which are significantly less than the other two theories. The data tend to follow the theory of Laitone more than any other which is a result also found by Daily

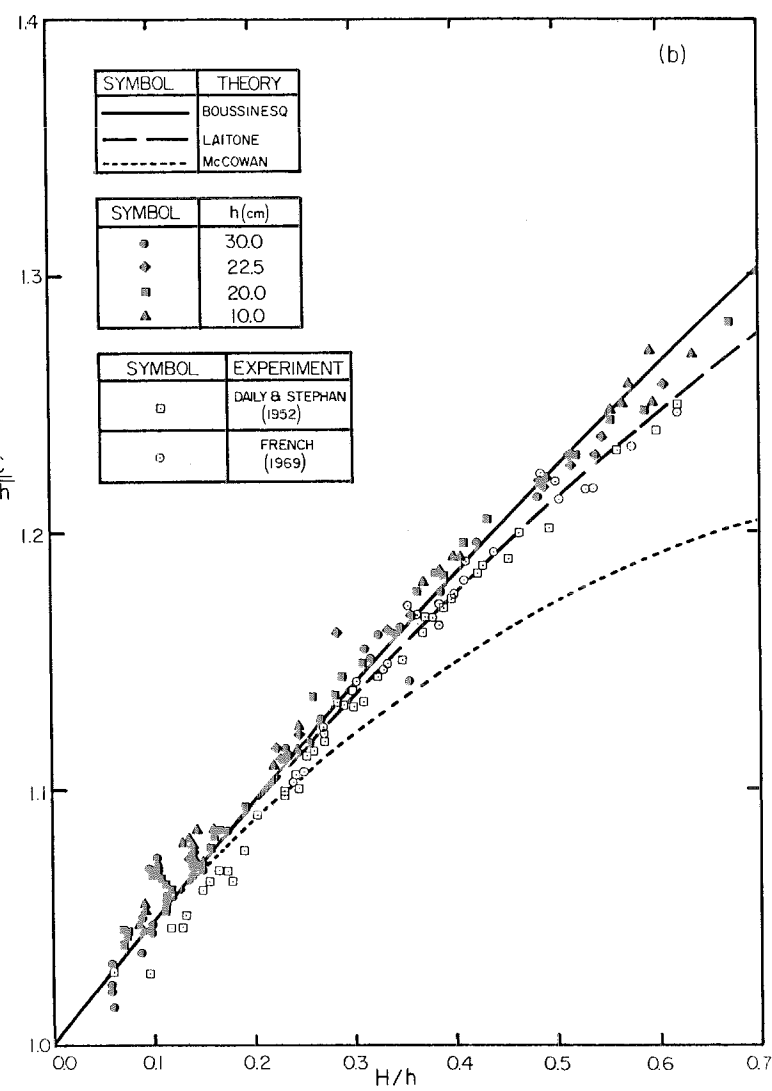
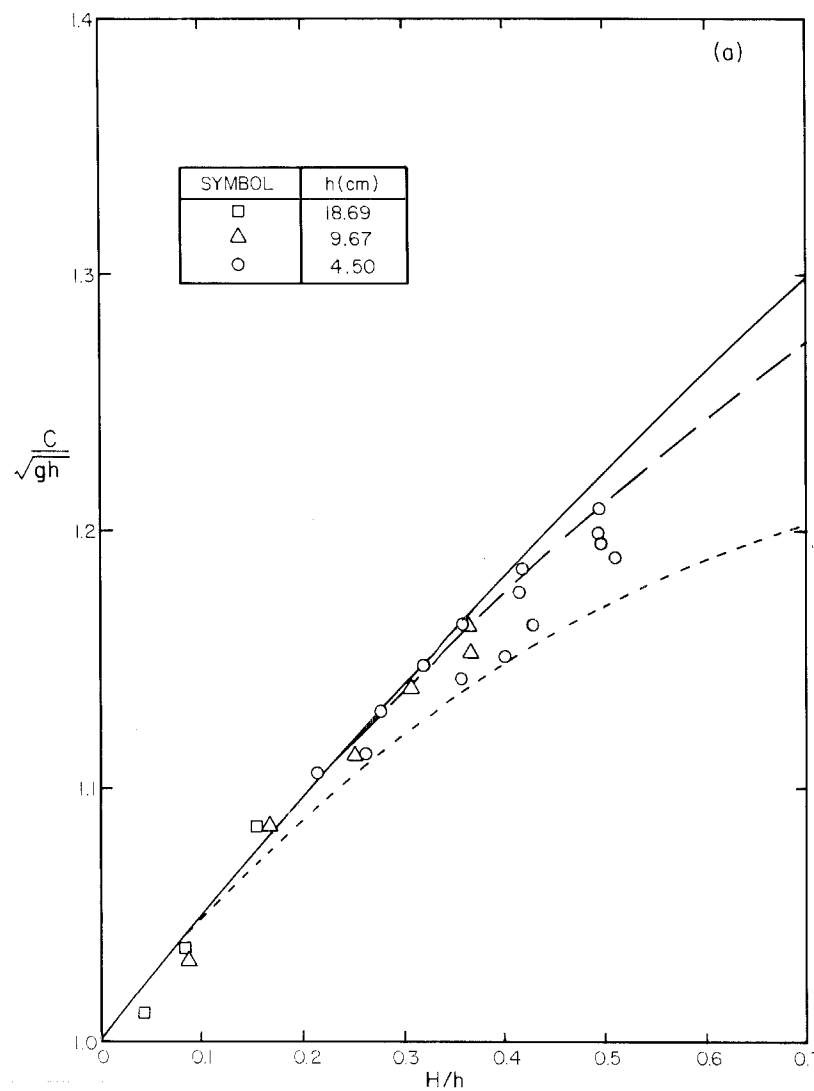


Fig. 5.14 Variation of celerity, c/\sqrt{gh} , with relative wave height, H/h , from (a) this study and (b) Naheer (1977).

and Stephan (1952) and French (1969). Their data along with those of Naheer (1977) are presented in Fig. 5.14(b) (from Naheer (1977)).

5.1.3 The Generation of Cnoidal Waves

The generation of long periodic waves of constant form in the laboratory is difficult because nonlinear effects can never be completely eliminated. This can be illustrated by considering a wave of form:

$$\eta(x, t) = a \sin(kx - \omega t) \quad , \quad (5.9)$$

and substituting into the KdV equation:

$$\eta_t + c_0 \left(1 + \frac{3}{2} \frac{\eta}{h} \right) \eta_x + \frac{1}{6} c_0 h^2 \eta_{xxx} = 0 \quad , \quad (5.10)$$

where $c_0 = \sqrt{gh}$. For nonlinear effects to be negligible, the magnitude of the nonlinear term $\frac{3}{2h} c_0 \eta \eta_x$ must be much less than the magnitude of the dispersive term $\frac{1}{6} c_0 h^2 \eta_{xxx}$, which, from Eqs. (5.9) and (5.10), implies:

$$\frac{3}{2} \frac{a}{h} \ll \frac{1}{6} k^2 h^2 \quad . \quad (5.11)$$

For long waves, it is usually assumed that $kh \leq \pi/10$, thus Eq. (5.11) implies:

$$\frac{a}{h} \ll \frac{\pi^2}{100} \quad . \quad (5.12)$$

Hence for a depth of, say, 30 cm in a laboratory flume, the long waves generated will be linear only for amplitudes $a \ll 0.2$ cm which is extremely small. Because of this, the periodic waves considered in this study were cnoidal waves which although nonlinear, propagate with

constant form.

The wave generation theory developed in Section 3.2 was applied to produce six cnoidal wave generation trajectories, named CN1 to CN6, which were stored on punched paper tape. The trajectories, the theoretical shape of the waves the trajectories generate, and other associated data are presented in Fig. 5.15, where the abscissas are time normalized by the wave period, t/T , and the ordinates are the displacement normalized by the stroke, ξ/S , and the wave amplitude normalized by the wave height, η/H . Trajectories CN1 to CN4 have a nondimensional period: $T\sqrt{g/h} = 20.3$ and wave heights which, starting with $H/h = 0.025$, double successively. For trajectories CN5 and CN6 the relative wave height is: $H/h = 0.6$ and the nondimensional periods are: $T\sqrt{g/h} = 20$ and 40. The trajectories in Fig. 5.15 correspond to a range of the complementary parameter, m' , of $0.470 \geq m' \geq 9.53 \times 10^{-14}$. As the complementary parameter, m' , decreases, the crest of the trajectory moves towards the left which means the average speed in the forward direction is greater than the average speed in the reverse direction. Since forward motion of the generator plate produces the wave crest while reverse motion produces the trough, greater speed in the forward direction produces a higher crest and consequently a shallower trough than if the average speed were the same in both directions. In addition, as the proportion of the period in which forward motion of the plate takes place decreases, the wave crest becomes more peaked.

The actual waves which trajectories CN1 to CN6 generated

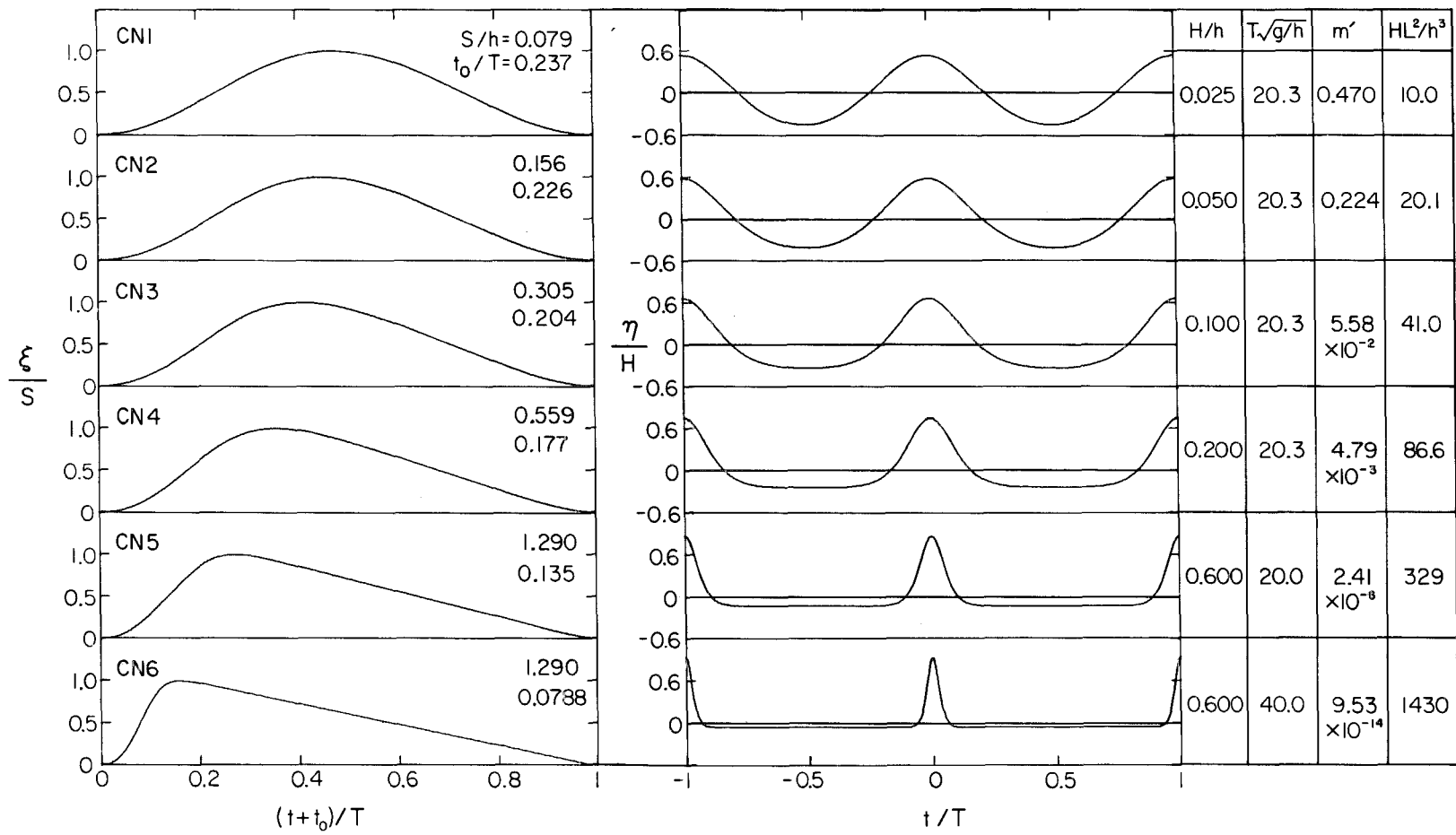


Fig. 5.15 Trajectory shapes, waves and associated data for cnoidal wave trajectories CN1 to CN6.

are compared to theoretical cnoidal wave shapes in Fig. 5.16. For these experiments a wave gauge was placed 1.0 m from the wave generator and a train of cnoidal waves was generated. The data for Fig. 5.16 were taken from the third cycle which passed the gauge. The wave height used for the theoretical wave was the measured wave height, which was in general less than what the generation theory predicted. Fig. 5.16 indicates that the generated wave shapes are predicted quite well by the theory.

Figure 5.17 is the oscillograph recording of the variation of the water surface during a typical wave generation experiment using trajectory CN4. The five wave gauges were spaced 2.5 m apart with Gauge 1 placed 1.0 m away from the wave generator. For this experiment the depth was $h = 20$ cm, the stroke was $S = 11.18$ cm and the period was $T = 2.90$ sec. The wave generator executed four cycles, as shown by the displacement time record at the bottom of the figure, and four waves resulted. The behavior of the leading and trailing waves will be discussed later. Attention is called here to the waves in the middle of the train which retain the same shape from gauge to gauge. Compare this with the recording shown in Fig. 5.18 in which everything is the same as for Fig. 5.17 except that the period was increased to 4.28 sec. In Fig. 5.18 the wave shape is not constant between gauges; there appears to be a secondary wave as indicated in the figure with a period half the main period. This phenomenon was examined by Madsen (1971) for waves with small Ursell Numbers, HL^2/h^3 . He showed, using Stokes second order theory, that the waves

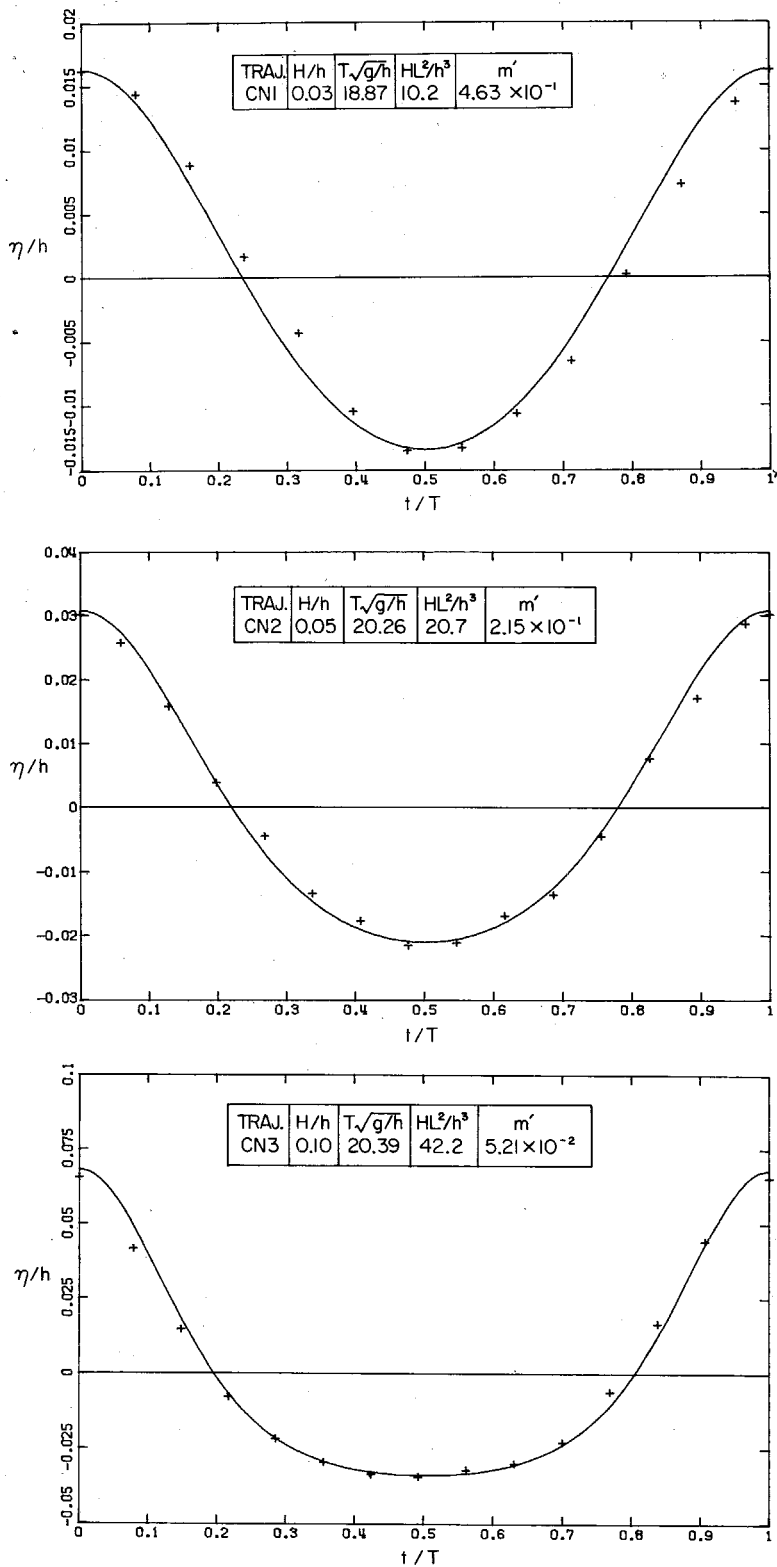


Fig. 5.16(a) Comparison of the shape of experimental cnoidal waves with theory. (Trajectories CN1, CN2 and CN3)

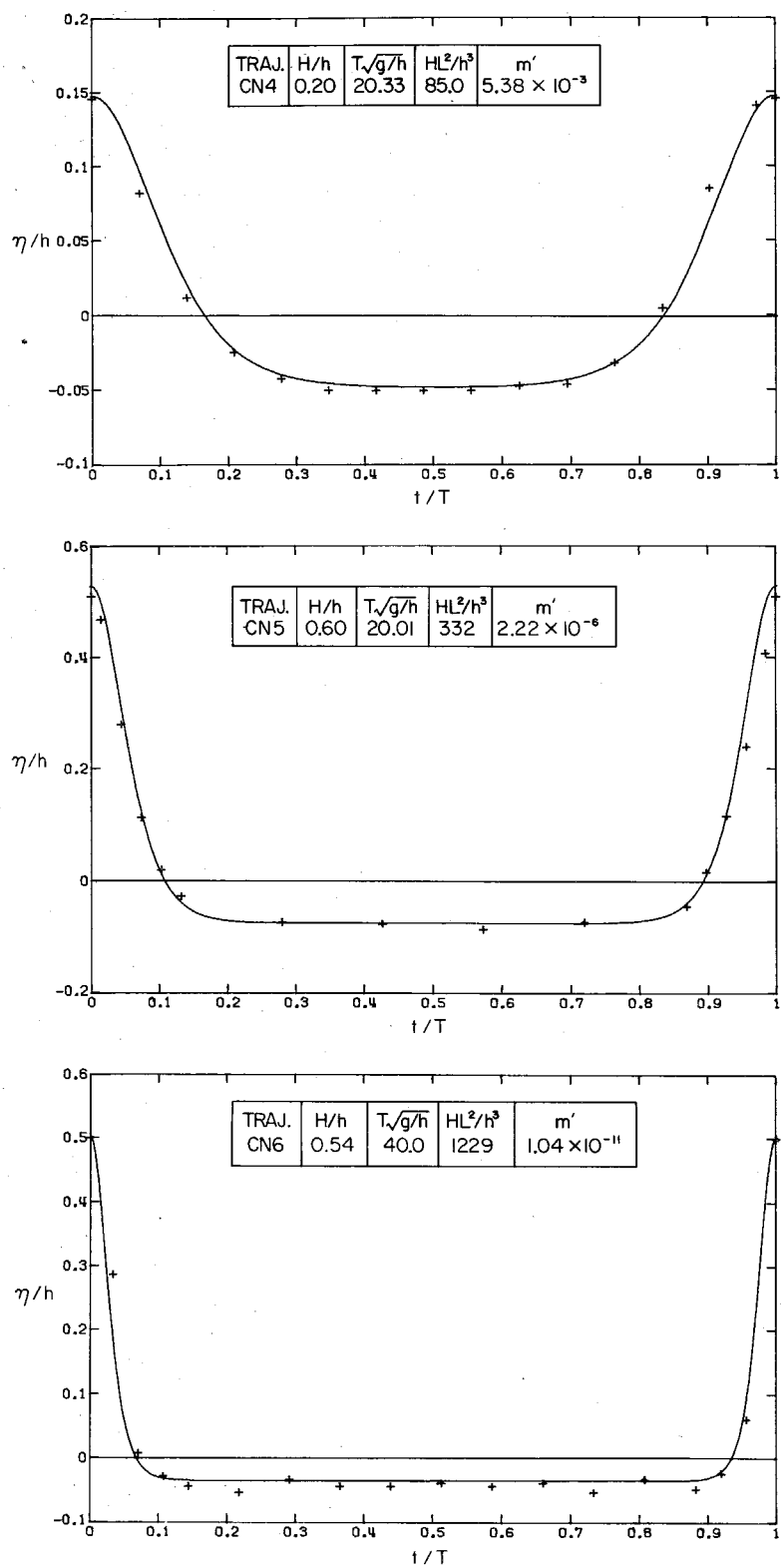
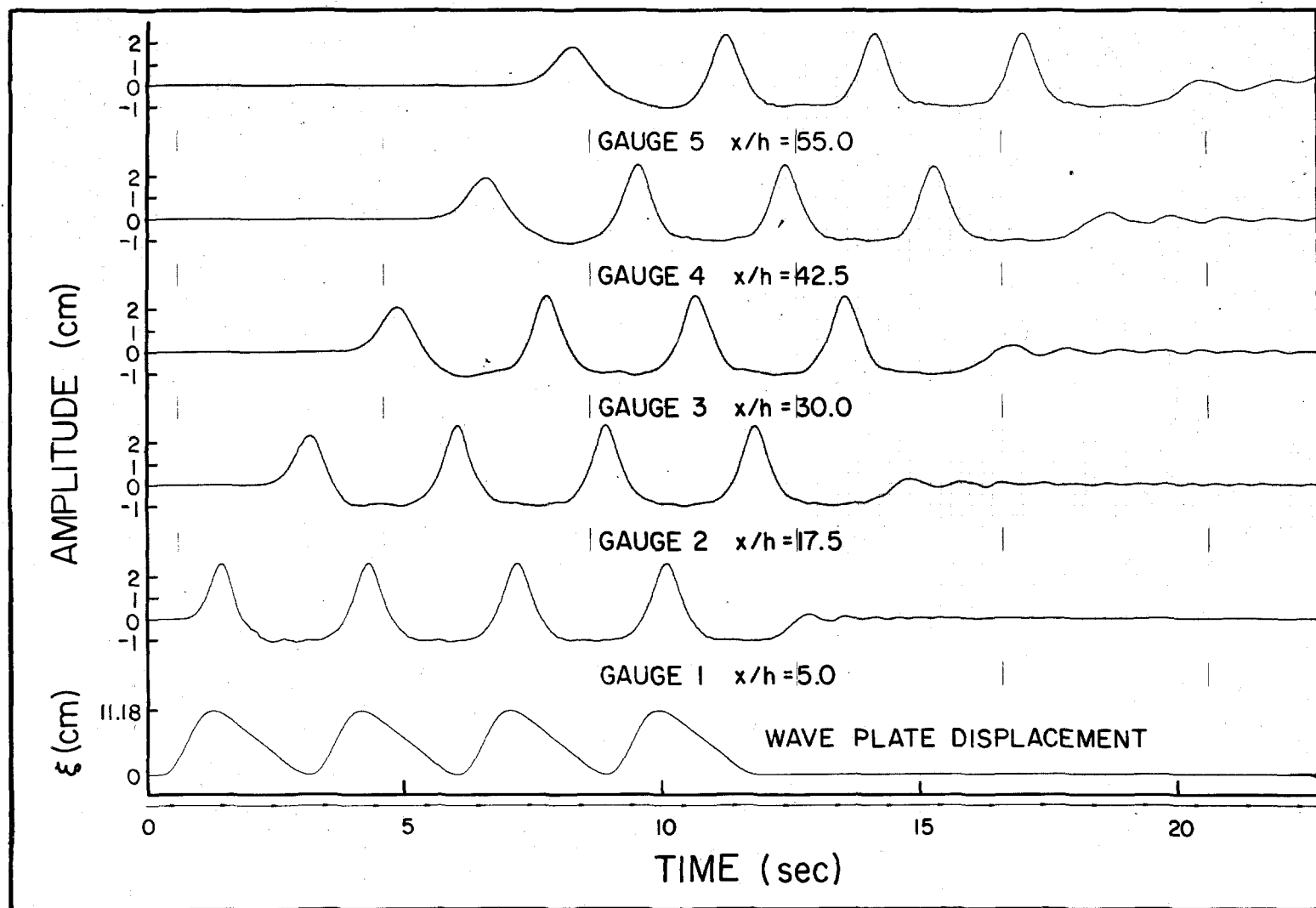


Fig. 5.16(b) Comparison of the shape of experimental cnoidal waves with theory. (Trajectories CN4, CN5 and CN6)



156

Fig. 5.17 Oscillograph record showing the waves generated by trajectory CN4 with $h = 20$ cm, $S = 11.18$ cm and $T = 2.90$ sec.

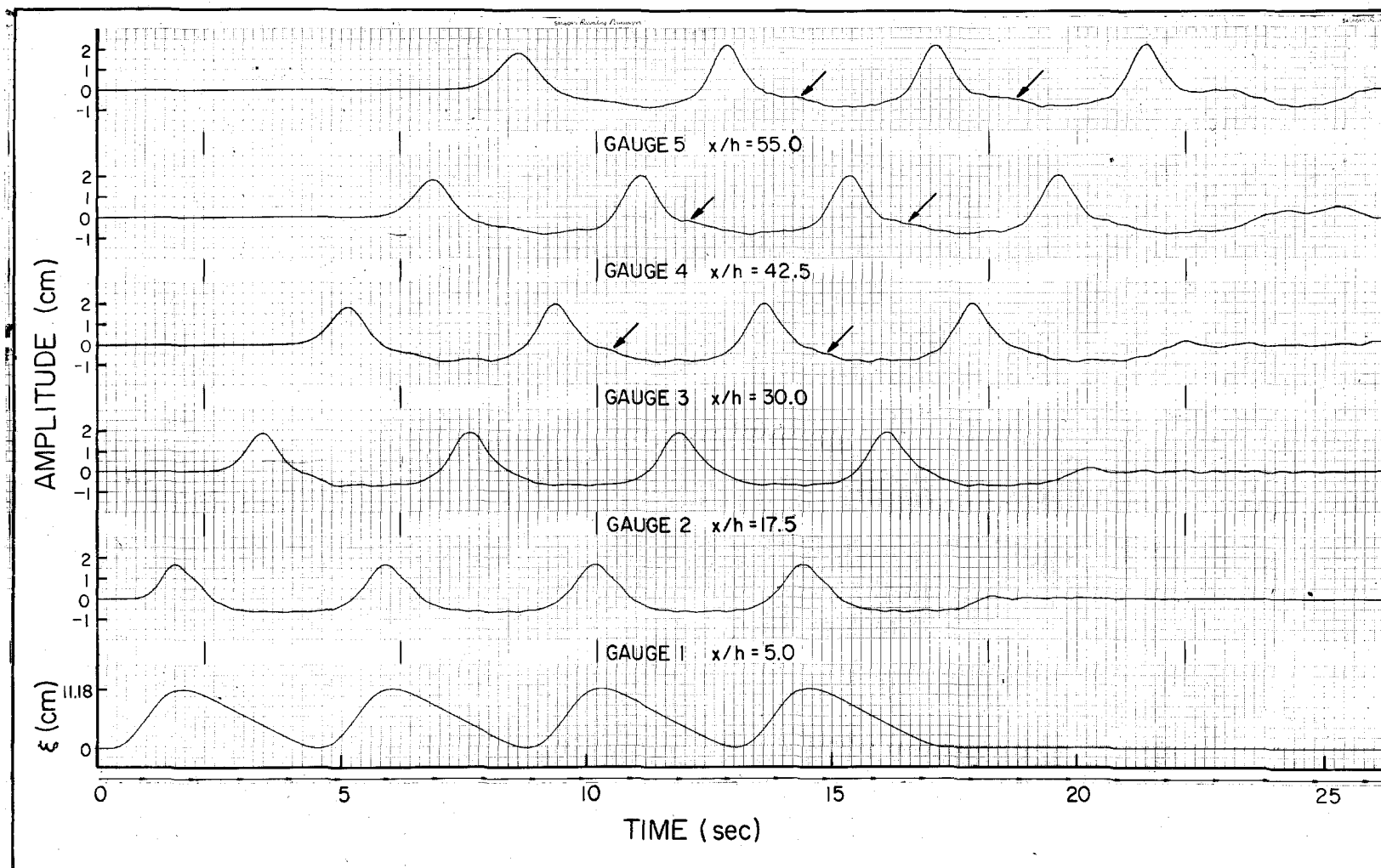


Fig. 5.18 Oscillograph record showing the waves generated by trajectory CN4 with $h = 20$ cm, $S = 11.18$ cm and $T = 4.28$ sec.

generated by sinusoidal trajectory, $\xi = \xi_1 \sin \omega t$, have the form:

$$\begin{aligned} \eta(x, t) = & a \sin(kx - \omega t) + a_p \sin 2(kx - \omega t) \\ & + a_L \sin(k_1 \omega - 2\omega t) \end{aligned} \quad (5.13)$$

where

$$\omega^2 = gk \tanh kh \text{ and } k_1 > 2k.$$

The first two terms represent a Stokes wave. The third term is a free second harmonic wave which travels at a slower speed than the Stokes wave and thus causes the wave shape to change as it propagates. Madsen showed that the second free harmonic wave can be eliminated by using a trajectory with the form:

$$\xi = \xi_1 \cos(\omega t) + \xi_2 \sin(2\omega t), \quad (5.14)$$

in which the second half-stroke ξ_2 is adjusted so as to make $a_L \equiv 0$. As was shown in Section 3.2, for $HL^2/h^3 \leq 10$, Stokes waves and cnoidal waves are coincident. Hence, the theory of Section 3.2 produces the same ξ_1 and ξ_2 in Eq. (5.14) as does Madsen's theory; however, for this theory the arguments of the trigonometric function in Eq. (5.14) are $(\omega t - k\xi)$ instead of ωt . The changing wave shape in Fig. 5.18 cannot be expressed in the form of Eq. (5.13) because for this case $HL^2/h^3 \sim 120$ which is well outside the range of applicability of Stokes waves ($HL^2/h^3 \leq 10$), however the phenomenon is similar. Cnoidal waves, therefore, are generated only by their unique trajectory and unless this trajectory is used, the waves change shape as they propagate.

This discussion seems to imply that trajectories CN1 to CN6 will produce only the waves for which they were designed. However, since the trajectories were stored on tape in the normalized form in which they are plotted in Fig. 5.15 (i.e. with displacement normalized by stroke), it was possible to generate other cnoidal waves with trajectories with the same shape but different stroke and period. To find which waves have trajectories with the same shape, it was noted in Fig. 5.15, the only parameter which obviously distinguishes one trajectory from another is the abscissal distance from the ordinate axis to the crest, i.e., the value of the ratio t/T to the crest. Referring back to Fig. 3.8, it can be seen this distance has been defined already: it is twice the time the origin was moved to start motion from zero, $2t_0/T$. Fig. 5.19 is a plot of t_0/T against the nondimensional period $T\sqrt{g/h}$. The curves are for constant wave height H/h and the horizontal lines are for the particular t_0/T corresponding to trajectories CN1 to CN6. It can be seen, for example, that for CN5 which was designed for period $T\sqrt{g/h} = 20$ and relative wave height $H/h = 0.60$, waves with (period, wave height) pairs of (21.4, 0.5), (23.3, 0.4), (26.2, 0.3), etc. have the same magnitude of $t_0/T = 0.135$.

The half trajectories of a number of period, wave height pairs for which $t_0/T = 0.200$ are compared in Table 5.2, where the displacement normalized with respect to the maximum displacement, ξ/ξ_{\max} , is listed. The table illustrates a feature common to all comparisons made: for a particular t_0/T and for $T\sqrt{g/h} \geq 20$ the trajectories are essentially the same. Therefore, for a given trajectory shape, it was possible

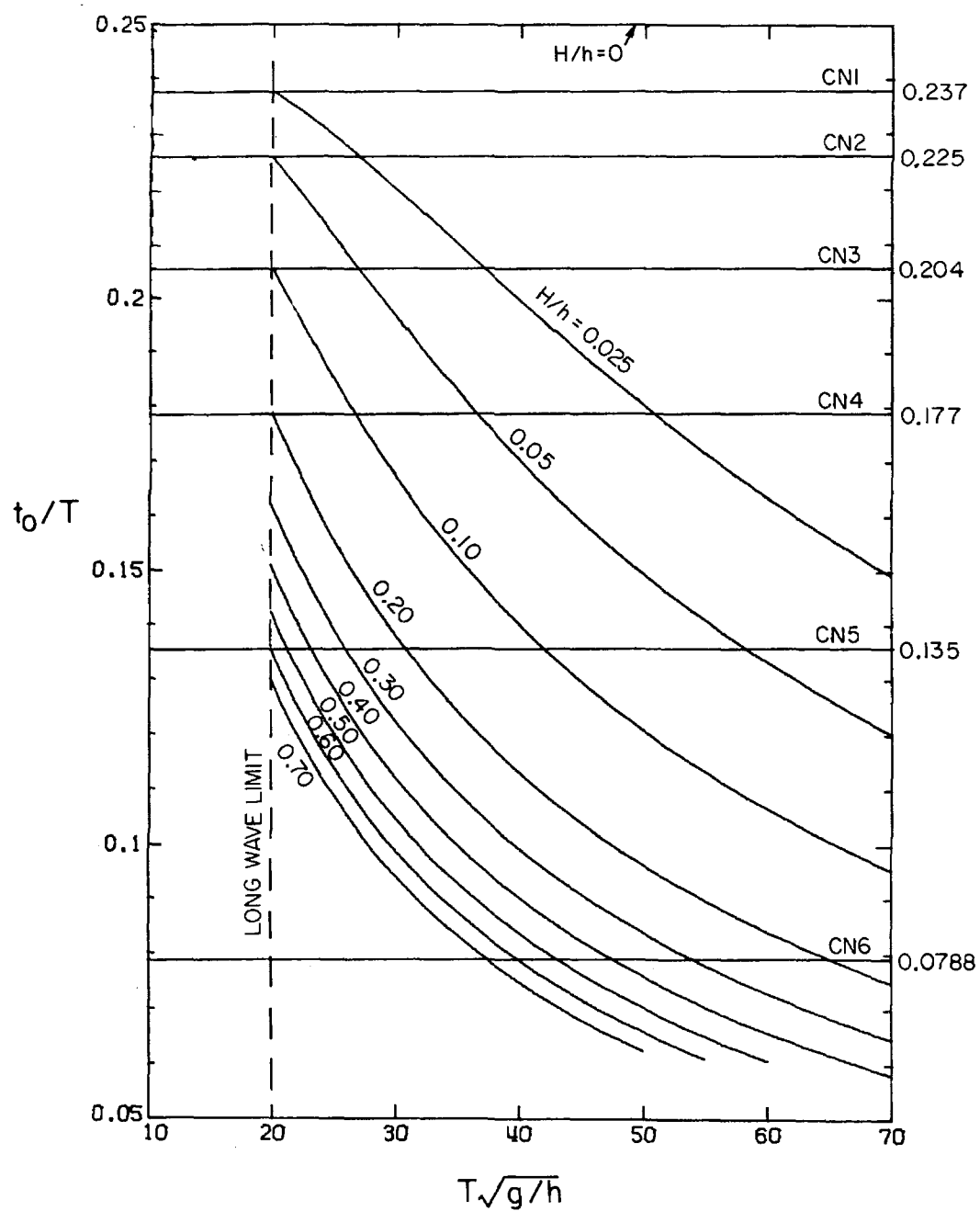


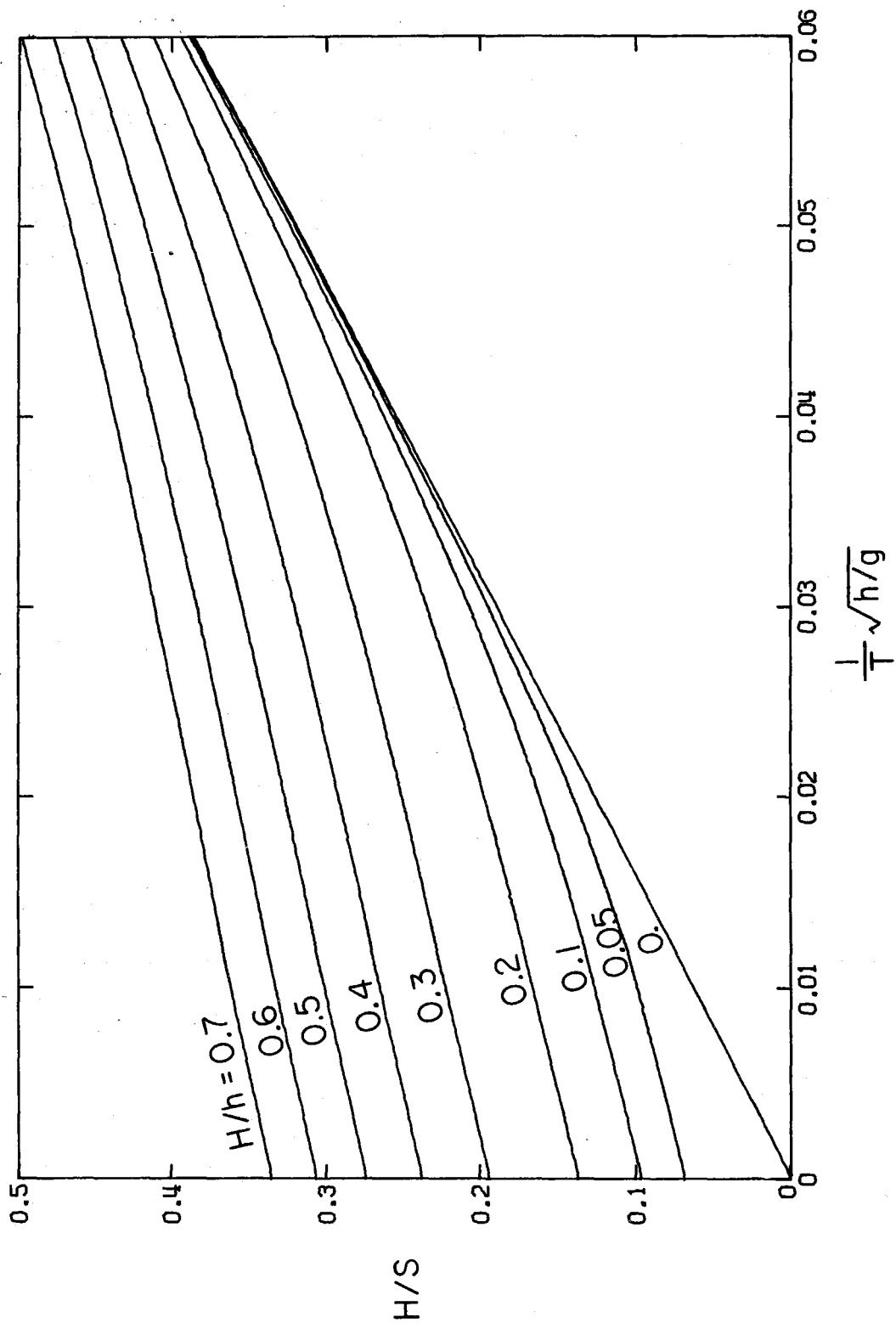
Fig. 5.19 Variations of the relative time, t_0/T , with nondimensional period, $T\sqrt{g/h}$, for cnoidal wave generation trajectories.

Table 5.2 Comparison of Generation Trajectories for $t_0/T = 0.200$.
 ξ/ξ_{\max} for a half period for various wave height and period combinations.

H/h	0.2	0.1	0.05	0.025
$\frac{T\sqrt{g/h}}{h}$	16.36	21.33	28.81	40.0
t/T	0.0	0.0	0.0	0.0
0.05	0.408	0.412	0.414	0.416
0.10	0.738	0.741	0.743	0.746
0.15	0.937	0.939	0.939	0.940
0.20	1.000	1.000	1.000	1.000
0.25	0.947	0.950	0.951	0.951
0.30	0.817	0.823	0.825	0.825
0.35	0.639	0.644	0.650	0.650
0.40	0.437	0.443	0.446	0.447
0.45	0.221	0.225	0.227	0.227
0.50	0.0	0.0	0.0	0.0

to set the period and the stroke to generate cnoidal waves other than those for which the trajectory was designed without generating secondary waves. That this was correct only for $T\sqrt{g/h} \geq 20$ raises an interesting point. The cnoidal wave relations (Appendix A) have no mathematical restrictions on the period (or, equivalently, the wave length). The relations apply equally as well to a wave with $T\sqrt{g/h} = 1$ as they do to a wave with $T\sqrt{g/h} = 100$. Thus, the long wave assumption is an external physical requirement. However, when the generation theory is extended to waves which are not long, i.e., $T\sqrt{g/h} < 20$, it produces results which are different from those for physically long waves ($T\sqrt{g/h} > 20$) with the same t_0/T . For example, the trajectory shapes change slightly for constant t_0/T as shown in Table 5.2, and the curves for various H/h in Fig. 5.19 converge. The reason for this is that although the long wave assumption is not explicit in the mathematical relations, it still must be there implicitly.

Another example of this is shown in Fig. 5.20 which is the long wave part of the H/S vs $1/T\sqrt{g/h}$ plot often used for small amplitude wave generation. The well-known small amplitude theory (see, e.g., Ursell *et al.* (1958)) is represented by the curve passing through the origin. The other curves are for cnoidal waves and each are for a constant relative wave height H/h . For $1/T\sqrt{g/h} = 0$, i.e., waves with infinite period (solitary waves), the variation of H/S with H/h is given by: $\frac{H}{S} = \sqrt{\frac{3}{16}} \frac{H}{h}$, which is Eq. (3.54). As the quantity $1/T\sqrt{g/h}$ increases, the curves in Fig. 5.20 converge and, in fact, actually



cross for $1/T\sqrt{g/h} > 0.06$. Clearly, the theory is invalid when this occurs, i.e., when the long wave criterion ($h/L \leq 0.05$) is violated.

The experiments performed to test the generation theory involved generating waves of various periods with each of the trajectories, CN1 to CN6, and measuring the wave heights 1.0 m from the wave plate. The results are presented in Fig. 5.21 which is the same as Fig. 5.20 but with the addition of curves of constant t_o/T (the dashed curves) and the experimental data. Comparison of experiment with theory takes place in two ways. First, the symbol shapes are associated with a particular trajectory represented by a dashed curve (e.g., the points represented by solid triangles were generated by trajectory CN6). Second, the position of the flag on the symbol defines the range of wave height in which a particular point lies, (e.g., symbols with a vertical flag imply the relative wave height: $H/h \leq 0.05$). Thus, the position of the point relative to the curves of constant wave height is also a comparison with the theory. It is evident that for trajectories CN5 and CN6 (which were designed for $H/h = 0.6$ and $T\sqrt{g/h} = 20$ and 40) all the experimental points lie below the theoretical curves. For the waves generated by trajectory CN4, H/S is either on or below the theoretical curve. For trajectories CN1, CN2 and CN3 the points lie above, below or on the theoretical curves. Thus, the agreement with the theory is better for larger t_o/T . A possible reason for this is that the trajectories with smaller t_o/T generate high frequency small amplitude waves which appear in the trough of the main wave. This can be seen in Fig. 5.16 where a wave with $H/h = 0.54$

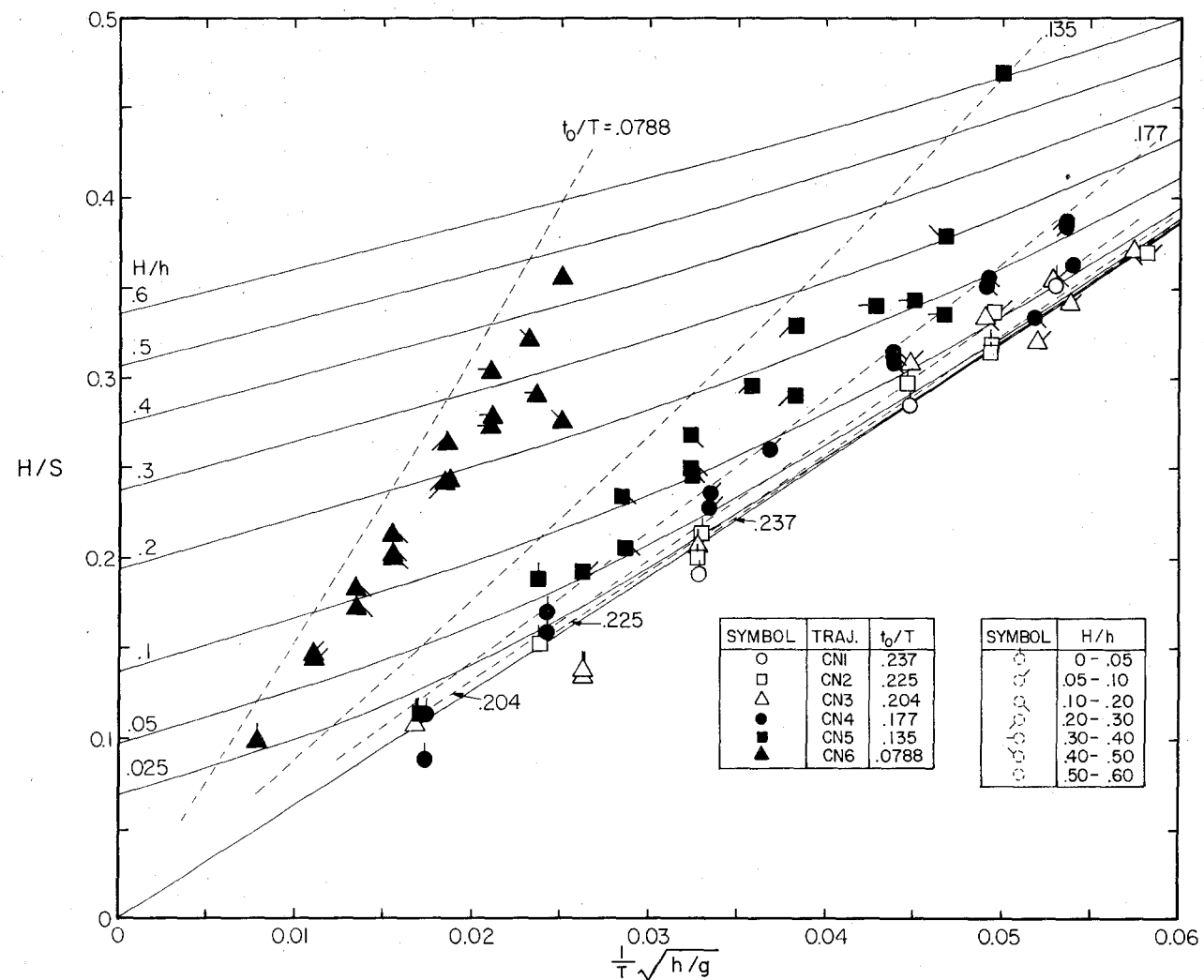


Fig. 5.21 Variation of H/S with the inverse nondimensional period $1/T\sqrt{h/g}$ for cnoidal wave generation.

was generated by trajectory CN6 and also to a lesser extent in Fig. 5.17 where the trajectory used was CN4. The effect is even more pronounced in Fig. 5.22 which shows the waves generated by trajectory CN6 in a depth of 5 cm with stroke $S = 6.07$ cm and period $T = 3.40$ sec, which corresponds to $H/S = 0.304$ and $1/T\sqrt{g/h} = 0.021$ in Fig. 5.21. (This figure will be discussed in more detail presently.)

The generation of spurious high frequency waves detracts from the energy available to generate the desired wave, so the effect is a reduction in wave height. Harmonic analysis proved fruitless for this problem because cnoidal waves have contributions at all frequencies so the spurious high frequency waves could not be separated from the cnoidal wave components. A period representative of the waves in the trough at Gauge 1 in Fig. 5.22 is 0.35 sec which gives a nondimensional period of $T\sqrt{g/h} \approx 5$ and a wave length of $L \approx 10$ cm. Capillary waves at an air/water interface have $L \approx 1.7$ cm which is an order of magnitude less than the observed waves so it is concluded that the waves are not caused by surface tension. Conversely, $T\sqrt{g/h} \approx 5$ is about a quarter of the minimum period for long waves so the spurious waves would not be predicted by any long wave theory. Having excluded the two extremes of capillary and long waves, only short and intermediate waves remain, but no theory other than the full Navier Stokes equations is known which could predict the simultaneous appearance of both cnoidal waves and short waves.

One approximation which is made in the generation theory and its application which can be eliminated as a cause of lower wave heights

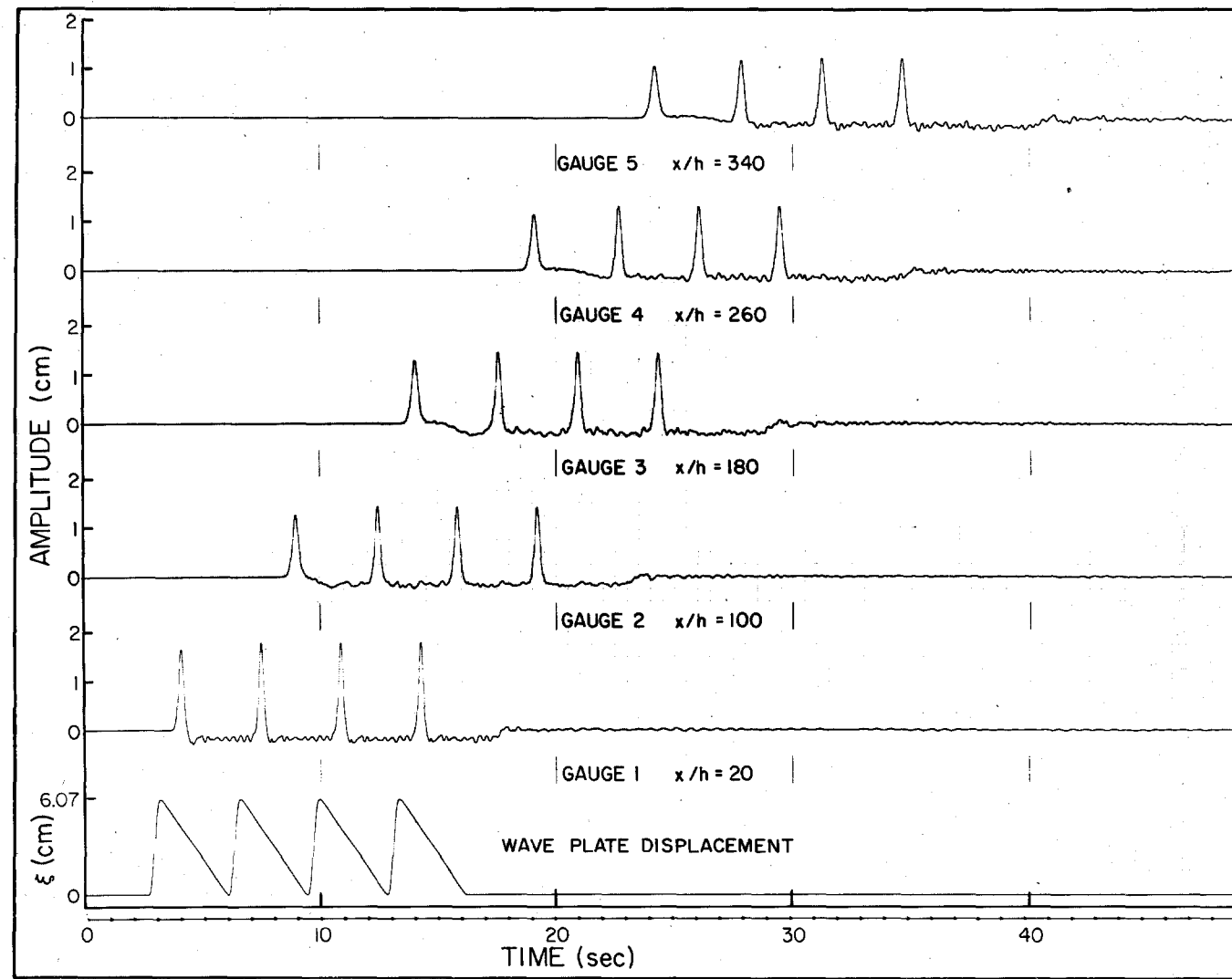


Fig. 5.22 Oscillograph record of the waves generated by trajectory CN6 with $h = 5$ cm, $S = 6.07$ cm and $T = 3.40$ sec.

than expected is the use of depth averaged velocities and a vertical wave plate. This is because the disagreement is worse for large periods where the velocity distribution with depth would be nearly constant than it is for smaller periods where the velocity distribution varies more with depth.

5.1.4 The Propagation of Cnoidal Waves in a Constant Depth

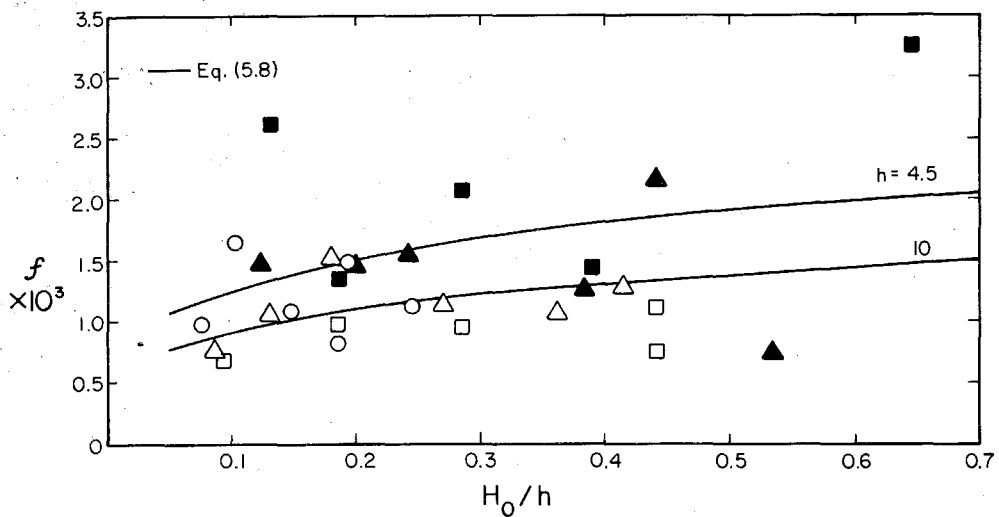
The propagation of cnoidal waves was considered in two phases: short range propagation which is relevant to this study and long range propagation which is of general interest.

An example of short range propagation was presented in Fig. 5.17 which shows a packet of four waves propagating 50 depths. At Gauge 1, five depths from the wave generator, the crest and trough amplitudes are the same for all four waves and the crests are equispaced in time. As the train propagates, the height of the leading wave decreases relative to the height of the other waves and the time between its crest and the crest of the next wave increases by about 1% of the period from gauge to gauge indicating the leading wave is travelling faster than the rest of the train. The trough at the rear of the train maintains the same amplitude as the two central troughs but increases in period as the train propagates. The small, oscillatory waves which follow this trough grow in amplitude and period from gauge to gauge.

However, in spite of these transient effects at either end of the train, the central part of the train between the second and fourth crests appears unaffected. Hence, the decrease in height from gauge

to gauge of the waves in the center of the train is attributed to friction entirely. Two sets of experiments were performed to test the effect of friction in which five wave gauges were spaced 2.5 m apart in water of depth 4.5 cm and 10.0 cm. A packet of waves was generated and the height of the third wave passing each gauge was recorded. A regression analysis was performed on these wave heights to determine the initial height H_0 and the exponent f in the damping equation, Eq. (5.7). The results of this analysis are presented in Fig. 5.23 which is a plot of the exponent f vs the initial relative wave height H_0/h . Included in the figure is a table which lists the data including the coefficient of determination, r^2 . For twenty of the twenty-eight experiments the latter exceeded 0.9 which indicates the decrease in wave height with propagation distance is reasonably well represented by the exponential equation, Eq. (5.7). The data exhibit considerable scatter but, even allowing for this, no variation of damping exponent f with wave height H_0/h is apparent in Fig. 5.23. Comparing Fig. 5.23 with Fig. 5.11 which showed the damping exponent for solitary waves, the magnitude of the damping exponents for cnoidal waves and solitary waves appear similar for the similar depths considered. (For comparison, the curves described by Eq. (5.8) for solitary wave damping are presented in Fig. 5.23.)

The wave gauge records of the experiments marked with an asterisk (*) in Fig. 5.22 were digitized using an A/D converter and an harmonic analysis was performed on a single wave cycle from each gauge. Of interest was the way in which the shape of the waves



Symbol	Trajectory	Depth (cm)	H_0/h	$f \times 10^3$	r^2
○	CN4 $\left(\frac{HL^2}{h^3} \sim 70\right)$	10.0	0.076 0.012* 0.147 0.185 0.193* 0.245	0.98 1.63 1.08 0.81 1.48 1.12	0.994 0.970 0.938 0.932 0.950 0.980
□	CN5 $\left(\frac{HL^2}{h^3} \sim 200\right)$	10.0	0.092 0.184 0.284 0.439 0.440	0.65 0.95 0.94 1.11 0.75	0.888 0.872 0.902 0.877 0.527
△	CN6 $\left(\frac{HL^2}{h^3} \sim 700\right)$	10.0	0.086 0.131 0.179 0.269 0.361 0.414	0.75 1.05 1.50 1.14 1.07 1.29	0.974 0.956 0.937 0.827 0.745 0.393
■	CN5 $\left(\frac{HL^2}{h^3} \sim 200\right)$	4.5	0.129 0.184* 0.284 0.391 0.642*	2.61 1.34 2.08 1.42 3.25	0.856 0.934 0.975 0.963 0.925
▲	CN6 $\left(\frac{HL^2}{h^3} \sim 700\right)$	4.5	0.122 0.199* 0.239 0.383* 0.441 0.536*	1.47 1.43 1.52 1.21 2.19 0.74	0.969 0.955 0.947 0.927 0.914 0.985

* Denotes waves for which an harmonic analysis was performed.

Fig. 5.23 Variation of the damping exponent, f , with relative wave height, H_0/h , for cnoidal waves.

change as their height decreases due to frictional effects and whether the shape remains cnoidal. Harmonic analysis was used only because it provides a means of quantitatively describing the complicated shape of a wave. The results for the first three frequency components are presented in Fig. 5.24 where the component amplitudes, normalized with respect to the wave height, are plotted against $\frac{HL^2}{h^3}$. The curves presented in Fig. 5.24 are the theoretical curves which were described in Section 3.1 and plotted in Fig. 3.5; they represent the first three theoretical Fourier components of cnoidal waves. As the wave propagates, the period remains constant but the wave height, H , and hence the celerity (and the wave length, L) decrease; therefore, $\frac{HL^2}{h^3}$ decreases. Hence, the progression from one wave gauge to another in a downstream direction corresponds to moving from right to left in Fig. 5.24 (i.e. in the direction of decreasing $\frac{HL^2}{h^3}$). For a particular experiment the point at the right will have come from Gauge 1 and the point at the left from Gauge 5. Apart from one experiment, the theoretical curves agree well with the data with no apparent trend of the data either towards or away from the theoretical curves. Thus, the waves retain cnoidal shape as they propagate even though the wave height decreases due to friction. The exception is the experiment with $T\sqrt{g/h} = 20$ which exhibits large variations in the second and third components. It is this experiment for which, in Fig. 5.23, the damping exponent f is considerably greater than for the other exponents ($f = 3.25 \times 10^{-3}$). Therefore, it is concluded that for this wave the wave shape was changing as it propagated due to improper

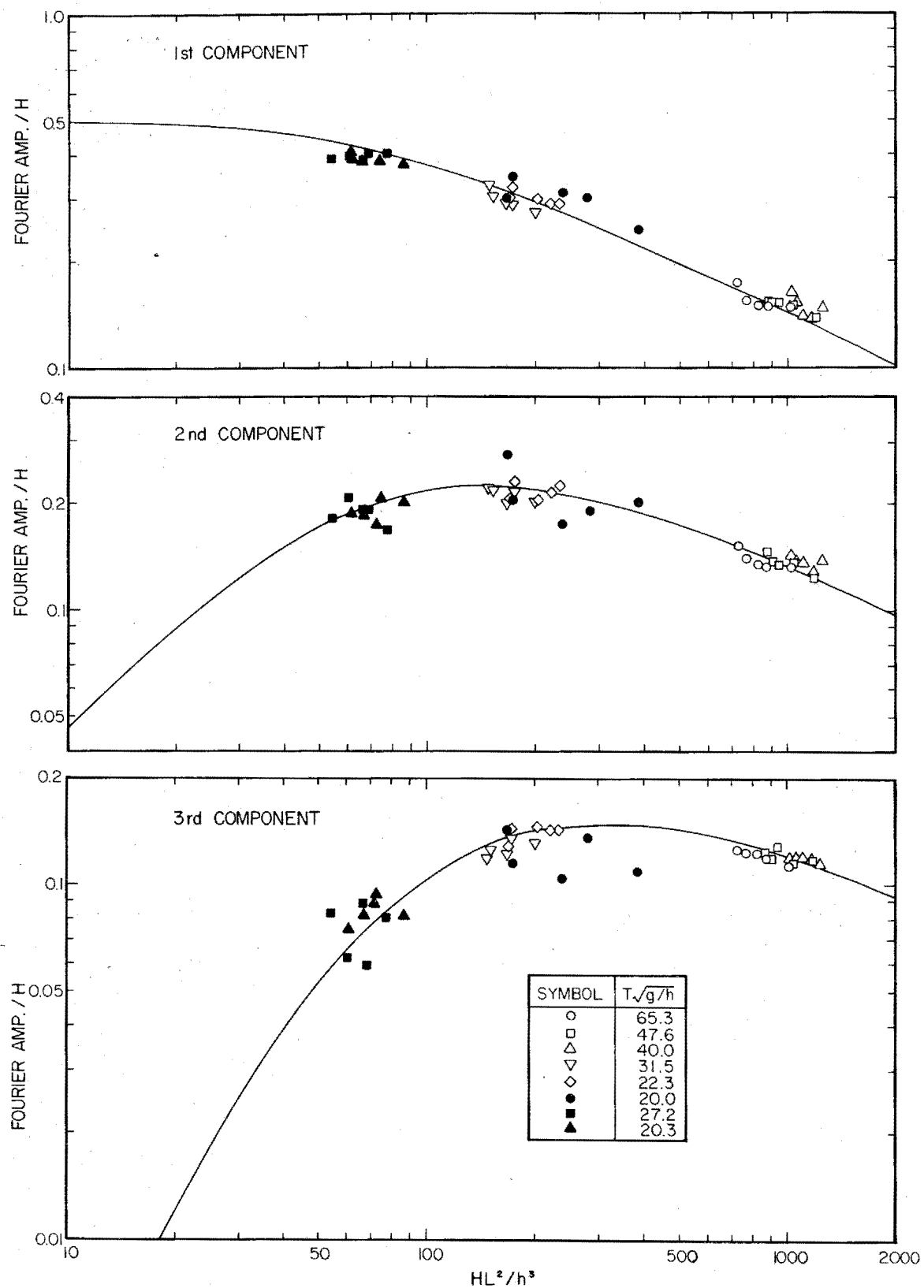


Fig. 5.24 Comparison of the amplitudes of the first three Fourier components of experimental cnoidal waves with the theory.

generation.

Another quantity of interest in the propagation of cnoidal waves is their speed of propagation or celerity. The theoretical relation for celerity (see, e.g., Svendsen (1974)) is:

$$\frac{c^2}{gh} = 1 + \alpha \frac{H}{h} \quad , \quad (5.15)$$

$$\alpha = \frac{2}{m} - 1 - 3 \frac{E}{mK} \quad , \quad (5.16)$$

where m is the elliptic parameter and K and E are the first and second complete elliptic integrals respectively. The parameter α , which is a function of only m or, equivalently, only $\frac{HL^2}{h^3}$, is plotted against $\frac{HL^2}{h^3}$, in Fig. 5.25. For large $\frac{HL^2}{h^3}$, α tends to unity and

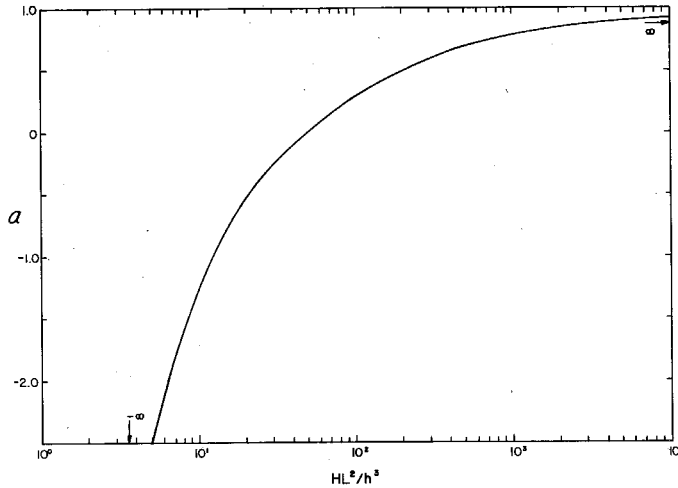


Fig. 5.25 Variation of the celerity parameter, α , with Ursell Number, HL^2/h^3 , for cnoidal waves.

the celerity tends to the solitary wave celerity, $c = \sqrt{gh\left(1 + \frac{H}{h}\right)}$.

As $\frac{HL^2}{h^3}$ goes to zero the parameter α goes to negative infinity but, since small $\frac{HL^2}{h^3}$ implies small wave height also, the celerity remains finite and tends to $c = \sqrt{gh}$.

The celerity of cnoidal waves generated in the laboratory was measured by placing five wave gauges 0.45 m apart, generating a group of waves and recording the time at which a particular crest passed each gauge. The celerity was calculated by linear regression from the five pairs of x and t and is plotted as a function of wave height in Fig. 5.26. With the gauges only 0.45 cm apart, the change in height of the waves between the first and fifth gauges was negligible so the average of the five wave heights was used. The numbers next to the points in Fig. 5.26 represent the value of $\frac{HL^2}{h^3}$ (∞ denotes a solitary wave). The curves are the theory as given by Eqs. (5.15) and (5.16), for constant values of $\frac{HL^2}{h^3}$. The dashed curve represents the long wave limit of $h/L < .05$. The scatter exhibited by the data is partially explained by the sensitivity of the graph exceeding the accuracy of the data. (For waves with large Ursell Number this is less of a problem because the wave crests are sharp and therefore well defined, but for waves with a small Ursell Number the crest is less peaked and its position is not as well defined.) In spite of the scatter the trend is for the cnoidal wave celerity to be generally less than the theory predicts, while the solitary wave celerity is well defined by the theory.

Only near field propagation has been considered so far. Also

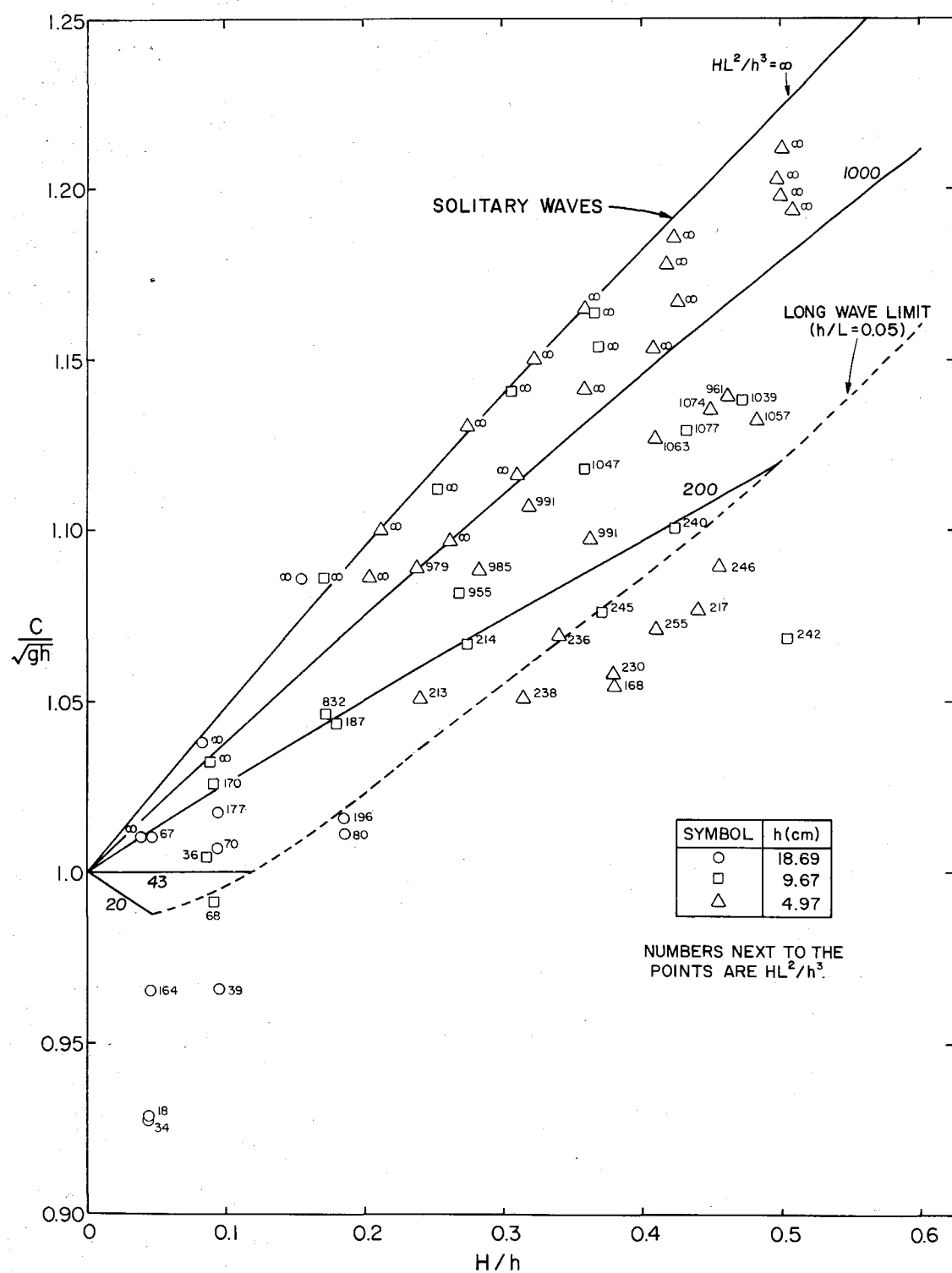


Fig. 5.26 Variation of celerity of solitary and cnoidal waves with relative wave height, H/h .

of interest is what happens to a train of cnoidal waves as it propagates to infinity. The inverse scattering theory predicts one solitary wave will emerge--the lead wave, but the theory does not provide information about the trailing waves. An example of the long distance propagation in the laboratory of a train of cnoidal waves was presented earlier in Fig. 5.22 which shows a packet of four cnoidal waves propagating 340 depths from generation. The behavior of the leading crest, which slowly separates from the train and the trailing trough, which increases in duration, was described earlier when considering near field propagation. Of more interest here are any changes which occur in the center of the train. Careful inspection of each wave shows the heights of the three central crests vary by up to 0.025 cm (i.e., 1.3% of the wave height). The period, set at 3.40 sec, varies between 3.37 sec and 3.40 sec. These fluctuations are considered too small to imply any change is taking place to the center of the train as it propagates the 340 depths from generation. However, it cannot be concluded from this limited aspect of the study that the train would continue to propagate in this manner to infinity even in the absence of friction.

5.2 The Reflection of Long Waves from a Change in Depth

5.2.1 The Reflection of Solitary Waves from a Step

The linear nondispersive theory described in Section 3.4, when applied to solitary waves propagating over a step onto a shelf, predicts the reflected wave will retain the same shape as the

incident wave, but the amplitude will be scaled by the reflection coefficient K_R (given by Eq. (3.113)). Hence, the predicted reflected wave would be given by:

$$n_R = H_R \operatorname{sech}^2 \sqrt{\frac{3}{4} \frac{H_I}{h_1^3}} (x + \sqrt{gh_1} t) \quad , \quad (5.17)$$

where H_I is the height of the incident solitary wave and H_R is the reflected wave height given by:

$$H_R = K_R H_I \quad . \quad (5.18)$$

A series of experiments were conducted, for a range of wave heights and depths, to test the validity of the linear nondispersive theory when applied to the reflection of solitary waves from a step. The experiments comprised essentially the arrangement described earlier and shown in Fig. 5.1 except that one of the gauges from the shelf was removed and placed adjacent to Gauge 1. This gauge was adjusted to be more sensitive than Gauge 1 so that maximum resolution of the reflected wave (which had height 10-45% of the incident wave) could be achieved. Electrical interference between the gauges was minimized by carefully and directly grounding the gauge support clamps.

The experiments were performed in two sets: in the first set the effect of the height of the incident wave on the reflected wave was examined; in the second set the effect of the depth ratio on the reflected wave was examined.

The first set comprised 51 experiments with incident wave height to depth ratios H_I/h_1 varying from 0.05 to 0.65 and with depth ratios: h_1/h_2 of 2, 3, 3.5, 4, 7 and 10. The height of the shelf was 15.54 cm and Gauge 1 was situated 5.7 m upstream of the step. A solitary wave was generated and the incident and reflected waves were recorded. Both waves were digitized and the following quantities were calculated: maximum wave amplitude, inverse scattered wave height and volume. The results for the incident waves were presented in Section 5.1.2; the results for the reflected waves relative to these incident waves are plotted as a function of the relative wave height, H_I/h_1 , in Figs. 5.27 to 5.29.

Figure 5.27 shows the ratio of measured wave heights H_R/H_I plotted as a function of the incident wave height ratio H_I/h_1 . The lines represent the best fit through the experimental points. They indicate that, as the incident wave height increases, the relative height of the reflected wave decreases and, as the depth ratio increases, this decrease takes place at a greater rate. Clearly this is contrary to the linear nondispersive theory which from Eq. (5.17) predicts, for constant depth ratio, h_1/h_2 , no variation in the wave height ratio H_R/H_I with incident wave height. Therefore, the linear nondispersive theory is invalid for some time between the time the incident wave leaves the gauge until the reflected wave reaches the same gauge. The propagation of the incident wave toward the step is expected to be predicted well by the linear nondispersive (as well as by the nonlinear dispersive theory) theory since the incident wave

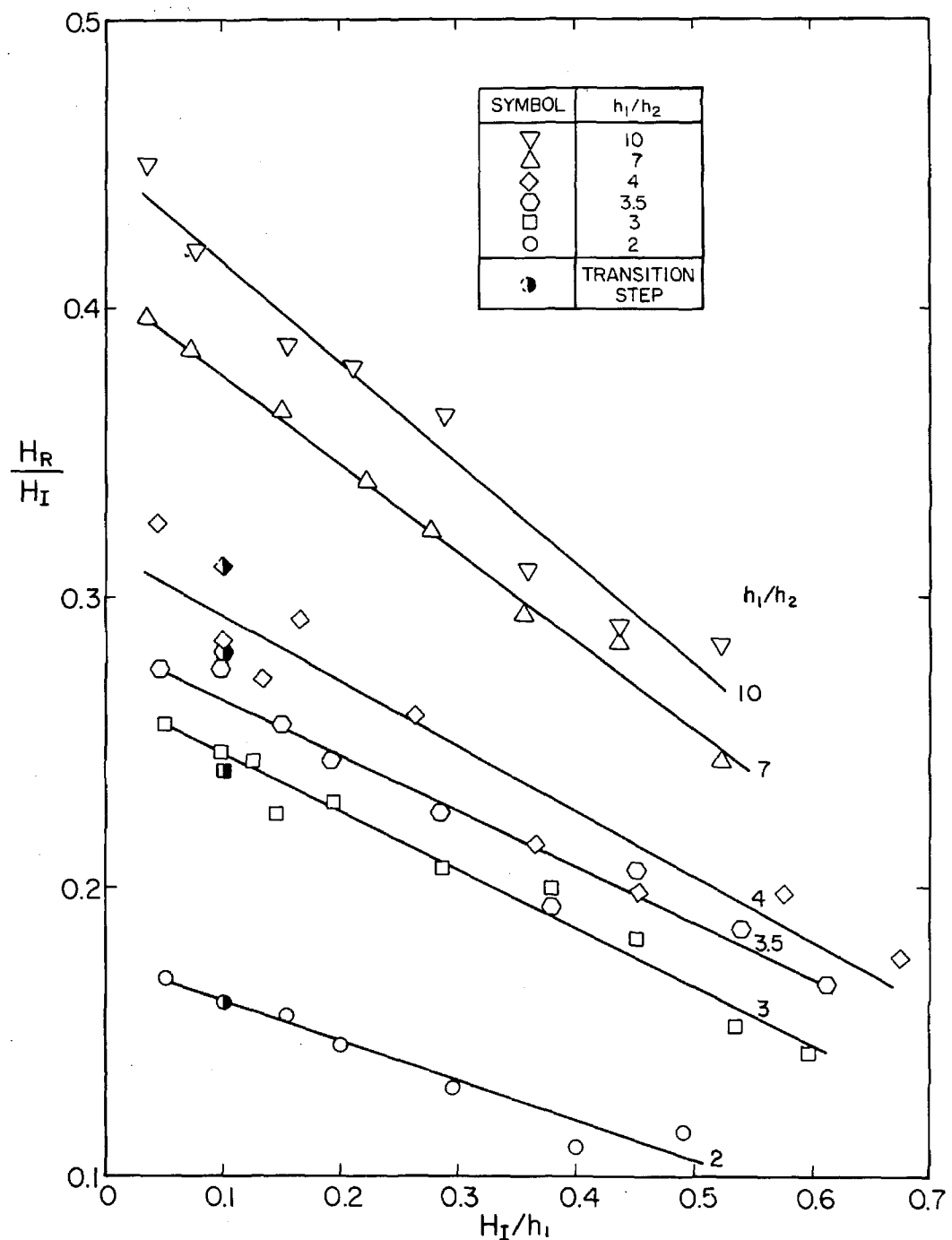


Fig. 5.27 Variation of the wave height ratio, H_R/H_I , with the relative incident wave height, H_I/h_I .

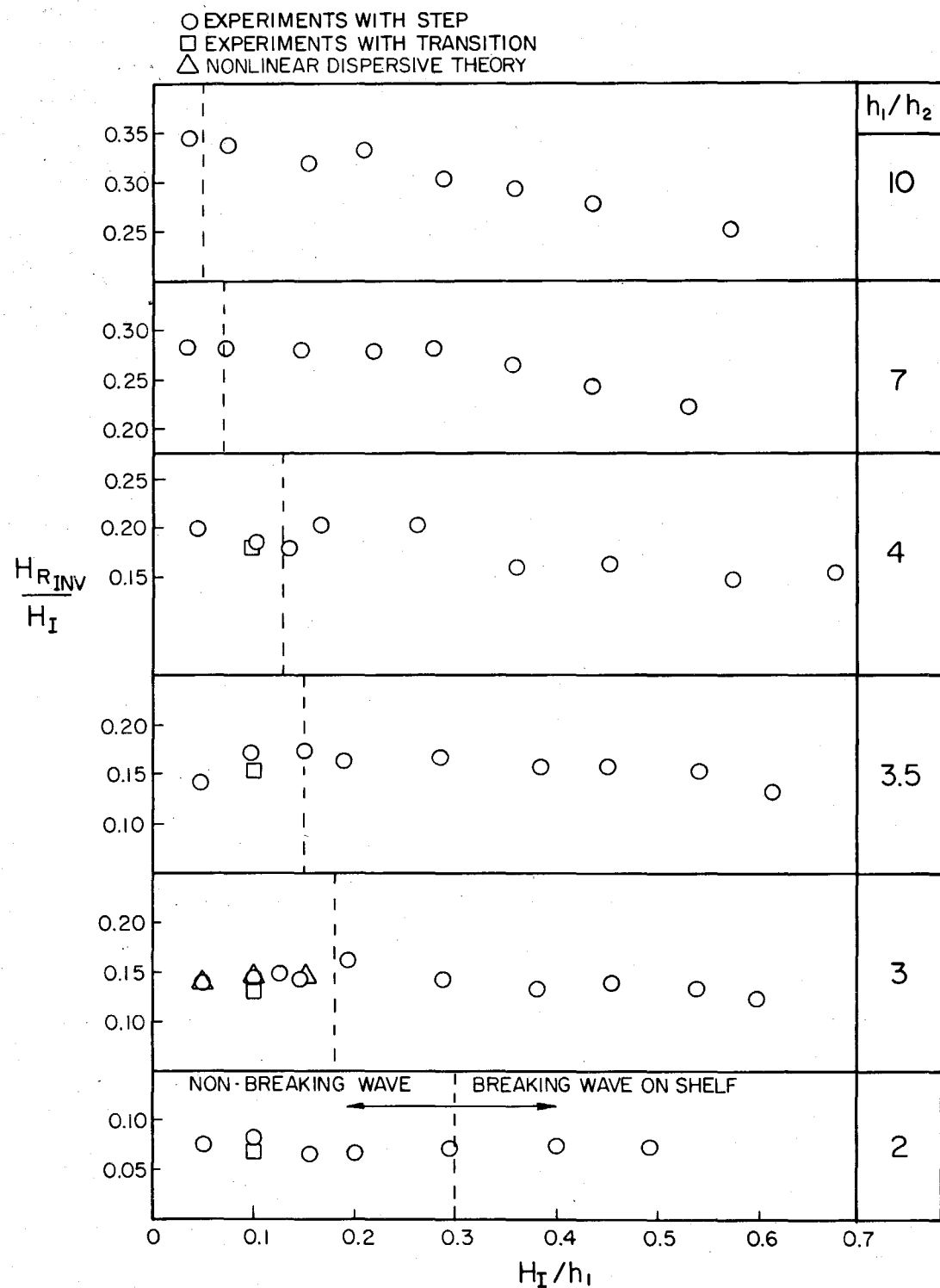


Fig. 5.28 Variation of the inverse scattered wave height ratio, $H_{R_{INV}}/H_I$, with the relative incident wave height, H_I/h_1 .

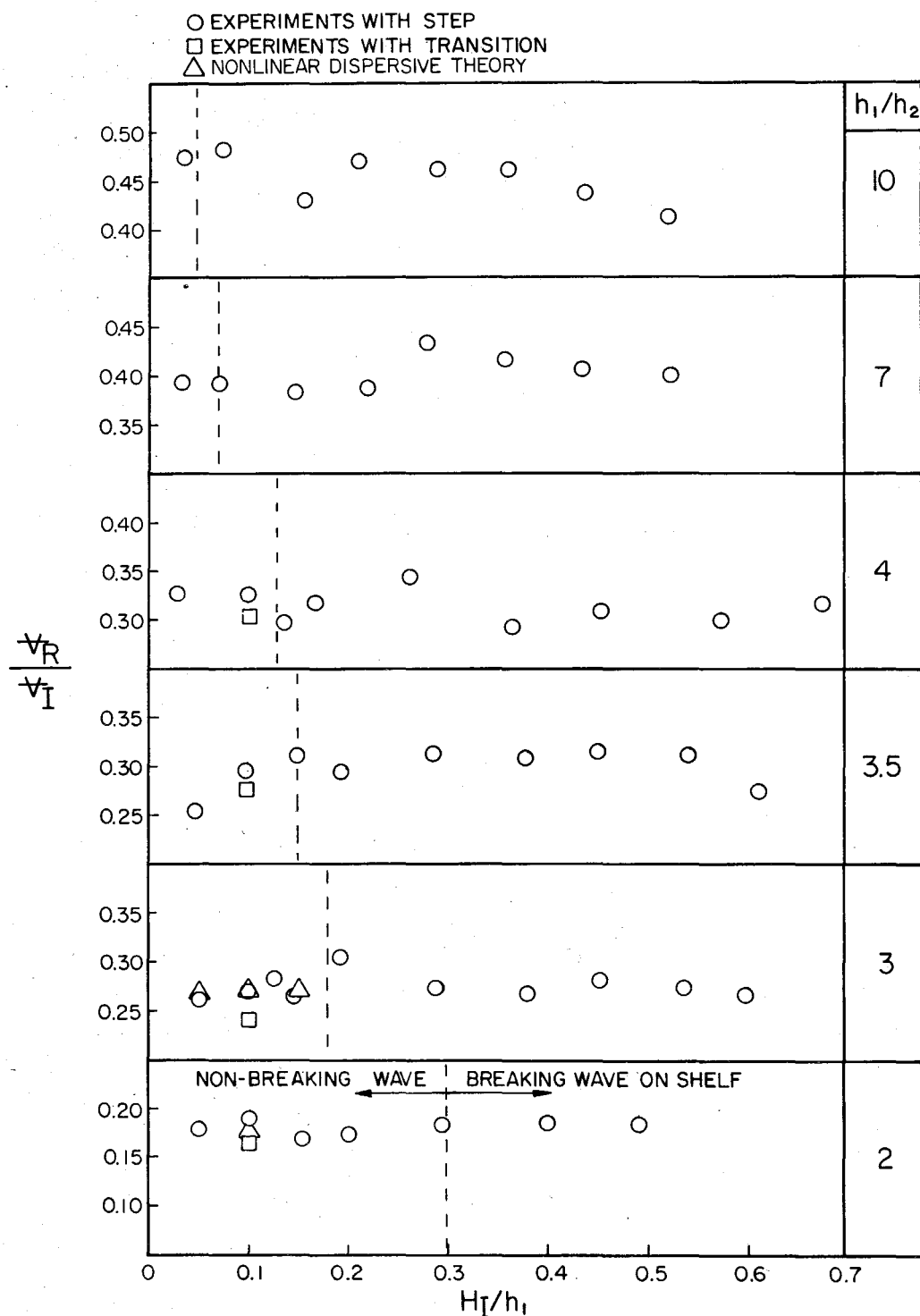


Fig. 5.29 Variation of the volume ratio, V_R/V_I , with the relative incident wave height, H_I/h_1 .

is a solitary wave which propagates with constant shape, however this is not true for the propagation of the reflected wave from the step back to the gauge. Assuming the reflected wave at the step ($x = 0$) is given by Eq. (5.17), then computing the Ursell Number after Hammack (1974) Eq. (3.141) gives $U = 2.25 K_R$, i.e. less than the Ursell Number of a solitary wave ($U = 2.25$). Hence, the wave will change its shape as it propagates until one or more solitary waves emerge followed by a train of oscillatory waves. Since the gauge measuring the reflected wave is a finite distance (18-34 depths) from the step, dispersive and possibly nonlinear effects will occur and cause the reflected wave to be different in shape from that at the step. In addition, since the distance for complete separation into solitary waves is a function of the wave height, waves with different heights will be in different stages of evolution as they pass the wave gauge. Thus, the ratio of the reflected wave height to the incident wave height H_R/H_I will be a function of the distance from the step and, therefore, dependent on the incident wave height. A solution of this problem would be to measure the reflected wave a large distance from the step after the separation process has taken place. This is not practical first because the length of the flume is limited and second because friction causes a reduction in the wave height. However, propagation to infinity in the absence of friction can be performed analytically by the method of inverse scattering discussed in Section 3.5. As was shown in Section 3.5, from a wave with the form of Eq. (5.17) one solitary wave emerges

with the height given by:

$$H_{R_{INV}} = \frac{1}{4} H_I \left\{ (1 + 8K_R)^{\frac{1}{2}} - 1 \right\}^2, \quad (5.19)$$

where K_R is the reflection coefficient from the linear nondispersive theory, Eq. (3.113). Hence, using the inverse scattered height of the reflected wave, $H_{R_{INV}}$, computed from the record of a wave gauge located at some position upstream of the step, the dependence of the results on the actual position of the gauge will be eliminated.

In addition, if the linear nondispersive theory accurately describes the reflection process at the step, from Eq. (5.19) there will be no variation of wave height ratio $H_{R_{INV}}/H_I$ with incident wave height.

The results of this analysis for the experiments plotted in Fig. 5.27 are presented in Fig. 5.28 where the wave height ratio $H_{R_{INV}}/H_I$ is plotted as a function of the incident wave height to depth ratio H_I/h_1 . The difference between Figs. 5.27 and 5.28 is quite marked in that most (but not all) of the variation of the wave height ratio with relative incident wave height has been removed, particularly for small relative wave heights and small depth ratios. In fact, for incident wave heights $H_I/h_1 < 0.3$ and depth ratios $h_1/h_2 \leq 7$ the data indicate no variation of the wave height ratio $H_{R_{INV}}/H_I$ with incident relative wave height H_I/h_1 . Hence, for these parameters the inverse scattered reflected wave height $H_{R_{INV}}$ is proportional to the incident wave height H_I as predicted by the linear nondispersive theory, Eq. (5.19).

For incident wave heights $H_I/h_1 > 0.3$ or depth ratios $h_1/h_2 > 7$ the variation of wave height ratio with incident wave height still occurs and since, by using inverse scattering, the propagation of the reflected wave back to the gauge is eliminated as the cause, it is concluded that the process at the step is not predicted by the linear nondispersive theory. An obvious reason for this is that for large wave heights or large depth ratios the wave breaks on the shelf close to the change in depth. In fact, using the linear nondispersive theory and the criterion that a wave will break if the height to depth ratio exceeds 0.7, the limiting relative incident wave height for a non-breaking wave on the shelf is:

$$\frac{H_I}{h_1} \leq 0.35 \frac{h_2}{h_1} \left(1 + \sqrt{\frac{h_2}{h_1}} \right) \quad . \quad (5.20)$$

The limiting relative incident wave heights for the depth ratios considered here obtained from Eq. (5.20) are presented in Table 5.3. A comparison of the limiting wave heights in Table 5.3 with the range of wave heights in Fig. 5.28 for which the reflected wave height is independent of the incident wave height indicates the linear nondispersive theory predicts the correct behavior for some cases even though the wave may break on the shelf.

This feature of the problem is further illustrated in Fig. 5.29 where, for the 51 experiments under consideration, the ratio of the reflected to the incident volumes of the waves, V_R/V_I , is plotted as a function of the relative incident wave height, H_I/h_1 . The volume

Table 5.3 Maximum relative incident wave heights for non-breaking waves on the shelf as predicted by the linear nondispersive theory.

h_1/h_2	2.	3.	3.5	4.	7.	10.
H_I/h_1	0.30	0.18	0.15	0.13	0.07	0.05

ratio appears independent of incident wave height for all depth ratios and even for waves which obviously break onto the shelf. Hence, the reflected volume appears to be a linear function of the incident volume, as predicted by linear nondispersive theory.

Included in Figs. 5.27 to 5.29 are data from experiments in which the step was replaced by the half-sine transition described in Section 4.1. These data lie close enough to the data for the step to imply the transition has no effect on the reflected wave.

The finite element numerical scheme described in Section 3.3 also was used to determine the waves reflected from a step. However, it was found the reflected waves were dependent on the incident wave height, an effect the physical experiments do not predict and an effect which did not occur when a slope instead of a step was used (this will be discussed in more detail in Section 3.2.3). Hence, it was concluded, the approximation used to match flow rates across a step, which was described in Section 3.3.2, caused errors in the numerical scheme in this case. To avoid this, the numerical scheme was used with the step replaced by the half-sine transition. This change, the physical experiments show, has essentially no effect on

the reflected wave, but it reduces the error given by Eq. (3.104) by reducing the change in depth between the elements, Δh . The effect of this is shown in Figs. 5.28 and 5.29 where for a depth ratio of $h_1/h_2 = 3$ and relative incident wave heights of $H_I/h_1 = 0.05, 0.10$ and 0.15 , the reflection coefficients calculated by the finite element scheme are the same for all three wave heights.

As was mentioned earlier, the experiments were conducted in two sets. The experiments described so far comprise the first set in which the variation with wave height was examined. The second set of experiments involved keeping the relative incident wave height constant and varying the depth ratio to determine the behavior with depth ratio. The experiments were arranged in the same manner as for the first set with adjacent gauges placed 5.7 m from the plate; one adjusted to measure the incident wave and the other adjusted with increased sensitivity to measure the reflected wave. The relative incident wave height was fixed nominally at $H_I/h_1 = 0.10$ and all the waves were within: $0.090 < H_I/h < 0.103$. Initially fourteen experiments were conducted with depth ratios in the range: $1.51 \leq h_1/h_2 \leq 68.4$; for $h_1/h_2 = 68.4$ the depth on the shelf was 0.19 cm. To determine if there was any dependence on the height of the shelf, two subsequent sets of experiments were conducted with shelves of smaller height. For the first set the shelf-height was 5.97 cm and the waves were measured at gauges located 3.0 m from the step. For the second set, the shelf-height was 5.68 cm and the waves were measured with gauges located 2.08 m from the step. (This latter set of experiments is

equivalent to those with the 15.54 cm step because the wave gauges were placed the same number of shelf-heights from the step.) The results in the form of the ratios of reflected to incident measured quantities: wave height H_R/H_I , inverse scattered wave height $H_{R_{INV}}/H_I$ and volume V_R/V_I are plotted as functions of depth ratio h_1/h_2 in Figs. 5.30 to 5.32. The curves in each of these figures represent the linear nondispersive theory. For Figs. 5.30 and 5.32 this is given by Eq. (3.113) which is the reflection coefficient for a step. For Fig. 5.31 the curve is given by Eq. (3.145) and also Eq. (5.19) which gives the ratio of the inverse scattered reflected wave height to the incident wave height, $H_{R_{INV}}/H_I$.

For all three plots, the data lie below the theoretical curves and the distance below increases with increasing depth ratio h_1/h_2 . One reason for this is that from the equation which predicts approximately the conditions for breaking onto the shelf, Eq. (5.20), the maximum depth ratio for an incident wave of height $H_I h_1 = 0.1$ to be a nonbreaking wave is $h_1/h_2 = 5$. Therefore the linear nondispersive theory would not be expected to predict accurately the reflected wave for depth ratios $h_1/h_2 > 5$, and the data do seem to depart more from the theory for $h_1/h_2 > 5$. Friction also is a cause of the wave height data lying below the theoretical curve but accounting for its effects only slightly increases the wave height ratios (by from 4% for $h_1/h_2 = 1.5$ to 11% for $h_1/h_2 = 60$) and this does not bring the data up to the theoretical curve. In addition, in Fig. 5.32, which shows the reflected volume ratio, the data are not affected by friction but

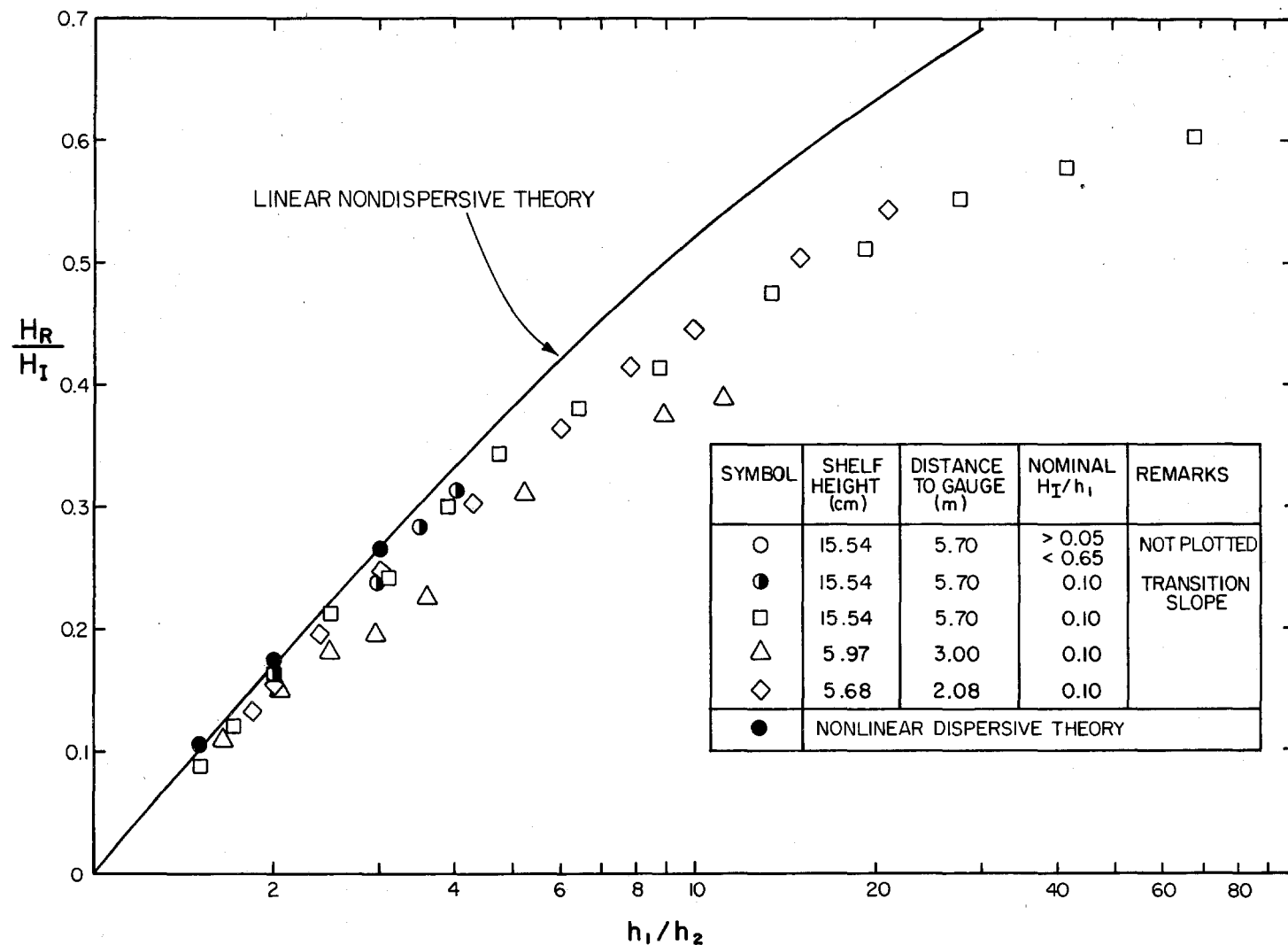


Fig. 5.30 Variation of the wave height ratio, H_R/H_I , with depth ratio, h_1/h_2 .

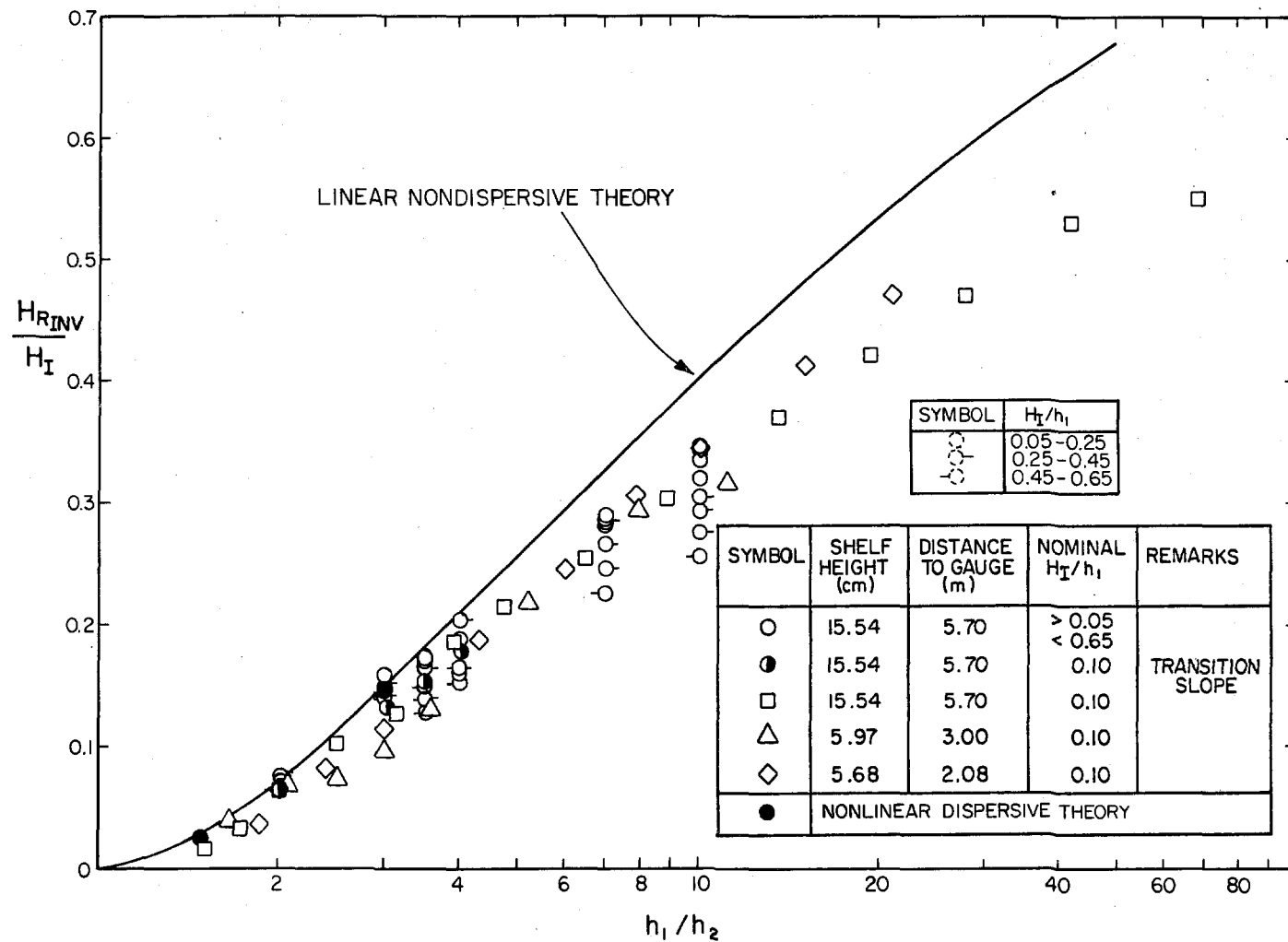


Fig. 5.31 Variation of the inverse scattered wave height ratio, $H_{R_{INV}} / H_I$, with depth ratio, h_1 / h_2 .

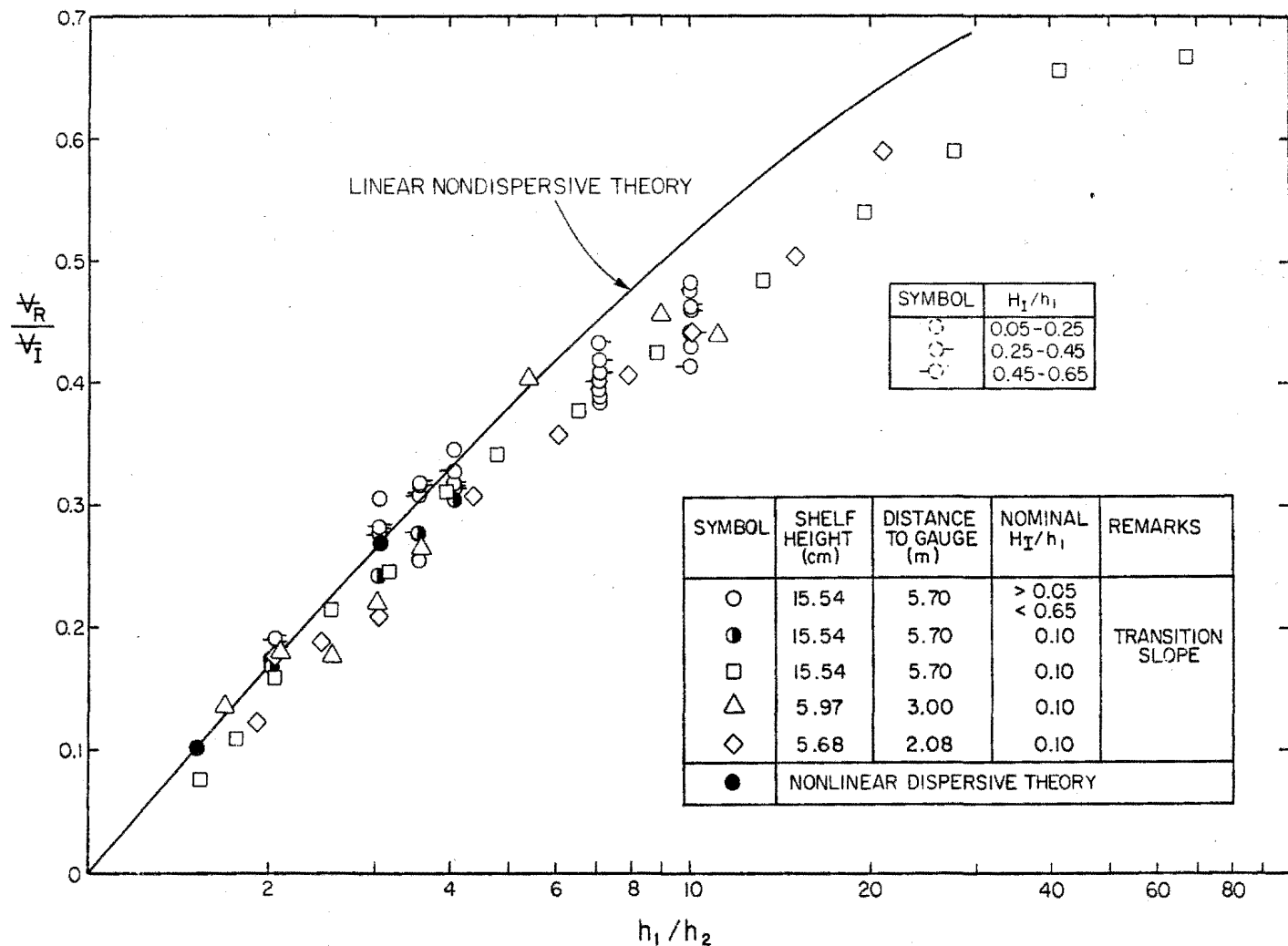


Fig. 5.32 Variation of the volume ratio, V_R/V_I , with depth ratio, h_1/h_2 .

still tend to be below the theoretical curve.

In Figs. 5.31 and 5.32 the data from the four different sets of experiments fit together well indicating there is no dependence on shelf-height. However, in Fig. 5.30, which shows the measured wave height ratio H_R/H_I , the data from the experiments with the 5.97 cm shelf placed 3.0 m from the gauge are generally less than the other data. The reason for this is that the distance from the step to the gauge for this set of experiments was 50.25 shelf-heights whereas the distance for the other experiments was 36.68 shelf-heights; thus, for the former, the wave had travelled further and dispersive and perhaps nonlinear effects had more time to develop. Notice that this tendency is substantially reduced in Fig. 5.31 which shows the inverse scattered wave height ratio $H_{R_{INV}}/H_I$.

Also included in Figs. 5.30 to 5.32 are the data from four experiments in which the half-sine transition instead of the step was used. The data show no difference from the data obtained when the step was used.

The results for the nonlinear dispersive theory, calculated using the finite element scheme with the half-sine transition, coincide with the linear nondispersive theory in Figs. 5.30 to 5.32. Thus, from this and from the experiments conducted, it may be concluded for depth ratios of $h_1/h_2 \leq 10$ the reflection of solitary waves from a step is a linear process, apart from the propagation and the reflected wave may be approximately predicted by the linear nondispersive theory.

5.2.2 The Reflection of Cnoidal Waves from a Step

Experiments conducted to measure the waves which are reflected when cnoidal waves propagate over a step onto a shelf require a different laboratory technique than that used if the waves were small amplitude, harmonic waves. In the latter case a standard procedure is to deduce the reflected waves from the combined incident and reflected waves using the principle of superposition. However for cnoidal waves, which propagate in accordance with the nonlinear dispersive theory, the principle of superposition is not valid, therefore an alternative method must be devised. The technique used in this study was to generate a finite number of cnoidal waves and measure the incident and reflected waves at a point in the flume where the trailing edge of the incident wave group had passed before the leading edge of the reflected wave group arrived. The method has two conflicting requirements:

(i) The wave group must contain a sufficient number of waves so that the waves in the center of the group where measurements will take place are not affected by transient effects at the leading and trailing edges of the wave group.

(ii) The wave group must be short enough that the incident and reflected wave groups are separated at the point of measurement.

As was demonstrated earlier (see Section 5.1.2), for short distance propagation, the requirement that transient effects do not affect the waves in the center of the packet may be satisfied by a group consisting of as few as four waves. Thus, the procedure used

here was to place the wave gauges midway between the wave generator and the step and to generate as many waves as possible (four or greater) but still satisfy the requirement that incident and reflected wave packets be separate at the point of measurement.

To illustrate the experimental details, the results of five experiments, in the form of the wave amplitude--time history are presented in Fig. 5.33, where the ordinate is the wave amplitude normalized with respect to the depth, and the abscissa is the non-dimensional time $t\sqrt{g/h_1}$. The experiments were conducted using the 15.54 cm shelf with the step situated 23.84 m from the wave generator and the wave gauge which gave the records presented in Fig. 5.29 situated midway between the step and the wave generator (i.e., 11.92 m from both). For each experiment, four waves were generated using trajectory CN4 with a stroke $S/h_1 = 0.378$ and a period $T\sqrt{g/h_1} = 27.2$, which theoretically should have produced waves with a relative height of $H/h_1 = 0.1$. The five experiments were performed with five different upstream depths and consequently five different depth ratios. The four waves to the left in each part of Fig. 5.33 are those which comprise the incident wave group; the four to the right in each part comprise the reflected waves. Progressing down the figure, the depth upstream of the step, h_1 , increases and, consequently, the depth ratio, h_1/h_2 , decreases as does the distance of the gauge from the step expressed as the number of depths, x/h_1 . The decreasing depth ratio, h_1/h_2 , produces reflected waves of smaller height; the decreasing relative distance, x/h_1 , causes the time between incident and reflected

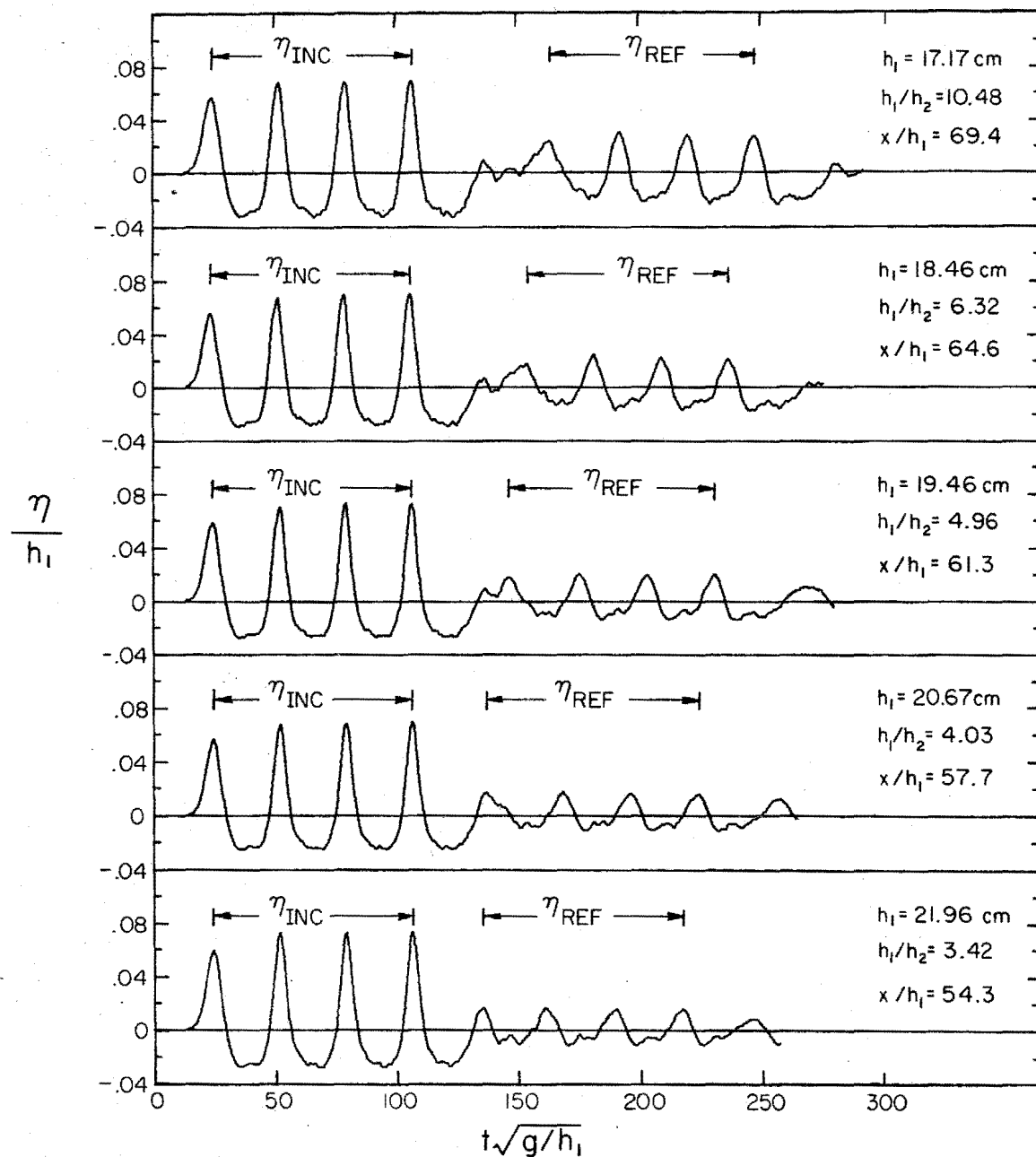


Fig. 5.33 Incident cnoidal waves ($H_1/h_1 = 0.1$, $T\sqrt{g/h_1} = 27.2$) and the waves reflected from the step for various depths.

wave packets also to decrease. Close inspection of Fig. 5.33 reveals that, for both incident and reflected waves, the amplitudes of the third and fourth crests are about equal, as are the second and third troughs. In addition to the constancy of period between the second, third and fourth crests for both incident and reflected waves, this indicates the transient effects at the leading and trailing edges of the wave group do not affect the central portion of the group, as was assumed previously. Figure 5.33 was introduced at this stage of the discussion for illustrative purposes; it will be discussed in more detail presently.

Using the arrangement just described, experiments were conducted for depth ratios: $h_1/h_2 = 3, 4, 7$ and 10 . The results are presented in Fig. 5.34 where the ratio of reflected to incident wave heights H_R/H_I is plotted as a function of the relative incident wave height H_I/h_1 . The numbers beside the points are the nondimensional quantity: $gH_I T^2/h_1^2$, which is a type of Ursell Number. It is used in preference to the Ursell Numbers described earlier (m and HL^2/h_1^3) because it can be calculated directly from experimentally measured quantities whereas the others must be deduced using complex numerical calculations. It is related to HL^2/h_1^3 by the celerity, $c = L/T$. The data exhibit scatter (some reasons for this will be presented shortly) but show no trend in the variation of reflection coefficient, H_R/H_I , with either the relative incident wave height, H_I/h_1 , or the Ursell Number, $gH_I T^2/h_1^2$. The dashed lines in the figure indicate the limiting wave height for a nonbreaking wave on the shelf as predicted by the linear

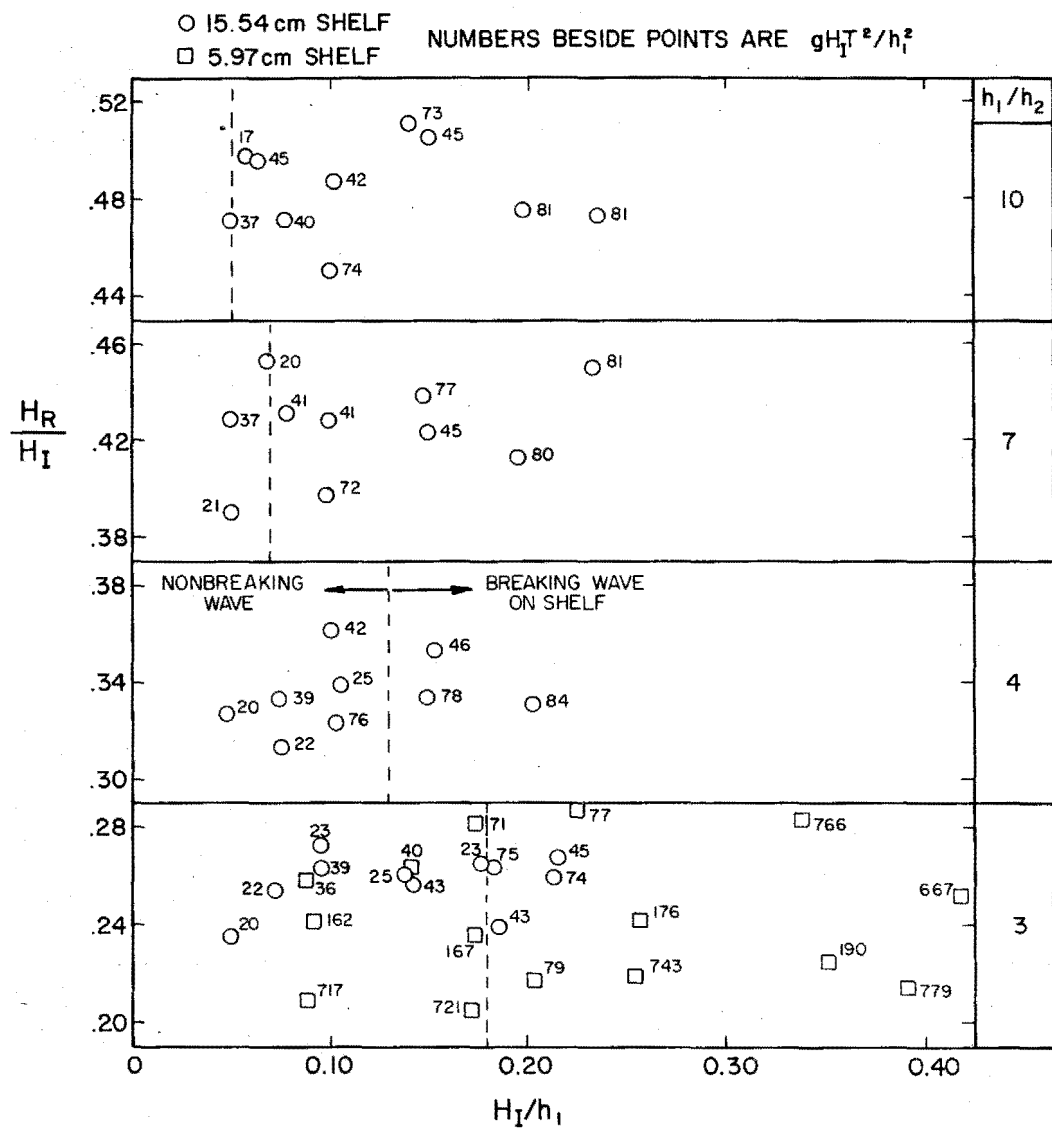


Fig. 5.34 Variation of the wave height ratio, H_R/H_I , with relative incident wave height, H_I/h_1 , for cnoidal waves.

nondispersive theory, Eq. (5.20).

Included in the figure are data from experiments in which a shelf with a height of 5.97 cm was used. For these experiments the wave gauge measuring incident and reflected waves was placed the same relative distance, x/h_1 , from the step as the equivalent experiments with the 15.54 cm shelf, i.e., $x/h_1 = 51$ for the depth ratio $h_1/h_2 = 3$. In Fig. 5.34, the data generally lie below the data for the 15.54 cm shelf and this is attributed to the increased effect of friction for the smaller depth.

In Fig. 5.35 the ratio of reflected to incident wave heights, H_R/H_I , is plotted as a function of the depth ratio, h_1/h_2 . The curve was obtained from the linear nondispersive theory (as given by Eq. (3.113)). The data were obtained from the experiments previously described and from experiments in which the relative incident wave height and period were set at $H_I/h_1 = 0.1$ and $T\sqrt{g/h_1} = 27.2$ and the depth, h_1 , was changed. The data follow the trend of the linear nondispersive theory but the reflection coefficient is generally less than theory predicts as was found to be true also for solitary waves. Part of the reason for this is, of course, the effect of friction first on the incident waves as they propagate the 11.92 m from the gauge to the step and second on the reflected waves as they propagate the same distance from the step back to the gauge. However, a more important effect is the change in shape of the reflected waves as they propagate, due to amplitude and frequency dispersion.

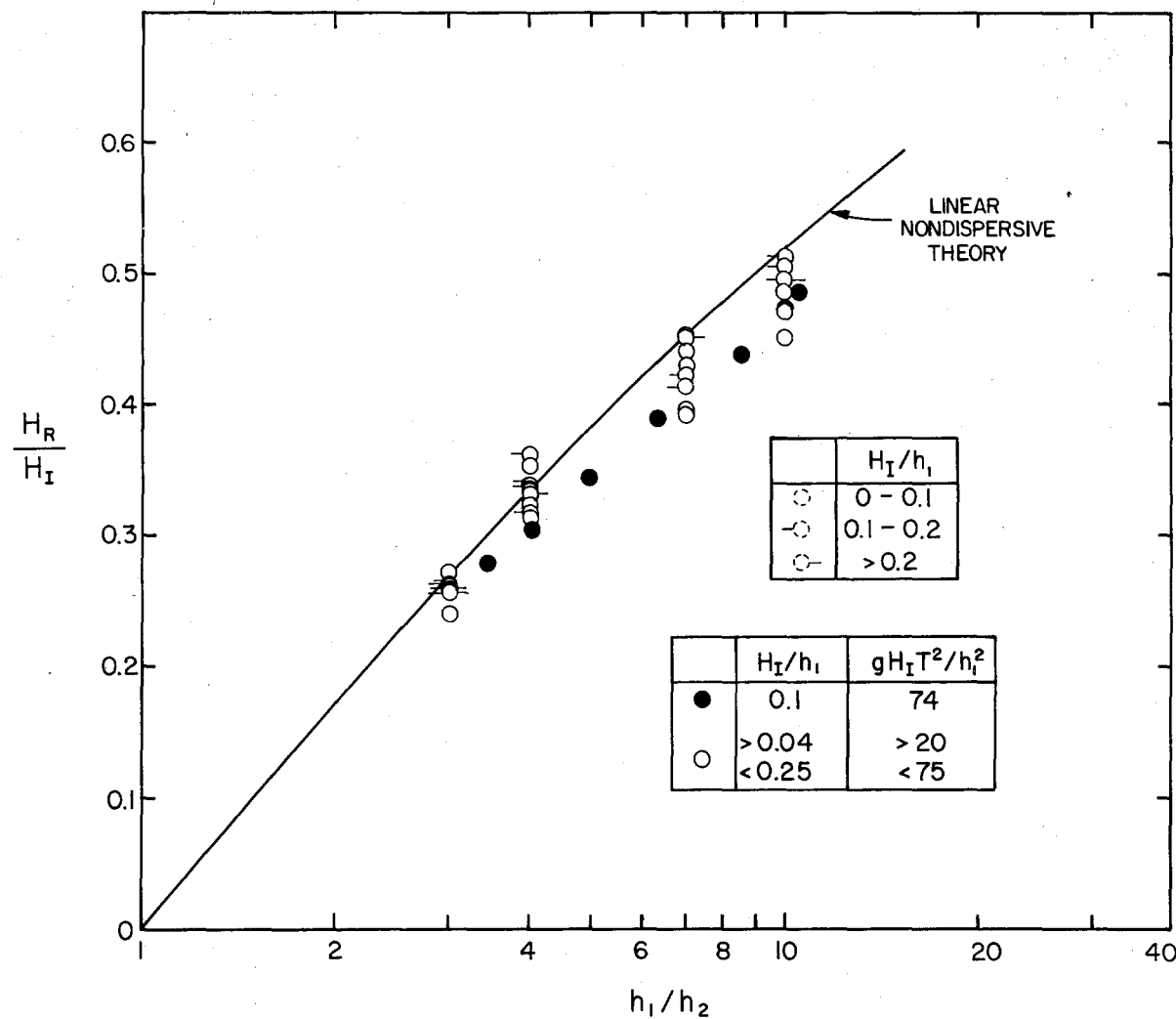


Fig. 5.35 Variation of the wave height ratio, H_R/H_I , with depth ratio, h_1/h_2 , for cnoidal waves.

This effect was examined for five of the seven experiments represented by solid circles in Fig. 5.35 (for which, it will be recalled, the nominal incident wave height was $H_I/h_1 = 0.1$ and the period was $T\sqrt{g/h_1} = 27.2$). These are the five records which were presented previously in Fig. 5.33 and now will be considered in detail. The linear nondispersive theory predicts the reflected waves will have the same shape as the incident waves and will retain this shape as they propagate. Examination of Fig. 5.33, however, indicates the crests of the reflected waves are only approximately symmetric, tending to be steeper on the back face of the wave than on the front face. In addition, the troughs exhibit secondary waves which vary from experiment to experiment. Hence the linear nondispersive theory appears to be invalid for some portion of the time between the time the incident waves leave the gauge and the time when the reflected waves reach it. The obvious region where the linear nondispersive theory does not apply is in the propagation of the reflected waves from the step back to the gauge.

For solitary waves, this effect was accounted for by propagating the reflected waves to infinity in an analytical manner using inverse scattering.

For cnoidal waves, to investigate the effect of amplitude and frequency dispersion, the following analysis was performed. First, the incident wave group was assumed to propagate without change of shape to the step. Second, the linear nondispersive reflection coefficient (Eq. (3.113)) was applied to the incident wave group to give

the theoretical reflected wave group. Thus, the shape of the reflected wave group at the step was assumed to be identical to that of the incident wave group. Finally, this reflected wave group was propagated numerically the 11.92 m back to the wave gauge by: (i) the linear dispersive theory using a Fourier transform method, and (ii) the KdV equation using Peregrine's finite difference scheme (from Peregrine (1966)). The latter was used in preference to the numerical scheme developed for this study because the waves were travelling in one direction only. The results are compared with the wave gauge record from Fig. 5.33 in Figs. 5.36 and 5.37 which are arranged in a similar manner to Fig. 5.33, with the normalized amplitude, n/h_1 , plotted as a function of the nondimensional time, $t\sqrt{g/h_1}$. The five reflected wave groups from Fig. 5.33 are represented by the solid curves and the theoretical results are represented by the dashed curves. In Fig. 5.36 which shows the linear dispersive theory compared with experiment, the theory predicts the reflected waves quite well for small depth ratios but as the depth ratio increases the reflected waves are more peaked than this theory predicts. The reason for this is the experimental Ursell Number, $gH_R T^2/h_1^2$, increases with depth ratio because the reflected wave height increases. Therefore, since the Ursell Number is a ratio of nonlinear to linear effects, the nonlinear effects are greater for larger depth ratios than for smaller depth ratios and consequently the linear dispersive theory is less likely to be applicable to large depth ratios. The veracity of this is illustrated by Fig. 5.37 where the nonlinear

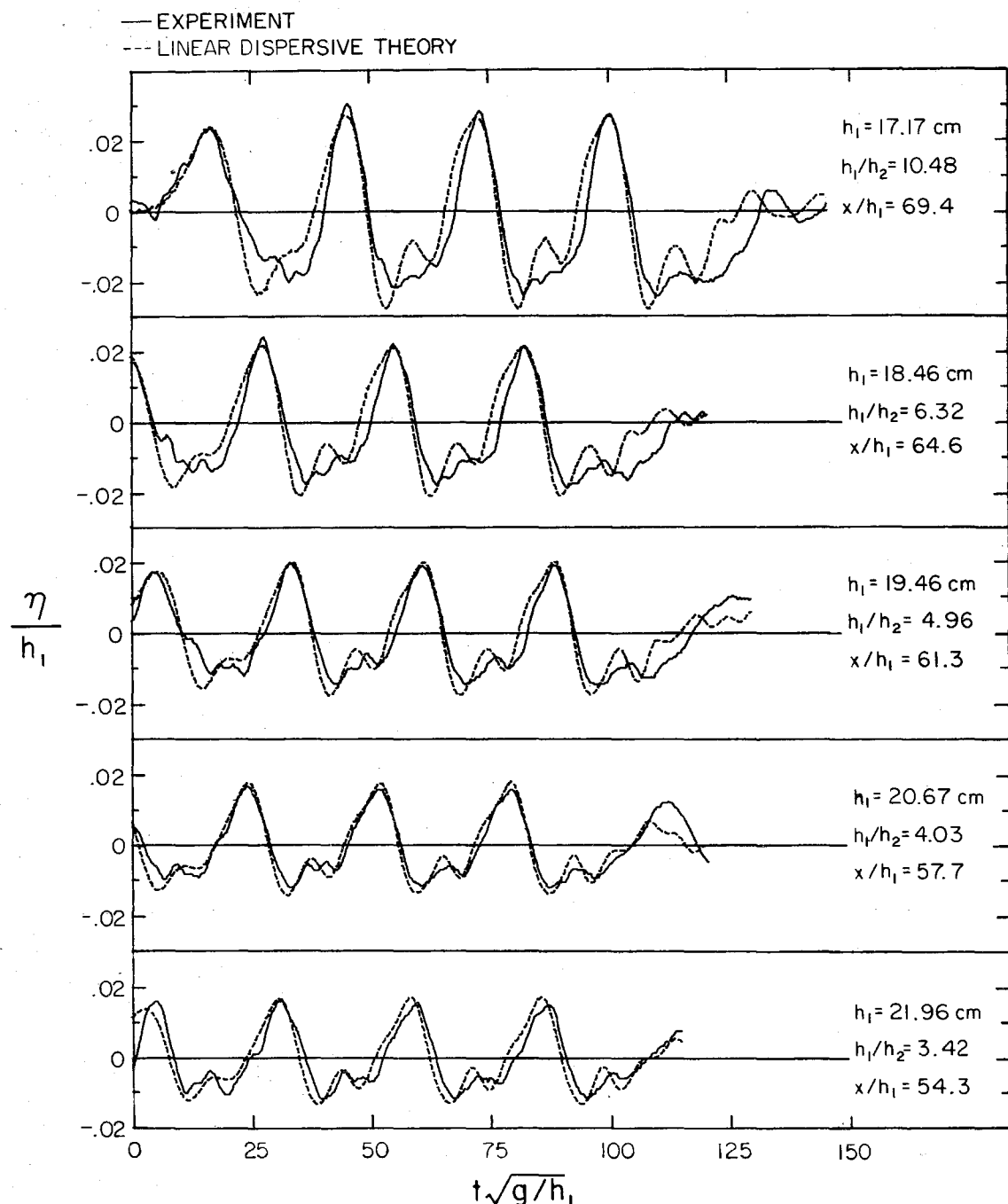


Fig. 5.36 Comparison of the experimental reflected cnoidal waves with those calculated from the linear dispersive theory.

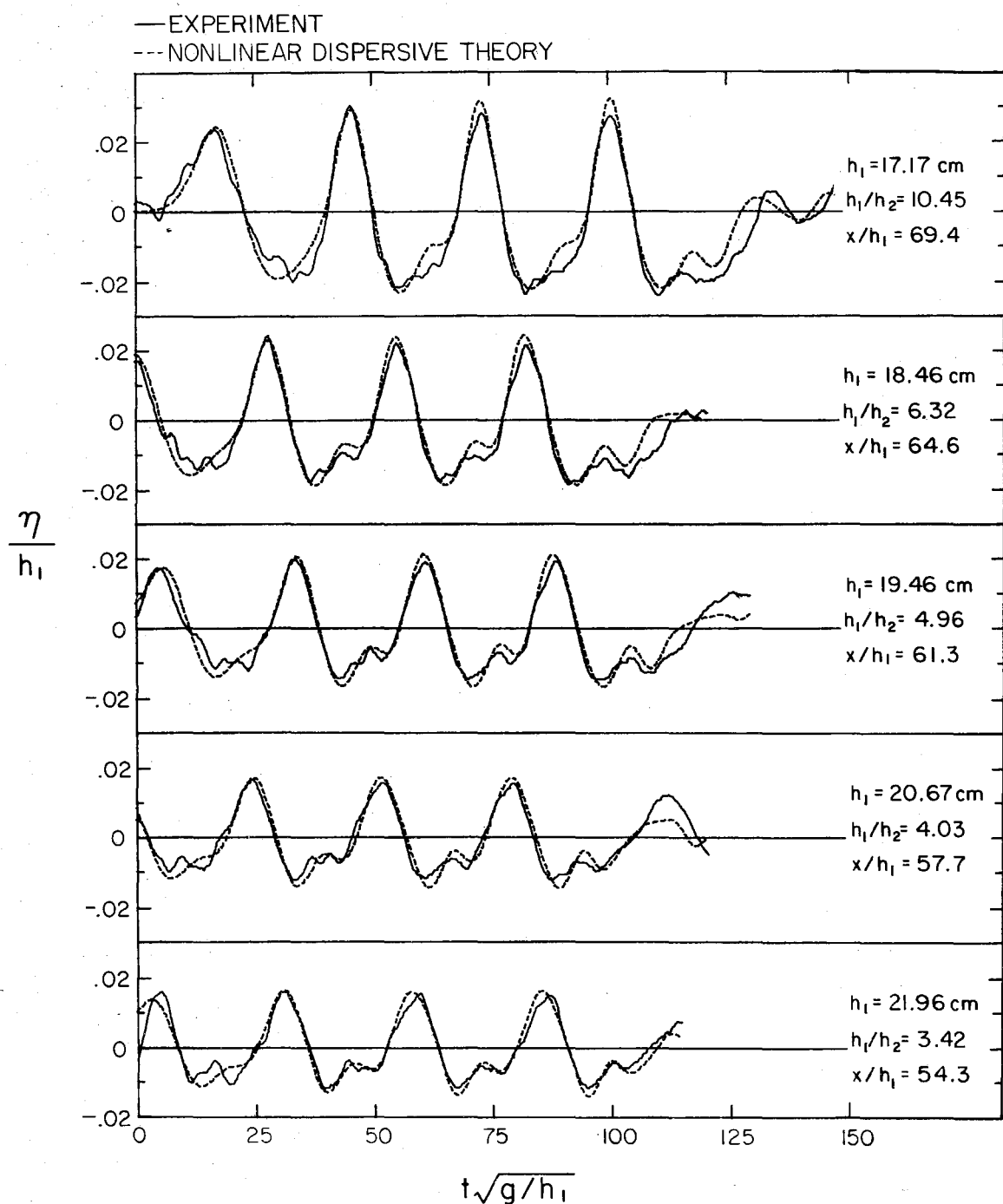


Fig. 5.37 Comparison of the experimental reflected cnoidal waves with those calculated from the nonlinear dispersive theory.

dispersive theory is compared with experiment. Here the agreement between theory and experiment is good, with even the secondary crests in the troughs predicted by the theory. The only difference between the theories in Figs. 5.36 and 5.37 is the inclusion, in the latter, of the nonlinear term. The good agreement between the theory and the experiments for the larger depth ratios is somewhat surprising considering, as was determined earlier, the wave breaks on the shelf for depth ratios $h_1/h_2 > 5$.

Recall that some of the data presented earlier in Fig. 5.35 were from the reflected waves shown in Figs. 5.36 and 5.37. In Fig. 5.35, the wave height ratio, H_R/H_I , is plotted as a function of depth ratio and the data are compared with the linear nondispersive theory. However, the comparison does not appear as good there as it does in Figs. 5.36 and 5.37. The reason for this is that the wave height, which is defined as the difference between the maximum and the minimum amplitudes, is a measure only of the extremes of the wave whereas Figs. 5.36 and 5.37 give the shape also.

The wave height ratios from the three theories and from the five experiments being considered are listed in Table 5.4. The wave heights were taken from the third wave in the group in each case.

The table shows the three theories predict essentially the same wave height ratio which is up to 10% greater than the experiments. The difference between the experiments and the theories is attributed to dissipative effects which are not included in the theories. Although the theories agree in the height of the reflected waves,

Table 5.4 Wave height ratios for experiments, (H_R/H_I) _{Expt}, linear nondispersive theory, (H_R/H_I) _{L.N.}, linear dispersive theory, (H_R/H_I) _{L.D.}, and nonlinear dispersive theory, (H_R/H_I) _{N.D.}

h_1/h_2	(H_R/H_I) _{Expt}	(H_R/H_I) _{L.N.}	(H_R/H_I) _{L.D.}	(H_R/H_I) _{N.D.}
10.48	0.510	0.528	0.529	0.529
6.32	0.406	0.431	0.429	0.434
4.96	0.337	0.380	0.376	0.381
4.03	0.289	0.335	0.331	0.339
3.42	0.277	0.298	0.302	0.298

the theories predict different shapes for the reflected waves. This can be seen by comparing the dashed curves in Fig. 5.36 which show the linear dispersive theory with those in Fig. 5.37 which show the nonlinear dispersive theory. The shape of the reflected waves predicted by the linear nondispersive is the same as that of the incident waves shown in Fig. 5.33.

Thus, the experiments conducted here, as was found for solitary waves, indicate the reflection process is linear and governed by the linear nondispersive theory. However, the propagation of the reflected waves requires a higher order theory in order to accurately determine the shape of the waves.

5.2.3 The Reflection of Solitary Waves from a Slope

In this section the results from two theories and from experiments will be presented. The theories are: the linear nondispersive theory, which was solved by the Fourier transform method described in Section 3.4, and, the nonlinear dispersive theory, which was solved by the finite element method described in Section 3.3.

The parameters involved in the problem of reflection of solitary waves from a slope in the absence of friction are:

- the upstream depth, h_1 ;
- the downstream depth, h_2 ;
- the slope length, L ;
- the incident wave height, H_I ; and
- the reflected wave height, H_R .

The characteristic horizontal length of the wave, ℓ , in general also is a parameter but for the particular case of solitary waves ℓ is a function of only the incident wave height and the upstream depth as given by Eq. (3.122) (i.e., $\ell = 1.5 (H_I/h_1)^{-\frac{1}{2}} h_1$). The problem has five variables and one dimension; hence, using the Buckingham π theorem, there are four dimensionless groups:

$$\frac{H_R}{H_I} = f\left(\frac{h_1}{h_2}, \frac{L}{\ell}, \frac{H_I}{h_1}\right) \quad . \quad (5.21)$$

That is, the reflected wave height ratio, $\frac{H_R}{H_I}$, is a function of the depth ratio h_1/h_2 , the length ratio L/ℓ and the incident wave height

to depth ratio H_I/h_1 . For both the experiments and the nonlinear dispersive theory, the reflected wave height ratio, H_R/H_I , is a function of all three of these parameters, but for the linear nondispersive theory it is a function of only the depth ratio and the length ratio. Hence, the results of the linear nondispersive theory are presented first and, with corresponding experimental data, the results of the nonlinear dispersive theory will be presented later.

It is recalled from Section 3.4 that the method used to solve the problem using the linear nondispersive theory is a Fourier transform method in which the incident wave is transformed into the frequency domain and the reflection coefficient, which is a function of frequency, is applied to each frequency component of the incident wave in turn. The resultant reflected wave is obtained by the synthesis of these components. In addition, it was shown in Section 3.4, using the dimensionless frequency $\omega L/\sqrt{gh_1}$, the Fourier transform of a solitary wave for the purposes of the analysis may be considered to be a function of the length ratio, L/λ , and the frequency, $\omega L/\sqrt{gh_1}$, while the reflection coefficient is a function of the depth ratio, h_1/h_2 , and the frequency, $\omega L/\sqrt{gh_1}$. This is illustrated in Fig. 5.38(a) and (b).

Figure 5.38(a) shows the Fourier transform of the incident solitary wave, as given by Eq. (3.131), with the amplitude normalized with respect to the amplitude at $\omega = 0$, $A_1(\omega)/A_1(0)$, plotted as a function of the nondimensional frequency $\omega L/\sqrt{gh_1}$. The curves, which are for various length ratios, L/λ , evidently have similar shape but rolloff

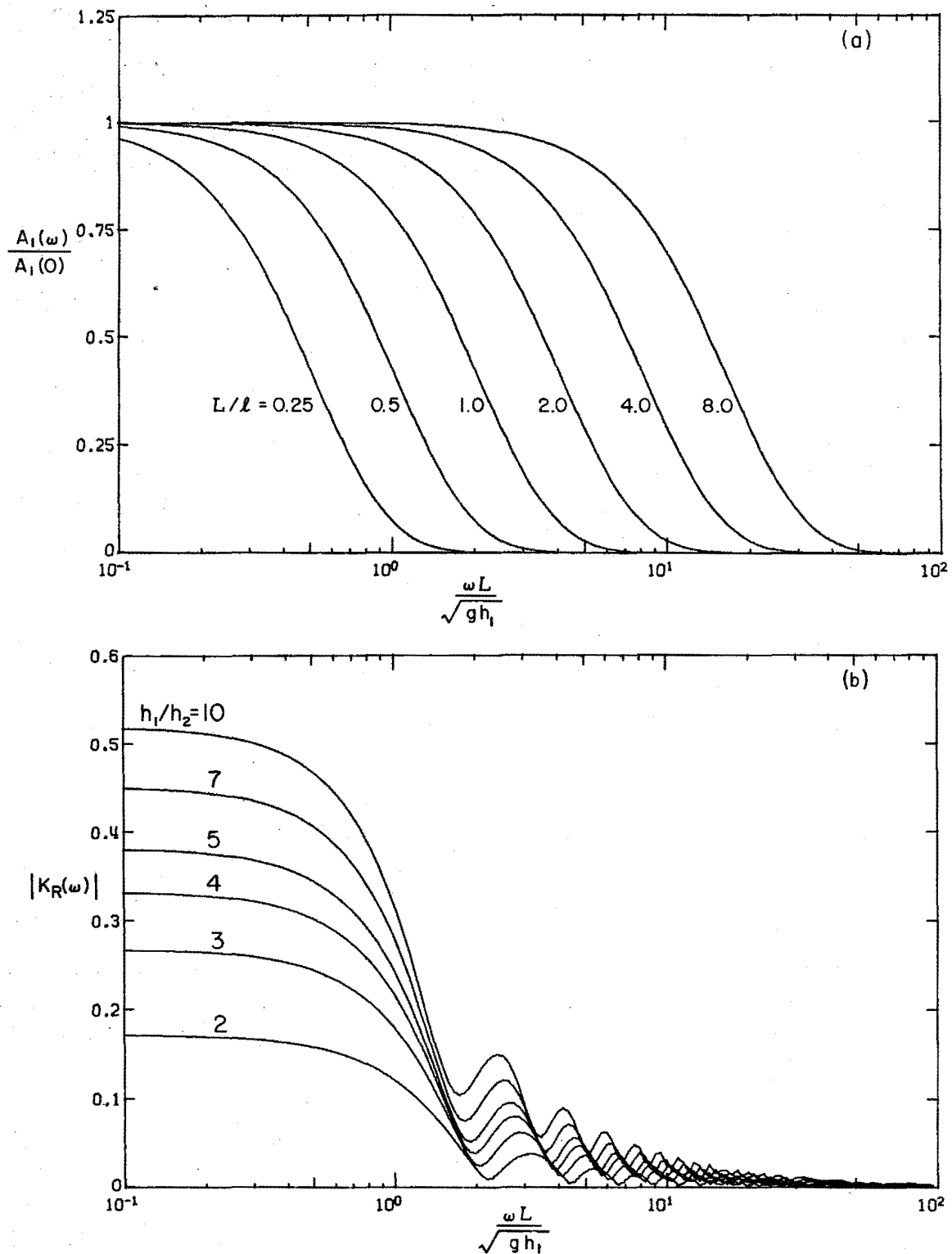


Fig. 5.38 Theoretical variation of (a) the Fourier transform of a solitary wave and (b) the reflection coefficient with frequency.

from unity at different frequencies which are a linear function of the length ratio (e.g. $A_1(\omega)/A_1(0) = 0.95$ occurs at $\omega L/\sqrt{gh_1} = 0.461 L/\ell$).

Figure 5.38(b) shows the modulus of the reflection coefficient, $|K_R(\omega)|$ (recall $K_R(\omega)$ in general is complex) plotted as a function of the nondimensional frequency $\omega L/\sqrt{gh_1}$. The curves, which are for various depth ratios, h_1/h_2 , have similar shape but are displaced from one another according to the magnitude of the reflection coefficient at $\omega = 0$.

Kajiwara (1961) presented curves similar to Fig. 5.38(b) but used as the abscissa L/L where L is the wave length of the harmonic wave under consideration. However, the abscissas are equivalent because using the relationship $L = \sqrt{gh_1} T$, the frequency $\omega L/\sqrt{gh_1}$ reduces to $2\pi L/L$. Kajiwara (1961) considered slopes in which the depth was a nonlinear function of the distance along the slope, whereas, in this study the depth was a linear function of distance along the slopes.

In principle, the process of calculating the reflected wave is to take the function describing a curve for a particular length ratio, L/ℓ , from Fig. 5.38(a) and multiply it by the function describing a curve for a particular depth ratio, h_1/h_2 , from Fig. 5.38(b). This gives the reflected wave in the frequency domain which can be transformed into the time domain by multiplying by $e^{-i\omega t}$ and integrating over the frequency range. (In practice, this procedure is performed numerically.)

Before presenting the results of these calculations, Fig. 5.38(a) and (b) can be used to deduce the overall behavior:

i) For small length ratios ($L/\ell < 1$) the majority of the Fourier transform curve lies in the frequency range $0 \leq \omega L / \sqrt{gh_1} \leq 10^{-1}$ where the reflection coefficient is essentially constant. Hence, the shape of the reflected wave is almost the same as that of the incident wave. A special case of this which already has been considered is when $L/\ell = 0$, i.e., a step.

ii) For large length ratios ($L/\ell > 1$) a considerable portion of the Fourier transform curve lies at frequencies $\omega L / \sqrt{gh_1} > 1$ where the reflection coefficient is essentially zero. Hence, when the multiplication of the two functions takes place, the high frequency components of the incident wave are reduced to zero and, since it is these high frequency components which affect the peakedness of the wave, the reflected wave is less peaked than the incident wave.

iii) Because the reflection coefficient curves are similar in shape but displaced vertically in Fig. 5.38(b), the shape of the reflected wave for a particular length ratio is almost independent of the depth ratio. However, the amplitude of the reflected wave for a particular length ratio is proportional to the reflection coefficient at $\omega = 0$ which is a function of the depth ratio.

The transition between the two extremes of length ratio described in i) and ii) above is illustrated in Fig. 5.39 where the reflected waves predicted by the linear nondispersive theory for a depth ratio of $h_1/h_2 = 3$ are plotted for length ratios of $L/\ell = 0, 0.25, 0.5, 1, 2$,

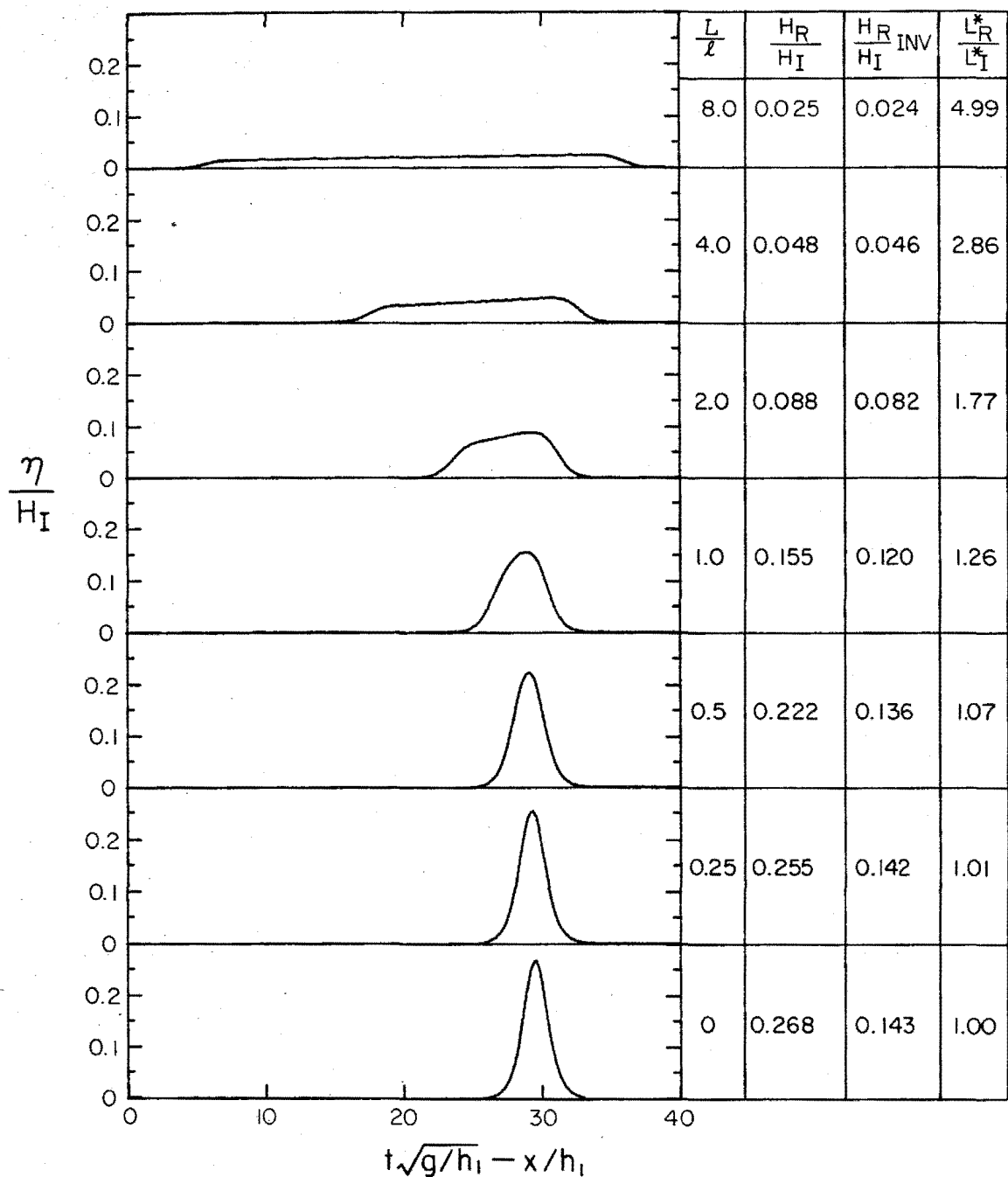


Fig. 5.39 The waves reflected when a solitary wave propagates up various slopes as predicted by the linear nondispersive theory.

4 and 8. In the table alongside the figure the quantities shown are as defined previously except for the length L^* which is defined as the distance between points in the wave where the ratio $n/H > 0.01$, i.e., the length occupied by the upper 99% of the wave; thus, L_R^*/L_I^* is the ratio of the length occupied by the upper 99% of the reflected wave to the corresponding length of the incident wave. The abscissa is $t\sqrt{g/h_1} - x/h_1$ which means the leading edge of the wave is towards the left in the plots (which can be thought of either as time records or as profiles with the wave moving to the left).

For $L/\ell < 1$ the shape of the reflected wave is similar to the shape of the incident wave and the slope can be thought of as relatively abrupt, since it does not affect significantly the shape of the wave. However, for length ratios greater than unity, the wave shape does change with the reflected wave taking the form of a "plateau" which slopes down towards the front of the wave. The higher amplitude near the rear of the wave indicates the proportion of the wave reflected increases as the wave climbs the slope.

The similarity of reflected waves for a particular length ratio but various depth ratios as discussed previously is illustrated in Fig. 5.40 which shows the reflected wave height ratio H_R/H_I plotted as a function of the length ratio, L/ℓ , for various depth ratios, h_1/h_2 . The curves in Fig. 5.40 appear to have similar shape and, in fact, can be collapsed almost to a single curve by normalizing the reflected wave height, $H_R(L/\ell)$, with respect to the reflected wave height for a step, $H_R(0)$, as shown in Fig. 5.41. Hence, for this linear

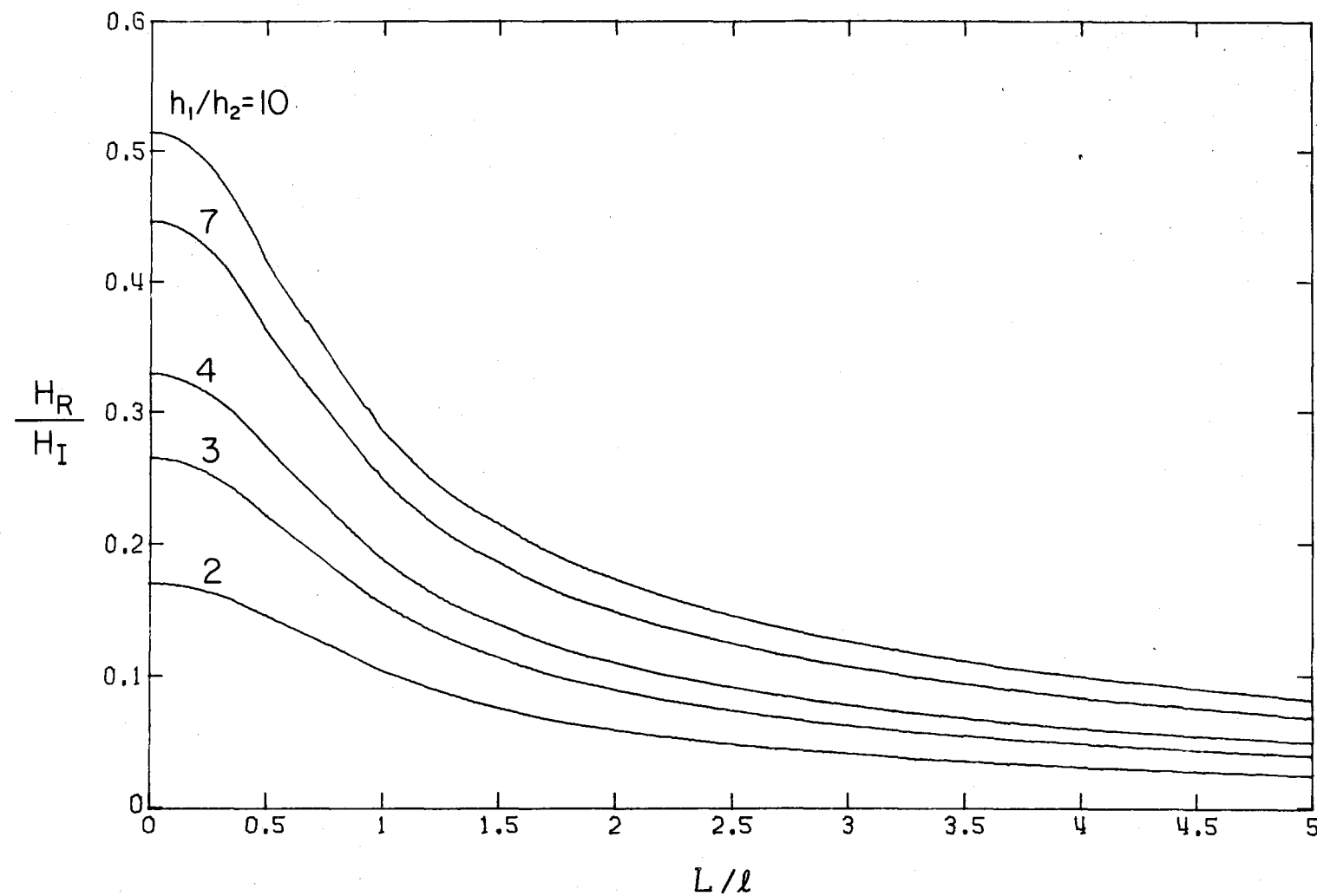


Fig. 5.40 Variation of the reflected wave height ratio, H_R/H_I , with length ratio, L/ℓ , as predicted by the linear nondispersive theory.

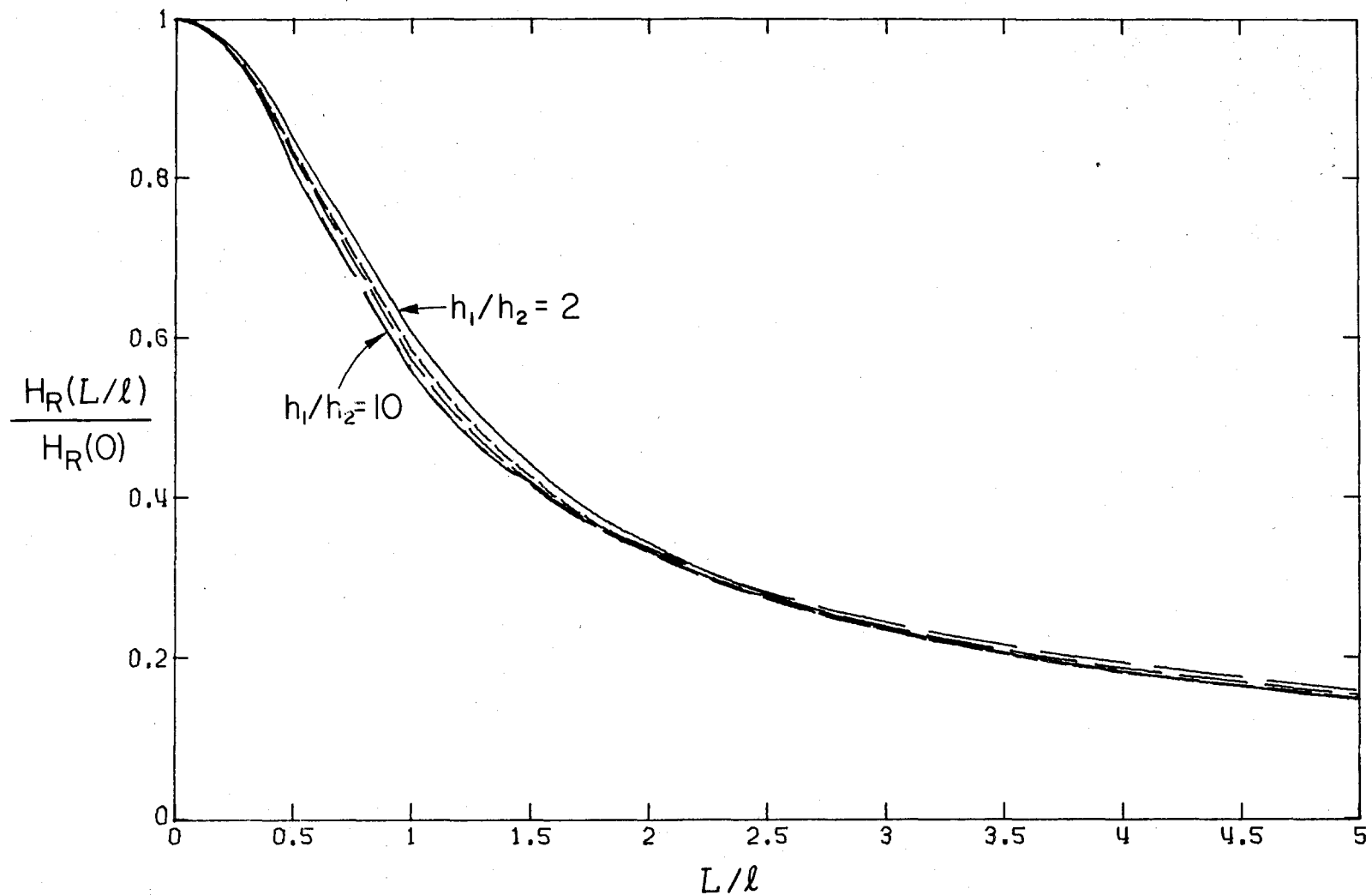


Fig. 5.41 Variation of the relative reflected wave height, $H_R(L/\ell)/H_R(0)$, with length ratio, L/ℓ , as predicted by the linear nondispersive theory.

nondispersive theory the depth ratio, just like the relative incident wave height, H_I/h_1 , is not a parameter in the solution.

Figure 5.41 shows as the length ratio increases from zero to unity the reflected wave height decreases rapidly but as the length ratio increases beyond unity the reflected wave height decreases at a slower rate.

The solutions described so far are solutions to the linear non-dispersive theory in which the relative incident wave height, H_I/h_1 , does not affect the shape of the reflected wave. However, in the actual physical problem it is expected the relative incident wave height would have some influence on the shape of the reflected wave. To investigate this, a series of numerical experiments and a series of physical experiments were performed. The numerical experiments comprised using the finite element program described in Section 3.3 for a range of conditions.

The physical experiments, in which the objective was to measure the wave reflected when a solitary wave propagates up a slope onto a shelf, had a number of difficulties which limited their extent. The main problems were:

- i) When one wishes to measure two waves, one of which is a tenth or less in height than the other, the accuracy of measurement of the smaller wave is considerably less than that of the larger wave. For example, if the waves trailing the incident wave are 1% of the height, they are negligible with respect to the incident wave. However, for a reflected wave which

is a tenth the height of the incident wave, the trailing waves represent 10% of the reflected wave and thus can affect the shape considerably.

- ii) As the length ratio increases, Fig. 5.39 shows the length of the reflected wave also increases. Hence, the length of tank upstream of the slope must be large enough to accommodate the reflected wave which may be many times longer than the incident wave.

The physical experiments were performed for two depth ratios, $h_1/h_2 = 3.0$ and 4.0 , and for three slopes, $L = 150$ cm, 300 cm and 450 cm, and the step ($L = 0$); the shelf height was 15.54 cm. The relative incident wave height was varied from $H_I/h_1 = 0.033$ to 0.125 ; the lower bound arose from the difficulty of accurately measuring waves with smaller height and the upper bound arose because waves of greater height broke on the slope. For a particular slope a four-fold increase in the incident wave height halves the length ratio, L/ℓ , because, it will be recalled, the characteristic length, ℓ , is defined as $\ell = 1.5(H_I/h_1)^{-\frac{1}{2}}h_1$. Hence, a range of length ratios could be covered with one slope simply by varying the incident wave height. However, to allow for the effects of incident wave height it was necessary to overlap the regions of length ratio which each of the slopes covered.

The results of the physical experiments, and the linear nondispersive theory and the nonlinear dispersive theory are presented in Figs. 5.42 and 5.43, in which the ratio of reflected to incident wave

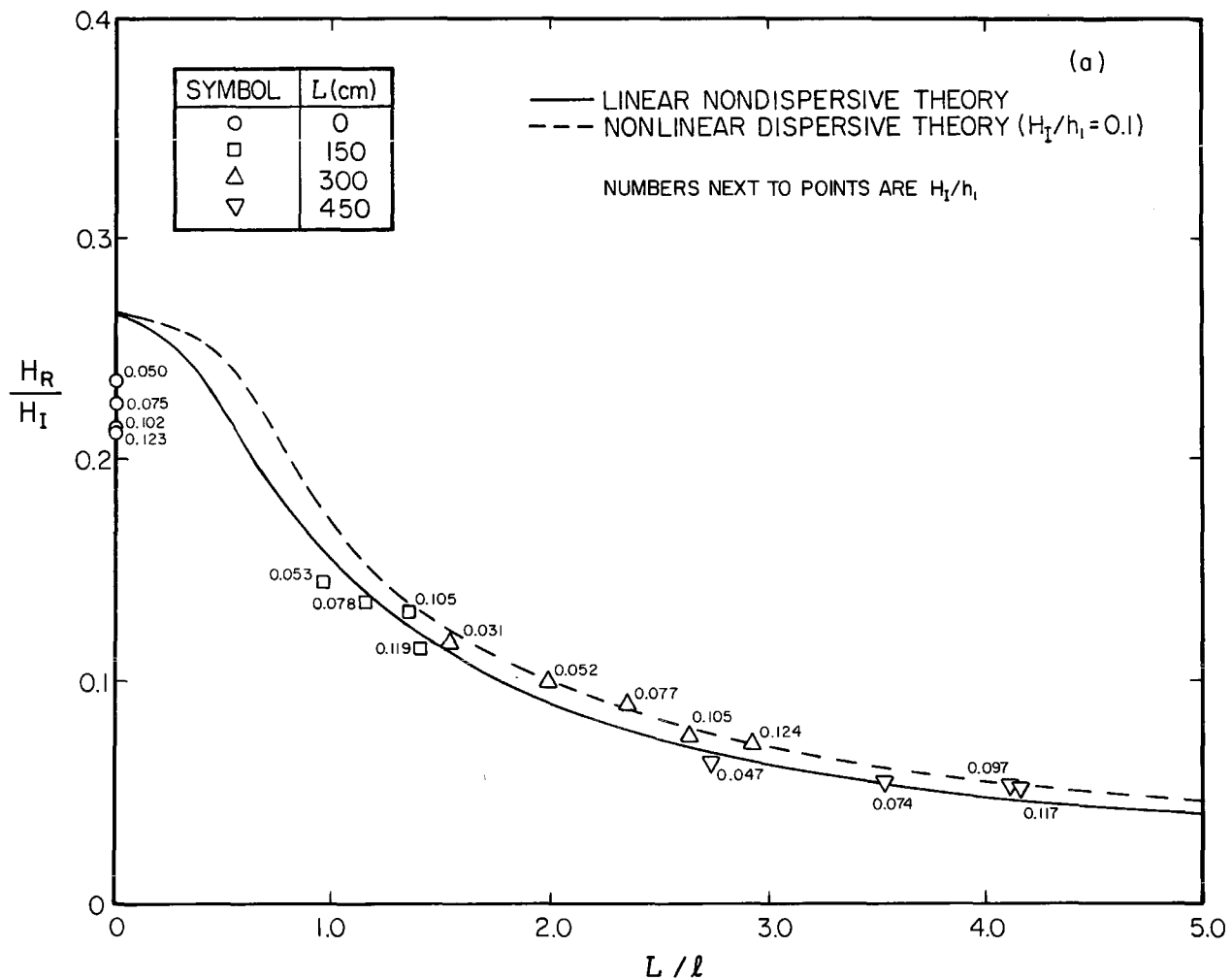
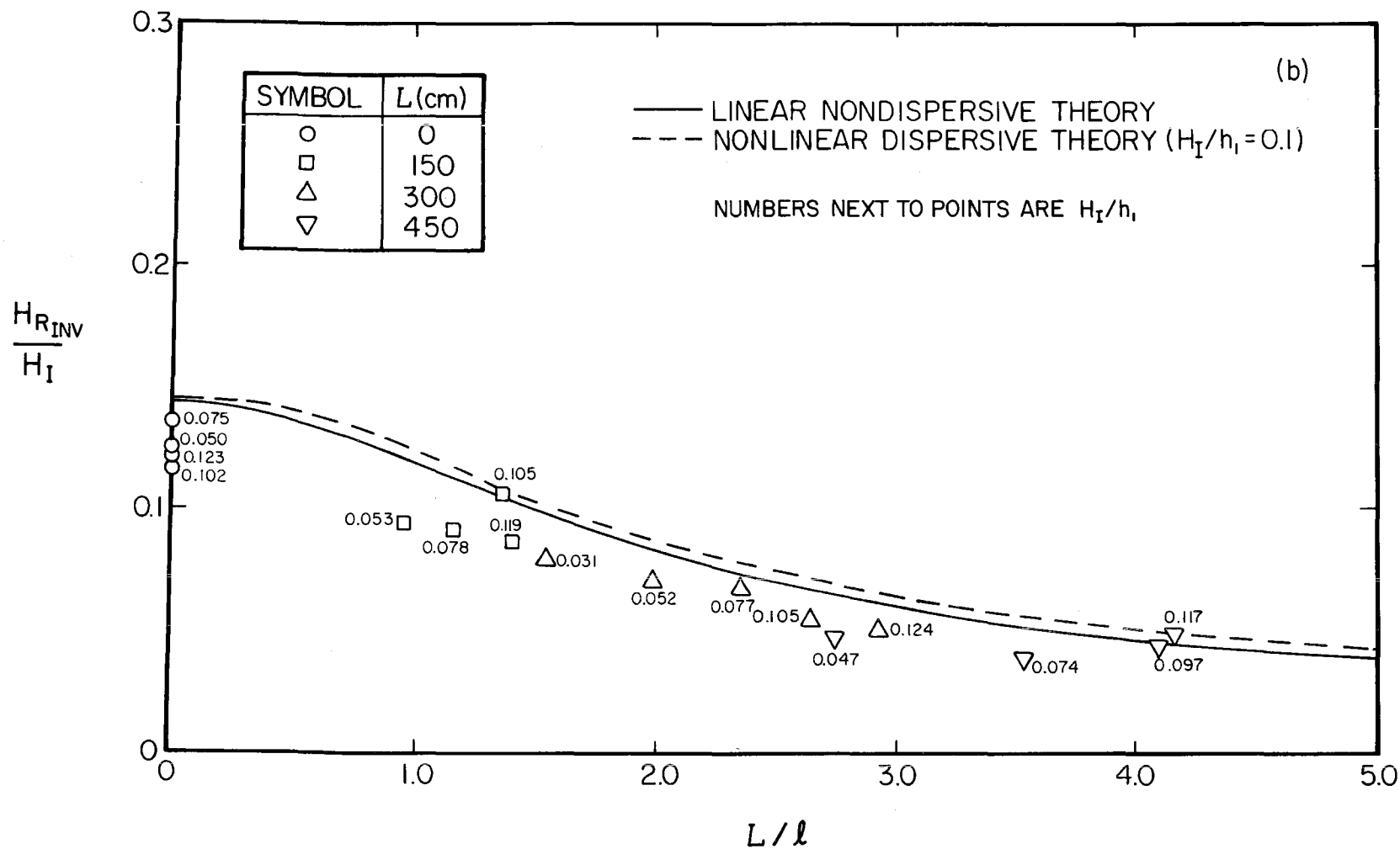
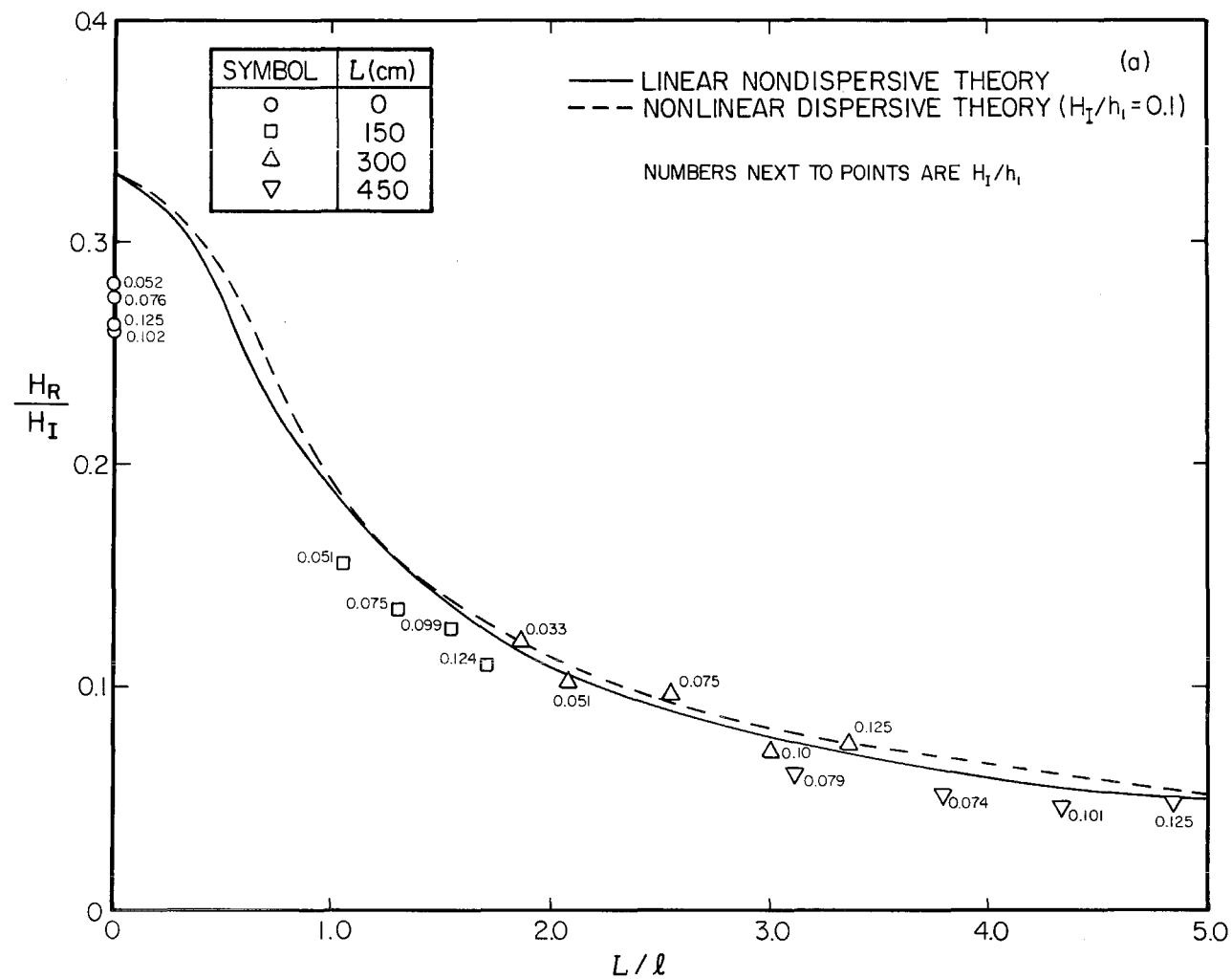


Fig. 5.42(a) Variation of the reflected wave height ratio, H_R/H_I , with length ratio, L/ℓ , for a depth ratio of $h_1/h_2 = 3$.





218

Fig. 5.43(a) Variation of the reflected wave height ratio, H_R/H_I , with length ratio, L/ℓ , for a depth ratio of $h_1/h_2 = 4$.

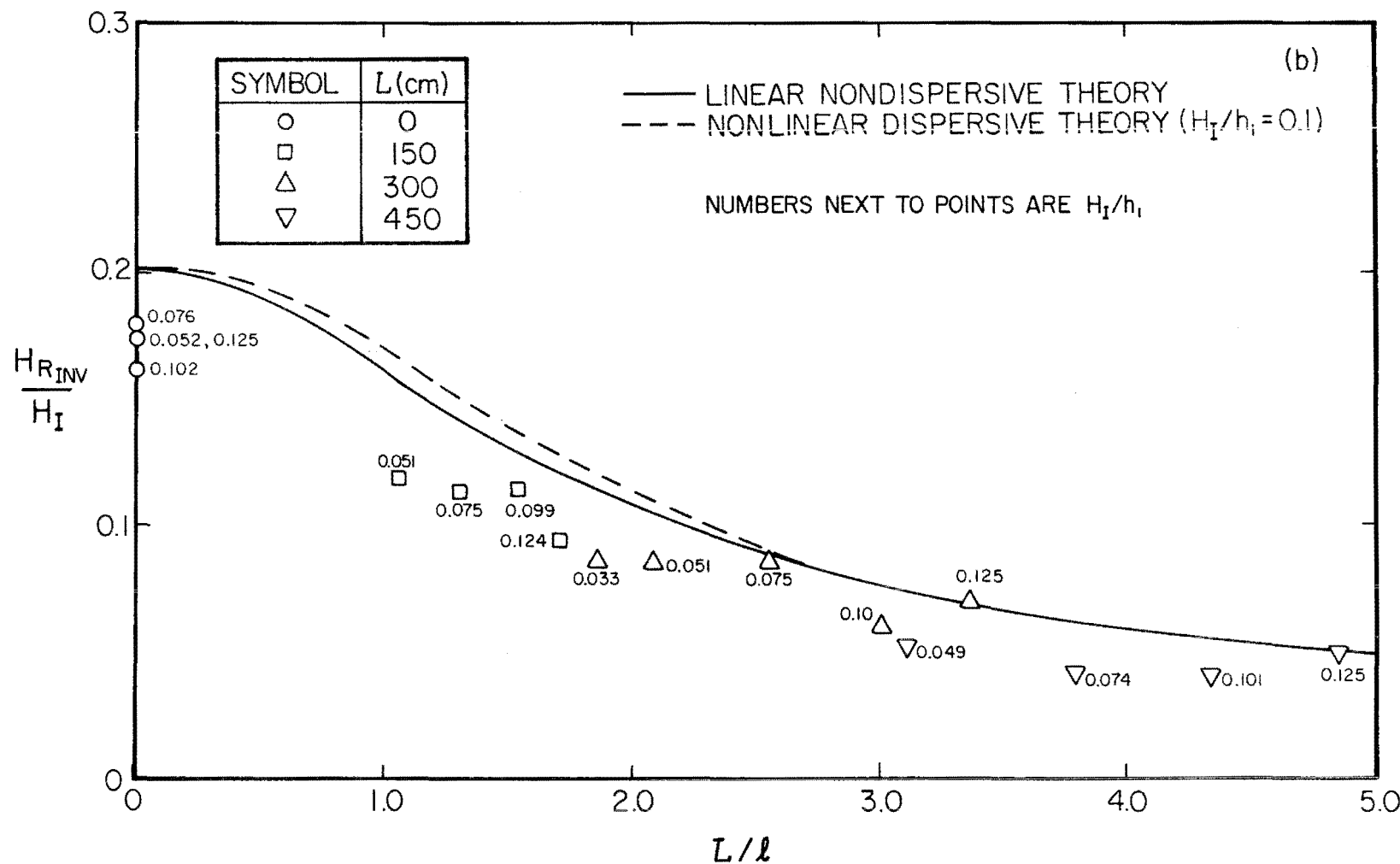


Fig. 5.43(b) Variation of the inverse scattered reflected wave height ratio, $H_{R_{INV}}/H_I$, with length ratio, L/l , for a depth ratio of $h_1/h_2 = 4$.

height is plotted as a function of the length ratio, L/ℓ . Figures 5.42(a) and (b) are for the depth ratio $h_1/h_2 = 3$; Figs. 5.43(a) and (b) are for the depth ratio $h_1/h_2 = 4$. Figures 5.42(a) and 5.43(a) are reflected wave height ratios H_R/H_I ; Figs. 5.42(b) and 5.43(b) are inverse scattered reflected wave height ratios $H_{R_{INV}}/H_I$. The solid curves are the linear nondispersive theory; the dashed curves are the nonlinear dispersive theory for a relative incident wave height of $H_I/h_1 = 0.1$. The experimental points have different symbols according to the slope which was used, and the numbers beside the points are the relative incident wave height H_I/h_1 .

The figures show the difference between the linear nondispersive theory and the nonlinear dispersive theory with $H_I/h_1 = 0.1$ is small, and the experiments show good agreement with the theories, particularly considering the problems of accuracy discussed earlier. For the experimental data, the data in the overlapping regions described earlier exhibit some differences but in such a random manner they are assumed to be scatter due to problems associated with experimental accuracy. Hence, the experimental data seem to indicate the incident wave height does not affect the reflected wave for the range of relative heights investigated.

To investigate this further, the finite element analysis was used for a depth ratio: $h_1/h_2 = 3$ and a range of incident wave heights and length ratios; the heights of the reflected waves are compared in Tables 5.5(a) and (b), where zero relative incident wave height represents the linear nondispersive theory. The tables show the

Table 5.5 Reflected wave height ratios, (a) H_R/H_I and (b) $H_{R_{INV}}/H_I$, for various length ratios and relative incident wave heights for depth ratio $h_1/h_2 = 3$. (nonlinear dispersive theory)

(a) H_R/H_I

H_I/h_1 L/ℓ	0	0.05	0.10	0.15
0.53	0.218	0.228	0.235	0.238
1.03	0.152	0.162	0.161	0.165
1.56	0.110	0.121	0.123	0.123
2.00	0.0888	0.0980	0.0978	0.0997

(b) $H_{R_{INV}}/H_I$

H_I/h_1 L/ℓ	0	0.05	0.10	1.15
0.53	0.137	0.138	0.139	0.139
1.03	0.119	0.120	0.120	0.122
1.56	0.101	0.099	0.101	0.098
2.00	0.0831	0.0884	0.0879	0.0871

results for the nonlinear dispersive theory agree with each other within 5% which indicates no detectable influence of incident wave height on the solution for the range used. However, for this depth ratio ($h_1/h_2 = 3$) the maximum incident wave for a nonbreaking wave on the shelf, as given by Eq. (5.20), is: $H_I/h_1 = 0.18$, which is not a very large wave. To increase the size of the incident wave but avoid breaking waves on the shelf, the depth ratio was reduced to $h_1/h_2 = 1.5$; then incident waves with relative heights up to $H_I/h_1 = 0.4$ could be considered. The results of the analysis, again using the finite element formulation, are presented in Table 5.6. Evidently, for these extreme cases, the height of the reflected wave is dependent on the height of the incident wave, however the dependence is only weak, with a fourfold increase in the incident wave height resulting in at most a 16% change in the reflected wave height ratio.

The linear nondispersive theory generally predicts lower wave heights than the nonlinear dispersive theory and a reason for this is shown in Fig. 5.44(a) and (b) where the profiles of two waves from the experiments and the theories are compared. The ordinates in the figures are amplitude normalized with respect to incident wave height, n/H_I , so that the reflected waves from incident waves of different heights can be compared directly. The waves from the nonlinear dispersive theory for various wave heights are shown as dashed curves and apart from small differences which can be attributed to numerical effects they predict the same wave profile. However,

Table 5.6 Reflected wave height ratios, (a) H_R/H_I and (b) $H_{R_{INV}}/H_I$,
 for various length ratios and relative incident wave
 heights for depth ratio, $h_1/h_2 = 1.5$. (nonlinear dispersive
theory)

(a) H_R/H_I

H_I/h_1 L/λ	0	0.1	0.2	0.3	0.4
0.26	0.0965	0.0961	0.0928	0.0889	0.0862
0.53	0.0849	0.0845	0.0815	0.0788	0.0764
1.06	0.0606	0.0647	0.0640	0.0638	0.0592
2.00	0.0356	0.0376	0.0389	0.0387	0.0378

(b) $H_{R_{INV}}/H_I$

H_I/h_1 L/λ	0	0.1	0.2	0.3	0.4
0.26	0.0259	0.0246	0.231	0.0219	0.0211
0.53	0.0256	0.0243	0.0225	0.0215	0.0195
1.06	0.0244	0.0233	0.0219	0.0204	0.0186
2.00	0.0211	0.0202	0.0195	0.0183	0.0170

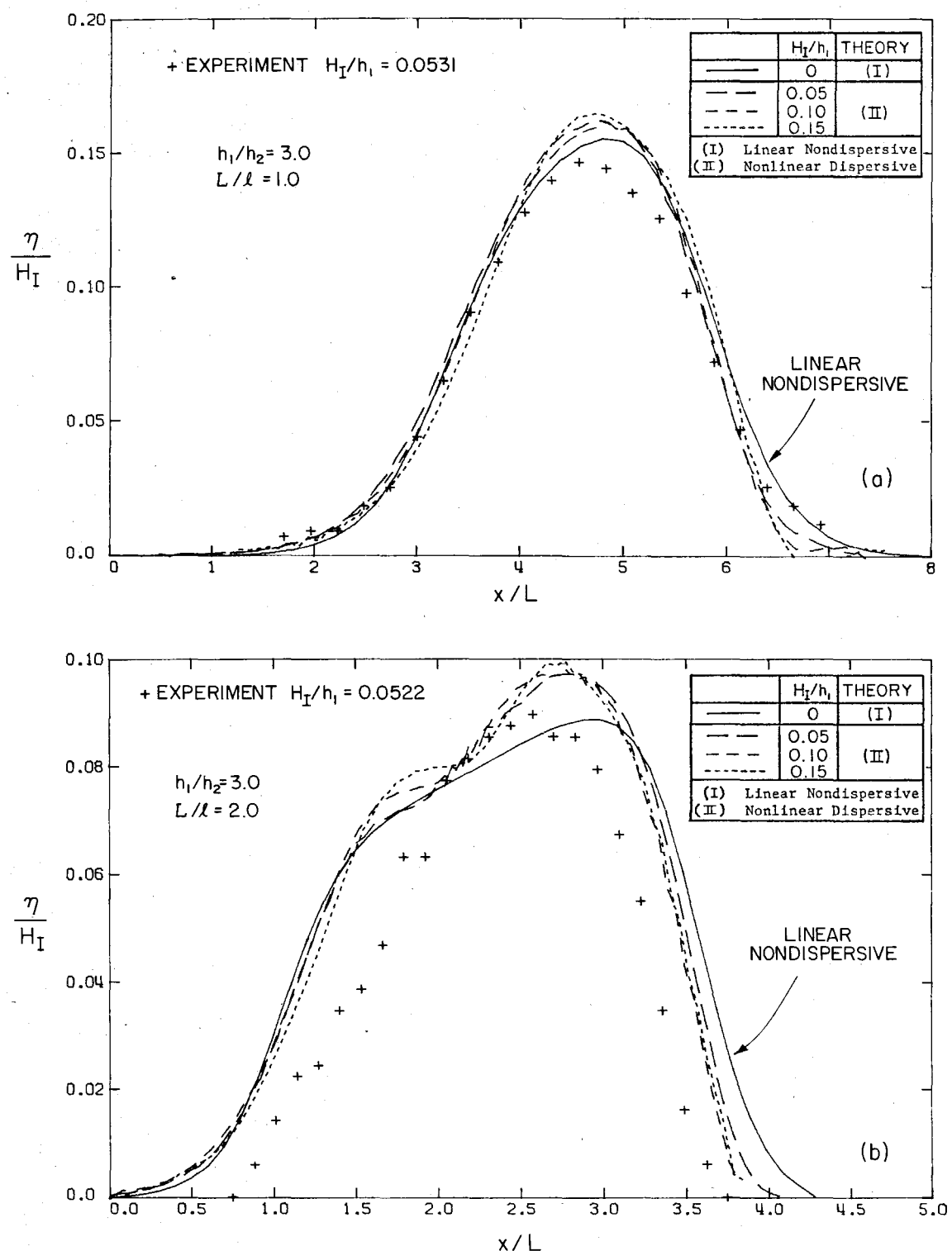


Fig. 5.44 Comparison of the theoretical reflected waves with the experimental wave.

the wave predicted by the linear nondispersive theory has a different shape and the difference is attributed to the effect mentioned earlier of amplitude and frequency dispersion in the propagation of the wave from the slope back to the point where the profile was taken.

The profiles from the two experiments also are plotted in Figs. 5.44(a) and (b). In Fig. 5.44(a) the data from the experiment agree with the theories except in the region of the crest and this difference is attributed to friction which is not included in either theory. In Fig. 5.44(b) the agreement is not as good although the overall shape of the wave predicted by the nonlinear dispersive theory also is evident in the experimental reflected wave. However, to illustrate the problem of accuracy mentioned earlier, an error of 0.01 cm in the measurement of the reflected wave becomes an error of 0.008 in the amplitude η/H_I , i.e., an error of about 8% of the wave height in Fig. 5.44(b).

The process of reflection of solitary waves from a slope in most cases may be predicted approximately by the linear nondispersive theory but the nonlinear dispersive theory should be used for propagation upstream of the slope.

5.3 The Transmission of Long Waves over a Change in Depth

For the purposes of this study the "transmitted wave" will be defined as the time-history of the variation of the water surface elevation (the wave) at the upstream edge of the shelf. This concept

arises from the linear nondispersive theory which predicts this wave is in fact the wave measured at any position on the shelf because under this theory waves propagate unchanged in shape in a constant depth.

The prediction of the transmitted wave is a particularly important aspect of the problem. Once it is known it can be used as the boundary condition of one of the more straightforward theories of propagation for waves travelling in one direction only (e.g., the KdV equation) to obtain the characteristics of the wave at any position on the shelf.

5.3.1 The Transmission of Solitary Waves over a Step

In the experiments described in Section 5.2.1, in addition to measuring the incident and reflected waves, the waves at the step also were recorded. The data from these experiments are presented in Fig. 5.45 where the ratio of the wave height at the step to the incident wave height, H_T/H_I , is plotted as a function of the relative incident wave height, H_I/h_1 , for various depth ratios, h_1/h_2 . The vertical dashed lines represent the incident wave height at which the linear nondispersive theory predicts the wave will break onto the shelf (see Table 5.3). In fact, in the experiments, the incident wave height at which the wave broke onto the shelf was not well defined, and in most cases the only indication of breaking was irregularities just past the crest in the recorded water surface-time history.

The data exhibit considerable scatter, but for depth ratios $h_1/h_2 \leq 3.5$ in the nonbreaking region there appears to be a slight trend for the transmitted wave height ratio to decrease with increasing relative incident wave height. However, this is not reflected in the results of the nonlinear dispersive theory applied to the case of the

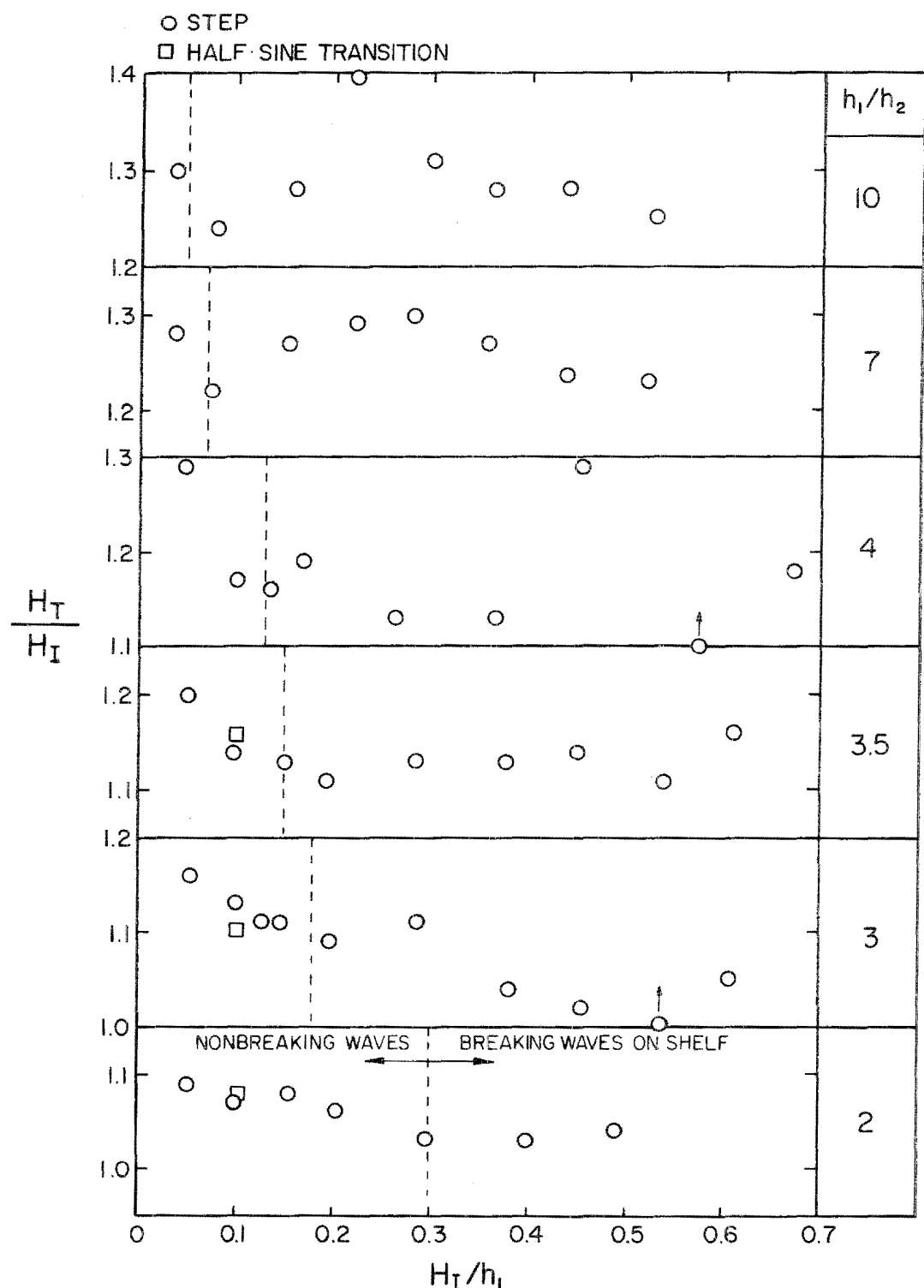


Fig. 5.45 Variation of the transmitted wave height ratio, H_T/H_I , with the relative incident wave height, H_I/h_1 , for solitary waves.

waves transmitted over the half-sine transition slope. These results, which are presented in Table 5.7, indicate no significant dependence of the transmitted wave height ratio, H_T/H_I , on the relative incident wave height, H_I/h_1 (although the frequency ratio, Ω_T/Ω_I , does vary with H_I/h_1 and this will be discussed presently). Hence, the trend in Fig. 5.45 is attributed to dissipative effects which increase with relative incident wave height.

Table 5.7 Transmitted waves calculated using the nonlinear dispersive theory for $h_1/h_2 = 3$.

$\frac{H_I}{h_1}$	$\frac{H_T}{H_I}$	$\frac{\Omega_T}{\Omega_I}$
0	1.268	1.000
0.05	1.261	0.973
0.10	1.256	0.946
0.15	1.258	0.936

The data from these experiments and also from the experiments described in Section 5.3.1 as the second set of experiments are compared with the linear nondispersive theory as given by Eq. (3.114) in Fig. 5.46 where the transmitted wave height ratio, H_T/H_I , is plotted as a function of the depth ratio, h_1/h_2 . The heights of the

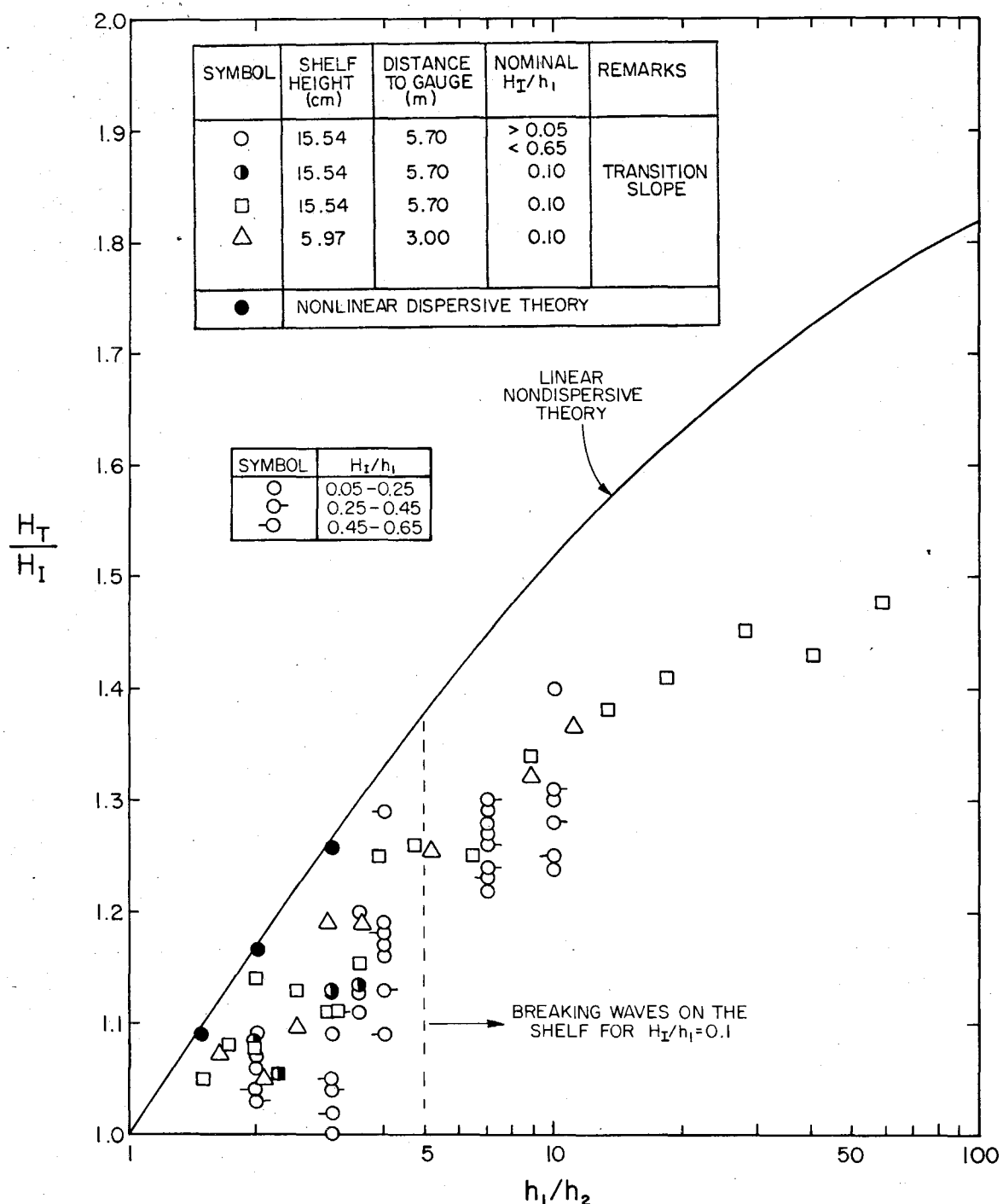


Fig. 5.46 Variation of the transmitted wave height ratio, H_T / H_I , with depth ratio, h_1 / h_2 , for solitary waves.

wave at the step evidently are less than the theory predicts for the entire range of depth ratios which is attributed to dissipative effects. The data depart more from the theory for depth ratios $h_1/h_2 > 5$. (Recall, as mentioned earlier, an incident wave, with a relative height of $H_I/h_1 = 0.1$ will break onto the shelf at depth ratios h_1/h_2 greater than 5.) The data from the experiments with different shelf heights agree sufficiently well to indicate there is no dependence on the actual shelf height.

Also plotted in Fig. 5.46 are data from experiments in which the vertical face on the shelf was replaced by the half-sine transition slope. These data lie close enough to the data from experiments in which a step was used to indicate the transition has no effect on the wave at the step.

The nonlinear dispersive theory when applied to the case of solitary waves with relative height $H_I/h_1 = 0.1$ propagating over the half-sine transition slope gave transmitted wave heights which are plotted as solid circles in Fig. 5.46 within 1% of those predicted by the linear nondispersive theory for $h_1/h_2 \leq 3$.

As mentioned earlier when describing Fig. 5.2, the shape of the transmitted wave appears the same as the shape of the incident wave, as the linear nondispersive theory predicts. To investigate this, the transmitted waves for experiments with the depth ratios $h_1/h_2 = 2, 3, 4$, and 10 were digitized and the frequency, Ω , and wave height, H_{Reg} , in Eq. (5.4) were calculated by performing a regression analysis on the upper 2/3 of the wave. The results are presented in Fig. 5.47

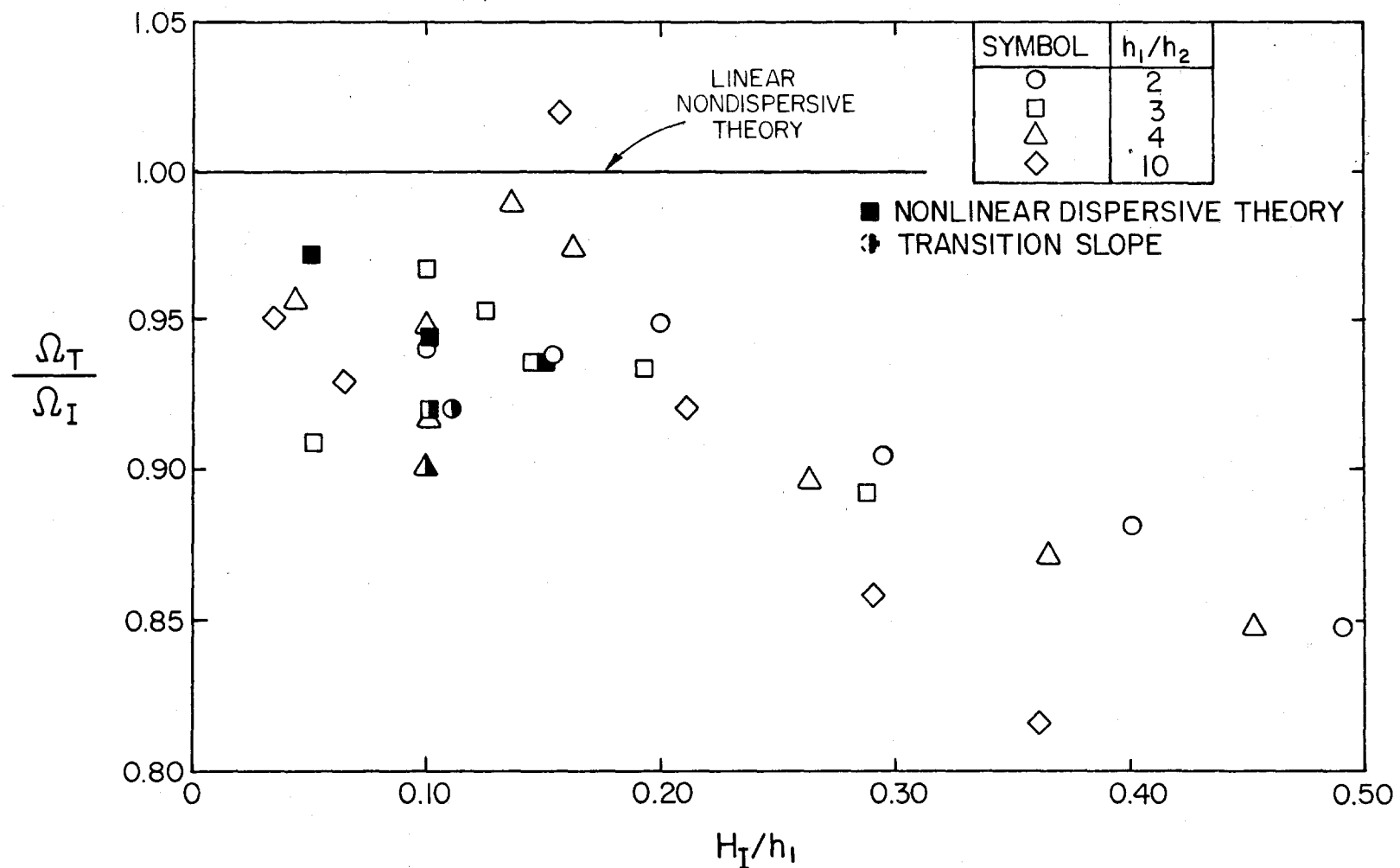


Fig. 5.47 Variation of the transmitted wave frequency ratio, Ω_T/Ω_I , with relative incident wave height, H_I/h_1 .

where the ratio of the frequency of the transmitted wave to the frequency of the incident wave, Ω_T/Ω_I , is plotted as a function of the relative incident wave height, H_I/h_1 . The data appear to lie about a ratio of frequencies $\Omega_T/\Omega_I \approx 0.95$ for wave heights $H_I/h_1 \leq 0.2$, then the ratio of frequencies decreases as the wave height increases with those for larger depth ratios decreasing at a faster rate.

The linear nondispersive theory predicts $\Omega_T/\Omega_I = 1.00$ as denoted by the horizontal line in Fig. 5.47. However, the nonlinear dispersive theory predicts the frequency ratio decreases with relative incident wave height as shown by the experimental data in Table 5.7 which also are plotted in Fig. 5.47.

Unlike the process of reflection, the process of transmission of a solitary wave over a step appears to be one in which nonlinear effects are important, particularly in the determination of the shape of the transmitted wave.

5.3.2 The Transmission of Cnoidal Waves over a Step

The results of experiments conducted to determine the wave height of cnoidal waves as they propagate over a step onto a shelf are presented in Fig. 5.48 where the transmitted wave height ratio, H_T/H_I , is plotted as a function of the relative incident wave height, H_I/h_1 , for depth ratios $h_1/h_2 = 3, 3.5, 4$ and 10 . The numbers beside the experimental points are the quantity $gH_I T^2/h_1^2$ which, as described earlier, is the Ursell Number with wavelength replaced by wave period. The vertical dashed lines represent the limits in incident wave height for the wave to break or not to break onto the shelf, predicted by the

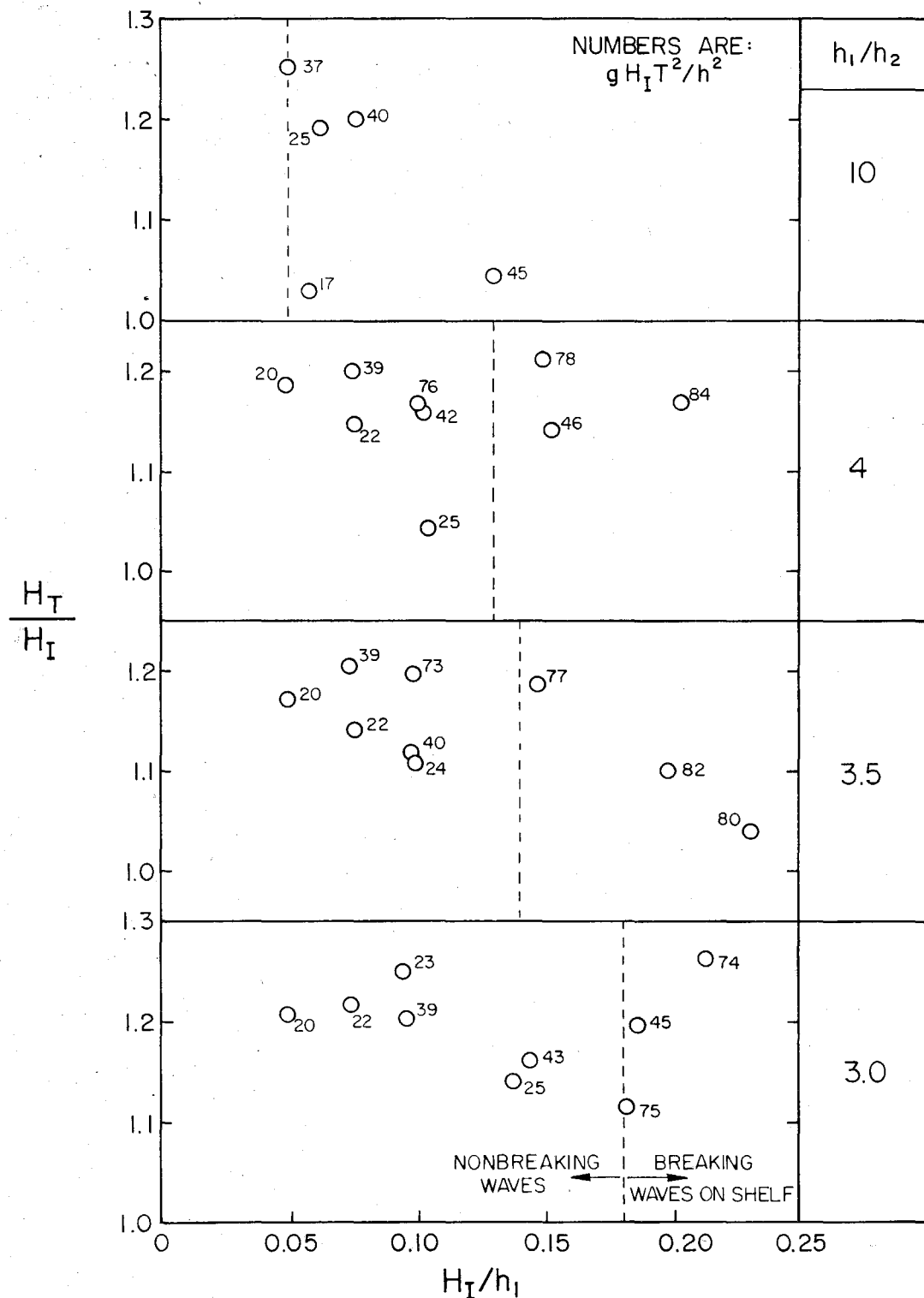


Fig. 5.48 Variation of the transmitted wave height ratio, H_T/H_I , with relative incident wave height, H_I/h_1 , for cnoidal waves.

linear nondispersive theory (described earlier) and listed in Table 5.3.

The data exhibit considerable scatter, part of the reason for this is the way in which these finite amplitude, periodic waves propagate onto the shelf. As the crest passes the step, the flow at the step is in the downstream direction, i.e., onto the shelf, and as the trough propagates onto the shelf, the flow is in the reverse direction, i.e., off the shelf. However, since the waves have finite amplitude, the depth of water under the trough on the shelf may be reduced to the extent that the flow off the shelf cannot be achieved without some irregularities occurring in the trough of the wave at the step. (As a crude analogy of this, the process can be likened to the flow over a weir.)

5.3.3 The Transmission of Solitary Waves over a Slope

The dimensional analysis performed in Section 5.2.3 when considering the reflection of solitary waves from a slope also is applicable here. Eq. (5.21) becomes:

$$\frac{H_T}{H_I} = f\left(\frac{h_1}{h_2}, \frac{L}{\lambda}, \frac{H_I}{h_1}\right) \quad , \quad (5.22)$$

where H_T is the transmitted wave height, h_1/h_2 is the depth ratio, L/λ is the length ratio where L is the length of the slope and λ is the characteristic length of the wave ($\lambda = 1.5(H_I/h_1)^{-1/2}h_1$), and H_I/h_1 is the relative incident wave height.

Initially, the effect of the relative incident wave height, H_I/h_1 , will be neglected and the linear nondispersive theory will be

used to illustrate the effect of the length ratio, L/ℓ , and the depth ratio, h_1/h_2 , of the transmitted wave. This is done using Fig. 5.49 which consists of two parts. Figure 5.49(a) shows the Fourier transform of the incident solitary wave which, as shown in Section 3.4, for the purpose of analysis, may be considered to be a function of the length ratio, L/ℓ , and the nondimensional frequency, $\omega L/\sqrt{gh_1}$. Figure 5.49(b) shows the transmission coefficient normalized with respect to the transmission coefficient $K_T(\omega)/K_T(0)$, which is a function of the depth ratio, h_1/h_2 , and the nondimensional frequency, $\omega L/\sqrt{gh_1}$. The latter have similar shape but have increasing transmission coefficient ratio for increasing depth ratios at large frequencies.

The technique mentioned earlier for calculating the reflected wave from Fig. 5.38 also applies for calculating the transmitted wave from Fig. 5.49. Selecting a particular length ratio and a particular depth ratio, the corresponding functions of frequency for the Fourier transform and the transmission coefficient are multiplied together to give the transmitted wave in the frequency domain. To obtain the transmitted wave in the time domain the product is multiplied by $e^{-i\omega t}$ and integrated over the frequency range.

The overall behavior can be deduced from Fig. 5.49 as follows:

- i) For small length ratios, $L/\ell \ll 1$, (i.e., an abrupt slope) the transmitted wave will have essentially the same shape as the incident wave because the majority of the frequency range where the Fourier transform is nonzero is the frequency range

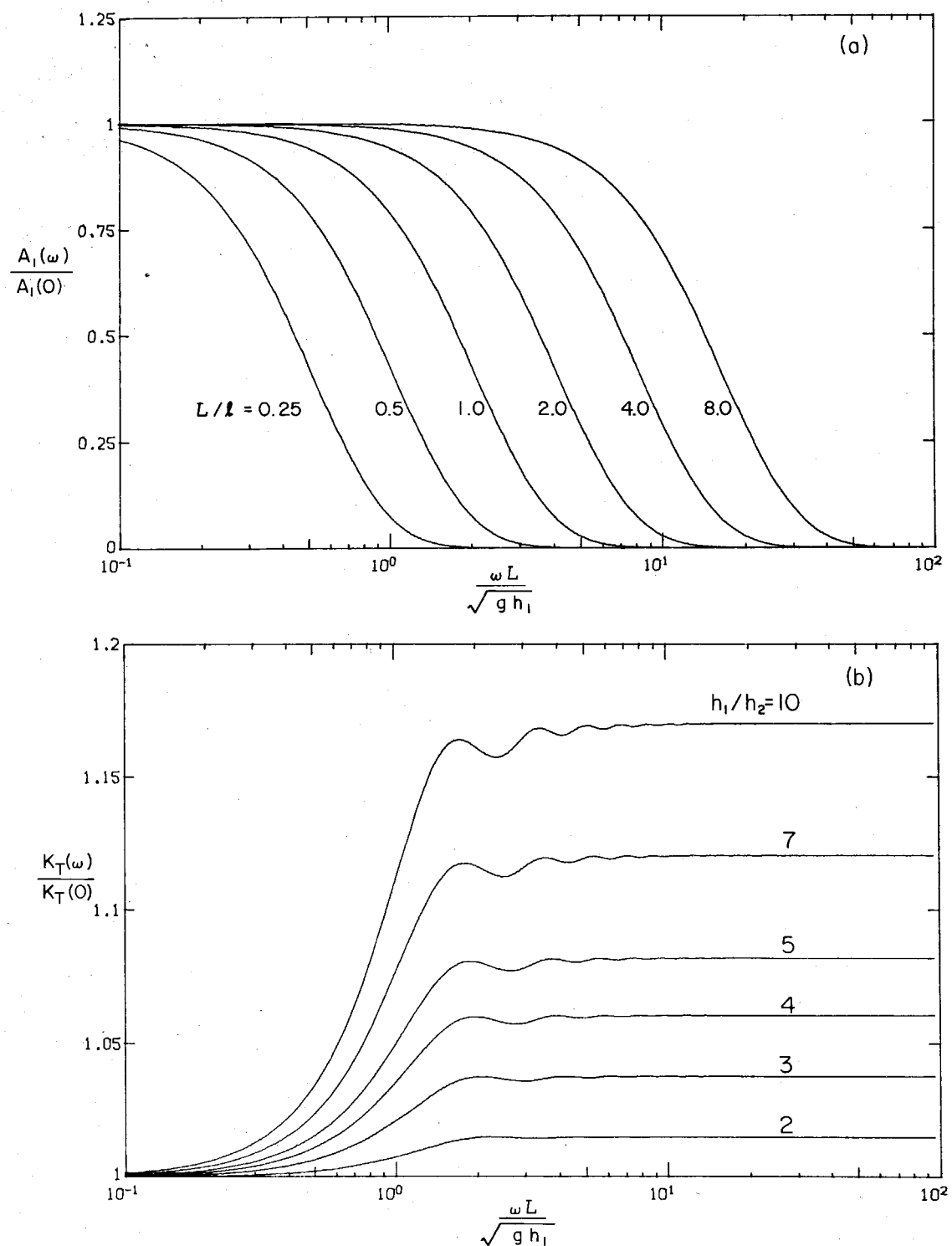


Fig. 5.49 Theoretical variation of (a) the Fourier transform of a solitary wave and (b) the transmission coefficient with frequency.

where the transmission coefficient is a constant.

ii) For large length ratios, $L/\lambda \gg 1$, (i.e., a gradual slope) the majority of the Fourier transform will be multiplied by a constant transmission coefficient; hence the shape of the transmitted wave should be almost the same as that of the incident wave in this case also, but the wave height would be larger than for the comparable case with small length ratio (i.e., $L/\lambda \ll 1$).

The transition between i) and ii) (i.e., the change from an abrupt to a gradual slope) is shown in Fig. 5.50. In Fig. 5.50(a) the transmitted wave height ratio, H_T/H_I , is plotted as a function of the length ratio, L/λ , for various depth ratios. The figure shows the difference in the height ratio for abrupt and gradual slopes is small for small depth ratios but increases with depth ratio. As the length ratio goes to zero the transmitted wave height ratio tends asymptotically to the value for a step given by Eq. (3.114). As the length ratio goes to infinity the transmitted wave height ratio tends asymptotically to Green's Law, Eq. (3.116).

The shape of the transmitted wave may be compared to the shape of the incident wave by the following procedure: (i) multiplying the incident wave by the wave height ratio, H_T/H_I , (ii) lining up the crests of this wave and the transmitted wave, (iii) taking the difference between the amplitudes, and (iv) squaring the difference and summing the squares. For a transmitted wave with exactly the same shape as the incident wave, the sum-of-the-squares must be zero;

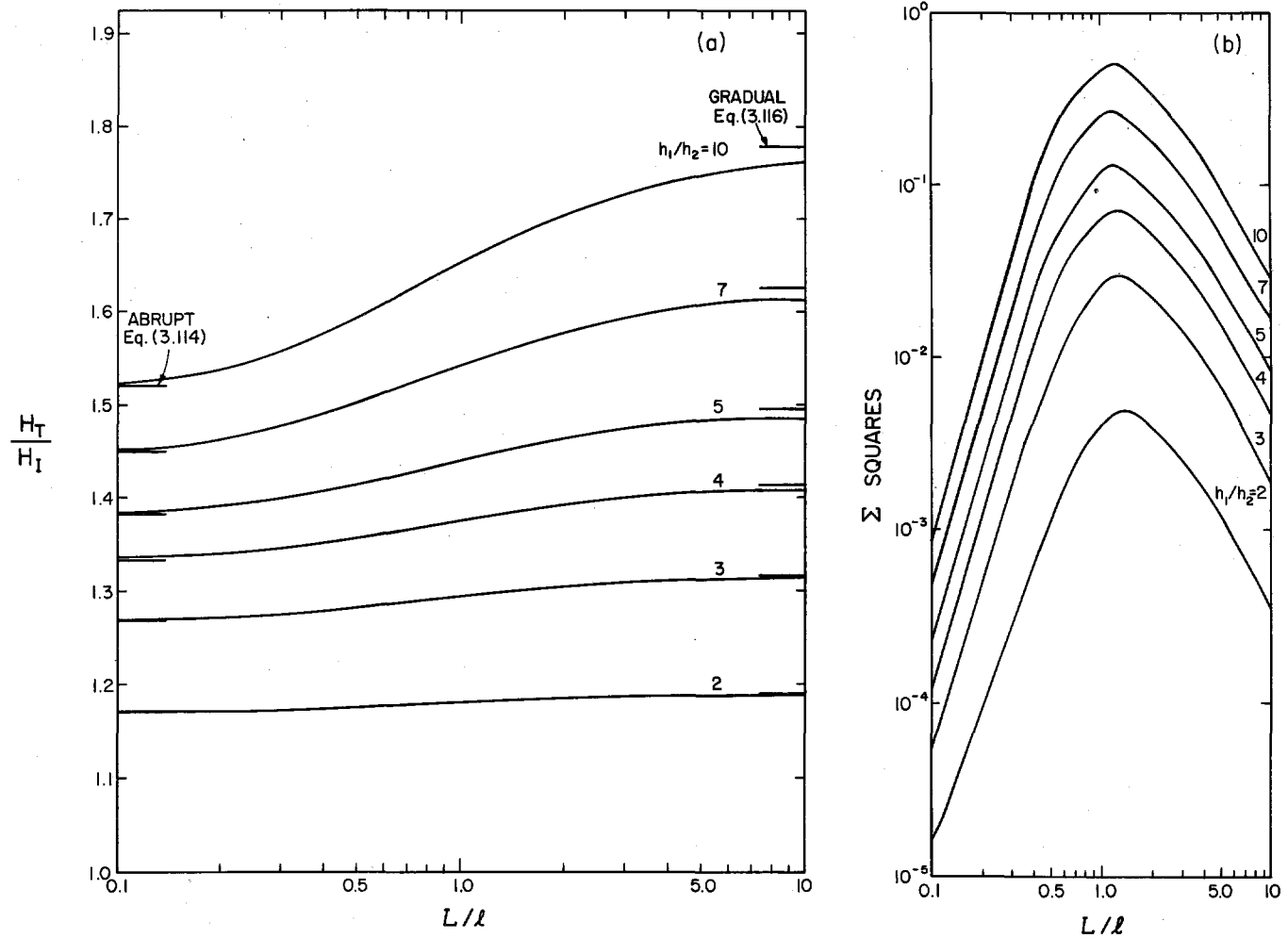


Fig. 5.50 Theoretical variation of (a) the transmitted wave height ratio, H_T/H_I , and (b) the sum-of-the-squares with length ratio, L/ℓ , for solitary waves as predicted by the linear nondispersive theory.

otherwise the sum-of-the-squares is greater than zero and the greater the magnitude, the poorer the shape of the transmitted wave compares with the shape of the incident wave. The results of this analysis are presented in Fig. 5.50(b) where the sum-of-the-squares is plotted as a function of length ratio for various depth ratios. For the depth ratios considered, the maxima all occur in the range $1.0 < L/\ell < 1.5$. Thus, the linear nondispersive theory predicts, except for a range of length ratios close to unity, the transmitted wave has essentially the same shape as the incident solitary wave.

For the linear nondispersive theory considered, the solution is not dependent on the relative incident wave height, H_I/h_1 (although it enters indirectly in the definition of the characteristic length, ℓ , as given by Eq. (3.122)). To examine the effect of the relative incident wave height on the transmitted wave for a range of conditions by physical experiments would have required a large number of experiments with slopes and shelves of various heights each with different viscous effects. In this investigation, experiments were performed with the 15.54 cm shelf and the slopes described previously, and these results were compared with those from the finite element numerical scheme to justify investigation using numerical methods alone. These comparisons will be presented first and the results of the numerical experiments later.

The experiments were conducted for an upstream depth of $h_1 = 31.08$ cm, a depth ratio of $h_1/h_2 = 2.0$, and for a nominal relative incident wave height $H_I/h_1 = 0.1$. Four slopes were used: the half-sine

transition slope and the linear slopes with lengths: 150 cm, 300 cm and 450 cm. Each experiment was conducted in three runs. In the first run the five wave gauges were placed at various locations along the flume and a wave was generated. The resulting displacement of the water surface was recorded on both the oscillosograph and the A/D converter. For the second run, Gauge 1 was placed in the position occupied by Gauge 5 in the first run and the other four gauges were positioned downstream of Gauge 1. The same wave which was generated for the first run also was generated for the second run and the waves were recorded in similar manner. This was repeated once more resulting in 15 wave gauge records at 13 different locations. The records were aligned in time by lining up the wave crests of the records from Gauge 5 of the first run and Gauge 1 of the second run and Gauge 5 of the second run with Gauge 1 of the third run.

In the numerical experiments, a wave of the same height as was generated in the physical experiments (nominally $H_I/h_1 = 0.1$) was used and the time records at locations equivalent to the thirteen locations of the wave gauges were computed. The numerical and physical experiments were aligned by lining up, in time, the crests of either the first or the second time record (i.e., either Gauge 1 or Gauge 2 of the first run).

The results of the four experiments are presented in Figs. 5.51 to 5.54 which correspond to the half-sine transition, the 150 cm slope, the 300 cm slope and the 450 cm slope respectively. The solid lines represent the physical experiments and the dashed lines represent the

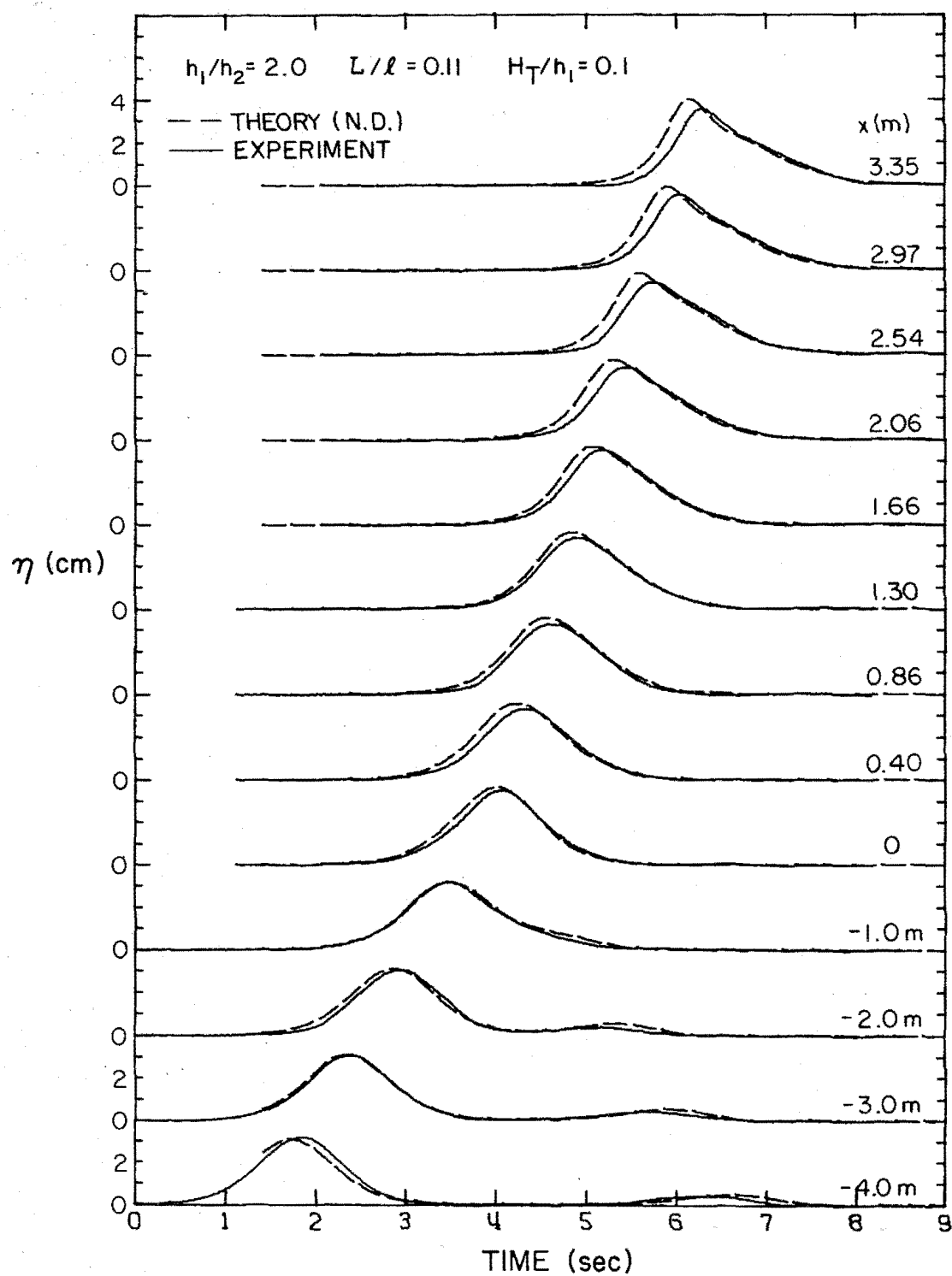


Fig. 5.51 Comparison of physical and numerical experiments for a solitary wave with height $H_T = 3.1$ cm propagating from a depth $h_1 = 31.08$ cm over a slope with length $L = 15.54$ cm onto a shelf with depth $h_2 = 15.54$ cm.

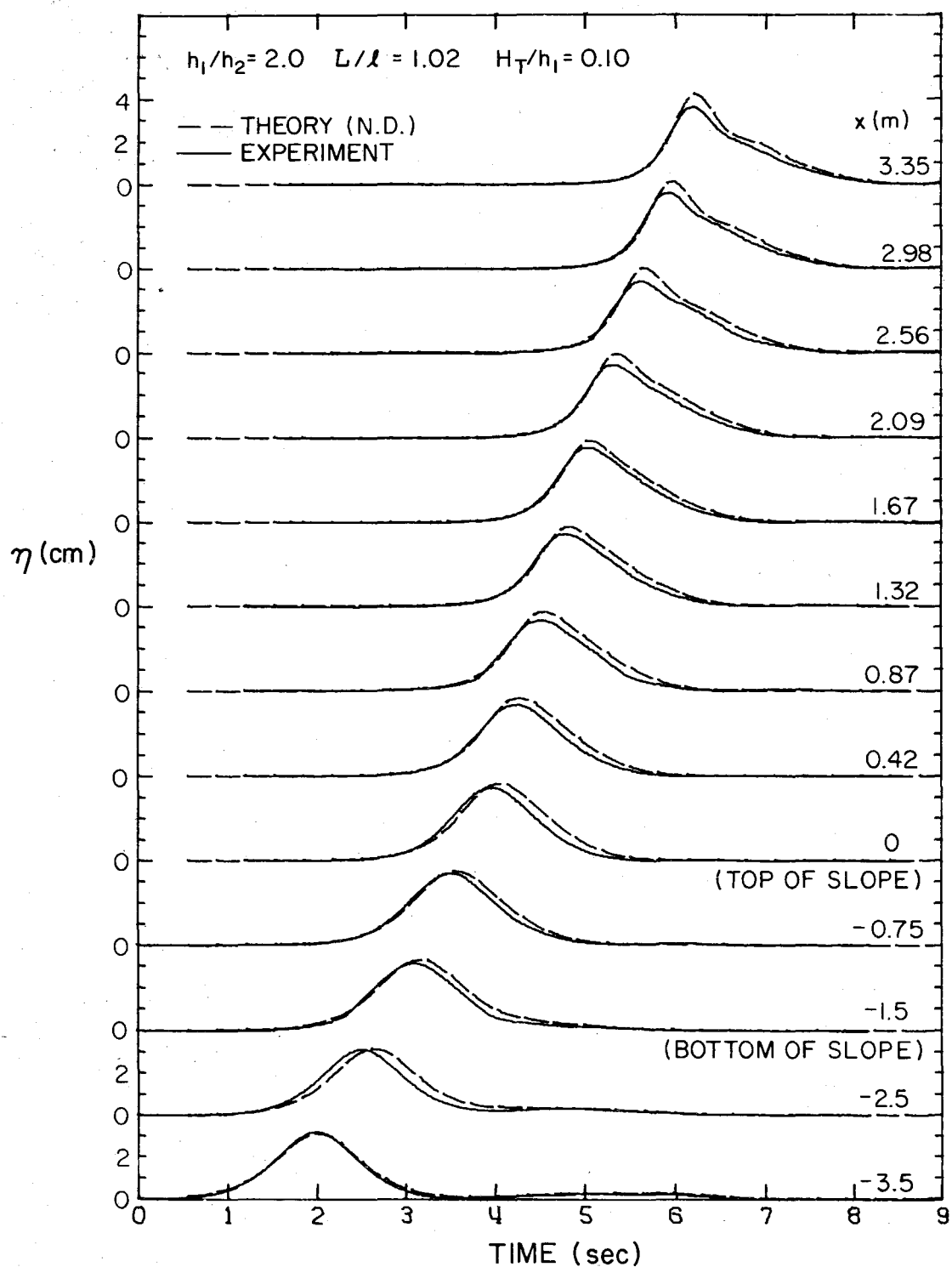


Fig. 5.52 Comparison of physical and numerical experiments for a solitary wave with height $H_I = 3.1$ cm propagating from a depth $h_1 = 31.08$ cm over a slope with length $L = 150$ cm onto a shelf with depth $h_2 = 15.54$ cm.

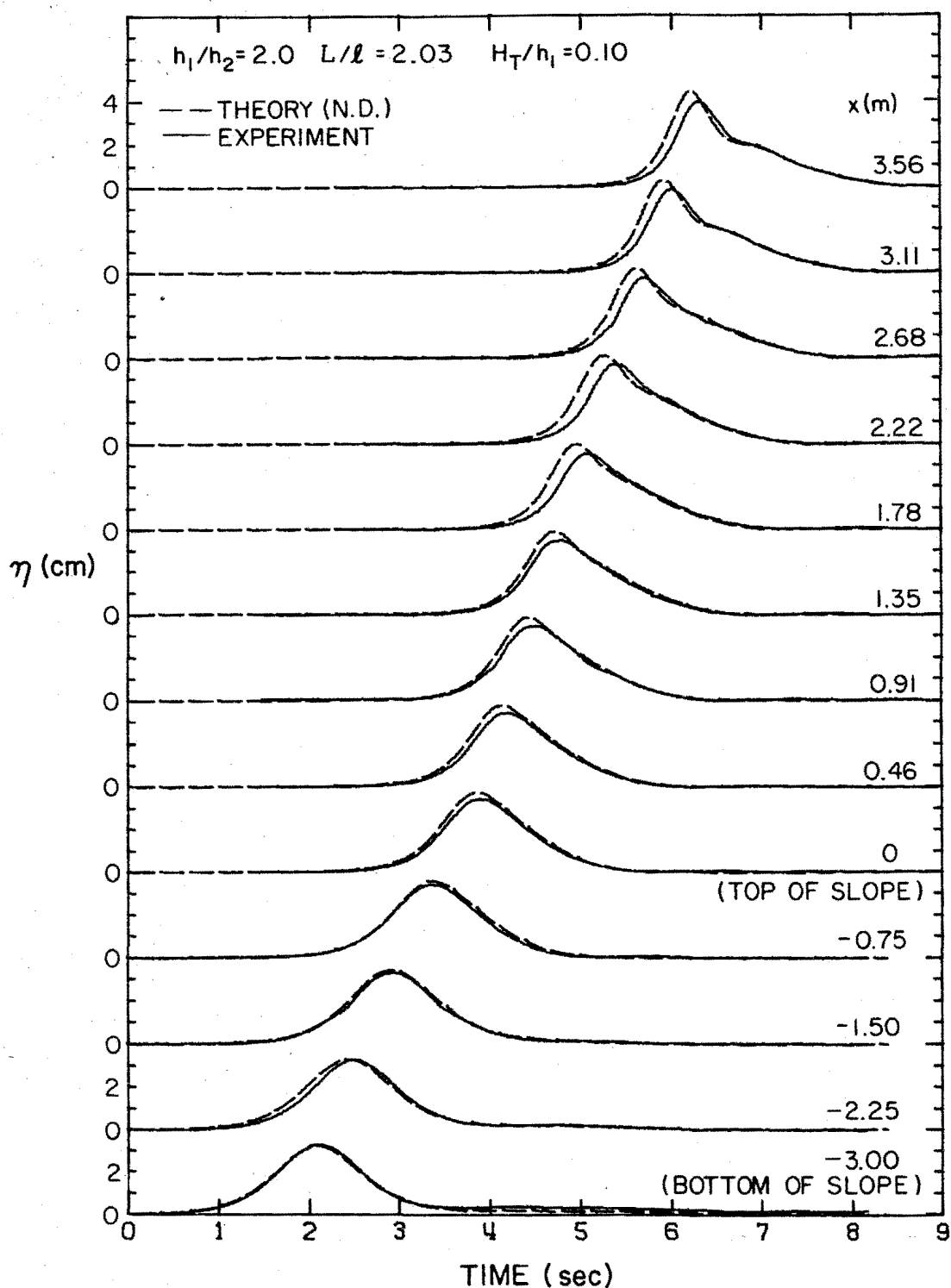


Fig. 5.53 Comparison of physical and numerical experiments for a solitary wave with height $H_T = 3.1$ cm propagating from a depth $h_1 = 31.08$ cm over a slope with length $L = 300$ cm onto a shelf with depth $h_2 = 15.54$ cm.

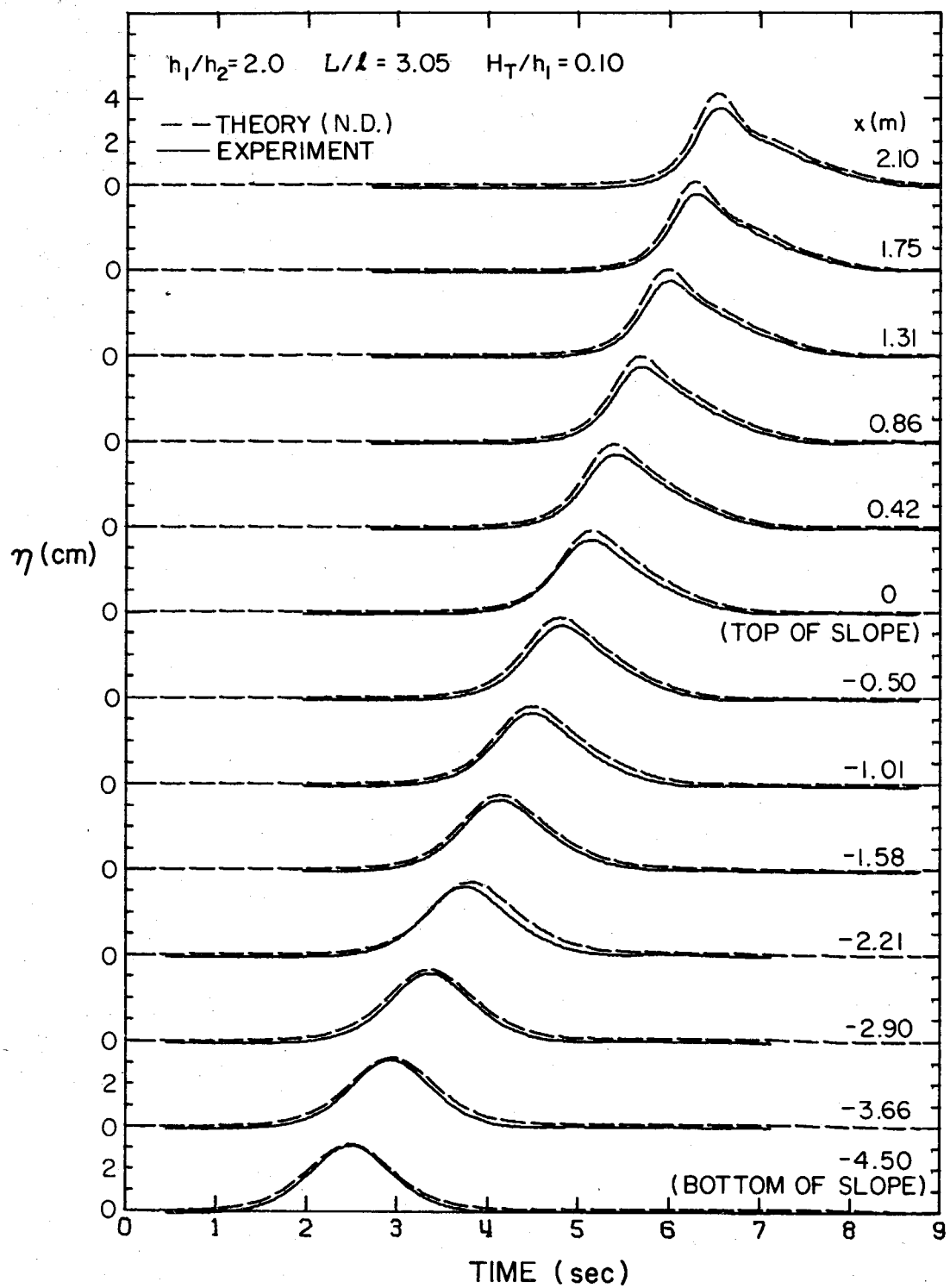


Fig. 5.54 Comparison of physical and numerical experiments for a solitary wave with height $H_T = 3.1$ cm propagating from a depth $h_1 = 31.08$ cm over a slope with length $L = 450$ cm onto a shelf with depth $h_2 = 15.54$ cm.

numerical results. The figures are presented in dimensional form because, although there are the three lengths: the upstream depth, h_1 , the slope length, L , and the depth on the shelf, h_2 , which are the important lengths for the three regions: upstream of the slope, the slope, and the shelf, none of these lengths is the important length for all three regions.

In Figs. 5.51 to 5.54 the origin of x was taken to be at the top of the slopes. The waves at the bottom of each figure, which are the amplitude-time history of waves at locations upstream of the slope, exhibit the incident wave with its crest at time $t \approx 2$ sec then at time $t \approx 6$ sec the reflected wave can be seen. As the length ratio increases from figure to figure this wave becomes longer and smaller as was discussed in Section 5.2.3. As the solitary wave propagates onto the shelf, the front face of the wave steepens and as the wave propagates a second wave begins to form behind the main crest. This process will be discussed in more detail shortly but first the physical and numerical experiments will be compared.

In Figs. 5.51 and 5.53 the waves from the numerical experiments appear to be propagating faster than those from the physical experiments, particularly on the shelf. However, this is not true of the waves shown in Figs. 5.52 and 5.54; therefore, the apparent shifting of the wave records in time which occurs in Figs. 5.51 and 5.53 is assumed to be caused by errors in the lining up of the time records. It will be recalled, the method used to assemble the three physical experiments and the single numerical experiment which comprise each

figure involved, for the physical experiments, lining up the record from Gauge 5 of one experiment with Gauge 1 of the next experiment. Hence, if an error occurred in this procedure, all other records in that experiment would be misaligned. The numerical scheme required only a single alignment since all the time records were taken from a single experiment. An example of misalignment occurs in Fig. 5.51 where, comparing the shift in time between the physical and the numerical waves, the lower four waves appear to be aligned correctly but the next five, i.e., at $x = 0, 0.4, 0.86, 1.3$ and 1.66 m, all appear to have been shifted by the same amount and the upper four waves appear to have been shifted by an even greater amount.

As the waves propagate, the physical experiments exhibit smaller wave amplitudes than the numerical experiments. This is attributed to frictional effects in the physical experiments which are not accounted for in the numerical experiments.

Apart from these two effects, the physical and numerical experiments show reasonably good agreement particularly with regard to the shape of the waves; the errors in alignment actually highlight some aspects of this. For example, Fig. 5.52, i.e., the experiments with the 150 cm slope shows the good agreement in the shapes of the front faces of the waves while Figs. 5.51 and 5.53, i.e., the experiments with the transition slope and the 300 cm slope, show the good agreement in the shapes of the back faces of the waves. In Fig. 5.54, i.e., the experiment with the 450 cm slope, the waves appear to be aligned better and this shows the overall shapes of the waves in the

two experiments agree well except for the difference in amplitude which is caused by friction in the physical experiments.

As mentioned previously, on the basis of the agreement between the numerical and the physical experiments, the effect of the incident wave height on the transmitted wave was investigated by means of numerical experiments. For depth ratios: $h_1/h_2 = 2, 3$ and 4 , experiments were conducted to find the time record of the transmitted wave for various length ratios, L/ℓ , and for incident wave heights of $H_I/h_1 = 0, 0.05, 0.10$ and 0.15 .

To compare the transmitted waves, the time records at the bottom of the slope were aligned as is shown in Fig. 5.55 which is the result of a typical set of numerical experiments, in this case for a constant length ratio of $L/\ell = 2.00$. Note, the characteristic length, ℓ , varies with the relative incident wave height, H_I/h_1 , therefore a constant length ratio, L/ℓ implies the slope length, L , is different for different relative incident wave heights. The abscissa in Fig. 5.55 is the nondimensional time $t\sqrt{gh_1}/L$ and the ordinates are the relative amplitude η/H_I . These allow waves of different incident height H_I propagating over slopes of different length L to be compared because, as the lower figure shows, the waves at the bottom of the slope collapse into essentially one profile. The solid curve represents the linear nondispersive theory and is denoted $H_I/h_1 = 0$ to indicate it is independent of the wave height. The dashed curves represent the nonlinear dispersive theory for various relative incident wave heights, H_I/h_1 . The maximum wave

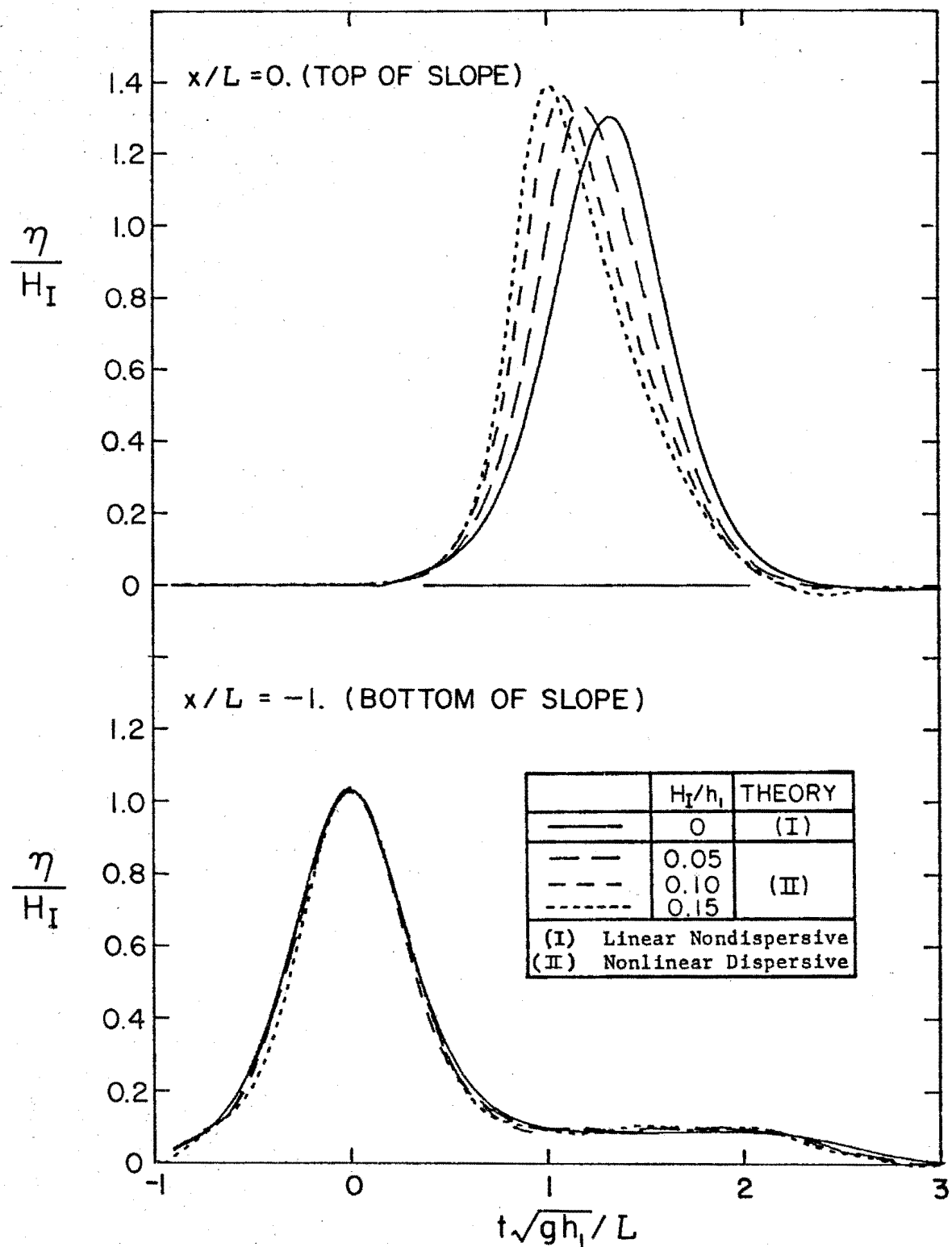


Fig. 5.55. Comparison of transmitted waves for incident waves of various heights for a length ratio of $L/\ell = 2.00$.

height considered was $H_I/h_1 = 0.15$ because incident waves higher than this resulted in transmitted waves whose height relative to the depth on the shelf (i.e., H_T/h_2) exceeded 0.7.

The figure shows, for a wave of finite height propagating over a slope, both the height and the slope of the front face of the transmitted wave increase with increasing relative incident wave height. As was mentioned in Section 3.1, the phenomenon of steepening of the front face of a wave is a nonlinear rather than a dispersive effect and, as shown in Fig. 3.3, nonlinear effects take place only after a certain propagation distance. Hence, the propagation distance for the cases shown in Fig. 5.55 must have been sufficient for nonlinear effects to develop. Waves with larger heights have steeper front faces which implies the propagation distance for nonlinear effects to become important is inversely proportional to the relative incident wave height, H_I/h_1 ; this will be discussed in quantitative manner, for waves propagating in constant depth, in Section 5.4.

Further illustration of the effects of wave height and length ratio on the transmitted wave is provided by the results of the numerical experiments (of which Fig. 5.55 was a typical example) presented in Figs. 5.56(a) and (b). Each experiment was for a different length ratio, L/λ , and comprised four waves with different relative incident wave heights. This resulted in a figure similar to Fig. 5.55 for each experiment but only the transmitted waves are presented in Figs. 5.56(a) and (b).

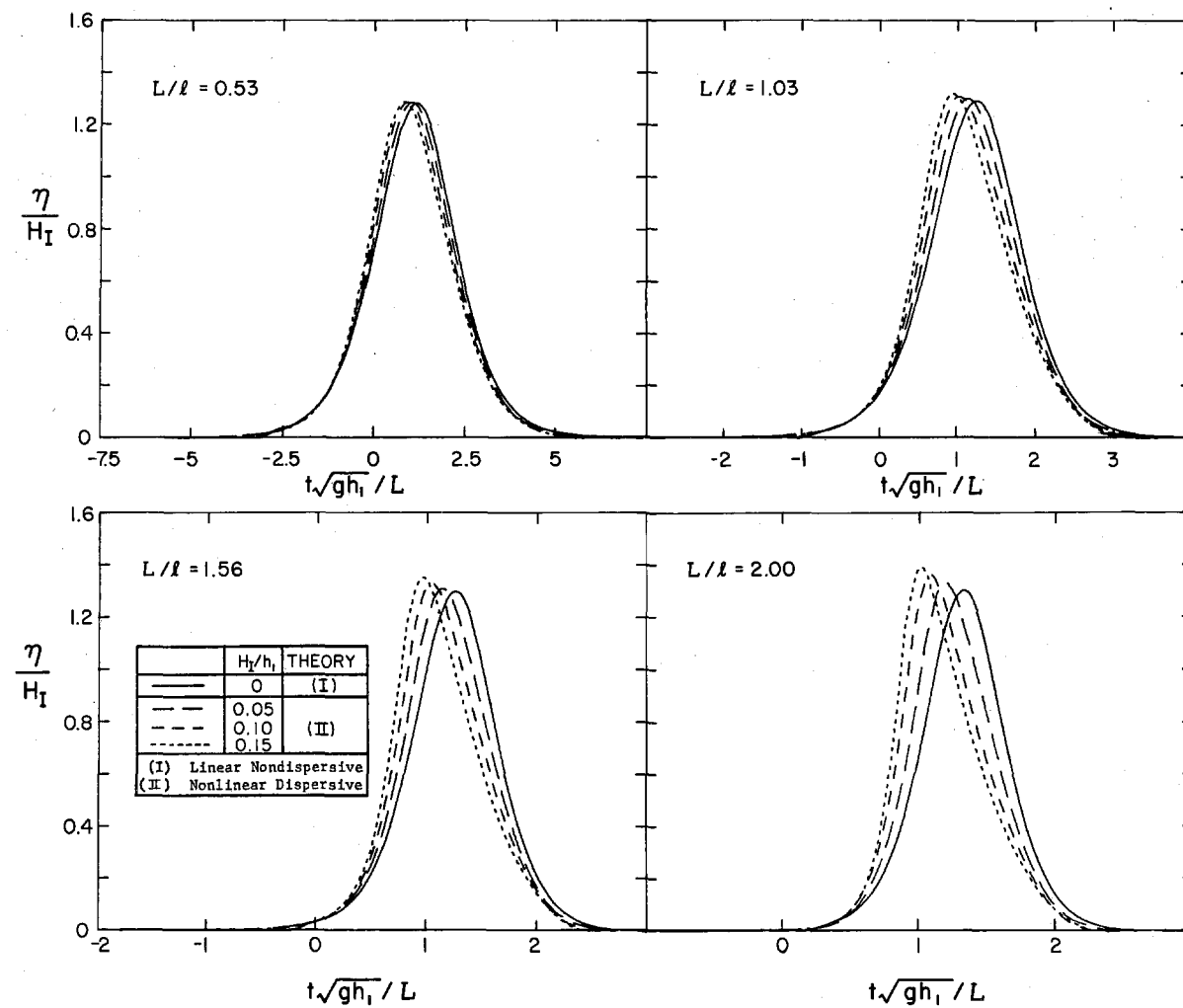


Fig. 5.56(a) Comparison of transmitted waves for incident waves of various heights and for various length ratios for a depth ratio of $h_1/h_2 = 3$.

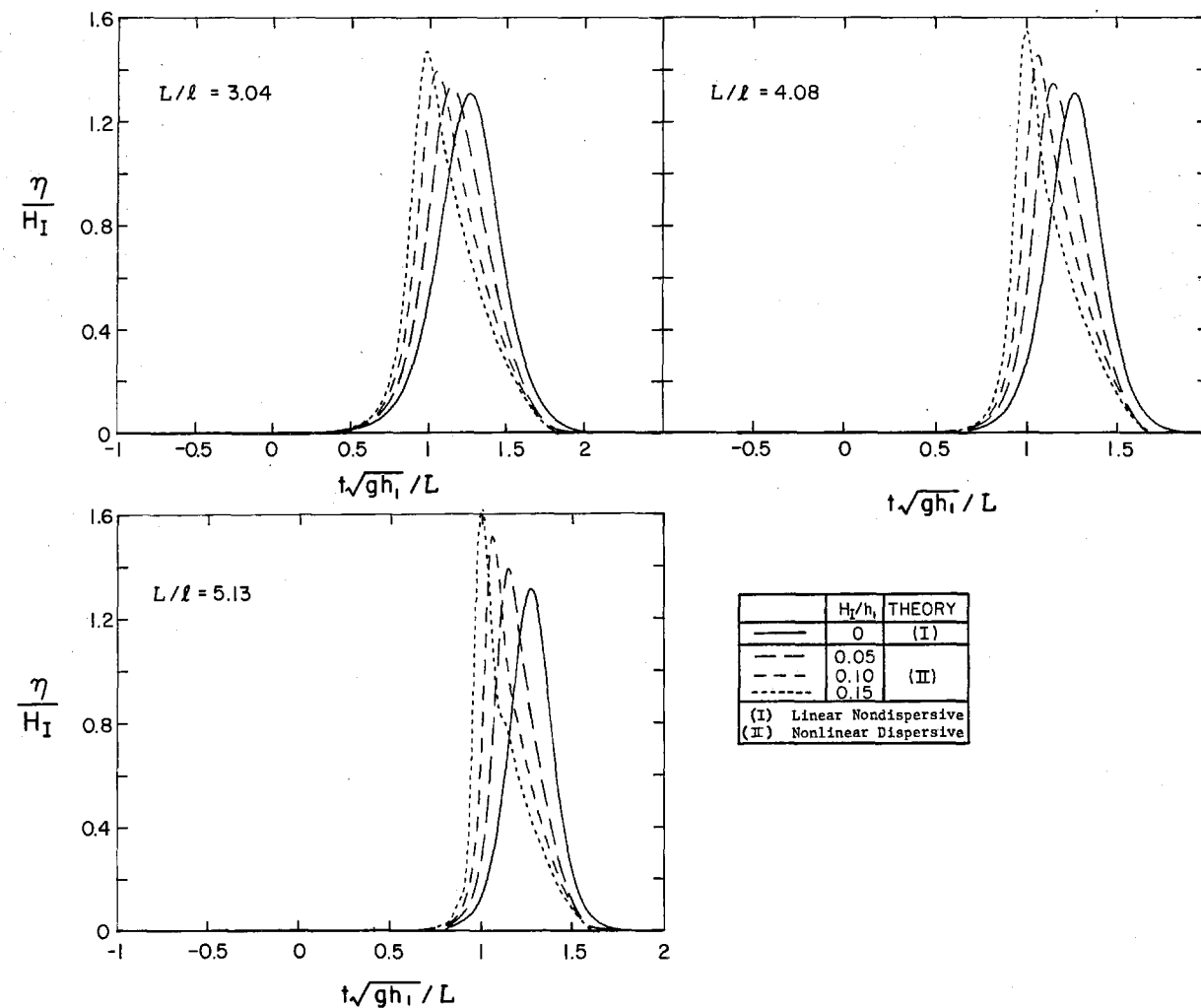


Fig. 5.56(b) Comparison of transmitted waves for incident waves of various heights and for various length ratios for a depth ratio of $h_1/h_2 = 3$.

In all cases the slope of the front face, i.e., the left face of the wave, for the larger waves is greater than for the smaller waves. As the length ratio increases for a given relative incident wave height, the slope of the front face also increases. For the length ratio of $L/\lambda = 0.53$, which would be considered an abrupt slope by the criterion described earlier for the linear nondispersing theory, there is evidence of steepening of the front face. This indicates, even when the characteristic length of the wave is twice the length of the slope, nonlinear effects are important to some degree.

For length ratios less than unity, the transmitted wave height ratio, H_T/H_I , is almost constant with relative incident wave height. However, as the length ratio increases the height increases and this is interpreted as indicating the growth in the importance of dispersive effects.

For the transmitted wave resulting from an incident wave with a relative height of $H_I/h_1 = 0.15$, when the length ratio is $L/\lambda = 3.04$ an abrupt change in slope appears in the back face of the wave and for larger length ratios this becomes more pronounced. Similarly for the wave resulting from the $H_I/h_1 = 0.10$ incident wave, a change in slope appears when the length ratio is $L/\lambda = 4.08$. However, no change in slope is evident in the back face of the waves resulting from the incident wave with the relative height of $H_I/h_1 = 0.05$. These changes in slope correspond to the emergence of a solitary wave from the main wave and its appearance is interpreted as an

indication nonlinear and dispersive effects are becoming equally important. This is the area investigated by Madsen and Mei (1969) and subsequently by Tappert and Zabusky (1971) and Johnson (1973) in which it was assumed the slope of the bottom was gradual, i.e., in terms of the parameters considered here, $(h_1 - h_2)/L \ll 1$.

In an effort to quantify these effects, for each of the numerical experiments performed, the following quantities were calculated:

- i) the maximum slope of the front face, $S = |\eta_t|_{\max}$,
- ii) the wave height, H_T , and
- iii) the Ursell Number defined as:

$$U = \frac{gH_T^3}{h_2^2 |\eta_t|_{\max}^2} , \quad (5.23)$$

(which is similar to the Ursell Number defined by Hammack (1972) except that the time derivative, η_t , is used instead of the space derivative, η_x).

To estimate what the difference in the solution would be if the linear nondispersive theory were used instead of the nonlinear dispersive theory, the relative difference in the maximum slope from that calculated by the linear theory, $(S - S_{\text{lin}})/S_{\text{lin}}$, and the relative difference in the transmitted wave height from that calculated by the linear theory, $(H_T - H_{T_{\text{lin}}})/H_{T_{\text{lin}}}$ were calculated. These quantities may be interpreted as indicating the relative importance of nonlinear and dispersive effects respectively. These data, for a depth ratio

of $h_1/h_2 = 3$, are plotted as functions of the length ratio in Fig. 5.57 (a) and (b). Figure 5.57(c) shows the Ursell Number defined by Eq. 5.23 plotted as a function of the length ratio; this figure will be discussed presently.

The curves in Fig. 5.57(a) and (b) represent the best fit of these data and also the data for depth ratios $h_1/h_2 = 2$ and 4 (which are presented in Appendix F) as given by the following expressions:

$$\frac{S - S_{\text{lin}}}{S_{\text{lin}}} = 1.49 \left(\frac{L}{\lambda} \right)^{0.77} \frac{h_1}{h_2} \left(\frac{h_1}{h_2} - 1 \right)^{0.28} \left(\frac{H_I}{h_1} \right)^{1.17}, \quad (5.24)$$

$$\frac{H_T - H_{T\text{lin}}}{H_{T\text{lin}}} = 0.18 \left(\frac{L}{\lambda} \right)^{1.28} \left(\frac{h_1}{h_2} - 1 \right)^{1.19} \left(\frac{H_I}{h_1} \right)^{1.38}. \quad (5.25)$$

Differences between the numerical results and the corresponding empirical expression (Eq. (5.24)) in Fig. 5.57(a) are primarily due to the fact that data for all values of h_1/h_2 (see Appendix F) were used to derive Eq. (5.24) whereas only those data for $h_1/h_2 = 3$ are presented in Fig. 5.57(a). The relative differences predicted by Eqs. (5.24) and (5.25) are compared to the actual data in Fig. 5.58(a) and (b). The scatter exhibited there is attributed to the approximate

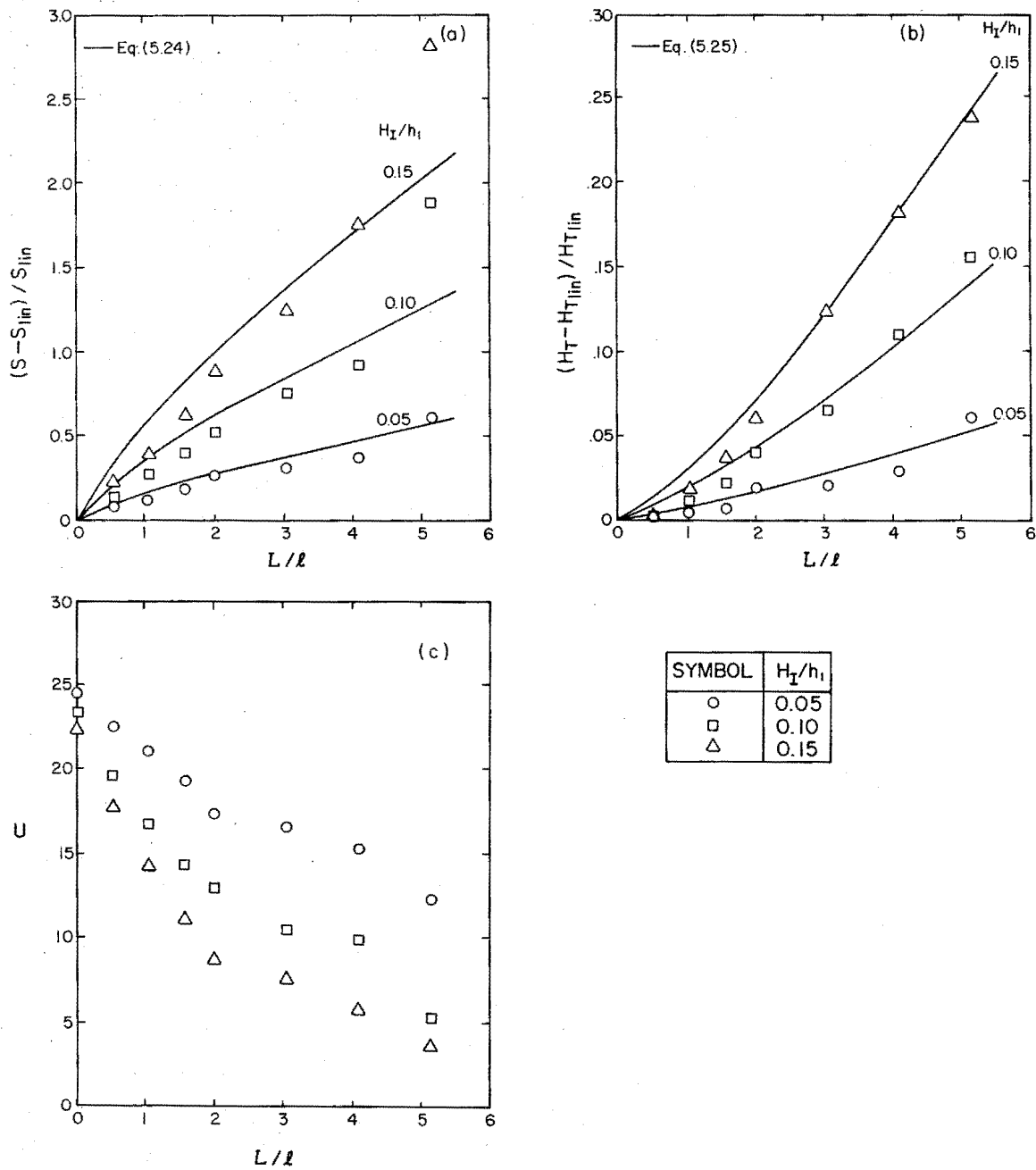


Fig. 5.57 Variation with length ratio of (a) the relative difference for slopes, $(S - S_{1\text{lin}})/S_{1\text{lin}}$, (b) the relative difference for wave heights, $(H_T - H_{T\text{lin}})/H_{T\text{lin}}$, and (c) the Ursell Number, U (for $h_1/h_2 = 3$).

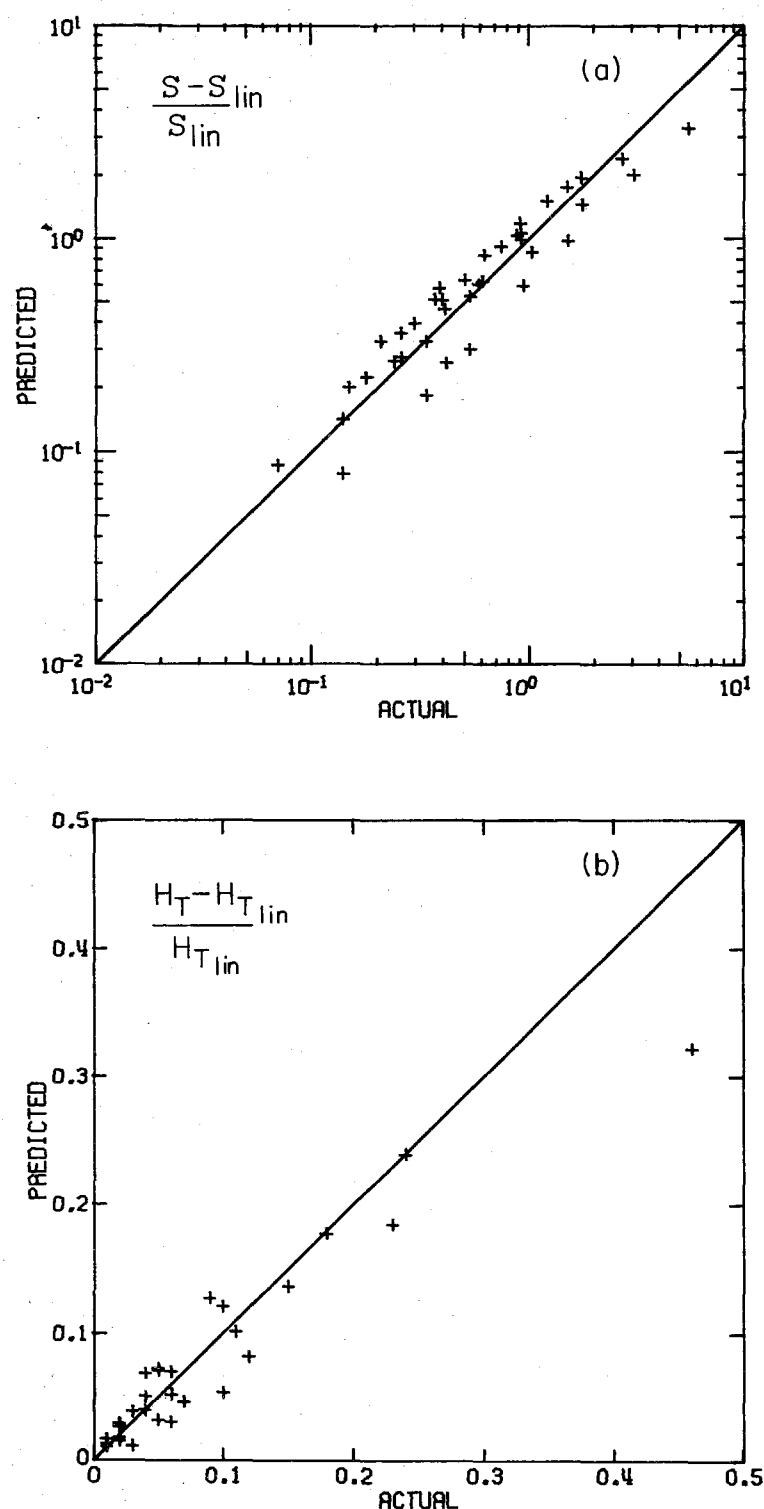


Fig. 5.58. Comparison of the actual and the predicted quantities given by (a) Eq. (5.24) and (b) Eq. (5.25).

nature of Eqs. (5.24) and (5.25) rather than to errors in the data which, it will be recalled, are from numerical experiments. Eqs. (5.24) and (5.25) may be used to give order-of-magnitude estimates of the conditions under which it is necessary to use the nonlinear dispersive theory rather than the linear nondispersive theory. For example, for a length ratio of $L/\ell = 2.0$ and a depth ratio of $h_1/h_2 = 3.0$, for the nonlinear analysis to be different by 10% from the linear analysis, the following relative incident wave heights would be required: $H_T/h_1 \geq 0.021$ for the slope of the front face and $H_T/h_1 \geq 0.19$ for the wave height.

In Fig. 5.57(c) the Ursell Number at $L/\ell = 0$ is approximately the Ursell Number of the incident wave multiplied by $(h_1/h_2)^2$. As the length ratio increases, the Ursell Number of the transmitted wave decreases which corresponds to the transmitted wave becoming more like a solitary wave for which the Ursell Number defined by Eq. (5.23) is $2.25/(1+H_T/h_2)$. The appearance of the changes in slope of the back face of the wave mentioned earlier occur when the Ursell Number is $U \approx 9$.

The transmission of solitary waves over a slope, in general, requires numerical solution of the nonlinear dispersive theory. However, in some circumstances, which can be determined using Eqs. (5.24) and (5.25), the simpler and more straightforward linear nondispersive theory may be used.

5.4 The Propagation of Long Waves on the Shelf

5.4.1 The Propagation of Solitary Waves on the Shelf

As a solitary wave propagates over a step onto a shelf, it was shown in Section 5.3.1 the wave height and frequency of the transmitted wave are of the same order as the incident solitary wave. Hence, using the Ursell Number defined by Eq. (5.23), the Ursell Number of the transmitted wave is approximately the Ursell Number of the incident solitary wave multiplied by $(h_1/h_2)^2$. Therefore, since the Ursell Number of the transmitted wave is not the Ursell Number of a solitary wave of the same height, the transmitted wave must change its shape as it propagates. Furthermore, since the Ursell Number of the transmitted wave is greater than the Ursell Number of the solitary wave of the same height, nonlinear effects will be more important than dispersive effects in the propagation. As was shown in Section 3.1, when nonlinear effects are greater than linear effects, the front face of the wave begins to steepen, (i.e., $|n_t|_{\max}$ and $|n_x|_{\max}$ increase). However, as this occurs the Ursell Number given by Eq. (5.23) decreases and thus nonlinear effects become relatively less important. In this section, this phenomenon is examined for the particular case of a transmitted wave with the form:

$$\eta = H_T \operatorname{sech}^2 \Omega_T t \quad . \quad (5.26)$$

Of particular interest is under what conditions and for what distance of propagation do nonlinear effects dominate.

For a transmitted wave given by Eq. (5.26) propagating on a shelf with a depth h_2 , the Ursell Number defined by Eq. (5.23) becomes:

$$U = \frac{27}{16} \left(\frac{H_T}{h_2} \right) \left[\frac{1}{\Omega_T \sqrt{h_2/g}} \right]^2. \quad (5.27)$$

There are two extremes to be considered:

- i) If the Ursell Number is small enough for a linear theory to apply, then for this linear theory the propagation is not dependent on the actual wave height, H_T . (One way this can take place is if $h_2 > h_1$, i.e., if the wave propagates into deeper water.)
- ii) If the Ursell Number is large enough for the nonlinear nondispersive theory to apply, it can be shown the propagation is not dependent on the frequency, Ω_T , and the independent variables, x and t , can be normalized with respect to the frequency Ω_T and the depth h_2 (for details of this and other aspects of the nonlinear nondispersive theory of propagation of sech^2 waves, see Appendix E).

Hence, if the linear dispersive theory applies, propagation is dependent on the frequency Ω_T but independent of the wave height H_T . Conversely, if the nonlinear nondispersive theory applies, propagation is dependent on the wave height H_T but independent of the frequency Ω_T . Between these extremes the nonlinear dispersive theory applies (represented by the KdV equation) where propagation is dependent on

both the frequency Ω_T and the wave height H_T .

To investigate these effects experiments were conducted using the results of Section 5.3.1, with the incident solitary wave height, H_I , and the upstream depth, h_1 , adjusted to give a range of relative wave heights, H_T/h_2 , and nondimensional frequencies, $\Omega_T\sqrt{h_2/g}$, for the transmitted wave. The wave propagating on the shelf was then recorded at eight locations downstream of the step. The desired wave heights and frequencies of the transmitted waves were $H_T/h_2 = 0.10, 0.30$ and 0.50 and $\Omega_T\sqrt{h_2/g} = 0.10, 0.13$ and 0.15 respectively. Of these nine experiments, only eight could be conducted because in the case of $H_T/h_2 = 0.50$ and $\Omega_T\sqrt{h_2/g} = 0.10$ the depth on the shelf was too small ($h_2 = 3$ cm).

The actual wave heights and frequencies are presented in Table 5.8 along with other experimental data. These include the distance between the locations at which the wave was recorded, Δx , and the Ursell Number of the transmitted wave, U_o . This Ursell Number varies from $U_o = 5.5$ which is 2.2 times that of the solitary wave of the same height to $U_o = 57.4$ which is 17 times that of the solitary wave of the same height.

The time records i.e., the variation of the water surface elevation with time, at various locations are presented in Figs. 5.59, 5.60 and 5.61 for the desired relative wave heights $H_T/h_2 = 0.10, 0.30$ and 0.50 , respectively. The ordinates are the amplitudes normalized with respect to the depth h_2 and the abscissas are the nondimensional time $t\sqrt{g/h_2}$. The distance between the locations at which the waves were

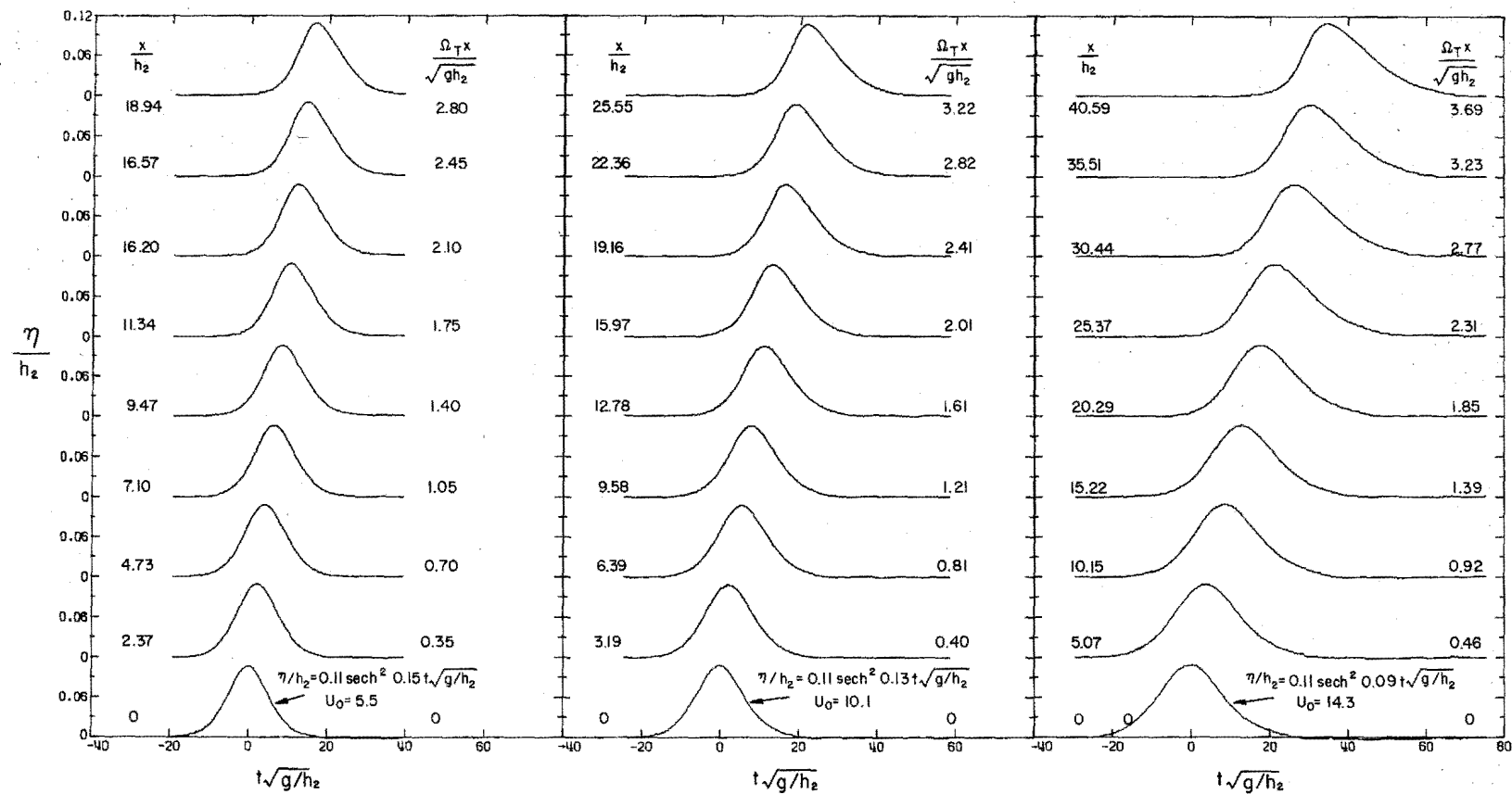


Fig. 5.59 Experimental wave records showing sech^2 waves with approximate relative wave height of $H_T/h_2 = 0.1$ propagating on the shelf.

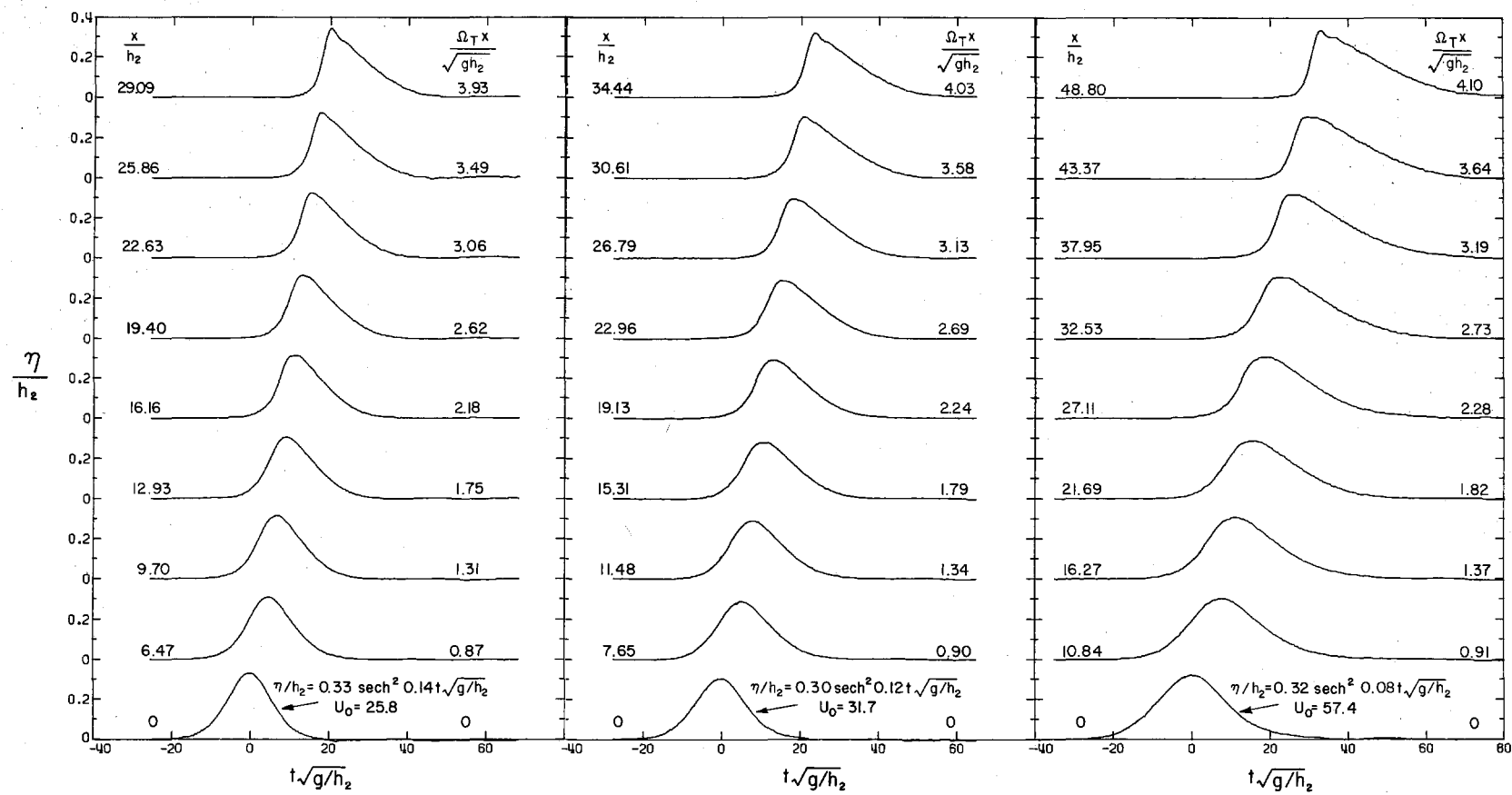


Fig. 5.60 Experimental wave records showing sech^2 waves with approximate relative wave height of $H_T/h_2 = 0.3$ propagating on the shelf.

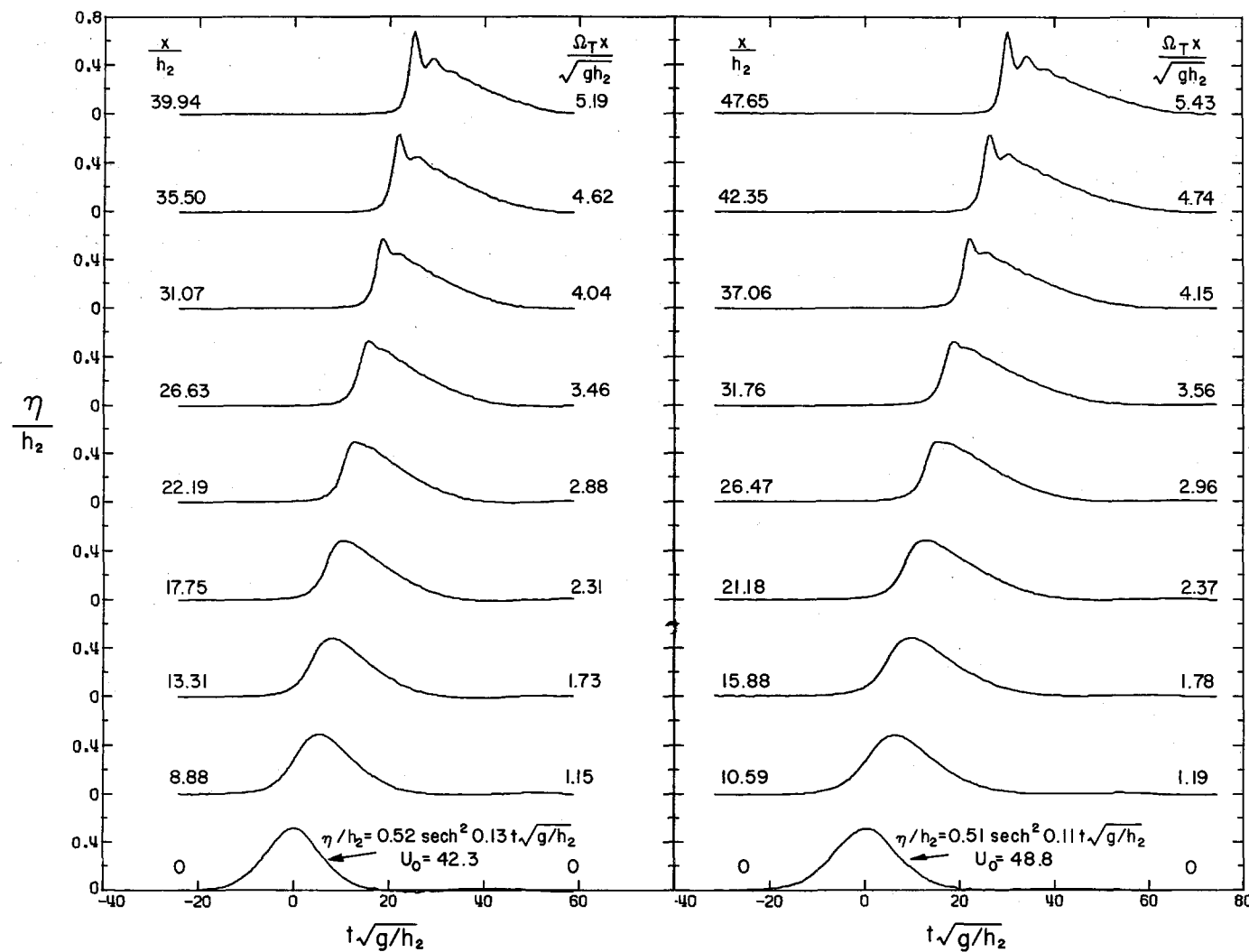


Fig. 5.61 Experimental wave records showing sech^2 waves with approximate relative wave height of $H_T/h_2 = 0.5$ propagating on the shelf.

Table 5.8 Details of the experiments for propagation of solitary waves on the shelf, shown in Figs. 5.58 to 5.60.

Expt No	Desired H_T/h_2	Desired $\Omega_T \sqrt{\frac{h_2}{g}}$	h_1 (cm)	h_2 (cm)	H_I (cm)	Δx (cm)	Measured H_T/h_2	Measured $\Omega_T \sqrt{\frac{h_2}{g}}$	U_o
1	0.1	0.15	34.55	19.01	2.01	45.0	0.106	0.148	5.5
2	0.1	0.13	29.63	14.01	1.48	45.0	0.108	0.126	10.1
3	0.1	0.10	24.41	8.87	0.92	45.0	0.109	0.091	14.3
4	0.3	0.15	22.50	6.96	2.21	22.5	0.330	0.135	25.8
5	0.3	0.13	21.42	5.88	1.77	22.5	0.304	0.117	31.7
6	0.3	0.10	15.37	4.15	1.22	22.5	0.322	0.084	57.4
7	0.5	0.15	20.61	5.07	2.51	22.5	0.519	0.130	42.3
8	0.5	0.13	19.79	4.25	2.05	22.5	0.512	0.112	48.8

recorded is listed as x/h_2 and also $\Omega_T x/\sqrt{gh_2}$. The latter quantity is of interest because as is shown in Appendix E if the propagation were predicted by the nonlinear nondispersive theory, the shape of the waves would be similar for waves with the same initial relative height, H_T/h_2 , at equal values of $\Omega_T x/\sqrt{gh_2}$. In fact, inspection of the figures, particularly Figs. 5.60 and 5.61 where the relative distances defined by $\Omega_T x/\sqrt{gh_2}$ are approximately the same, shows the shape of the waves are similar as the nonlinear nondispersive theory predicts. However the increase in the height of the crest with propagation distance evident for each experiment in Figs. 5.60 and 5.61 is not predicted by the nonlinear nondispersive theory and hence must be caused by the interaction of nonlinear effects and dispersion. To find the distance over which the nonlinear nondispersive theory applies, the waves at $x/h_2 = 0$ were propagated by this theory

and by the nonlinear dispersive theory (i.e., the KdV equation) and compared with the experiments. The comparisons for the experiment with desired relative wave height $H_T/h_2 = 0.5$ and desired nondimensional frequency $\Omega_T \sqrt{h_2/g} = 0.15$ which are considered typical are presented in Figs. 5.62 to 5.64, where the experiment is represented by the solid curves and the theories by the dashed curves. The nonlinear nondispersive theory is not presented in Fig. 5.64 because it predicts the wave breaks at $x/h_2 \approx 29$ and the theory is invalid after this occurs. In addition to the nonlinear nondispersive theory and the nonlinear dispersive theory, the linear nondispersive theory also is presented. As mentioned earlier the latter predicts the shape of the wave remains the same and the wave propagates with celerity $c = \sqrt{gh_2}$. Figure 5.62 shows the nonlinear dispersive theory and the nonlinear nondispersive theory are almost coincident for the initial 13.3 depths from the step and both predict a greater celerity than the linear nondispersive theory. The experimental data follow the nonlinear theories better than the linear theory but have a smaller wave height and smaller front face slope, $|n_t|_{\max}$, than the nonlinear theories predict. Some reasons for this will be discussed presently.

Figure 5.63 shows as the wave propagates further onto the shelf the results from the two nonlinear theories diverge; i.e., the nonlinear nondispersive theory predicts the wave height will remain constant but the front face of the wave will continue to steepen until the wave breaks, while the nonlinear dispersive theory predicts the wave will begin to transform into a series of solitary waves.

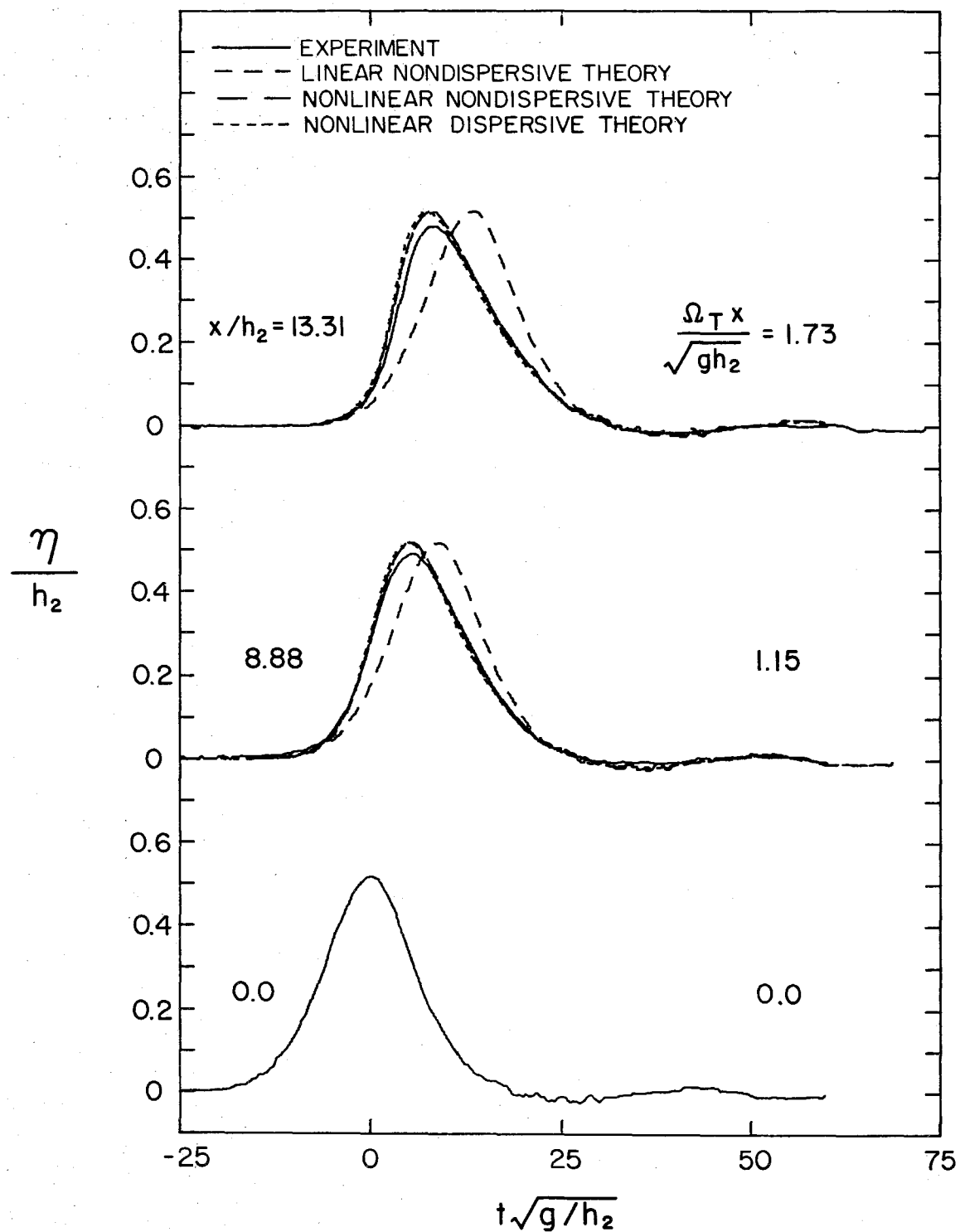


Fig. 5.62 Comparison of waves measured experimentally with those calculated by various theories at locations given by $x/h_2 = 0, 8.88$ and 13.31 .

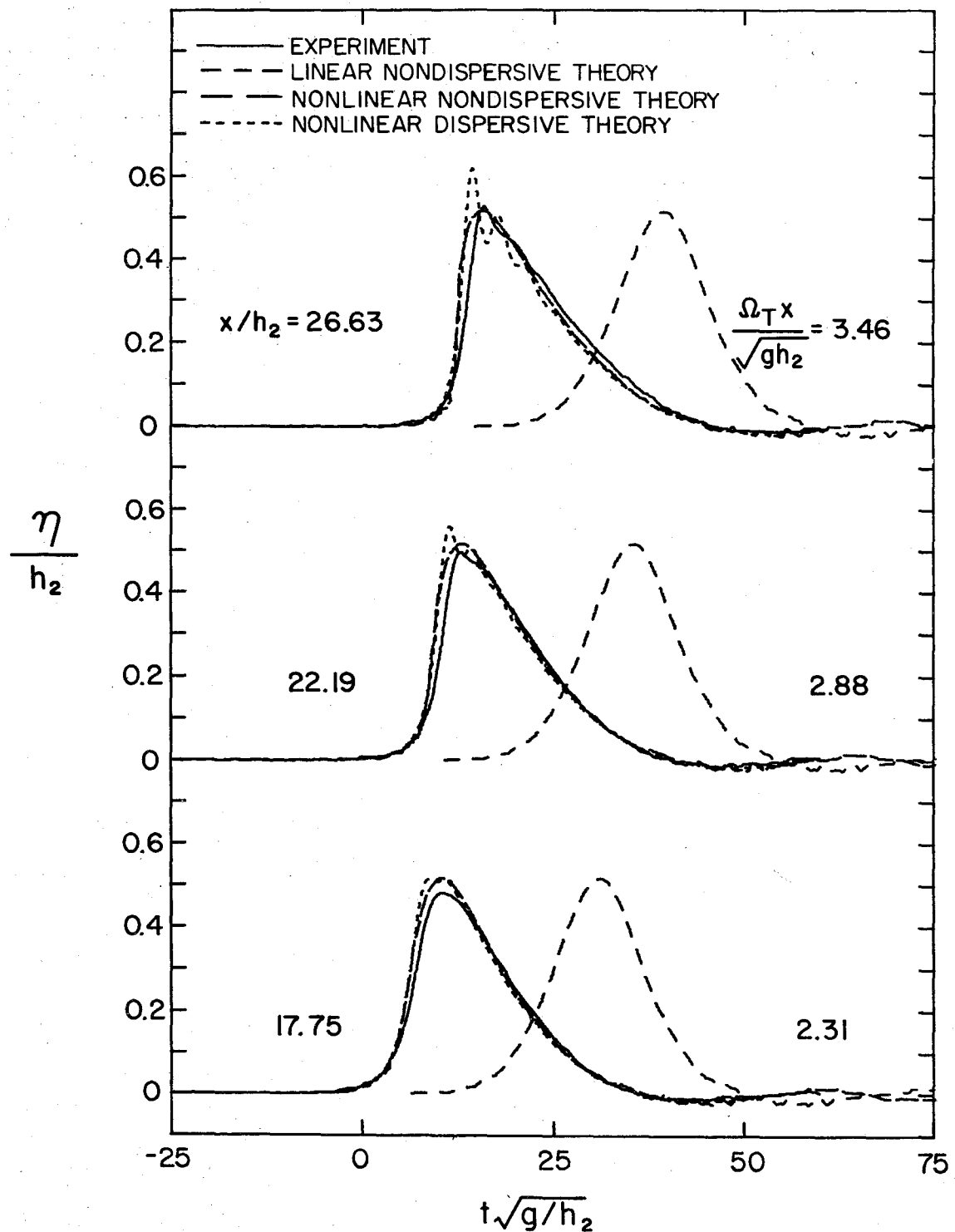


Fig. 5.63 Comparison of waves measured experimentally with those calculated by various theories at locations given by $x/h_2 = 17.75, 22.19$ and 26.63 .

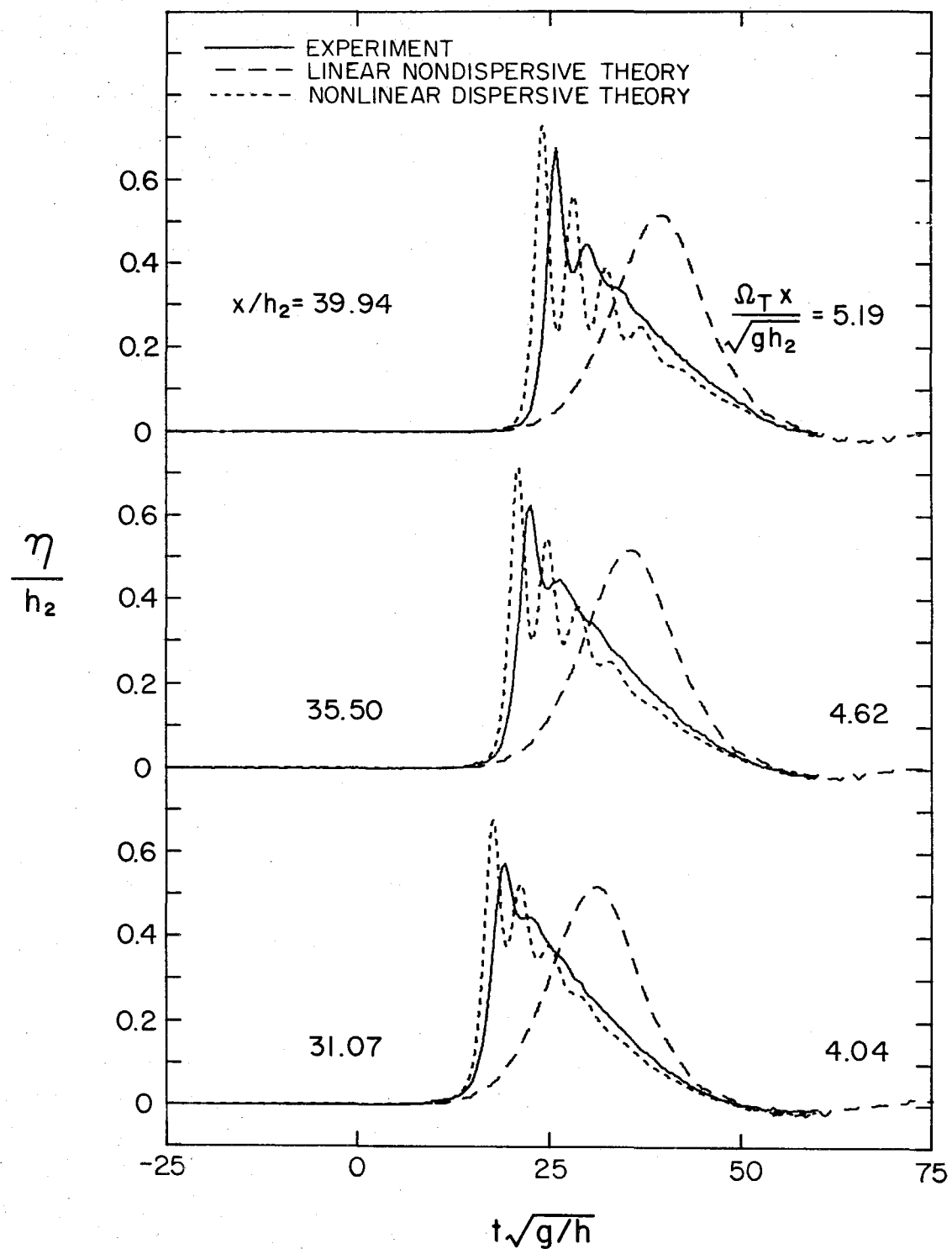


Fig. 5.64 Comparison of waves measured experimentally with those calculated by various theories at locations given by $x/h_2 = 31.07, 35.50$ and 39.94 .

The experimental profiles again exhibit a smaller wave height and smaller front face slope, but notice at $x/h = 26.63$ the experimental wave height is slightly greater than the wave height predicted by the nonlinear nondispersive theory and on the back face of the wave there is a small trough indicating a second wave is beginning to emerge.

In Fig. 5.64 the nonlinear nondispersive theory is omitted because it predicts the wave breaks between $x/h_2 = 26.63$ and 31.07. This figure shows there is a considerable difference between the results of the experiment and those of the nonlinear dispersive theory; some possible reasons for this are proposed as follows.

As the wave propagates from deep water into shallow water one would expect boundary layer separation to occur on the shelf close to the step. To investigate this, the water in the region of the step was mixed with fine aluminum powder, a wave was generated and the resulting motion of the aluminum particles was photographed. The results for an incident solitary wave of height $H_I = 2.0$ cm propagating from a depth $h_1 = 20.5$ cm into a depth $h_2 = 5.0$ cm (a) over the step and (b) over the half-sine transition slope are presented in Fig. 5.65. The photographs were taken at intervals of $\frac{1}{4}$ sec, and from left to right show the leading edge, the crest and the trailing edge of the wave propagating onto the shelf. The still water level is denoted in each photograph by the horizontal line. For the step, the region of separation appears to grow to be about 60% of the depth on the shelf. However, this is reduced to about 20% of the depth when the



(a)



(b)

Fig. 5.65 Views of the separation caused by a solitary wave propagating over (a) the step and (b) the half-sine transition.
($h_1 = 20.50$ cm, $h_2 = 4.96$, $H_I = 2.0$ cm)

half-sine transition slope is used.

To examine the effect the different regions of separation have on the height of the wave as it propagates, experiments were conducted with the step and with the half-sine transition and the changing height of the waves as they propagate was compared. The results are presented in Fig. 5.66 where for four different depths on the shelf the relative wave height, H/h_2 , is plotted as a function of the relative distance from the edge of the shelf, x/h_2 . For each of the experiments the incident solitary wave had a relative height of $H_I/h_1 = 0.1$. The transmitted waves, i.e., the waves at $x = 0$, evidently have almost the same height for the step as they do for the half-sine transition. In fact, as is shown in Table 5.9 which compares the transmitted wave data, the shape of the transmitted waves in the form of the transmitted wave frequency, Ω_T , also is essentially the same for the step as it is for the half-sine transition. Thus, as was noted in Section 5.3.1 the transition slope has no effect on the transmitted wave. However, for the smaller depths, i.e., $h_2 = 7.77$ and 6.22 cm, the height of the wave propagating on the shelf which had propagated over the half-sine transition increases faster than the wave which had propagated over the step. This reflects the effect of the different extents of the zone of boundary layer separation shown in Fig. 5.65.

In addition, dissipation due to friction on the sidewalls and the bottom which would be expected to be common to waves both from the step and from the half-sine transition causes the wave height to

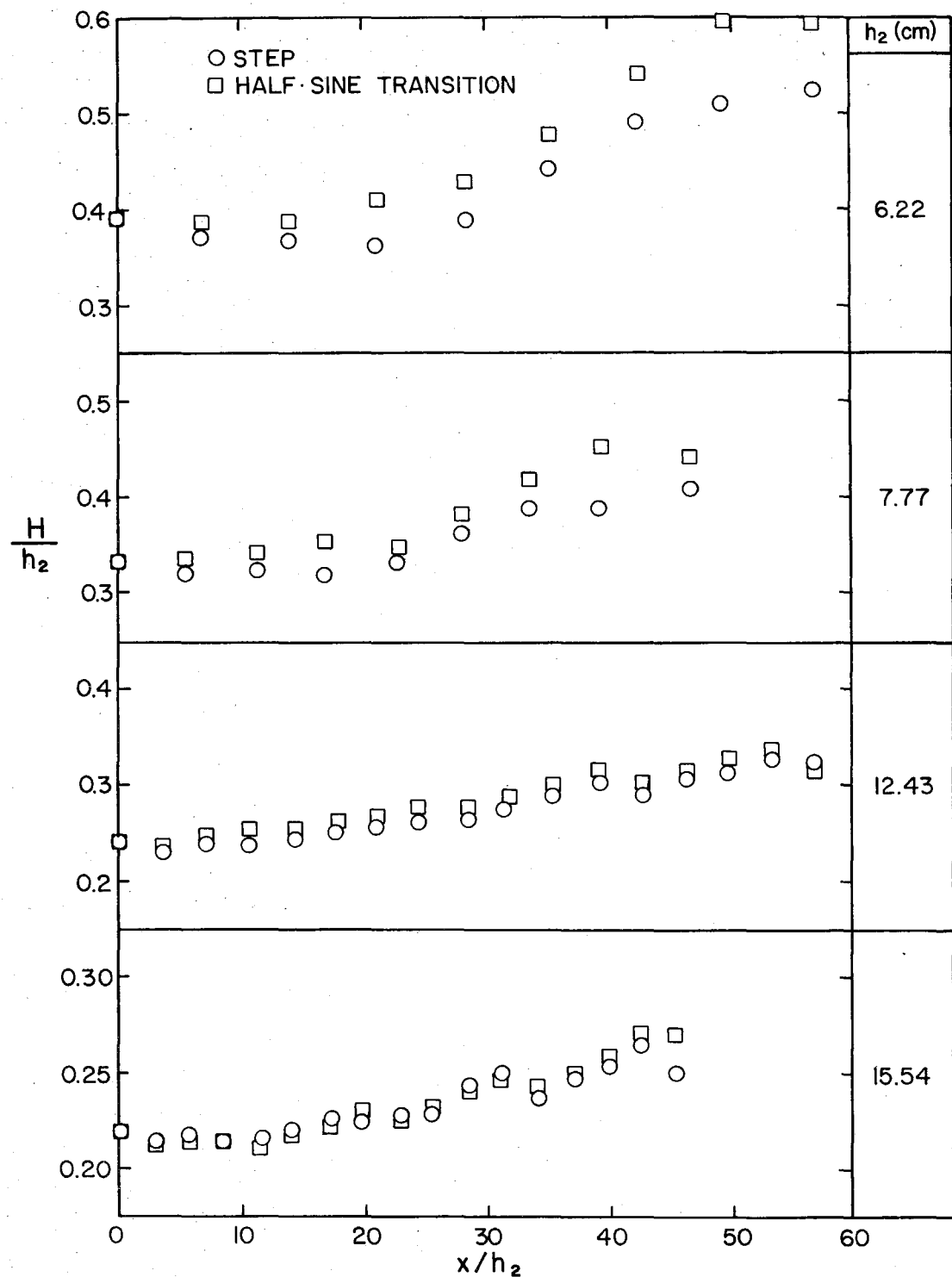


Fig. 5.66 Variation of the relative height, H/h_2 , of a wave as it propagates on the shelf. Comparison of experiments in which the step was used with those in which the half-sine transition was used.

Table 5.9 Comparison of the transmitted wave data for the experiments presented in Fig. 5.66.

h_2 (cm)	H_T/h_2		$\Omega_T \sqrt{h_2/g}$	
	STEP	TRANS	STEP	TRANS
6.22	0.393	0.385	0.138	0.135
7.77	0.331	0.339	0.144	0.142
12.43	0.246	0.246	0.201	0.193
15.54	0.218	0.217	0.193	0.192

be less than the theories predict. The cumulative effect on the shape of the wave which friction may have is postulated in the following way. If the shape of the wave is changing in a way which is proportional to the wave height, and the wave height is decreasing because of friction, then the shape of the wave will be different than if friction were absent.

Hence, the differences between experiment and theory exhibited in Fig. 5.64 are attributed to dissipative effects. Thus, in view of these problems and of the difficulty of accurately prescribing the transmitted wave, further analysis of the propagation of a sech^2 wave was conducted by analytical means. As mentioned earlier, for some distance from the step the nonlinear dispersive theory and the nonlinear nondispersive theory appear to predict the same results. However, the theories eventually diverge and the distance which the wave has travelled when they diverge a given amount represents the propagation distance necessary for dispersive effects to become important. To find this distance it was necessary to propagate waves with both theories and determine the location at which they diverged. For this study the location of the divergence of the

theories was defined as the point at which the Ursell Numbers defined by Eq. (5.23) became different by 10%. The Ursell Number was used because it is sensitive to changes in both the maximum slope of the wave, $|\eta_t|_{\max}$, and the maximum wave amplitude, η_{\max} . The latter is of particular importance because the nonlinear nondispersive theory predicts the amplitude of the crest remains constant, hence any change in the crest height indicates dispersive effects have become important. However differences in the maximum slope of the wave also indicate a difference in the theories so its effect needs to be included also.

The problem of comparing the two theories for waves given by Eq. (5.26) with various heights and frequencies is simplified considerably by recalling that the nonlinear nondispersive theory is independent of the nondimensional frequency $\Omega_T \sqrt{h_2/g}$. Hence, for a particular relative wave height H_T/h_2 the solution is the same for all frequencies, $\Omega_T \sqrt{h_2/g}$, providing the independent variables x and t are normalized with respect to the frequency (i.e., $\Omega_T x/\sqrt{gh_2}$ and $\Omega_T t$ respectively). The propagation distance over which most of the numerical experiments were conducted was the distance the nonlinear nondispersive theory predicts the wave will travel from the point at which its time record is given by Eq. (5.26) to the point at which the maximum slope, $|\eta_t|_{\max}$, is infinite, i.e., the wave breaks. This distance, denoted x_b , is plotted as a function of the relative wave height, H_T/h_2 , in Fig. 5.67 where the ordinate is the normalized distance $\Omega_T x_b/\sqrt{gh_2}$. The relationship plotted in Fig. 5.67 cannot be expressed in closed form (see Appendix E); however, for $H_T/h_2 < 0.05$,

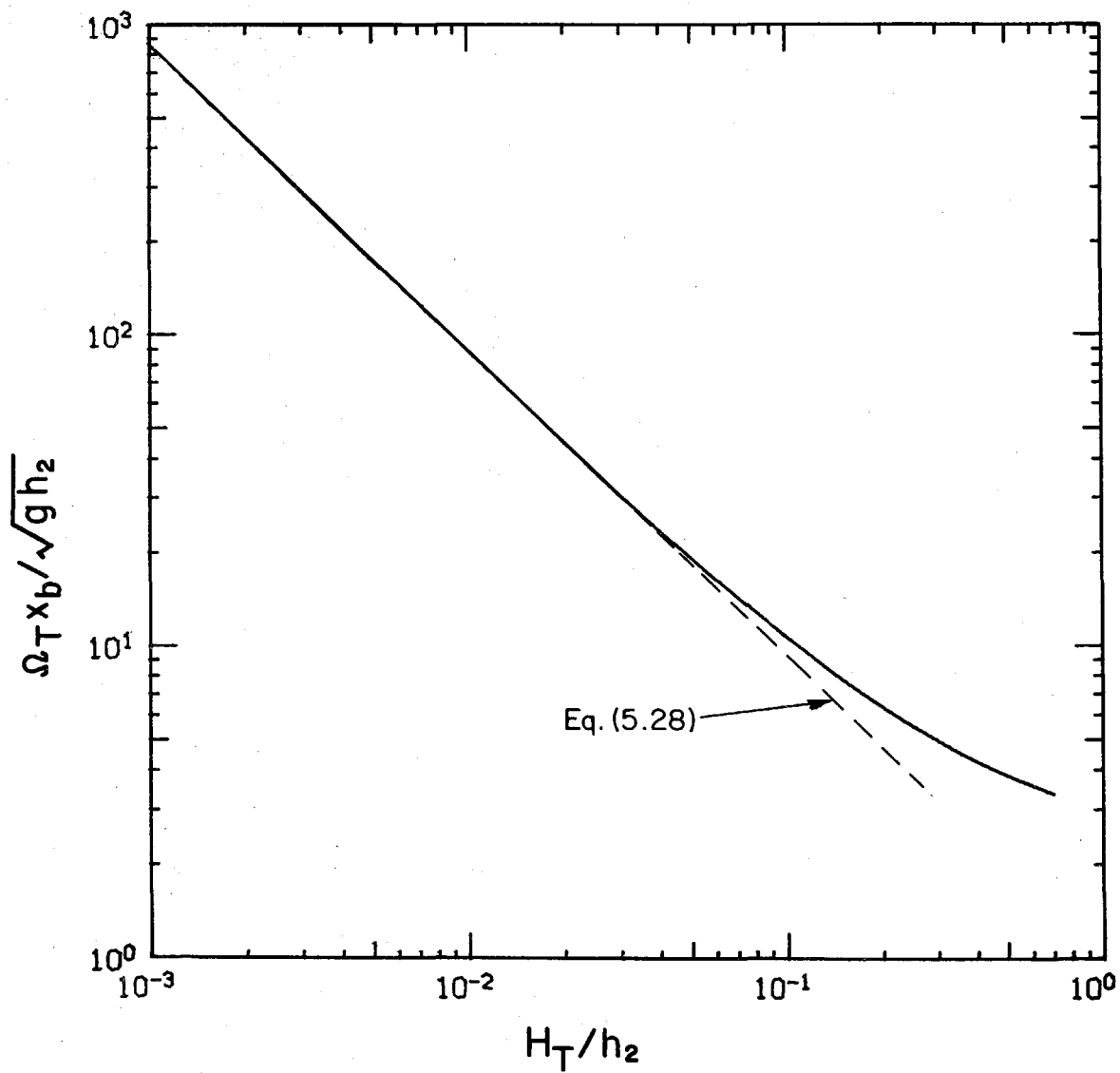


Fig. 5.67 Theoretical variation of the distance a sech² wave propagates to breaking, $\Omega_T x_b / \sqrt{gh_2}$, with relative wave height, H_T / h_2 .

the curve in Fig. 5.67 is essentially linear and is given by the relationship:

$$\frac{\Omega_T x_b}{\sqrt{gh_2}} \approx 0.93 \left(\frac{H_T}{h_2} \right)^{-0.99} . \quad (5.28)$$

The significance of Eq. (5.28) for waves with small height, i.e., $H_T/h_2 < 0.05$, will be discussed presently.

Comparisons of propagation by the two theories for relative wave heights $H_T/h_2 = 0.1, 0.3$ and 0.5 are presented in Figs. 5.68, 5.69 and 5.70 in each of which the quantity $U\Omega_T^2 h_2/g$ is plotted as a function of the propagation distance normalized with respect to the distance to breaking, x/x_b . The ordinate, $U\Omega_T^2 h_2/g$, where U is defined by Eq. (5.23), can be thought of as an Ursell Number in which the time used is the normalized time $\Omega_T t$, since:

$$\frac{U\Omega_T^2 h_2}{g} = \frac{n_{\max}^3}{h_2 |n_t|_{\max}^2} \Omega_T^2 . \quad (5.29)$$

In each of the figures the lower curve corresponds to the nonlinear nondispersive theory. (Using the ordinate, $\Omega_T^2 h_2/g$, this is a single curve for all values of the frequency Ω_T .) The theory predicts the quantity $U\Omega_T^2 h_2/g$ decreases as the wave propagates which corresponds to the front face of the wave steepening, i.e., $|n_t|_{\max}$ increases. Eventually $U\Omega_T^2 h_2/g$ becomes zero when the front face becomes vertical and the wave breaks.

The other curves in the figures are the variation of $U\Omega_T^2 h_2/g$

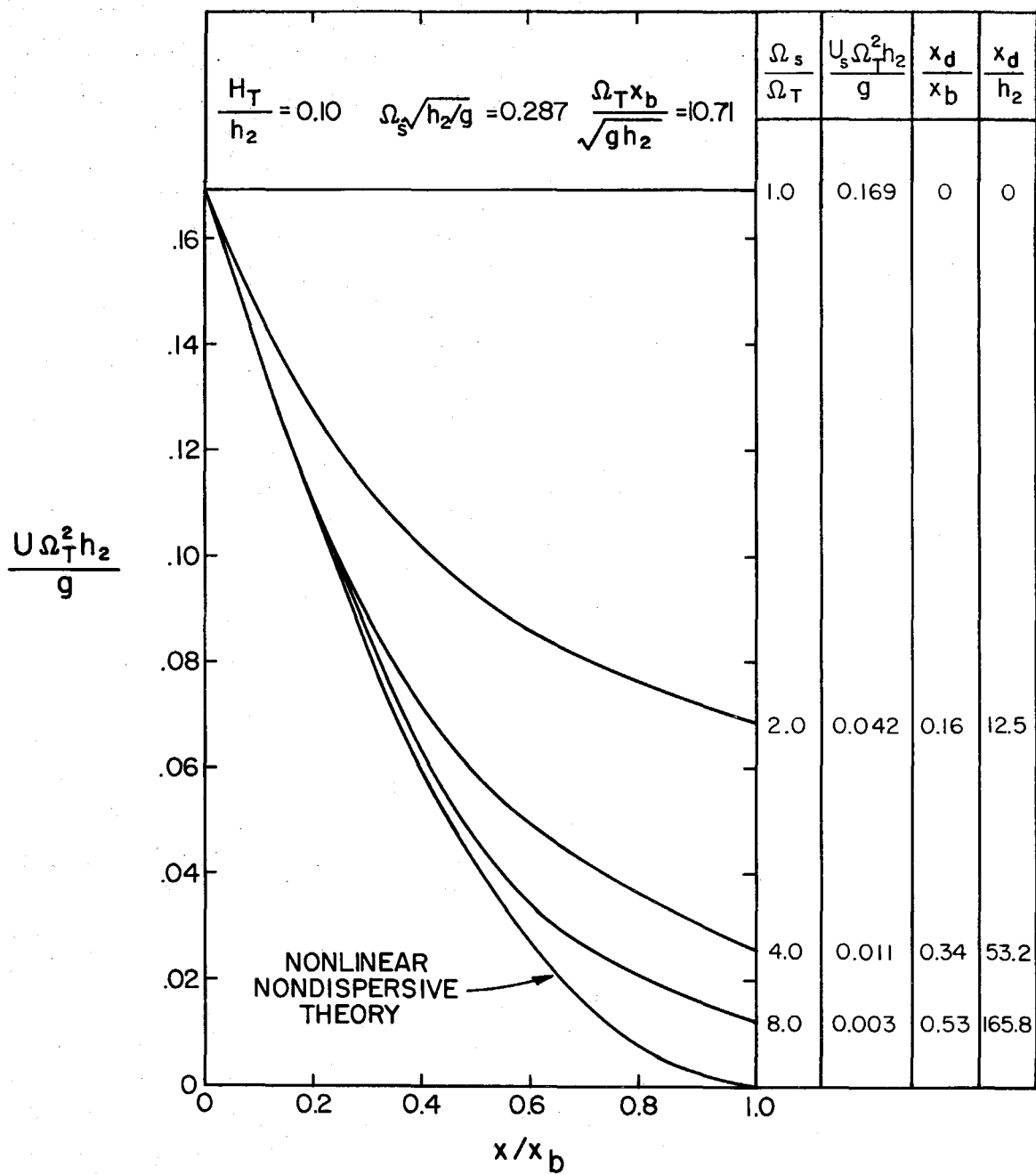


Fig. 5.68 Theoretical variation of the Ursell Number, $U_s \Omega_T^2 h_2 / g$, with propagation distance, x/x_b , for an initial relative wave height of $H_T/h_2 = 0.1$; nonlinear dispersive and nondispersive theories.

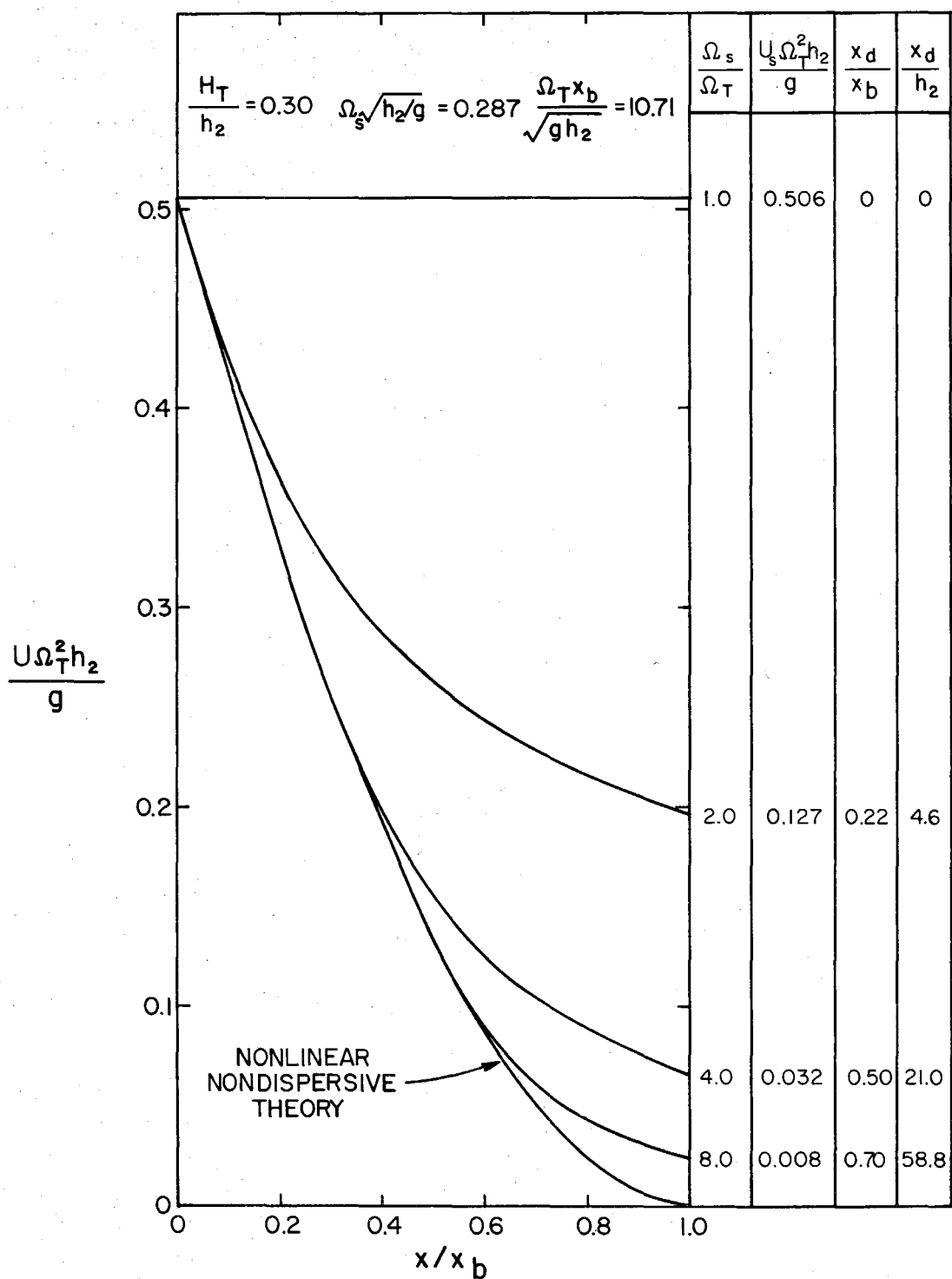


Fig. 5.69 Theoretical variation of the Ursell Number, $U_s \Omega_T^2 h_2 / g$, with propagation distance, x/x_b , for an initial relative wave height of $H_T/h_2 = 0.3$; nonlinear dispersive and nondispersive theories.

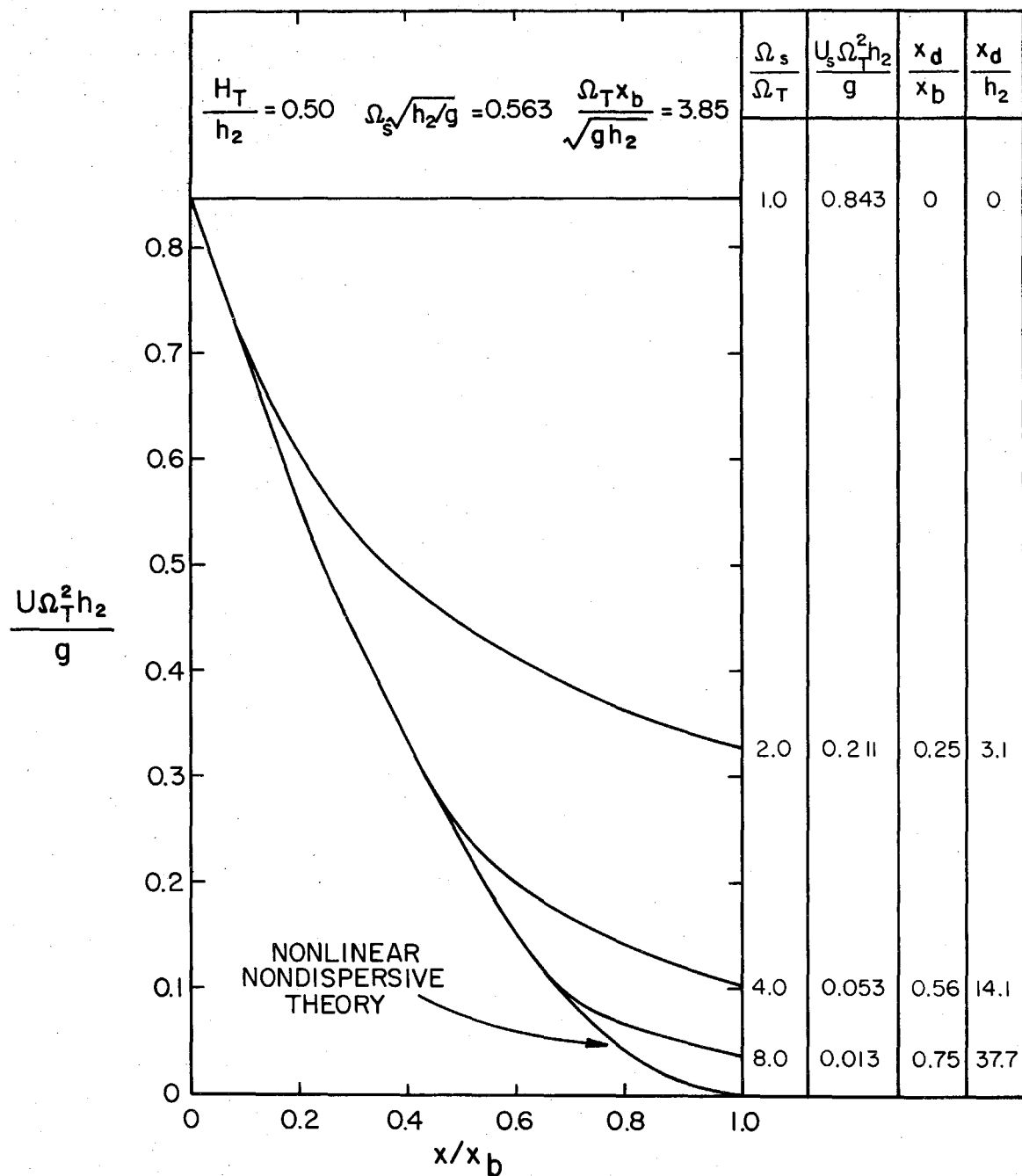


Fig. 5.70 Theoretical variation of the Ursell Number, $U_s \Omega_T^2 h_2 / g$, with propagation distance, x/x_b , for an initial relative wave height of $H_T/h_2 = 0.5$; nonlinear dispersive and nondispersive theories.

with propagation distance calculated by the nonlinear dispersive theory for frequencies relative to the frequency of the solitary wave, Ω_s , of $\Omega_T/\Omega_s = 1., 1/2, 1/4$ and $1/8$. These correspond to waves which are less peaked than the solitary wave of the same height. Clearly, if the wave at $x=0$ is a solitary wave, the nonlinear dispersive theory predicts the quantity $U\Omega_T^2 h_2/g$ will remain constant. However, Figs. 5.67 to 5.70 show if the frequency of the wave at $x=0$ is less than the frequency of the solitary wave of the same height, the quantity $U\Omega_T^2 h_2/g$ decreases as the wave propagates. This corresponds partly to the steepening of the front face of the wave as for the nonlinear nondispersive theory but, in addition, dispersive effects cause the wave height to increase (as was evident in Figs. 5.60 and 5.61); the combination results in $U\Omega_T^2 h_2/g$ increasing relative to the nonlinear nondispersive theory for the same propagation distance. The curves tend asymptotically to the value of $U\Omega_s^2 h_2/g$ for a solitary wave (denoted $U\Omega_s^2 h_2/g$) which is reached when the leading wave emerges from the group. $U\Omega_s^2 h_2/g$ is listed in the column at the right of each figure.

The distance to the point at which the theories diverge by 10%, x_d , (i.e., the propagation distance for dispersive effects to become important) is presented in the tables in Figs. 5.68 to 5.70 as x_d/h_2 and x_d/x_b . From the data, an approximate relationship for x_d/h_2 as a function of the relative wave height, H_T/h_2 and the relative frequency, Ω_T/Ω_s , can be determined. Using regression analysis, the expression:

$$\frac{x_d}{h_2} \approx 1.68 \left(\frac{\Omega_s}{\Omega_T} - 1 \right)^{1.31} \left(\frac{H_T}{h_2} \right)^{-0.88} , \quad (5.30)$$

was found to give the best fit of the data, with coefficient of determination of $r^2 = 0.9988$. This equation along with the numerical data used to obtain it are plotted in Fig. 5.71.

For a solitary wave propagating onto a shelf, if it is assumed the frequency, Ω_T , and the height, H_T , of the transmitted wave are the same as those of the incident wave, as was shown to be approximately true in Section 5.3.1, the ratio of frequencies is given by

$\Omega_s/\Omega_T \approx h_1/h_2$ and Eq. (5.30) becomes:

$$\frac{x_d}{h_2} \approx 1.68 \left(\frac{h_1}{h_2} - 1 \right)^{1.31} \left(\frac{H_T}{h_2} \right)^{-0.88} , \quad (5.31(a))$$

or, in terms of the incident wave:

$$\frac{x_d}{h_2} \approx 1.68 \left(\frac{h_1}{h_2} - 1 \right)^{1.31} \left(\frac{h_1}{h_2} \right)^{-0.88} \left(\frac{H_I}{h_1} \right)^{-0.88} . \quad (5.31(b))$$

The use of Eqs. (5.30) and (5.31) is restricted to the range of the data used to obtain them, i.e., $0.1 \leq H_T/h_2 \leq 0.5$ and $\Omega_T \leq \Omega_s$. (It was not realistic to generate data for waves with relative heights $H_T/h_2 < 0.1$ because the distance to breaking, which is given by Eq. (5.28) in this case, becomes prohibitively large and the numerical solution of the nonlinear dispersive theory requires thousands of time steps instead of the hundreds of time steps required for waves with $H_T/h_2 \geq 0.1$.)

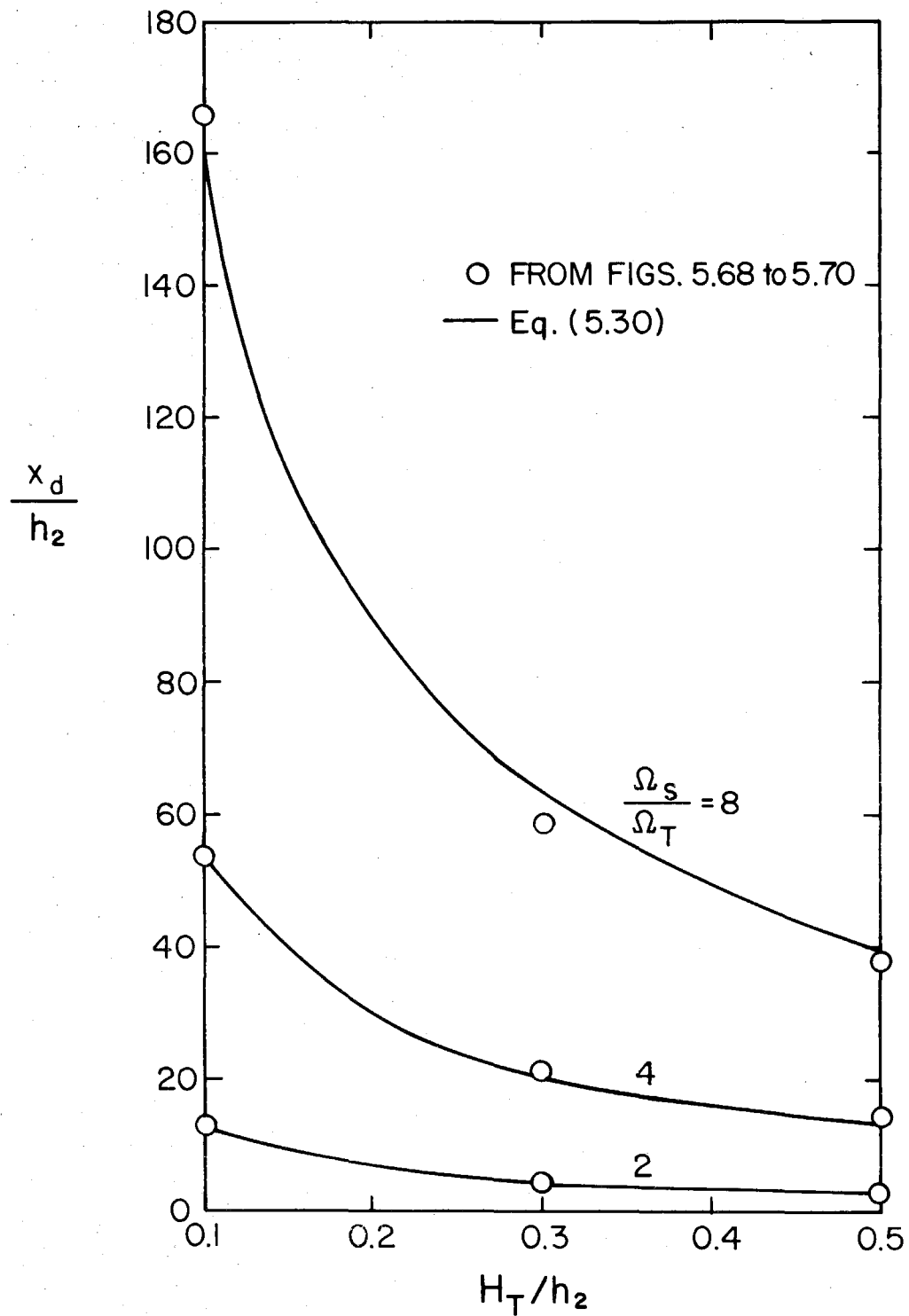


Fig. 5.71 Theoretical variation of the distance for dispersive effects to become important, x_d/h_2 , with relative wave height, H_T/h_2 .

For the sech^2 waves considered, the distance for nonlinear effects to become important can be calculated in a manner similar to the way the distance for dispersive effects to become important was calculated. This involves propagating a wave by the linear nondispersive theory and by the nonlinear nondispersive theory and finding the distance, x_n , for the quantities $U\Omega_T^2 h_2/g$ to become different by 10%. Recall, the linear nondispersive theory predicts the wave retains its original shape, hence for this theory $U\Omega_T^2 h_2/g$ is constant. For the nonlinear nondispersive theory, the propagation distance for $U\Omega_T^2 h_2/g$ to change by 10% can be expressed analytically but not in closed form (see Appendix E). Hence the nondimensional distance $\Omega_T x_n / \sqrt{gh_2}$ is presented graphically as a function of the relative wave height, H_T/h_2 , in Fig. 5.72. Notice the similarity in the shape of the curve to that of the curve in Fig. 5.67 which is for the nondimensional distance to breaking $\Omega_T x_b / \sqrt{gh_2}$. As for that curve, the curve in Fig. 5.72 is essentially linear for $H_T/h_2 < 0.05$ and is given by the approximate relationship:

$$\frac{\Omega_T x_n}{\sqrt{gh_2}} \approx 0.046 \left(\frac{H_T}{h_2} \right)^{-1.00} , \quad (5.32)$$

Comparison with Eq. (5.28) for the distance to breaking shows the distance for nonlinear effects to become important is approximately 1/20 of the distance to breaking, i.e., $x_n \approx x_b/20$.

To summarize the results of this section, when a wave of sech^2 shape propagates onto a shelf, initially, for a distance x_n (given

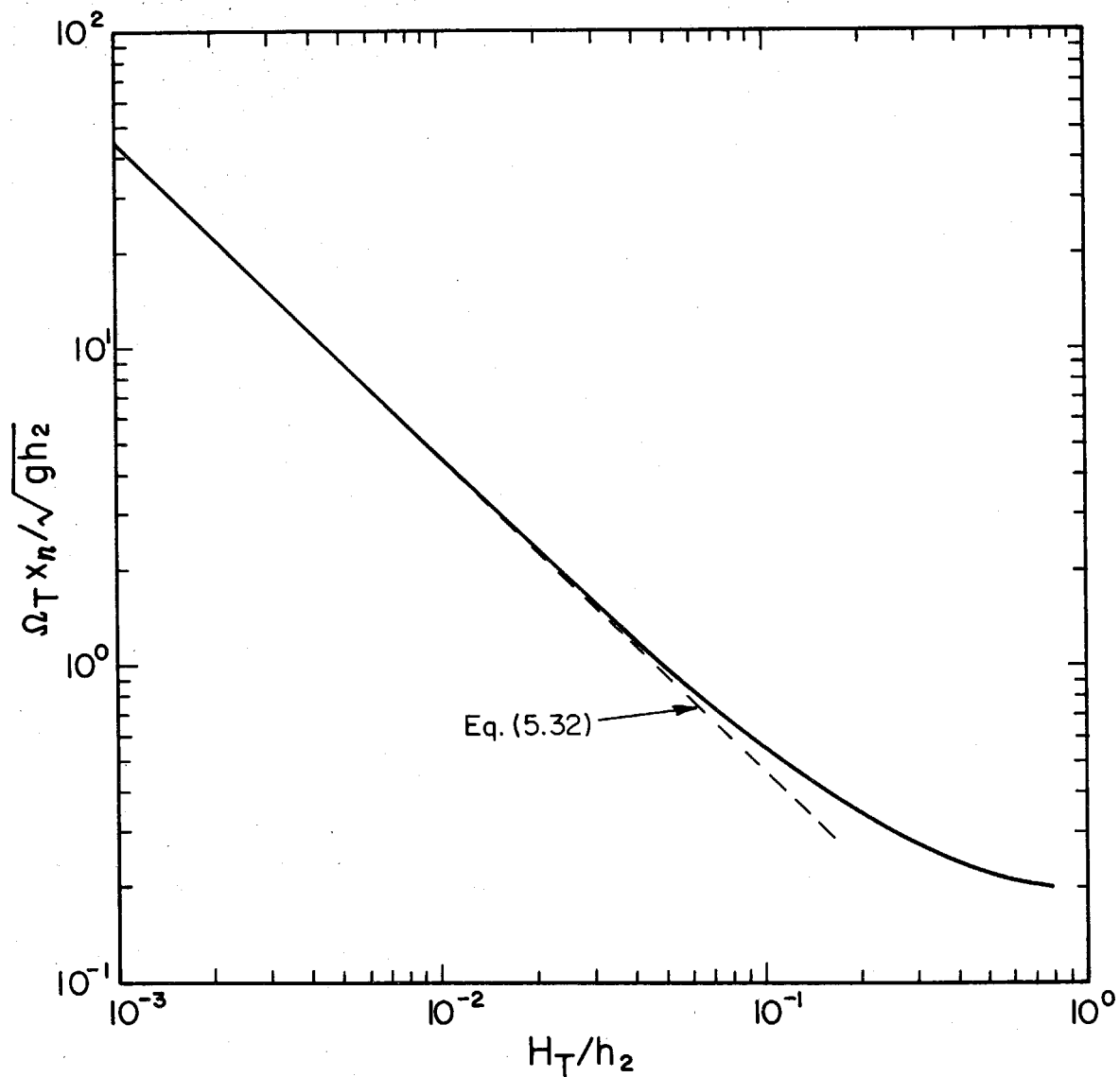


Fig. 5.72 Theoretical variation of the distance for nonlinear effects to become important, $\Omega_T x_n / \sqrt{gh_2}$, with relative wave height, H_T/h_2 .

by Fig. 5.72 or Eq. (5.32) the linear nondispersive theory applies; but if the propagation distance exceeds x_n the nonlinear nondispersive theory must be used. This theory is applicable for a propagation distance x_d (given by Fig. 5.71 or Eq. (5.30)) when the nonlinear dispersive theory must be used.

5.4.2 The Propagation of Cnoidal Waves on the Shelf

As cnoidal waves propagate over a step onto a shelf, the period appears to remain constant (for a simple proof of this for linear waves, the interested reader is referred to Ippen (1966) p. 21), and it was shown in Section 5.3.2 the height of the transmitted wave is approximately the same as that of the incident wave. Hence, the Ursell Number, defined as gHT^2/h^2 , increases by a factor of $(h_1/h_2)^2$ as the waves propagate onto the shelf. However, as was shown in Fig. 3.4 in Section 3.1, a particular Ursell Number completely defines the shape of the cnoidal waves in terms of the relative amplitude, η/H , as a function of the relative time, t/T . Thus, since the transmitted waves have an Ursell Number different from that of the cnoidal waves of the same shape, the transmitted waves cannot be cnoidal waves. Therefore, since only cnoidal and solitary waves propagate with permanent form, the shape of the transmitted waves must change as they propagate on the shelf.

To investigate the way in which this takes place, experiments were conducted in which cnoidal waves were generated in a depth of $h_1 = 20.23$ cm and allowed to propagate over a step onto a shelf where the depth was $h_2 = 4.69$ cm. The waves were recorded at five locations:

at the step and at 1.0 m intervals downstream on the shelf. The resulting oscillograph records are presented in Fig. 5.73 which shows three experiments in which the relative height of the transmitted waves was kept constant at $H_T/h_2 = 0.28$ and the period was varied ($T\sqrt{g/h_2} = 42.1, 57.1$ and 77.4) and in Fig. 5.74 which shows three experiments in which the period was kept constant at $T\sqrt{g/h_2} = 57.1$ and the relative height of the transmitted wave was varied ($H_T/h_2 = 0.16, 0.28$ and 0.50).

In Fig. 5.73 which shows the experiments in which the wave height was held constant, the transmitted waves (i.e., $x/h_2 = 0$) for each experiment evidently have different shape; the amplitude of the trough decreases from 50% of the wave height for the record at the left of the figure (i.e., for $T\sqrt{g/h_2} = 42.1$) to 35% of the wave height for the record at the right of the figure (i.e., for $T\sqrt{g/h_2} = 77.4$). The transmitted waves are approximately symmetrical about the crest, but 21.3 depths downstream, for the three cases the front face of the waves is steeper than the back face. At $x/h_2 = 42.6$ secondary troughs appear on the back face of the waves and as the waves propagate secondary waves emerge in a manner similar to what was seen to occur for solitary waves (e.g., see Fig. 5.58) except that in this case the wave groups are periodic and there is a trough below still water level. Although the number of waves emerging is different for each experiment, the development of the secondary waves appears to be similar for each experiment, namely, the front face steepens and secondary troughs emerge on the back face after the same distance of propagation in each case.

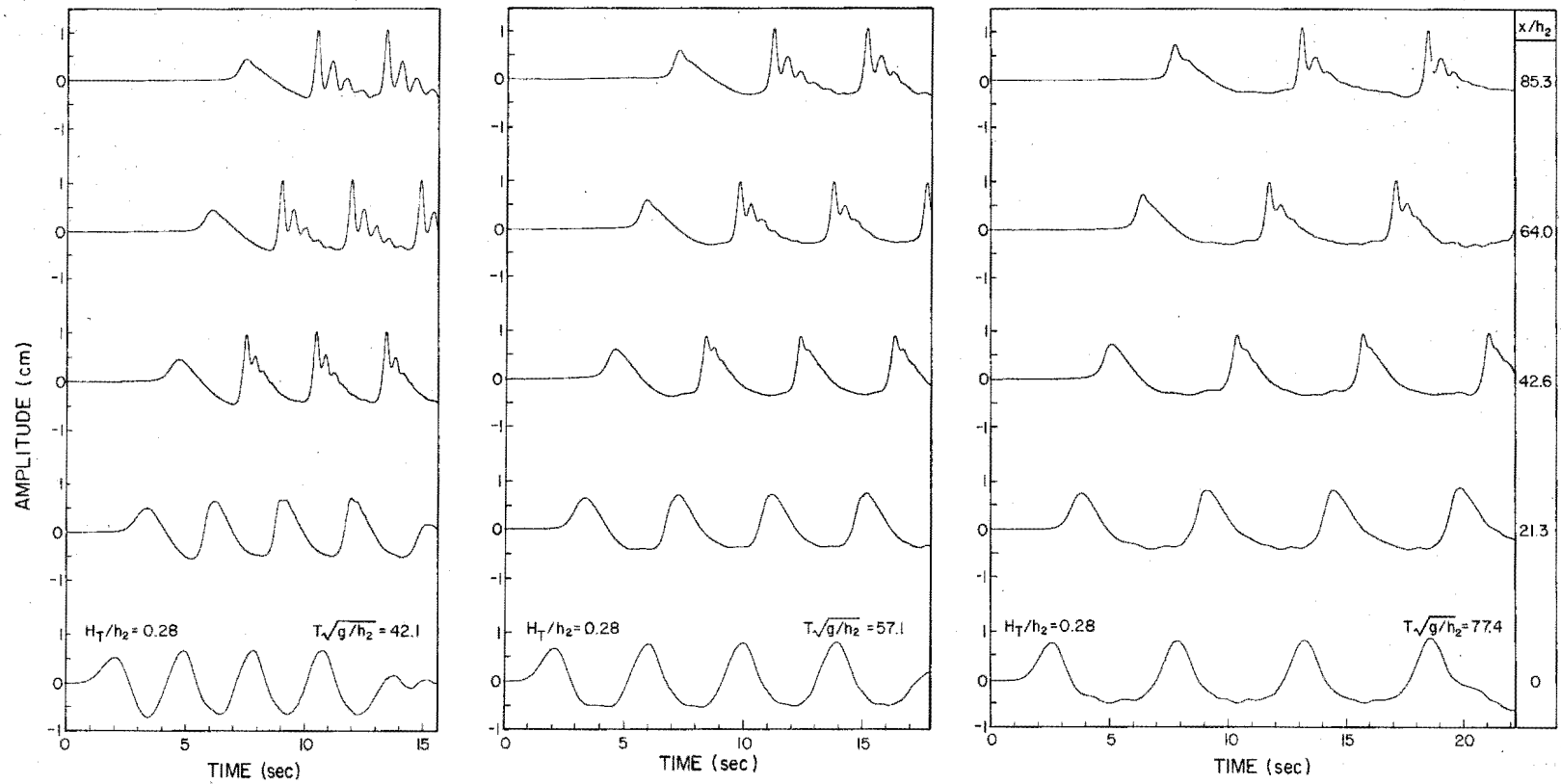


Fig. 5.73 Oscillograph records of experiments in which cnoidal waves of the same height, $H_T/h_2 = 0.28$, propagate on the shelf.

In addition, although the shape of the waves at $x/h_2 = 85.3$ is different for each experiment, the height of the waves measured from the main crest to the main trough is the same ($H/h_2 = 0.30$) and the amplitude of the main trough is 23% of the wave height for all three experiments. This is somewhat surprising because, it will be recalled, the amplitudes of the troughs of the transmitted waves varied from 50% of the wave height to 35% of the wave height. It may be inferred from these experiments the wave period governs the number of secondary crests which emerge but it is the wave height which determines the manner in which the waves propagate.

This is illustrated further in Fig. 5.74 which shows the records of the experiments in which the period was set at $T\sqrt{g/h_2} = 57.1$ and the wave height was varied. In these experiments also, the transmitted waves have different shape but in each case the waves are approximately symmetrical about the crest. As the waves propagate, the front face steepens then secondary troughs appear on the back face of the waves and finally secondary waves emerge. The height of the transmitted waves approximately doubles between each experiment and it is interesting to compare the shapes of the waves after they have propagated distances proportional to the inverse of the relative height of the transmitted wave, i.e., $x/h_2 \propto (H_T/h_2)^{-1}$. For example, comparing the waves at $x/h_2 = 85.3$ of the record at the left ($H_T/h_2 = 0.16$) with those at $x/h_2 = 42.6$ of the record in the center ($H_T/h_2 = 0.28$) with those at $x/h_2 = 21.3$ of the record at the right ($H_T/h_2 = 0.50$), the shape of the waves appears similar with a secondary trough just

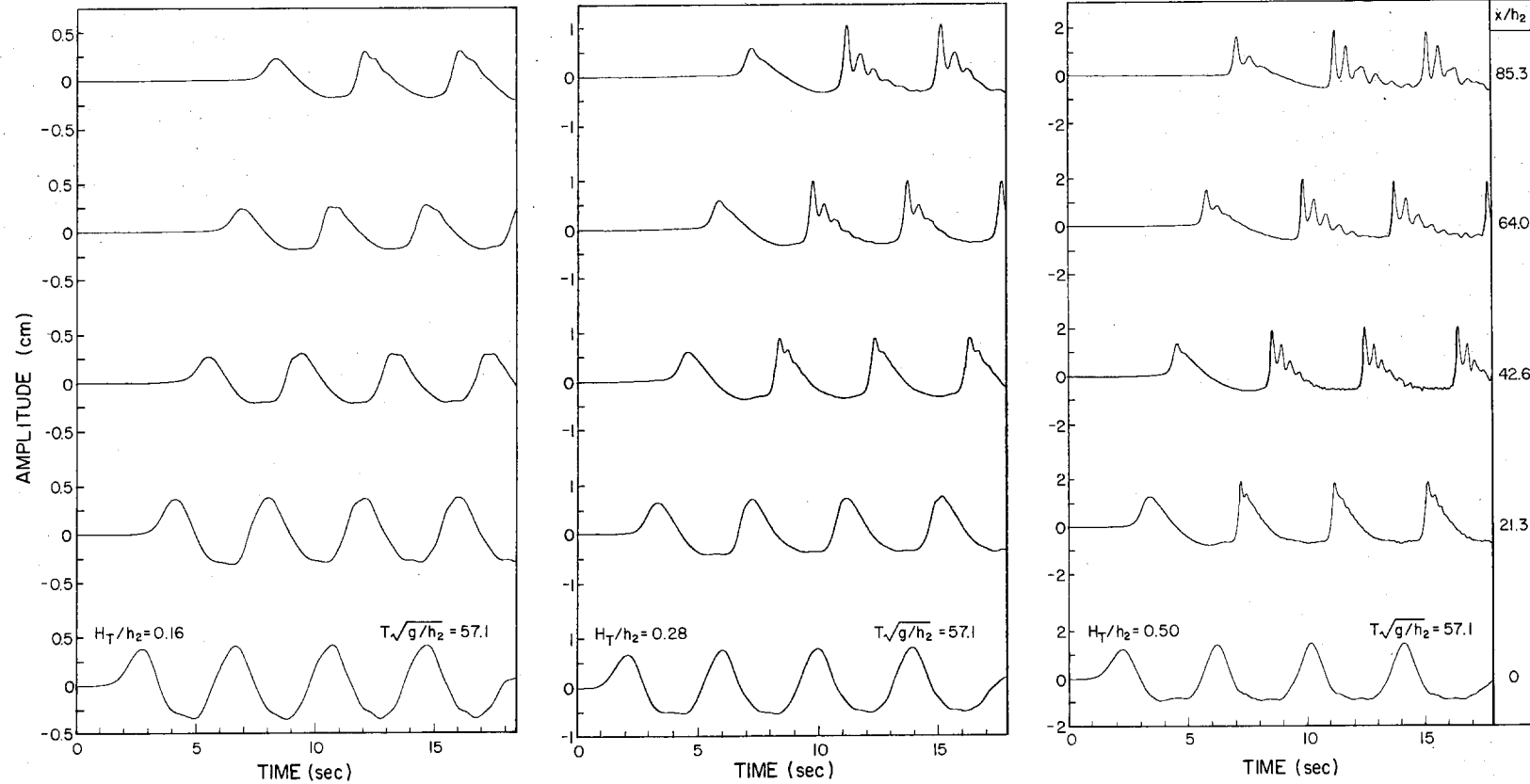


Fig. 5.74 Oscillograph records of experiments in which cnoidal waves of the same period, $T\sqrt{g/h_2} = 57.1$, propagate on the shelf.

beginning to emerge on the back face of the wave. Similarly comparing the waves at $x/h_2 = 85.3$ of the record in the center with those at $x/h_2 = 42.6$ of the record at the right, the shape in this case also appears similar, with three crests evident and a number of other crests emerging. Hence, as was found for the case of solitary waves propagating onto a shelf, when cnoidal waves propagate onto a shelf the propagation distance for nonlinear and dispersive effects to occur is approximately proportional to the inverse of the relative wave height.

The numerical solution of the nonlinear dispersive theory, in principle, is no different for this problem than for the case of solitary waves propagating on the shelf. However, the discretization interval, i.e., the time step, must be made small enough to describe each wave emerging in the group. Hence, for wave groups which break up into many waves, the time step must be made small, which implies large numbers of calculations. An example of the numerical solution of the nonlinear dispersive theory for cnoidal waves is presented in Fig. 5.75, where the theory is compared with a portion of the experiment shown at the right in Fig. 5.74, i.e., for $H_T/h_2 = 0.50$. The experiment and the theory agree quite well with regard to the leading wave, however the theory predicts the emergence of secondary waves on waves further back in the group occurs more rapidly than observed in the experiment. One possible reason for this is the dissipative effects which were mentioned earlier when considering solitary waves propagating on the shelf. In spite of these effects the overall behavior agrees between experiment and theory.

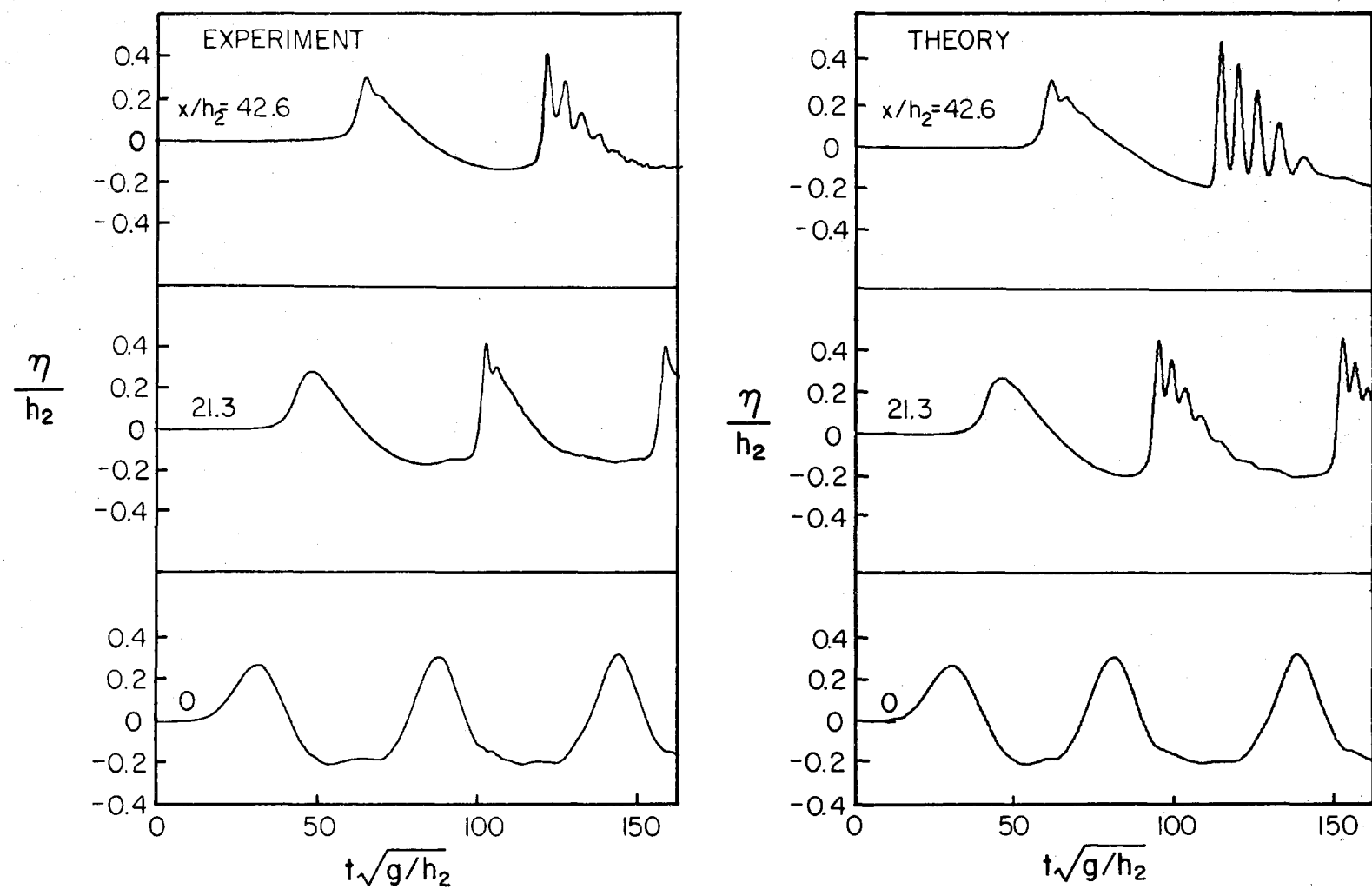


Fig. 5.75 Comparison for the propagation of cnoidal waves on the shelf between experiment and the nonlinear dispersive theory.

5.5 Waves Propagating Off the Shelf

Although it is outside the scope of this investigation, the process of waves propagating from shallow into deeper water over a step is presented for a single case to demonstrate one way by which it can be treated.

In an experiment similar to that shown in Fig. 5.2, a solitary wave was generated and allowed to propagate over a step and onto the shelf. The reflected wave from the shelf was trapped by dropping a gate after it had passed. The main wave reflected off the rear wall of the tank and propagated back towards the step separating into a group of solitary waves in a manner similar to that shown in Fig. 5.2. Wave gauges were located at the step and at four other locations 2.4 m apart in the region downstream of the step where the depth was $h_1 = 21.73$ cm. The waves were recorded on the oscillograph and on an A/D converter and are presented as the solid curves in Fig. 5.76. The wave group at the step ($x/h_1 = 0$) consists of four solitary waves and a tail which gradually decreases in amplitude and from which more solitary waves may have emerged if propagation in constant depth had continued. In fact, the depth increased abruptly to be 3.5 times that on the shelf. Hence, for any of the waves within the group, the Ursell Number given by Eq. (5.23) was reduced to 1/12 (i.e., $(h_2/h_1)^2$) that on the shelf. Thus, dispersive effects became more important than nonlinear effects and this is reflected in the wave records as the group propagated in the deep water.

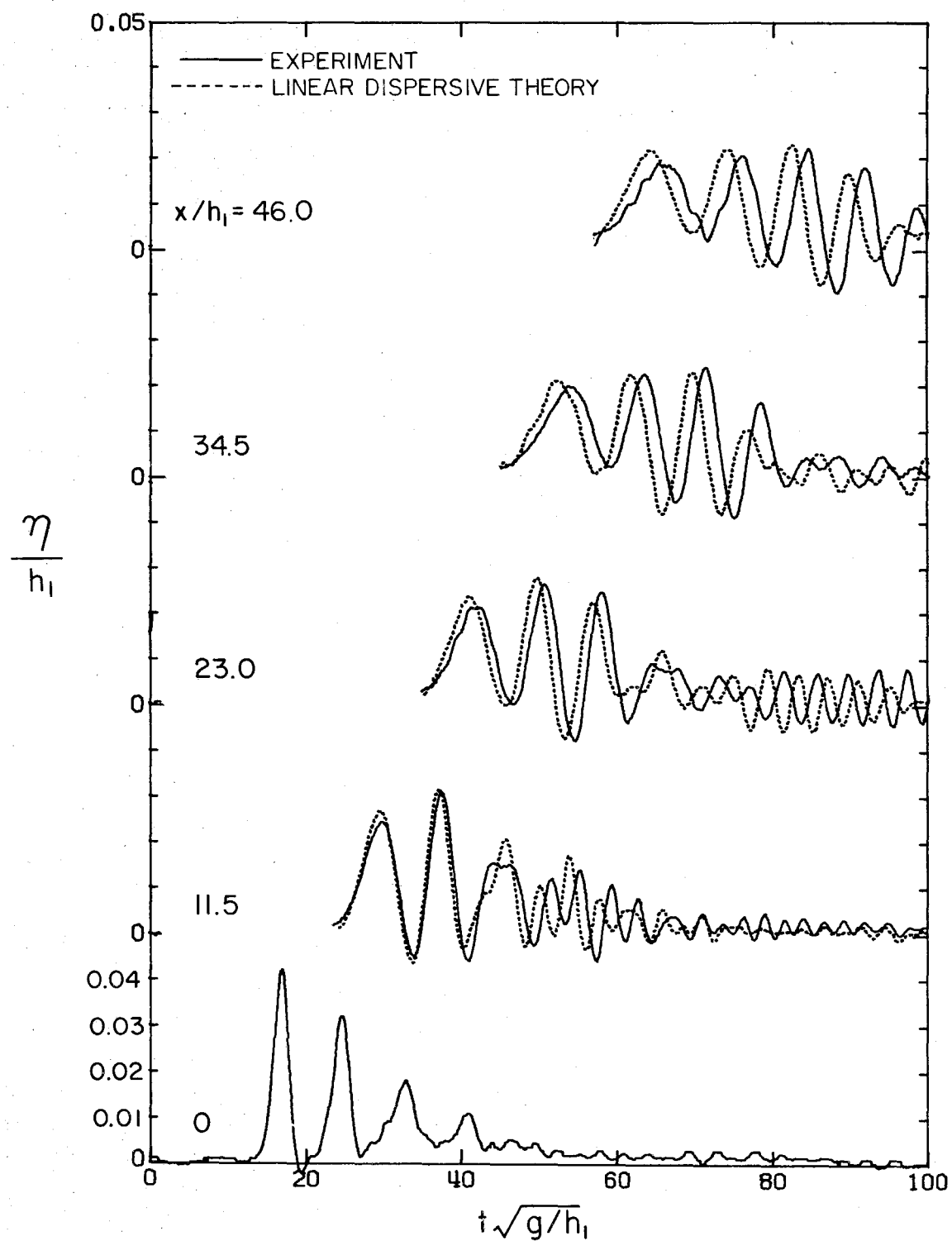


Fig. 5.76 Comparison for the propagation of solitary waves off the shelf into deep water between experiment and the linear dispersive theory.

The dashed curves in Fig. 5.76 are the linear dispersive theory and were calculated from the wave record at $x/h_1 = 0$ using the dispersion relation in Eq. (3.15). The shape of the waves predicted by the theory agrees well with the experiment, particularly for the longer waves at the front of the train as would be expected since the dispersion relation, Eq. (3.15), is a valid approximation for long waves only. However, there is a difference in time between the theoretical and the experimental time records with the theory predicting a greater celerity than the experiment exhibits and the difference increases with propagation distance. The reasons for the time shift are not understood but, apart from this, the behavior is predicted well by the linear dispersive theory.

5.6 Application of the Results to the Tsunami Problem

In this section, the results presented in previous sections are applied to the problem of a tsunami propagating onto the continental shelf.

A typical cross-section of the continental slope off the coast of California is shown in Fig. 5.77 where, for clarity, the vertical scale has been distorted; the continental slope off New Zealand has similar characteristics. The depth in the deep ocean varies from 2700 to 3900 m with an average of 3500 m. Defining the start of the continental shelf to occur where the contours begin to increase their spacing markedly, the depth on the shelf at the shelf-break is found to be about 1000 m. Hence, the ratio of the depth in the deep

ocean to that on the shelf-break, h_1/h_2 , varies from 2.7 to 3.9. The length of the slope, L , varies between 11 and 90 km with an average of 30 km.

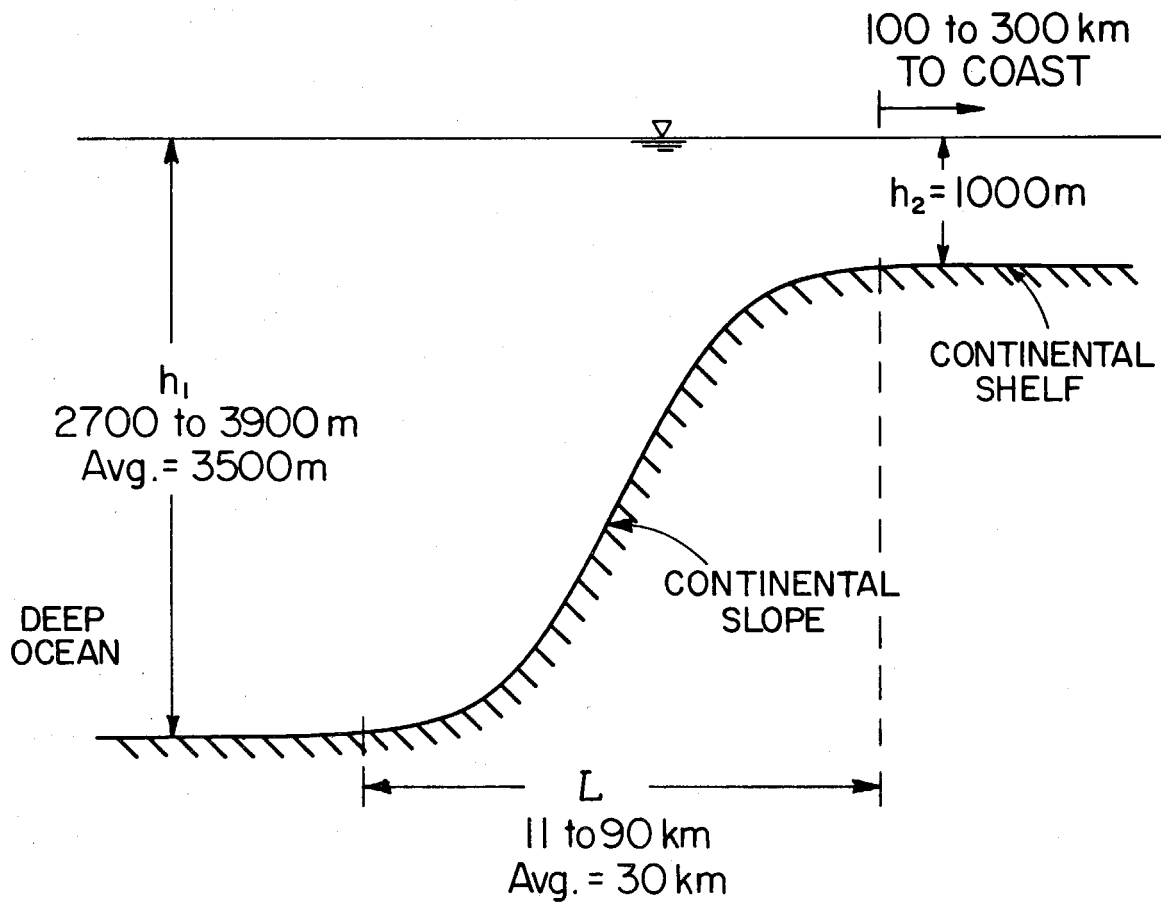


Fig. 5.77 Schematic drawing of the continental slope off the coast of California.

A problem in applying the results of this chapter to the tsunami problem is that each tsunami is unique; the form it takes depends both on the earthquake which generated it and on its propagation from the generation region. Furthermore, three-dimensional effects

in the propagation, which were not considered in this investigation, probably are important.

An assumption sometimes made in the analysis of tsunamis is that the tsunami takes the form of a solitary wave. In fact, Hammack and Segur (1974) show this will be true only if the initial wave has non-negative net volume and the wave has propagated a sufficient distance for the solitary wave to emerge. However, if the initial wave has negative net volume, no solitary waves will emerge and if it has zero net volume solitary waves may or may not emerge depending on the detailed structure of the initial wave. Furthermore, Hammack and Segur (1978) postulate that the maximum distance of propagation possible across any ocean is not sufficient for solitary waves to emerge. Hence, the assumption of a tsunami having the form of a solitary wave may not be accurate. However, both tsunamis and solitary waves are long waves; therefore, the behavior of both is described by the long wave equations and it is on this basis the application of the results of the present study to tsunamis is made.

To apply the results, some assumption must be made with respect to the wave height of the tsunami in the deep ocean near the slope. Following the example used by Hammack and Segur (1978), incident wave heights, H_I , of 0.35 m and 3.5 m will be considered. Assuming the depth in the deep ocean is 3500 m this implies relative incident wave heights, H_I/h_1 , of 1×10^{-4} and 1×10^{-3} , respectively.

For reflection, as was shown in Section 5.2, the linear nondispersive theory and the nonlinear dispersive theory agree well except for large waves propagating over small depth ratios. Hence, the reflection coefficient for the linear theory as shown in Fig. 5.40 is applicable to the assumed height of this example. Thus, for a depth ratio, h_1/h_2 , of 3.5, the reflected wave will have 30% of the volume and up to 30% of the height of the incident wave near the shelf.

As will be recalled from Section 5.3, the transmitted wave is best predicted by the nonlinear dispersive theory; however, if the linear nondispersive theory is used, the difference between the theories in the slope of the front face of the wave and in the wave height are given approximately by Eqs. (5.24) and (5.25). In Table 5.10 these differences are presented for solitary waves with heights of $H_I = 0.35$ m and 3.5 m propagating over slopes with lengths of $L = 10$ and 100 km for a depth ratio of $h_1/h_2 = 3.5$. As the table shows, for this example, the differences are so small the linear nondispersive theory can be used. (For the nonlinear dispersive theory to be necessary, i.e., for there to be a 10% difference in the slopes, the incident wave height, H_I , would have to be 175 m.)

Eqs. (5.24) and (5.25), developed for solitary waves, are applied to an arbitrary wave to determine the characteristic length, ℓ , which would be necessary for the theories to be different by 1%. Inspection of the equations indicates the difference will be a maximum when the length ratio and the wave height ratio both are

Table 5.10 Relative differences between the theories in (a) the slope of the front face and (b) the transmitted wave height for tsunamis which are solitary waves.

$$(a) (S - S_{1\text{in}})/S_{1\text{in}}$$

H_T (m)	L (km)	
	10	100
0.35	6.7×10^{-6}	3.9×10^{-5}
3.5	2.4×10^{-4}	1.4×10^{-3}

$$(b) (H_T - H_{T\text{lin}})/H_{T\text{lin}}$$

H_T (m)	L (km)	
	10	100
0.35	3.0×10^{-8}	5.6×10^{-7}
3.5	3.1×10^{-6}	6.0×10^{-5}

maximum, hence, the characteristic length calculated will represent the maximum length for the theories to be different by 1%. Using a depth ratio of $h_1/h_2 = 3.5$, a relative incident wave height of $H_I/h_1 = 1 \times 10^{-3}$ and a slope length of $L = 100$ km, the maximum characteristic length is $\lambda = 13$ km. Thus, for tsunamis with characteristic lengths greater than 13 km, which it is expected will be the case, the linear and nonlinear theories are different by less than 1%. Thus, the transmitted wave probably will be predicted by the linear nondispersive theory. Referring to Fig. 5.50, since the maximum length ratio of the slope relative to the wave is $L/\lambda = 0.06$, (corresponding to a slope length of $L = 100$ km and a solitary wave height of $H_I = 3.5$ m) the slope is considered abrupt. This implies the shape of the transmitted wave is the same as that of the incident wave and the amplitude is scaled by the transmission coefficient given by Eq. (3.114). ($K_T = 1.30$ for $h_1/h_2 = 3.5$).

For sech^2 waves propagating on a shelf with constant depth, the distance to breaking predicted by the nonlinear nondispersive theory was found to be given by Eq. (5.28). Thus, for an incident solitary wave with height of $H_I = 3.5$ m which is transmitted in the manner described above, the distance to breaking on the shelf where the depth is assumed to be constant and equal to 1000 m is $x_b \approx 1.5 \times 10^4$ km. The distance for nonlinear effects to become important was found to be $x_n \approx x_b/20$, thus $x_n \approx 700$ km. However, as shown in Fig. 5.77, the distance from the continental slope to the coast is only 100 to 300 km. Hence, for a shelf with constant depth, the linear nondispersive theory

can be used for the propagation of the tsunami from the slope to the region near the coast where shoaling begins. (It should be realized that depth changes on the shelf may be important and shoaling effects may take place on the shelf which were not treated in this study.)

From these examples it may be concluded, because of the small relative height of tsunamis and their large lengths relative to the lengths of the continental slope, the propagation of tsunamis from the deep ocean to the continental shelf-break and for some distance onto the shelf will be predicted as well by the linear nondispersive theory as by the nonlinear theories.

CHAPTER 6

CONCLUSIONS

The major objective of this study has been to investigate, experimentally and theoretically, the propagation of long waves onto a shelf. The generation and propagation in the laboratory of long waves of permanent form have been investigated and the experimental results have been compared with the theory. The propagation of solitary and cnoidal waves over a step onto a shelf and the propagation of solitary waves over a slope onto a shelf have been investigated experimentally and also theoretically using both the linear nondispersive theory and the nonlinear dispersive theory. (Generally, the experimental results indicate the finite element technique used to solve the Boussinesq equations predicts the processes well.) A single case of solitary waves propagating off the shelf into deep water also has been investigated experimentally and theoretically using the linear dispersive theory.

For convenience, the major conclusions drawn from this study are arranged in the order in which the results were presented in Section 5: The Generation and Propagation of Long Waves of Permanent Form in a Constant Depth

1. The generation of a solitary wave without oscillatory trailing waves requires the precise programming of a wave generator (see, e.g., Eq. (3.50)).
2. The shape and celerity of solitary waves generated in the

laboratory are predicted well by the theories of Boussinesq, McCowan and Laitone for small relative wave heights ($H/h < 0.3$). However, for large relative wave heights, i.e., $H/h > 0.3$, the shape and celerity of the solitary waves are somewhat different from these theories.

3. Cnoidal waves also require precise programming of a wave generator (see, e.g., Eq. (3.58)); if the trajectory is incorrect, secondary waves which travel at a different speed from the main waves are generated.

4. The shape of cnoidal waves is well predicted by the KdV equation, but the experimentally measured celerities are somewhat less than those predicted theoretically.

5. In the laboratory, the inner waves of a limited group of cnoidal waves propagate over short distances essentially as the theory predicts an infinite number of waves would, i.e., without change in shape.

6. The reduction of the height of solitary waves and cnoidal waves due to friction is accompanied by corresponding changes in the shape of the wave. The effect of friction on the height for solitary waves is reasonably well predicted by the theory of others. Experiments with cnoidal waves gave similar results as experiments conducted with solitary waves.

The Reflection of Long Waves from a Change in Depth

7. At a step, the reflected wave measured experimentally is described well by the linear nondispersive theory for both

solitary waves and cnoidal waves.

8. The propagation of the wave reflected from a step for both solitary and cnoidal waves is governed by the nonlinear dispersive theory.

9. The height of the wave reflected when a solitary wave propagates up a slope, for most cases investigated, is predicted as well by the linear nondispersive theory as by the nonlinear dispersive theory. However, the shape of the wave predicted by the two theories is somewhat different and the nonlinear dispersive theory tends to agree better with experiment. The numerical theory predicts nonlinear effects become important for waves with a large height propagating onto a shelf with a small depth ratio.

The Transmission of Long Waves over a Change in Depth

10. For a step, from experiment and theory, the height of the transmitted wave (for both solitary and cnoidal waves) is not a function of the relative incident wave height. However, in the case of solitary waves, the shape of the transmitted wave is a function of the relative incident wave height.

11. For solitary waves propagating over a slope, the linear nondispersive theory and the nonlinear dispersive theory predict different transmitted waves. The difference increases with increasing slope length and incident wave height, and hence, the nonlinear dispersive theory must be used to describe this aspect of the propagation.

The Propagation of Long Waves on the Shelf

12. As a solitary wave propagates over a step onto a shelf, close to the step all three theories: the linear nondispersive theory, the nonlinear nondispersive theory and the nonlinear dispersive theory, predict the same result. However, at some distance from the step, the linear nondispersive theory predicts a different wave from the nonlinear theories; this distance (Eq. (5.30)) is the distance for nonlinear effects to become important. At a larger distance from the step the nonlinear nondispersive and nonlinear dispersive theories predict different results; this distance (Eq. (5.32)) is the distance for dispersive effects to become important.

13. As cnoidal waves propagate onto the shelf, each wave splits up into a series of waves of different height with the largest first. The distance over which the change in shape takes place is inversely proportional to the relative wave height; the shape of the waves is related to the nondimensional period ($T\sqrt{g/h}$) of the cnoidal waves.

The Propagation of Waves off the Shelf

14. As waves propagate off the shelf into deeper water, the waves disperse in a manner predicted by the linear dispersive theory. An exploratory experimental and theoretical investigation indicates the linear dispersive theory predicts the propagation of long waves from shallow to deeper water reasonably well.

The Application of the results to the Tsunami Problem

15. For tsunamis propagating from the deep ocean, in the vicinity of the continental shelf, the relative wave heights are probably small; hence, the linear nondispersive theory predicts the same results locally as would the nonlinear theories.

LIST OF REFERENCES

Abramowitz, M. and Stegun, I. A. (1972), Handbook of Mathematical Functions, Eighth Edition, Dover Publications, New York.

Bourodimos, E. L. and Ippen, A. T. (1966), "Wave Reflection and Transmission in Open Channel Transitions," Hydrodynamic Laboratory Technical Report No. 98, August 1966, Massachusetts Institute of Technology, Cambridge, Massachusetts.

Boussinesq, J. (1872), "Théorie des Ondes et des Remous qui se Propagent le Long d'un Canal Rectangulaire Horizontal, en Communiquant au Liquide Contenu dans ce Canal de Vitesses Sensiblement Parallèles de la Surface au Fond," Journal de Mathématiques Pures et Appliquées, 2nd Series, Vol. 17, pp. 55-108.

Brigham, O. E. (1974), The Fast Fourier Transform, Prentice-Hall, Inc., New Jersey.

Camfield, F. E. and Street, R. L. (1967), "An Investigation of the Deformation and Breaking of Solitary Waves," Stanford University Technical Report No. 81, December 1967.

Chwang, A. T. and Wu, T. Y. (1976), "Cylindrical Solitary Waves," Proc. IUTAM Symposium on Water Waves in Water of Varying Depth, Canberra, Australia.

Daily, J. W. and Stephan, S. G. (1952), "The Solitary Wave," Proceedings, 3rd Conference on Coastal Engineering, Cambridge, Massachusetts, pp. 13-30.

Dean, R. G. (1964), "Long Wave Modification by Linear Transitions," Journal of Waterways and Harbors Division, ASCE, Vol. 90, No. WWI, February 1964, pp. 1-29.

French, J. A. (1969), "Wave Uplift Pressures on Horizontal Platforms," W. M. Keck Laboratory of Hydraulics and Water Resources, Report No. KH-R-19, California Institute of Technology, Pasadena, Calif.

Gardner, C. S., Green, J. M., Kruskal M. D. and Miura, R. M. (1967), "Method for Solving the Korteweg-de Vries Equation," Physical Review Letters, Vol. 19, No. 19, pp. 1095-1097.

Gilbert, G., Thompson, D. M. and Brewer, A. J. (1971), "Design Curves for Regular and Random Wave Generators," Journal of Hydraulic Research, Vol. 9, pp. 163-196.

Hammack, J. L. (1972), "Tsunamis--A Model of Their Generation and Propagation," W. M. Keck Laboratory of Hydraulics and Water Resources, Report No. KH-R-28, California Institute of Technology, Pasadena, California.

Hammack, J. L. and Segur, H. (1974), "The KdV Equation and Water Waves. Part 2. Comparison with Experiment," Journal of Fluid Mechanics, Vol. 65, pp. 289-314.

Hammack, J. L. and Segur, H. (1975), Water Wave Propagation--Linear and Nonlinear Theories," Proc. Civil Engineering in the Oceans, III, pp. 1249-1265.

Hammack, J. L. and Segur, H. (1978), "The Korteweg-de Vries Equation and Water Waves. Part 3. Oscillatory Waves," Journal of Fluid Mechanics, Vol. 84, Part 2, pp. 337-358.

Hammack, J. L. and Segur, H. (1978), "Modelling Criteria for Long Water Waves," Journal of Fluid Mechanics, Vol. 84, Part, pp. 359-373.

Hansen, J. B., Schiolten, P. and Svendsen, I. A. (1975), "Laboratory Generation of Waves of Constant Form," Series Paper 9, Institute of Hydrodynamics and Hydraulic Engineering, Technical University of Denmark.

Henderson, F. M. (1966), Open Channel Flow, The MacMillan Company, New York.

Hughes, T.J.R. (1977), "Stability of One-Step Methods in Transient Nonlinear Heat Conduction," Transactions of the Fourth International Conference on Structural Mechanics in Reactor Technology, San Francisco, California, August 1977.

Hughes, T.J.R., Liu, W. K. and Brooks, H. (1978), "Finite Element Analysis of Incompressible Viscous Flows by the Penalty Function Formulation," To appear in the Journal of Computational Physics.

Hughes, T.J.R., Liu, W. K. and Zimmermann, T. K. (1978), "Lagrangian-Eulerian Finite Element Formulation for Incompressible Viscous Flows," Presented at U.S.-Japan Conference on Interdisciplinary Finite Element Analysis, Cornell University, August 7-11, 1978.

Ippen, A. T. (1966), Estuary and Coastline Hydrodynamics, McGraw-Hill.

Ippen, A. T. and Kulin, G. (1955), "Shoaling and Breaking Characteristics of the Solitary Wave," Hydrodynamic Laboratory Technical Report No. 15, Massachusetts Institute of Technology, Cambridge, Massachusetts.

Ippen, A. T., Kulin, G. and Raza, M. A. (1955), "Damping Characteristics of the Solitary Wave," Hydrodynamic Laboratory Technical Report No. 16, Massachusetts Institute of Technology, Cambridge, Massachusetts.

Iwasa, Yoshiaka (1959), "Attenuation of Solitary Waves on a Smooth Bed," Transactions ASCE, Paper No. 2972, pp. 193-206.

Johnson, R. S. (1973), "On the Development of a Solitary Wave Moving Over an Uneven Bottom," Proc. Cambridge Philosophic Society (1973), 73, 183.

Kajiura, K. (1961), "On the Partial Reflection of Water Waves Passing Over a Bottom of Variable Depth," UGGI Tsunami Committee, Proc. of the Tsunami Meetings associated with the 10th Pacific Science Congress.

Kawai, T. and Watanabe, M. (1975), "Finite Element Analysis of the Tsunami Problem," Bulletin of the Earthquake Resistant Structure Research Center, No. 9, The Institute of Industrial Science, University of Tokyo.

Keulegan, G. H. (1948), "Gradual Damping of Solitary Waves," U.S. Department of Commerce, National Bureau of Standards, Research Paper RP 1895, Vol. 40, pp. 487-498.

Keulegan, G. H. and Patterson, G. W. (1940), "Mathematical Theory of Irrotational Translation Waves," Journal of Research of the National Bureau of Standards, Vol. 24, Jan. 1940.

Klinting, P. and Svendsen, I. A. (1974), "A Discussion of Characteristic Horizontal Lengths in Long Waves," Progress Report 34, pp. 11-17, Institute of Hydrodynamic and Hydraulic Engineering, Technical University of Denmark.

Korteweg, D. J. and deVries, G. (1895), "On the Change of Form of Long Waves Advancing in a Rectangular Canal, and on a New Type of Long Stationary Wave," London, Edinburgh, and Dublin Philosophical Magazine, Series 5, Vol. 39, pp. 422-443.

Laitone, E. V. (1963), "Higher Order Approximation to Nonlinear Waves and the Limiting Heights of Cnoidal, Solitary and Stokes' Waves," Beach Erosion Board, U.S. Department of the Army, Corps of Engineers, Technical Memorandum No. 133.

Lamb, H. (1932), Hydrodynamics, Dover, 6th Edition.

Lighthill, M. J. and Whitham, G. B. (1955), "On Kinematic Waves I. Flood Movement in Long Rivers," Proceedings Royal Society of London, Series A, Vol. 229, pp. 281-316.

Long, R. L. (1964), "The Initial-Value Problem for Long Waves of Finite Amplitude," Journal of Fluid Mechanics, Vol. 20, Part 1, pp. 161-170.

McCowan, J. (1891), "On the Solitary Wave," London, Edinburgh and Dublin Philosophical Magazine, Vol. 32, pp. 45-58.

Madsen, O. S. (1970), "Waves Generated by a Piston-Type Wavemaker," Proc. of Coastal Engineering Conference, 1970, Chapter 36, Vol. 1.

Madsen, O. S. (1971), "On the Generation of Long Waves," Journal of Geophysical Research, Vol. 76, No. 36.

Madsen, O. S. and Mei, C. C. (1969), "The Transformation of a Solitary Wave Over an Uneven Bottom," Journal of Fluid Mechanics, Vol. 39, pp. 781-791.

Masch, F. D. and Wiegel, R. L. (1961), "Cnoidal Waves, Tables of Functions," Council on Wave Research, The Engineering Foundation.

Mei, C. C. and Le Méhauté, B. (1966), "Note of the Equations of Long Waves Over an Uneven Bottom," Journal of Geophysical Research, Vol. 71, No. 2, January 15, 1966, p. 393.

Munk, W. H. (1948), "The Solitary Wave Theory and Its Application to Surf Problems," New York Academy of Science Annals, 51, pp. 376-424.

Naheer, E. (1977), "Stability of Bottom Armoring Under the Attack of Solitary Waves," W. M. Keck Laboratory of Hydraulics and Water Resources, Report No. KH-R-34, California Institute of Technology, Pasadena, California.

Okoye, J. K. (1970), "Characteristics of Transverse Mixing in Open-Channel Flows," W. M. Keck Laboratory of Hydraulics and Water Resources, Report No. KH-R-23, California Institute of Technology, Pasadena, California.

Peregrine, D. H. (1966), "Calculations of the Development of an Undular Bore," Journal of Fluid Mechanics, Vol. 25, Part 2, pp. 321-330.

Peregrine, D. H. (1967), "Long Waves on a Beach," Journal of Fluid Mechanics, Vol. 27, Part 4, pp. 815-827.

Raichlen, F. (1970), "Tsunamis: Some Laboratory and Field Observations," Proc. of 12th Coastal Engineering Conference, Washington, DC, pp. 2103-2122.

Raichlen, R. (1965), "Wave-Induced Oscillations of Small Moored Vessels," W. M. Keck Laboratory of Hydraulics and Water Resources, Report No. KH-R-10, California Institute of Technology, Pasadena, California.

Scott-Russell, J. (1844), "On Waves," Reports to the British Association, pp. 311-390.

Segur, H. (1973), "The Korteweg-deVries Equation and Water Waves. Part 1. Solutions of the Equation," Journal of Fluid Mechanics, Vol. 59, pp. 721-736.

Stokes, G. G. (1847), "On the Theory of Oscillatory Waves," Transactions, Cambridge Philosophical Society, Vol. 8, pp. 441-455.

Street, R. L., Burgess, S. J. and Whitford, P. W. (1968), "The Behavior of Solitary Waves on a Stepped Slope," Stanford University Technical Report 93, August 1968.

Svendsen, I. A. (1974), "Cnoidal Waves Over a Gently Sloping Bottom," Series Paper No. 6, Institute of Hydrodynamics and Hydraulic Engineering, Technical University of Denmark.

Tappert, F. D. and Zabusky, N. J. (1971), "Gradient Induced Fission of Solitons," Physical Review Letters, Vol. 27, No. 26, December 1971.

Ursell, F. (1953), "The Long-Wave Paradox in the Theory of Gravity Waves," Proc. Cambridge Philosophical Society, Vol. 49, pp. 685-694.

Ursell, F., Dean, R. G. and Yu, Y. S. (1958), "Forced Small-Amplitude Water Waves, A Comparison of Theory and Experiment," Hydrodynamic Laboratory Technical Report No. 29, July 1958, Massachusetts Institute of Technology, Cambridge, Massachusetts.

Van Dorn, W. G. (1966), "Boundary Dissipation of Oscillatory Waves," Journal of Fluid Mechanics, Vol. 24, Part 4, pp. 769-779.

Whitham, G. B. (1974), Linear and Nonlinear Waves, A. Wiley-Interscience Publication.

Wiegel, R. L. (1960), "A Presentation of Cnoidal Wave Theory for Practical Application," Journal of Fluid Mechanics, Vol. 7, pp. 273-286.

Wong, K. K., Ippen, A. T. and Harlemann, D.R.F. (1963), "Interaction of Tsunamis with Oceanic Islands and Submarine Topographies," Hydrodynamic Laboratory Technical Report No. 62, August 1963, Massachusetts Institute of Technology, Cambridge, Massachusetts.

Zabusky, N. J. and Galvin, C. J. (1971), "Shallow-water Waves, the Korteweg-deVries Equation and Solitons," Journal of Fluid Mechanics, Vol. 47, Part 4, pp. 811-824.

LIST OF SYMBOLS

A	Wave height
A_1, A_2, B_1, B_2, C_1	Coefficients in the solution of the <u>linear nondispersive</u> theory
α	Celerity parameter
a	Amplitude
B	Wave number
b	Width of the channel
c	Celerity
d_i, e_i	Nodal velocity and amplitude
E	Second elliptic integral
f	Damping exponent
\tilde{f}^c, \tilde{f}^M	Continuity and momentum vectors
$G(x), H(x)$	Initial conditions
g	Acceleration of gravity
H	Wave height
H_o	Initial wave height
H_R	Reflected wave height
$H_{R\text{INV}}$	Inverse scattered reflected wave height
H_T	Transmitted wave height
h	Depth
h_1	Upstream depth
h_2	Depth on shelf
i, j, k	Integers
i	$\sqrt{-1}$

I	Integral
J_0, J_1	Bessel functions of the first kind
K	First complete elliptic integral
K_R	Reflection coefficient
K_T	Transmission coefficient
k	Wave number
L	Wave length
L	Slope length
λ	Characteristic length of the wave
λ^*	Length of the wave over which the amplitude exceeds 1% of the wave height
$\underline{M}^C, \underline{M}^M$	Mass matrices for continuity and momentum equations
$\underline{m}_0, \underline{m}_m$	Mass vectors at the boundaries
m	Elliptic parameter
m'	Complementary elliptic parameter ($= 1 - m$)
N, n	Integers
P	Parameter in inverse scattering theory
Q	Rayleigh quotient
q	Flow rate per unit width
r	Distance in inverse scattering theory
S	Stroke
S	Slope of front face of a wave
T	Period
t	Time
t_o	Time interval between crest and still water level

<i>t</i>	Parametric time for <u>nonlinear nondispersive</u> theory
<i>u</i>	Horizontal component of velocity
\bar{u}	Depth averaged horizontal velocity
<i>U</i>	Ursell Number
<i>U_s</i>	Ursell Number of a solitary wave
<i>V</i>	Volume
<i>v, w</i>	Variations in velocity and amplitude
<i>X</i>	Total distance
<i>x</i>	Horizontal coordinate distance
<i>x_b</i>	Distance to breaking
<i>x_d</i>	Distance for dispersive effects to become important
<i>x_n</i>	Distance for nonlinear effects to become important
<i>Y₀, Y₁</i>	Bessel functions of the second kind
<i>Y</i>	Distance above the bottom
<i>y</i>	Vertical coordinate distance
<i>y_t</i>	Distance of trough from the bottom
<i>α, β</i>	Parameters in long wave theory
<i>ε</i>	Error
<i>η</i>	Free surface elevation above still water level
<i>θ</i>	Periodic arguments
<i>κ</i>	Solitary wave number $(\kappa = \sqrt{\frac{3}{4} \frac{H}{h^3}})$
<i>ν</i>	Kinematic viscosity
<i>ξ</i>	Wave plate displacement
<i>π</i>	3.14159...
<i>τ</i>	Time
<i>Φ</i>	Velocity potential

ϕ, ψ	Trial functions
Ω	Frequency of sech ² wave
Ω_T	Frequency of transmitted wave
ω	Frequency

Operators

$\frac{d(\dots)}{d(\dots)}$	Total derivative
$\frac{\partial(\dots)}{\partial(\dots)}$	Partial derivative
$(\dots)_x, (\dots)_t, \dots$	Partial differentiation with respect to subscript
$\Delta \dots$	Difference (e.g., $\Delta h = h_1 - h_2$)
$\nabla^2 \dots$	Laplacian
$f(\dots)$	Function of
$0(\dots)$	Order of magnitude
$(\vec{\dots})$	Vector if lower case; matrix if upper case
$(\overline{\dots})$	Depth averaged value
$a(\dots, \dots)$	Bilinear form
(\dots, \dots)	Inner product

APPENDIX ACnoidal Wave Relationships and Numerical Methods of Evaluation

The four relationships which follow are sufficient to describe cnoidal waves:

$$\eta = (y_t - h) + H \operatorname{cn}^2 \left\{ 2K \left(\frac{x}{L} - \frac{t}{T} \right) \mid m' \right\} , \quad (A.1)$$

$$y_t = \frac{H}{K(1-m')} (K - E) + h - H , \quad (A.2)$$

$$\frac{HL^2}{h^3} = \frac{16}{3} K^2 (1-m') , \quad (A.3)$$

$$c = \frac{L}{T} = \sqrt{gh} \left\{ 1 + \frac{H}{h} \left[\left(\frac{2}{1-m'} \right) - \left(\frac{3E}{(1-m')K} \right) \right] \right\} , \quad (A.4)$$

where h is the depth, H is the wave height, K and E are the first and second complete elliptic integrals respectively, y_t , is the distance to the trough from the bottom, L is the wave length, and T is the period. The elliptic parameter m has been replaced by its complement $m' = (1-m)$, which makes the relationships more cumbersome, but is more suitable for numerical evaluation since the parameter m can take values as close to unity as, for example, $1-m = 1 \times 10^{-40}$.

Relationships A.1, A.2 and A.3 were presented by Wiegel (1960). Svendsen (1974) points out an error in Wiegel's expression for celerity and presents (A.4) as an alternative. This is also the expression for celerity given by Keulegan and Patterson (1940).

Numerical Evaluation of Elliptic Functions

Since the complementary parameter m' can be as small as 10^{-40} ,

the numerical evaluation of elliptic functions for cnoidal waves requires different treatment than for most other applications.

The methods of evaluation given here were extracted from Abramowitz and Stegun (1965), and represent the most efficient and accurate methods found.

The first step in computing any of the elliptic function is to set up the Arithmetic/Geometric Mean (AGM) scale:

$$a_0 = 1$$

$$b_0 = \sqrt{m'}$$

$$c_0 = \sqrt{1 - m'}$$

$$a_1 = \frac{1}{2} (a_0 + b_0)$$

$$b_1 = \sqrt{a_0 b_0}$$

$$c_1 = \frac{1}{2} (a_0 - b_0)$$

$$a_N = \frac{1}{2} (a_{N-1} + b_{N-1}) \quad b_N = \sqrt{a_{N-1} b_{N-1}} \quad c_N = \frac{1}{2} (a_{N-1} - b_{N-1})$$

Stop at the N^{th} step, where $a_N = b_N$ (i.e. $c_N = 0$) to the accuracy desired. (Typically, $c_6 < 10^{-5}$.)

From the AGM, the elliptic functions are calculated as follows:

1. First Complete Elliptic Integral K.

$$K = \pi / 2a_N$$

2. Second Complete Elliptic Integral E.

$$E = K \{ 1 - \frac{1}{2} (c_0^2 + 2c_1^2 + 2^2 c_2^2 + \dots + 2^N c_N^2) \}$$

3. Jacobian Elliptic Function $P = cn(w)$.

a) Find $\phi_N = 2^N a_N w$ in radians.

b) Compute successively $\phi_{N-1}, \phi_{N-2}, \dots, \phi_1, \phi_0$ from the recursive relation:

$$\sin(2\phi_{n-1} - \phi_n) = \frac{c_n}{a_n} \sin \phi_n .$$

c) Evaluate $P = cn(w) = \cos \phi_0$.

4. Inverse Jacobian Elliptic Function $w = cn^{-1}(P)$.

a) Find ϕ_0 from:

$$\cos \phi_0 = P = cn(w) .$$

b) Compute successively $\phi_1, \phi_2, \dots, \phi_N$ from the recursive relation:

$$\tan(\phi_{n+1} - \phi_n) = \frac{b_n}{a_n} \tan \phi_n .$$

c) Evaluate:

$$w = cn^{-1}(P) = \phi_N / 2^N a_N .$$

The recursive relation is ambiguous by multiples of π . However w converges to the exact value from below so the correct ϕ_n can be found by evaluating w at each step and using:

$$w(\phi_n) \geq w(\phi_{n-1})$$

5. Second Incomplete Elliptic Integral $E(w)$.

$$E(w) = \frac{E}{K} w + c_1 \sin \phi_1 + c_2 \sin \phi_2 + \dots + c_N \sin \phi_N ,$$

where ϕ_n are those calculated from the recursive relations above.

Using the relationships A.1 to A.4 and the numerical methods described above, most cnoidal wave problems can be solved in straight-

forward manner by computer. However, one important problem that requires special treatment is: given H and T , find m' . Iterative schemes (fixed point, Newton's Rule, Regula Falsi) do not converge; hence, an *ad hoc* trial-and-error scheme was developed. The scheme is presented with no claims of elegance.

For the given H , period can be expressed as a function of m' :

$$T(m') = L/c$$

The object is to find the m' for which $T(m')$ equals the given period T , that is:

$$T - T(m') = 0$$

The first step is to compute $T - T(m')$ for:

$$m' = 10^{-j} \quad j = 0, 1, 2, 3, \dots$$

until:

$$\operatorname{sgn}(T - T(10^{-j})) \neq \operatorname{sgn}(T - T(10^{-j+1}))$$

Then it is inferred that $T - T(m') = 0$ for $10^{-j} \leq m' \leq 10^{-j+1}$.

The second step involves finding k_1 in:

$$m' = k_1 \times 10^{-j}$$

and:

$$m'_1 = (k_1 + 1) \times 10^{-j}$$

such that:

$$\operatorname{sgn}(T - T(m')) \neq \operatorname{sgn}(T - T(m'_1))$$

where k_1 is a digit between 1 and 9.

The third step is to find k_2 in:

$$m' = (k_1 + k_2 \times 10^{-1}) \times 10^{-j} ,$$

and:

$$m'_1 = (k_1 + (k_2 + 1) \times 10^{-1}) \times 10^{-j} ,$$

such that:

$$\operatorname{sgn}(T - T(m')) \neq \operatorname{sgn}(T - T(m'_1)) ,$$

where k_2 is a digit between 1 and 9.

The n^{th} step is to find k_n in:

$$m' = (k_1 + k_2 \times 10^{-1} + k_3 \times 10^{-2} + \dots + k_n \times 10^{-n+1}) \times 10^{-j} ,$$

and:

$$m'_1 = m' + 10^{-n-j+1} ,$$

such that:

$$\operatorname{sgn}(T - T(m')) \neq \operatorname{sgn}(T - T(m'_1)) ,$$

where k_n is a digit between 1 and 9. This process is continued for as many times as the number of significant figures required for m' .

To elucidate the procedure, consider an example where 3 significant figures are required and it is found that $j = 3$. Then the required m' is one of the 900 numbers between 0.00100 and 0.00999. The second step will determine the first nonzero digit after the decimal point (k_1), the third step will determine the second nonzero digit (k_2) and the fourth step will determine the third nonzero digit (k_3). The final result will be $m' = 0.00k_1k_2k_3$.

APPENDIX BThe Equation from Boussinesq (1872), the Boussinesq Equations and Solitary Waves

In Section 3.3.1.5, in discussing the accuracy of the numerical scheme it was pointed out that although the solitary wave is an exact solution of the KdV equation (Eq. (3.22)), it is not an exact solution of the Boussinesq equations (Eqs. (3.67) and (3.68)). However, the original equation derived by Boussinesq (1872) (and also by Keulegan and Patterson (1940)):

$$\eta_{tt} = g\eta_{xx} + gh \frac{\partial^2}{\partial x^2} \left(\frac{3\eta}{2h} + \frac{h^2}{3} \eta_{xx} \right) , \quad (B.1)$$

does have the solitary wave as an exact solution.

A question which arises is: how can the Boussinesq equations, Eqs. (3.67) and (3.68), and the equation from Boussinesq (1872), Eq. (B.1), have different exact solutions if they are of the same order of approximation, i.e., $O(\alpha^2, \alpha\beta, \beta^2)$, in terms of the parameters defined in Section 3.1?

The answer is found in the early stages of the derivations of the equations. In the method used by Boussinesq (1872) and Keulegan and Patterson (1940), in evaluating the nonlinear terms in the dynamic boundary condition:

$$\phi_t + \frac{1}{2} (u^2 + v^2) + g\eta = 0 , \quad (B.2)$$

the approximations $v \approx 0$ and $u \approx \sqrt{\frac{g}{h}} \eta$ are used. Similarly in the kinematic boundary condition:

$$\eta_t + u\phi_x = \phi_y \quad , \quad (B.3)$$

the approximation $u \approx \sqrt{\frac{g}{h}} \eta$ is used.

Although of the same order of approximation, this is slightly different to the approach of Korteweg and de Vries (1895) and Whitham (1974) where u and v are expressed as ϕ_x and ϕ_y respectively and order of magnitude sorting is done with all the terms included. In addition, in deriving Eq. (B.1) the approximation $\frac{\partial}{\partial t} \approx -\sqrt{gh} \frac{\partial}{\partial x}$ is used but it is not necessary to make this approximation in deriving the Boussinesq equations, Eqs. (3.67) and (3.68).

APPENDIX CThe Linear Nondispersive Theory for a Single Harmonic Wave

The theory developed here is essentially that presented by Wong *et al.* (1964). Using the nomenclature of Section 3.4, the variables are normalized as follows:

$$x = x^*/L \quad t = t^* \sqrt{gh_1} / L$$

$$\eta = \eta^*/h_1 \quad h = h^*/h_1$$

Equation (3.108) becomes:

$$\eta_{tt} = (h\eta_x)_x \quad . \quad (C.1)$$

Considering only the steady state solution, the time dependence of $\eta(x, t)$ can be separated from the x dependence by assuming the solution has the form:

$$\eta(x, t) = \zeta(x)e^{-i\omega t} \quad . \quad (C.2)$$

Substituting (C.2) in (C.1) results in the nondimensional ordinary differential equation:

$$(h\zeta_x)_x + \omega^2 \zeta = 0 \quad . \quad (C.3)$$

Referring to Fig. 3.17, the general solutions of (C.3) for Regions I, II, and III are:

$$\text{Region I:} \quad \zeta_1 = A_1 e^{i\omega x} + A_2 e^{-i\omega x} \quad , \quad (C.4)$$

$$\text{Region II: } \zeta_2 = B_1 J_0 \left(\frac{2\omega}{1-h_2} \sqrt{h_2 - (1-h_2)x} \right) + B_2 Y_0 \left(\frac{2\omega}{1-h_2} \sqrt{h_2 - (1-h_2)x} \right) , \quad (C.5)$$

$$\text{Region III: } \zeta_3 = C_1 e^{i\omega x / \sqrt{h_2}} + C_2 e^{-i\omega x / \sqrt{h_2}} , \quad (C.6)$$

where A_1 , A_2 , B_1 , B_2 , C_1 and C_2 are constants to be determined and $J_0(\cdot)$ and $Y_0(\cdot)$ are the Bessel functions of zero order of the first and second kind respectively.

The 6 constants are determined as follows:

- (1) In Region I the rightward travelling wave is the incident wave which has amplitude A . Thus $A_1 = A$.
- (2) In Region III it is assumed that there is no wave travelling leftward from $x = \infty$, therefore $C_2 = 0$.
- (3) The surface elevation at the boundary of Region I and Region II must be the same:

$$\zeta_1(-1) = \zeta_2(-1) ,$$

thus:

$$A e^{-i\omega} + A_2 e^{i\omega} = B_1 J_0 \left(\frac{2\omega}{1-h_2} \right) + B_2 Y_0 \left(\frac{2\omega}{1-h_2} \right) . \quad (C.7)$$

Similarly at the boundary of Regions II and III:

$$\zeta_2(0) = \zeta_3(0) ,$$

thus:

$$B_1 J_0 \left(\frac{2\omega}{1-h_2} \sqrt{h_2} \right) + B_2 Y_0 \left(\frac{2\omega}{1-h_2} \sqrt{h_2} \right) = C_2 . \quad (C.8)$$

(4) The surface slope must also be continuous at the boundary of Regions I and II:

$$\zeta_{1_x}(-1) = \zeta_{2_x}(-1) ,$$

thus:

$$A_1 e^{-i\omega} - A_2 i e^{i\omega} = B_1 J_1\left(\frac{2\omega}{1-h_2}\right) + B_2 Y_1\left(\frac{2\omega}{1-h_2}\right) . \quad (C.9)$$

Similarly at the boundary of Regions II and III:

$$\zeta_{2_x}(0) = \zeta_{3_x}(0) ,$$

thus:

$$B_1 J_1\left(\frac{2\omega}{1-h_2} \sqrt{h_2}\right) + B_2 Y_1\left(\frac{2\omega}{1-h_2} \sqrt{h_2}\right) = i C_1 , \quad (C.10)$$

Equations (C.7), (C.8), (C.9) and (C.10), which must be solved simultaneously, may be written in matrix form:

$$\begin{bmatrix} e^{i\omega} & -J_0 & -Y_0 & 0 \\ ie^{i\omega} & J_1 & Y_1 & 0 \\ 0 & J_0^* & Y_0^* & -1 \\ 0 & J_1^* & Y_1^* & -i \end{bmatrix} \begin{Bmatrix} A_2 \\ B_1 \\ B_2 \\ C_1 \end{Bmatrix} = \begin{Bmatrix} -A \\ A_1 \\ 0 \\ 0 \end{Bmatrix} \quad (C.11)$$

where

$$J_0 \equiv J_0\left(\frac{2\omega}{1-h_2}\right)$$

$$Y_0 \equiv Y_0\left(\quad\right)$$

$$J_1 \equiv J_1\left(\quad\right)$$

$$Y_1 \equiv Y_1\left(\quad\right) ,$$

and

$$\begin{aligned} J_o^* &\equiv J_o \left(\frac{2\omega}{1 - h_2} \sqrt{h_2} \right) \\ Y_o^* &\equiv Y_o \left(\quad \right) \\ J_1^* &\equiv J_1 \left(\quad \right) \\ Y_1^* &\equiv Y_1 \left(\quad \right) \end{aligned} .$$

Defining:

$$\begin{aligned} \alpha &= J_o^* Y_o - J_o Y_o^* + J_1^* Y_1 - J_1 Y_1^* & , \\ \beta &= -J_o^* Y_1 - J_o Y_1^* + J_1^* Y_o + J_1 Y_o^* & , \\ \gamma &= J_o^* Y_o - J_o Y_o^* - J_1^* Y_1 + J_1 Y_1^* & , \\ \delta &= J_o^* Y_1 - J_o Y_1^* + J_1^* Y_o - J_1 Y_o^* & , \end{aligned} \quad (C.12)$$

the determinant of the matrix in (C.11) is:

$$\Delta = e^{i\omega} (\alpha + i\beta) \quad . \quad (C.13)$$

The solution of (C.11) is:

$$\left\{ \begin{array}{l} A_2 \\ B_1 \\ B_2 \\ C_1 \end{array} \right\} = \frac{\Delta}{e^{i\omega} (\alpha + i\beta)} \left\{ \begin{array}{l} e^{-i\omega} (\gamma + i\delta) \\ 2(Y_o^* + iY_1^*) \\ -2(J_o^* - iJ_1^*) \\ \frac{-2i(1 - h_2)}{\pi\omega\sqrt{h_2}} \end{array} \right\} , \quad (C.14)$$

where, in evaluating C_1 , use has been made of the identity:

$$J_0(z)Y_1(z) - J_1(z)Y_0(z) \equiv \frac{-2}{\pi z} . \quad (C.15)$$

The full solution is:

$$\text{Region I: } \eta_1(x, t) = A e^{i\omega(x-t)} + A_2(\omega) e^{-i\omega(x+t)} , \quad (C.16)$$

$$\begin{aligned} \text{Region II: } \eta_2(x, t) = & B_1(\omega) J_0 \left[\frac{2\omega}{1-h_2} \sqrt{h_2 - (1-h_2)x} \right] e^{-i\omega t} \\ & + B_2(\omega) Y_0 \left[\frac{2\omega}{1-h_2} \sqrt{h_2 - (1-h_2)x} \right] e^{-i\omega t} , \end{aligned} \quad (C.17)$$

$$\text{Region III: } \eta_3(x, t) = C_1(\omega) e^{i\omega(x/\sqrt{h_2} - t)} , \quad (C.18)$$

with $A_2(\omega)$, $B_1(\omega)$, $B_2(\omega)$ and $C_1(\omega)$ given by equations (C.14)

APPENDIX DTests of the Inverse Scattering Numerical Schemes

Since the majority of the waves under consideration in this investigation were of sech^2 shape, the tests performed on the numerical schemes described in Section 3.5.3 also were for waves with sech^2 shape. These waves have the advantage that exact analytical results are available for comparison (see Eq. (3.140)).

It was found for both schemes the wave height H in the initial condition:

$$\eta(x,0) = H \text{ sech}^2 kx , \quad (D.1)$$

did not affect the results. To illustrate this, the results for Scheme 2, in which no parameters other than H and k are involved, will be presented first and later the results for Scheme 1, which involves several parameters, will be presented for one relative wave height, H/h .

The results for Scheme 2 are presented in Table D.1 where the ratio of the calculated to the exact height of the leading solitary wave is listed as a function of the relative initial wave height, H/h , and the wave number relative to that of the solitary wave of the same height, i.e., k/κ where $\kappa = \sqrt{\frac{3}{4} \frac{H}{h^3}}$. The calculated height is obtained from the numerical theory discussed in Section 3.5 and for purposes of this comparison the exact height is defined as that given by Eq. (3.140). Recall from Section 3.5.2 that for wave number ratio

Table D.1 Ratio of the calculated to the exact wave height of the leading solitary wave using Scheme 2.

$k/\kappa > 1$ only one solitary wave emerges and for $k/\kappa < 1$ more than one solitary wave emerges. The table shows the accuracy of the numerical scheme is independent of the relative wave height H/h . However, it is dependent on the wave number ratio k/κ and it has an accuracy of better than 1% for waves from which more than one solitary wave will emerge but an error of up to 30% for waves from which only one solitary wave emerges.

For Scheme 1, it will be recalled, as discussed in Section 3.5.3.1, two other parameters must be prescribed: the length, L , defining the trigonometric functions and the number of functions, N . For the relative wave height $H/h = 0.1$, a number of tests were conducted for wave number ratios $k/\kappa = 0.25, 0.5, 1, 2$ and 4 where, for $k/\kappa = 1, 2$ and 4 , only one wave emerges but for $k/\kappa = 0.5$, three waves emerge and for $k/\kappa = 0.25$, six waves emerge. The results, in the form of the ratios of the computed to the exact wave heights, are presented in Table D.2 where (a) is for $k/\kappa = 1, 2$ and 4 , (b) is for $k/\kappa = 0.5$ and (c) is for $k/\kappa = 0.25$. The results are listed as functions of the length ratio L/L_s where $L_s = 10.6/k$ (which was used because $\text{sech}^2 5.3 = 1 \times 10^{-4}$) and for (a) 20 trigonometric functions were used while for (b) and (c) 50 functions were used. The tables show there is an optimum length, L , for maximum accuracy. For waves from which a single solitary wave emerges, Table D.2(a) shows a good rule of thumb is to make the length ratio the same as the wave number ratio or, equivalently, put $L \approx 10.6/\kappa$, i.e., the "length" of the solitary wave of the same height as the initial wave. For waves from which

Table D.2 Ratio of the calculated to the exact heights of the emerging solitary waves using Scheme 1.

(a) $N = 20$. Single wave emerges.

$\frac{k/\kappa}{L/L_s}$	1.0	2.0	4.0
0.75	0.9965		
1.0	1.0000		
1.5	1.0000	0.9852	
2.0	0.9979	0.9973	
3.0		0.9949	0.8609
4.0		0.9802	0.9567
6.0			0.9743
8.0			0.9507

(b) $N = 50$. $k/\kappa = 0.5$ Three waves emerge.

$\frac{L}{L_s}$	Wave 1	Wave 2	Wave 3
1.5	0.9995	0.9996	0.9660
2.0	0.9995	0.9995	0.9923
2.5	0.9992	0.9995	0.9953
3.0	0.9977	0.9897	0.9258

(c) $N = 50$. $k/\kappa = 0.25$ Six waves emerge.

$\frac{L}{L_s}$	Wave 1	Wave 2	Wave 3	Wave 4	Wave 5	Wave 6
1.0	0.9995	0.9995	0.9993	0.9994	0.9966	-3.76
1.5	0.9993	0.9995	0.9993	0.9998	0.9900	0.0959
2.0	0.9994	0.9994	0.9979	0.9953	0.9829	0.6161
2.5	0.9993	0.9955	0.9797	0.9522	0.8563	0.0205
3.0	0.9941	0.9582	0.8846	0.7158	0.4585	-1.10

more than one solitary wave emerge, the best length ratio appears to be $L/L_s \approx 2.0$.

In using this scheme it was found advisable to allow the number of functions, N , to increment until the desired accuracy was reached rather than to use a pre-set value of N . However, the computation cost increases considerably with N so some upper limit needs to be placed on N .

APPENDIX EThe Nonlinear Nondispersive Theory for the Propagation of sech^2 Waves

In this section the solution of the nonlinear nondispersive theory as given in characteristic form by Eqs. (3.17) will be applied to the particular case of a wave given by:

$$\eta(o, t) = H \text{ sech}^2 \Omega t \quad , \quad (E.1)$$

propagating into still water with a constant depth, h .

For the case of waves propagating into still water the method of characteristics simplifies considerably because as shown by, e.g., Henderson (1966) the characteristics are straight lines with slope:

$$\frac{dx}{dt} = \bar{u} + c \quad , \quad (E.2)$$

where

$$c = \sqrt{g(h + \eta)} \quad , \quad (E.3)$$

and between these characteristics the quantity $(\bar{u} - 2c)$ is constant. Hence, referring to Fig. E.1, which shows the $x - t$ plane for the case of a wave given by Eq. (E.1); the velocity \bar{u} and the celerity c are constant along the characteristics and the velocity can be expressed as a function of the celerity:

$$\bar{u} = 2(c - c_o) \quad , \quad (E.4)$$

where $c_o = \sqrt{gh}$.

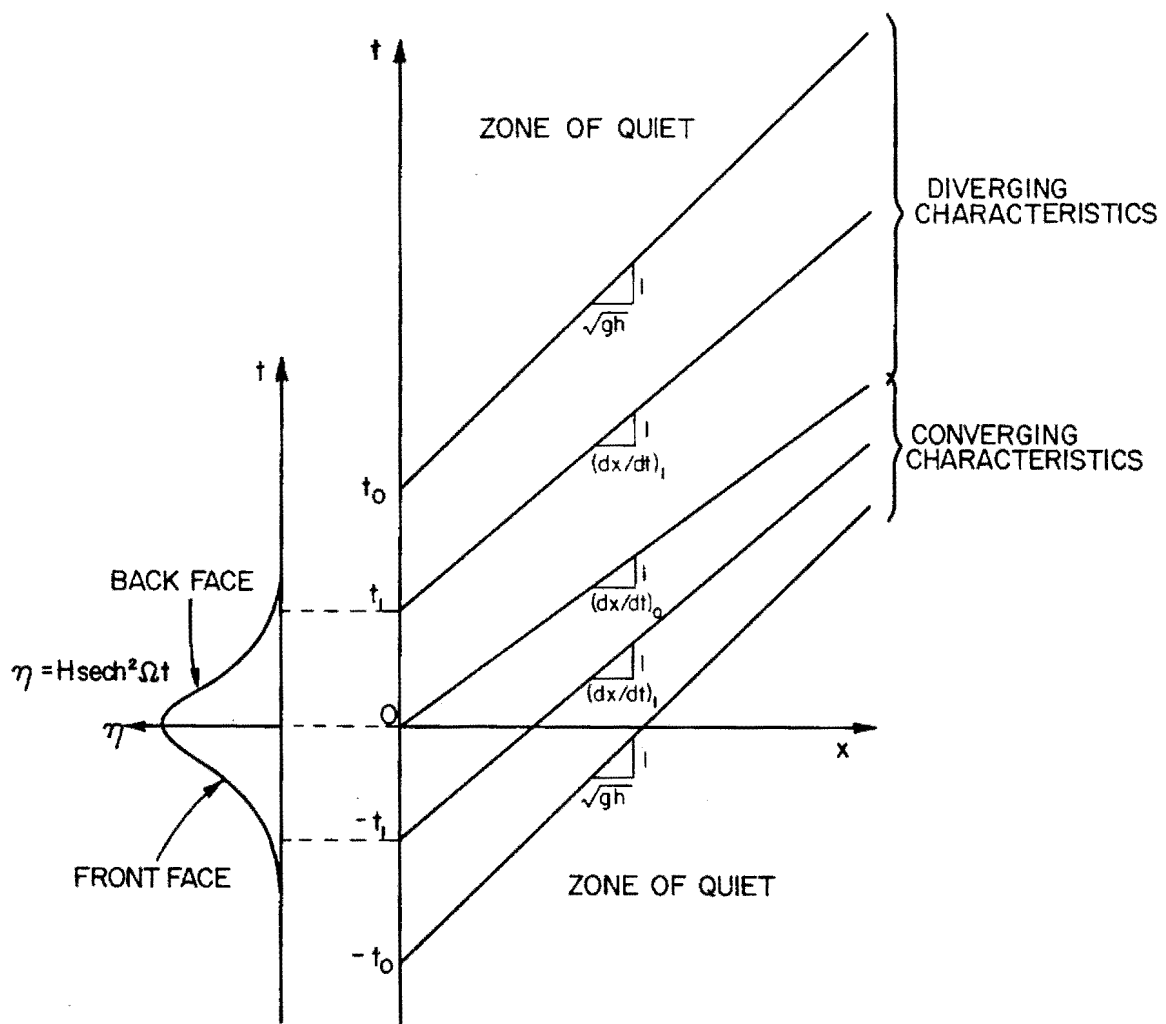


Fig. E.1 The $x-t$ plane for a sech^2 wave propagating into still water by the nonlinear nondispersive theory.

Substituting Eq. (E.4) into Eq. (E.2) gives:

$$\frac{dx}{dt} = 3c - 2c_o \quad , \quad (E.5)$$

and since the celerity c is constant along the characteristics Eq. (E.5) can be integrated to yield:

$$x = (3c - 2c_o) (t - t) \quad , \quad (E.6)$$

or, equivalently:

$$t = \frac{x}{3c - 2c_o} + t \quad , \quad (E.7)$$

where t is the intercept of the characteristic with the t axis and thus $\eta(t) \equiv \eta(0, t)$. Eqs. (E.6) and (E.7) are not in the usual functional form because the variables usually considered the independent variables, x and t , are expressed as functions of the variable usually considered the dependent variable, η , instead of vice versa. However, it is found more convenient to use the solutions in the form of Eqs. (E.6) and (E.7) because of their relative simplicity.

The time slope of the wave, η_t , is found by differentiating Eq. (E.7) partially with respect to t to yield:

$$1 = -3x(3c - 2)^{-2} \frac{\partial c}{\partial t} + \frac{\partial t}{\partial t} \quad , \quad (E.9)$$

and, using the relation $\frac{\partial \eta}{\partial t} = \frac{d\eta}{dt} \frac{\partial t}{\partial t}$, one obtains:

$$\frac{\partial \eta}{\partial t} = \frac{d\eta}{dt} \left[1 - \frac{3}{2} x \sqrt{\frac{g}{h}} \frac{d\eta}{dt} (3c - 2c_o)^{-2} \left(1 + \frac{\eta}{h} \right)^{-\frac{1}{2}} \right]^{-1} . \quad (E.10)$$

Eq. (E.10) is applicable to any wave, $\eta(t)$, but for the case of

a wave given by Eq. (E.1), Eq. (E.10) becomes:

$$\frac{\partial \eta}{\partial t} = -2\Omega \eta \left(1 - \frac{\eta}{H}\right)^{\frac{1}{2}} \left[1 - 3\Omega x \sqrt{\frac{g}{h}} \eta \left(1 - \frac{\eta}{H}\right)^{\frac{1}{2}} (3c - 2c_0)^{-2} \left(1 + \frac{\eta}{h}\right)^{-\frac{1}{2}} \right]^{-1} \quad (E.11)$$

For a sech^2 wave the front face of the wave steepens as it propagates while the back face flattens as is indicated by the converging and diverging characteristics in Fig. E.1. Breaking occurs at the location where the front face of the wave becomes vertical, i.e., where the derivative $\frac{\partial \eta}{\partial t} = \infty$, which occurs when the expression in the brackets [] in Eq. (E.11) is zero. Notice that for this theory the wave height, H , remains constant even at breaking. This is because the celerity and the velocity are constant along the characteristics which are straight lines. The actual point of breaking is where the front face first becomes vertical, i.e. the minimum x for the expression in brackets to be zero. This minimum x , denoted the distance to breaking and defined as x_b , is found by algebraic manipulation of Eq. (E.11) to be:

$$\frac{\partial x_b}{\partial t} = \frac{1}{3} (c_*^2 - 1)^{-1} \left(\frac{H}{h}\right)^{\frac{1}{2}} \left(\frac{H}{h} + 1 - c_*^2\right)^{-\frac{1}{2}} (3c_* - 2)^2 c_* \quad , \quad (E.12)$$

where c_* is the root of:

$$4c_*^4 - 3\left(\frac{H}{h} + 3\right)c_*^3 - 2\left(\frac{H}{h} + 1\right)c_*^2 + 9\left(\frac{H}{h} + 1\right)c_* - 2\left(\frac{H}{h} + 1\right) = 0 \quad , \quad (E.13)$$

which lies in the interval $1 < c_* < \sqrt{1 + \frac{H}{h}}$.

The maximum absolute slope, $|\eta_t|_{\max}$, at any location in the interval $0 \leq x \leq x_b$ is:

$$|\eta_t|_{\max} = 2\Omega h \left[\left(\frac{H}{h} \right)^{\frac{1}{2}} (c_*^2 - 1) \left(1 + \frac{H}{h} - c_*^2 \right)^{-\frac{1}{2}} - \frac{3\Omega x}{\sqrt{gh}} (3c_* - 2)^{-2} c_*^{-1} \right]^{-1} \quad (E.14)$$

where c_* is the root of:

$$-c_*^3 (3c_* - 2)^3 \left(\frac{H}{h} \right)^{\frac{1}{2}} \left(3c_*^2 - 3 - 2 \frac{H}{h} \right) + \frac{3\Omega x}{\sqrt{gh}} (c_*^2 - 1)^2 \left(1 + \frac{H}{h} - c_*^2 \right)^{3/2} (2 - 9c_*) = 0 \quad (E.15)$$

which lies in the interval $1 < c_* < \sqrt{1 + \frac{H}{h}}$.

The location at which the front face reaches a particular maximum absolute slope, $|\eta_t|_{\max}$, is:

$$\frac{\Omega x}{\sqrt{gh}} = (3c_* - 2)c_* \left(\frac{H}{h} \right)^{\frac{1}{2}} (c_*^2 - 1)^{-1} \left(1 + \frac{H}{h} - c_*^2 \right)^{-\frac{1}{2}} - 2\Omega h / |\eta_t|_{\max} \quad (E.16)$$

where c_* is the root of:

$$c_*^2 (3c_* - 2) \left(3c_*^2 - 3 - 2 \frac{H}{h} \right) - (c_*^2 - 1) \left(1 + \frac{H}{h} - c_*^2 \right) (2 - 9c_*) + 2\Omega h |\eta_t|_{\max}^{-1} \left(\frac{H}{h} \right)^{-\frac{1}{2}} (c_*^2 - 1)^2 \left(1 + \frac{H}{h} - c_*^2 \right)^{3/2} (2 - 9c_*) = 0 \quad (E.17)$$

which lies in the interval $1 < c_* < \sqrt{1 + \frac{H}{h}}$.

Notice in Eqs. (E.12) to (E.17) the explicit dependence on the frequency, Ω , can be removed by normalizing the independent variables, x and t , to be $\Omega x / \sqrt{gh}$ and Ωt respectively. Hence, the frequency, Ω , like the depth, h , is an independent parameter.

APPENDIX FTable F.1 Solitary waves transmitted over a slope: the difference between the linear nondispersive and the nonlinear dispersive theories.

L/ℓ	h_1/h_2	H_T/h_1	$\frac{H_T - H_{T_{lin}}}{H_{T_{lin}}}$	$\frac{S - S_{lin}}{S_{lin}}$
0.530	3.000	0.050	0.002	0.070
		0.100	0.002	0.150
		0.150	0.002	0.210
1.030	2.000	0.050	0.001	0.140
		0.100	0.001	0.340
		0.150	0.010	0.540
1.030	4.000	0.050	0.030	0.420
		0.100	0.060	0.950
		0.150	0.100	1.530
1.560	3.000	0.050	0.010	0.180
		0.100	0.020	0.400
		0.150	0.040	0.630
2.000	2.000	0.050	0.001	0.140
		0.100	0.020	0.340
		0.150	0.050	0.540
2.000	3.000	0.050	0.020	0.260
		0.100	0.040	0.510
		0.150	0.060	0.890
2.000	4.000	0.050	0.020	0.410
		0.100	0.050	0.930
		0.150	0.090	1.510
3.040	3.000	0.050	0.020	0.300
		0.100	0.040	0.750
		0.150	0.100	1.230
4.080	2.000	0.050	0.020	0.240
		0.100	0.070	0.590
		0.150	0.120	0.930
4.080	3.000	0.050	0.030	0.370
		0.100	0.110	0.920
		0.150	0.180	1.760
4.080	4.000	0.050	0.050	1.040
		0.100	0.230	3.070
		0.150	0.460	5.530
5.130	3.000	0.050	0.060	0.610
		0.100	0.150	1.780
		0.150	0.240	2.720